Measurement of the ^{23} U fission antineutrino spectrum by the STEREO experiment and preparation of the NUCLEUS coherent neutrino scattering experiment

Rudolph Rogly

université
PARIS-SACLAY

Measurement of the ^{235}U fission antineutrino spectrum by the STEREO experiment and preparation of the NUCLEUS coherent neutrino scattering experiment.

Mesure du spectre antineutrino de fission de l' ^{235}U *par l'expérience* STEREO *et préparation de l'expérience* NUCLEUS *de diffusion cohérente de neutrinos.*

Thèse de doctorat de l'université Paris-Saclay

École doctorale n°576 particules hadrons énergie et noyau : instrumentation, imagerie, cosmos et simulation (PHENIICS)
Spécialité de doctorat: Physique des Particules
Graduate School: Physique, Référent: Faculté des sciences d'Orsay

Thèse préparée dans l'unité de recherche:
Département de Physique Nucléaire - DRF-IRFU (Université Paris-Saclay, CEA)
sous la direction de David LHUILLIER, directeur de recherche.

Thèse soutenue à Paris-Saclay, le 3 octobre 2022, par

Rudolph ROGLY

Composition du jury

Guillaume Mention Directeur de recherche, CEA, IRFU/DPhP, Université Paris-Saclay	Président
Christine Marquet Directrice de recherche, LP2i, Université de Bordeaux	Rapporteure & Examinatrice
Susanne Mertens Professeure adjointe, Technical University of Munich Directrice de recherche, MPIK-Munich	Rapporteure & Examinatrice
Nathaniel Bowden Directeur de recherche, Lawrence Livermore National Laboratory	Examinateur
Joachim Kopp Professeur, Johannes Gutenberg University Mainz Directeur de recherche, CERN/Theoretical Physics Department	Examinateur
David Lhuillier Directeur de recherche, CEA, IRFU/DPhN, Université Paris-Saclay	Directeur de thèse

THESE DE DOCTORAT
NNT : 2022UPASP104

Contents

Introduction

First postulated in 1930 by Pauli [1] to save the principle of energy conservation in the β decay process, and discovered in 1956 by the reactor antineutrino experiment of Cowan and Reines [2], neutrinos are particles whose history has been entangled with nuclear reactors since the last century. These particles were proved to come in three active flavors, coupling to matter via the weak (and gravitational) interaction. They also brought the first experimental evidence of physics beyond the Standard Model, with the identification of neutrino oscillations. Reactor antineutrino experiments played a key role in the characterization of this mechanism. They still constitute a portal of interest to investigate the neutrino properties as nuclear reactors are a very intense source of this weakly-interacting particle.

There remains indeed two pending data-to-prediction discrepancies in reactor antineutrino physics, namely the reactor antineutrino anomalies. They consist in a significant disagreement between the measured and predicted reactor antineutrino spectra. To solve this puzzle, one can either search for potential biases in the prediction, or interpret these anomalies as the sign of new physics. In particular, the so-called flux anomaly can be seen as the short-baseline disappearance of the electronic antineutrinos emitted by nuclear reactors, that would oscillate towards a new neutrino state, that would necessarily be sterile. Such discovery would be the first experimental evidence of an additional neutrino state beyond the Standard Model three-flavor pattern.

As a further probe to test the Standard Model, a new interaction channel involving neutrinos is now within experimental reach: the Coherent Elastic Neutrino-Nucleus Scattering (CEνNS). Postulated by Freedman in 1974 [3] and measured for the first time in 2017 by the COHERENT collaboration [4], the physics and technological potential of this process triggered a vast experimental program, including experiments operated in nuclear reactor experimental sites.

In this doctoral thesis, we report the final results of the Stereo experiment and the preparatory work on the muon veto of the forthcoming Nucleus experiment.

Stereo was designed to investigate the reactor anomalies, for the specific case of the antineutrino spectrum induced by the sole fission of the ^{235}U isotope. It aimed at investigating the sterile neutrino hypothesis as the explanation for the flux anomaly, while performing a precision measurement of the ^{235}U induced antineutrino spectrum. This measurement is to serve as a reference for the comparisons with the most recent predictions of the reactor antineutrino spectrum as well as a benchmark for other reactor antineutrino experiments. This will be detailed in the first part of this dissertation.

Nucleus is a reactor antineutrino experiment, conceived to measure the CEνNS process. Given the moderate counting rate that is expected for the signal, efficient background rejection technics are required in order to perform a precision measurement of the cross-section of this process. As a ground-level particle physics experiment, the main background

to be discriminated against is the cosmogenic background. In this work, we focused on the complete commissioning of a prototype panel of the muon veto, that will be used to reject part of this background, induced by the atmospheric muons. This will be reported in the last part of this dissertation.

In the introductory Chapter 1, we remind some key elements of neutrino physics, with special focus on the discovery and description of neutrino oscillations, the reactor antineutrino anomalies and the two detection channels used in reactor antineutrino experiments, the Inverse Beta Decay (IBD) that applies to the STEREO experiment, and the CEνNS process that is investigated by the NUCLEUS experiment.

In Chapters 2 and 3, we present the STEREO experiment and the simulation that was implemented to describe the response of the STEREO detector. In Chapter 4, we detail a key contribution of this doctoral work to the STEREO analysis, consisting in the derivation and constraining of the energy scale of the experiment. This is a prerequisite for an accurate comparison of the experimental data with a model, as well as for a precision study on the sterile neutrino search. After outlining the STEREO antineutrino signal extraction procedure in Chapter 5, we focus in Chapter 6 on the final results of the STEREO experiment, starting with the oscillation analysis for the sterile neutrino search, and finishing with the precision analysis of the STEREO unfolded spectrum. The deconvolution procedure that was developed and implemented to extract this spectrum from the data is another major contribution of this doctoral work to the STEREO analysis. At last, in Chapter 7, we extend our deconvolution framework to experimental data sets other than that of STEREO in order to gain further insights on the reactor anomalies.

The last two chapters are dedicated to NUCLEUS. In Chapter 8, we briefly describe the experiment, whereas Chapter 9 details the various studies carried out in this thesis to characterize and validate the performance of a prototype panel for the preparation of the NUCLEUS muon veto assembly.

Chapter 1

Scientific context and motivations

Amongst the most abundant particles in the Universe after photons, neutrinos yet remain elusive particles to this date, playing a prominent role at the cross-road of various research fields in fundamental physics.

In cosmology, the neutrinos produced subsequently to the Big Bang potentially offer a window to study the Universe at a time prior to the epoch accessible by the cosmic microwave background analysis. This cosmic neutrino background is still to be observed, and will be tracked by current [5] and future [6, 7] experiments. In astrophysics, the Diffuse Supernova Neutrino Background (DSNB) allows to probe the supernovae neutrino emission and the cosmic core-collapse rate [8]. Its detection is still to be observed, but is now within experimental reach [9, 10].

Man-made neutrino sources such as neutrino beams from accelerators have also been employed to probe the structure of hadronic matter via deep inelastic scattering (DIS), and have provided strong evidence to validate quantum chromodynamics (QCD) as the theory for the strong interaction [11].

On top of being probes to various physical processes and intrinsic particle properties, neutrinos constitute one of the building blocks of the Standard Model (SM) of particle physics. Notably, processes involving the production and interaction of neutrinos, such as the Wu experiment that shed light on the parity violation in the weak interaction [12], provided key inputs for the formulation of the electroweak theory.

The neutrinos that will be studied in this doctoral thesis are the nuclear reactor induced electronic (anti)neutrinos. As we will see, reactor neutrino physics has a long-established history, starting from the very discovery of this particle by the reactor neutrino experiment of Cowan and Reines [2], and focuses at the present time on the measurement of neutrino oscillation parameters − that popped out over the last decades as an unambiguous evidence of physics beyond the Standard Model in the neutrino sector −, the determination of the neutrino mass hierarchy, and the investigation on potential other neutrino eigenstates than the three flavor eigenstates postulated in the Standard Model. Furthermore, as we will see, measurements of reactor antineutrino spectra, when confronted to predictions, can bring supplemental information on the nuclear physics models in themselves, such that reactor neutrino physics is found to be intertwined not only with particle physics but also with nuclear physics. In line with this idea, neutrinos may as well find a direct societal application, in the monitoring of reactors for nuclear safety [13].

1.1 Neutrino oscillations

In the formulation of the SM, neutrinos are considered as massless particles, coming in three active flavor eigenstates (electronic, muonic, tauic) and are left-handed in terms of helicity, whereas the antineutrinos are right-handed. Whereas the measurement of the width of the Z boson confirmed the second assertion [14], and the third assertion has never failed to agree with the observations, experimental evidence of the so-called neutrino oscillation mechanism proved that the first assertion turned out to be wrong.

1.1.1 PMNS matrix

Neutrino oscillation is a mechanism that occurs only if neutrinos have non-zero mass. It originates from the fact that the interaction/flavor eigenstates differ from the propagation/mass eigenstates. For a neutrino propagating in the vacuum, the two eigenbases can be mapped to each other through the Pontecorvo-Maki-Nakagawa-Sakata (PMNS) matrix [15, 16], assumed to be unitary:

$$\underbrace{\begin{bmatrix}\nu_e\\ \nu_\mu\\ \nu_\tau\end{bmatrix}}_{\text{flavor eigenstates}} = \underbrace{\begin{bmatrix}U_{e1} & U_{e2} & U_{e3}\\ U_{\mu 1} & U_{\mu 2} & U_{\mu 3}\\ U_{\tau 1} & U_{\tau 2} & U_{\tau 3}\end{bmatrix}}_{:= U_{\text{PMNS}}\ \text{(PMNS matrix)}} \underbrace{\begin{bmatrix}\nu_1\\ \nu_2\\ \nu_3\end{bmatrix}}_{\text{mass eigenstates}} \tag{1.1}$$

As a 3×3 unitary matrix, the PMNS matrix can be parameterized with three real parameters, called the mixing angles (θ_{12}, θ_{13}, θ_{23}), and one or three charge-parity (CP) violating phases, depending respectively on the Dirac or Majorana nature of the neutrino [17].

$$U_{\text{PMNS}} = \begin{bmatrix}1 & 0 & 0\\ 0 & c_{23} & s_{23}\\ 0 & -s_{23} & c_{23}\end{bmatrix}\begin{bmatrix}c_{13} & 0 & s_{13}e^{-i\delta_{\text{CP}}}\\ 0 & 1 & 0\\ -s_{13}e^{i\delta_{\text{CP}}} & 0 & c_{13}\end{bmatrix}\begin{bmatrix}c_{12} & s_{12} & 0\\ -s_{12} & c_{12} & 0\\ 0 & 0 & 1\end{bmatrix} P_{\text{Majorana}} \tag{1.2}$$

where c_{ij} and s_{ij} respectively denote $\cos(\theta_{ij})$ and $\sin(\theta_{ij})$, and P_{Majorana} is a diagonal matrix that merely equals the identity matrix if the neutrino is a Dirac fermion, or equals $diag(1, e^{i\frac{\alpha_{21}}{2}}, e^{i\frac{\alpha_{31}}{2}})$, thus containing two additional CP-violating phases α_{21} and α_{31}, if it is of Majorana nature.

In the PMNS formalism, a neutrino emitted with an energy E at a point of space-time in a given flavor eigenstate ν_l is described as a coherent superposition of the different mass eigenstates. When projected back in the flavor eigenbasis after a distance of propagation L, it can be detected in a flavor eigenstate $\nu_{l'}$ different from the emission eigenstate. In the plane-wave approximation for the wave function describing the propagation of the neutrino and in the ultra-relativistic limit, the oscillation probability between the emission and detection flavor eigenstates reads [17]:

$$\mathbb{P}(\nu_l \to \nu_{l'}) = \sum_j |U_{l'j}U_{lj}|^2 + 2\sum_{j>k} |U_{l'j}U^*_{lj}U_{lk}U^*_{l'k}| \cos\left(\frac{\Delta m^2_{jk}}{2E}L - \phi_{l'l;jk}\right) \tag{1.3}$$

where $l, l' = e, \mu, \tau$, $\phi_{l'l;jk} = \arg(U_{l'j}U^*_{lj}U_{lk}U^*_{l'k})$ and $\Delta m^2_{jk} = m^2_j - m^2_k$ the mass-square splitting parameters. Noticeably, the oscillation probability is independent of the two (potential) additional Majorana phases. Let's note as well that if one knows the values

of two mass-square splitting parameters, the value of the third one can be automatically derived.

On top of the values of the mixing angles, encapsulted in the PMNS matrix elements, and the mass-square splitting parameters, encoding the features of the mass eigenbasis, the oscillation probability prominently depends on the baseline L that features the distance between the emission and detection vertices, and the energy of the interacting neutrino.

1.1.2 Experimental evidence

Solar oscillation

Nuclear fusion reactions taking place within the Sun generate a high flux of pure electronic neutrinos. The Homestake [18], Kamiokande [19] and its successor Super-Kamiokande [20], SAGE [21] and GALLEX [22] experiments were alternatively able to measure the flux of these solar neutrinos. It was found to be discrepant with the prediction given by the Standard Solar Model by a factor of $\sim 2-3$, as shown in Figure 1.1.

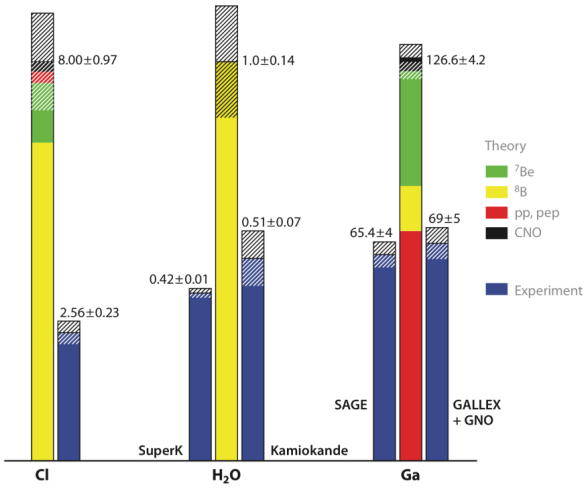

Figure 1.1: **Measured solar electronic neutrino flux**, from the Homestake, Kamiokande, Super-Kamiokande, SAGE and GALLEX experiments (from left to right). The Cl, H_2O, Ga subscripts refer to the target used for the detection of electronic neutrinos. The blue bars are the measurements and the middle bars are the predictions. All measured fluxes lead to a significant deficit of electronic neutrinos with respect to the prediction. Source [23].

The Homestake, GALLEX and SAGE experiments all used a pure charged-current (CC) interaction to detect the electronic neutrinos:

$$\nu_e + {}^{A}_{Z}\mathrm{X} \rightarrow {}^{A}_{Z+1}\mathrm{Y} + e^- \tag{1.4}$$

where $X = {}^{37}_{17}Cl$ for Homestake and $X = {}^{71}_{31}Ga$ for GALLEX/SAGE. Given that the spectrum of solar neutrinos does not extend beyond 20 MeV, these experiments were only sensitive to the electronic neutrino flavor[1].

[1]Given that the charged-current interaction with a muon (resp. tau) neutrino implies the creation of a muon (resp. tau) particle, of mass 106 MeV (resp. 1.78 GeV), the available energy in the detection channel of solar neutrinos is insufficient to allow these processes.

On the other hand, Kamiokande used the neutrino elastic scattering (ES) as a detection channel:

$$\nu + e^- \rightarrow \nu + e^- \tag{1.5}$$

This process can not only occur as a CC interaction, but also occurs as a neutral-current interaction (NC) that is sensitive to all neutrino flavors. Yet, all in all, taking into account the NC and CC channels for the ES process, one ends up with a suppression factor of ≈ 0.16 for the ν_μ and ν_τ flux (only sensitive to NC channel) with respect to the ν_e flux (sensitive to both CC and NC channels).

The solution to this "solar neutrino puzzle" was hinted by the SNO experiment [24]. SNO used three detection channels: pure CC- (as GALLEX/SAGE), ES- or mixed CC/NC- (as Kamiokande and Super-Kamiokande) and pure NC- channels:

$$\begin{aligned} \nu_e + d &\rightarrow e^- + p + p \quad \textbf{(CC)} \\ \nu + e^- &\rightarrow \nu + e^- \quad \textbf{(CC/NC)} \\ \nu + d &\rightarrow \nu + p + n \quad \textbf{(NC)} \end{aligned}$$

From these three channels, SNO was able to extract the pure electronic and muon+tau solar neutrino fluxes, indicating that the solar neutrinos initially emitted in the electronic flavor oscillated towards muon and tau flavors.

Atmospheric oscillation

The so-called "atmospheric neutrinos" are produced when cosmic ray particles interact with the nuclei of the Earth's atmosphere, producing mesons whose decay chain will subsequently generate neutrinos:

$$\begin{aligned} \pi^\pm &\rightarrow \mu^\pm + \nu_\mu(\bar{\nu}_\mu) \\ \mu^\pm &\rightarrow e^\pm + \bar{\nu}_\mu(\nu_\mu) + \nu_e(\bar{\nu}_e) \end{aligned}$$

These decay schemes suggest the ratio of muon to electron neutrinos to be of ~ 2. To compare data to prediction and reduce the systematic effects due to normalization uncertainties, it is convenient to define the double ratio:

$$R = \frac{(N_\mu/N_e)_{\text{data}}}{(N_\mu/N_e)_{\text{pred}}} \tag{1.6}$$

Indications for a deficit of muon neutrinos, inducing a value of the double ratio significantly lower than 1, were reported by the Kamiokande [25] and IMB [26] experiments. This discrepant value of the ratio was later confirmed by the Super-Kamiokande experiment, that established: $R = 0.61 \pm 0.03$ [stat] ± 0.05 [syst] [27]. They reported as well a significant deviation to the expectation of the zenith-angle distribution of μ-like events whereas the zenith-angle distribution of e-like events was found compatible with the expectation, as shown in Figure 1.2. For the energy range that was considered ($1 \sim 10$ GeV), this feature was interpreted as an oscillation of the upward-going muon neutrinos, coming from the opposite side of the Earth's atmosphere at a baseline of ~ 10000 km, whereas downward-going muon neutrinos that travelled only a few to a few tens km could not (sizeably) oscillate due to the shorter baseline. In their oscillation analysis in [28], they confirmed that their data were consistent with a two-flavor $\nu_\mu \rightarrow \nu_\tau$ oscillation. This interpretation was later strengthened by the study of muon neutrino disappearance probability as a function L/E [29]. A dip in the L/E distribution was observed in the data, as predicted from the sinusoidal flavor transition probability of neutrino oscillation.

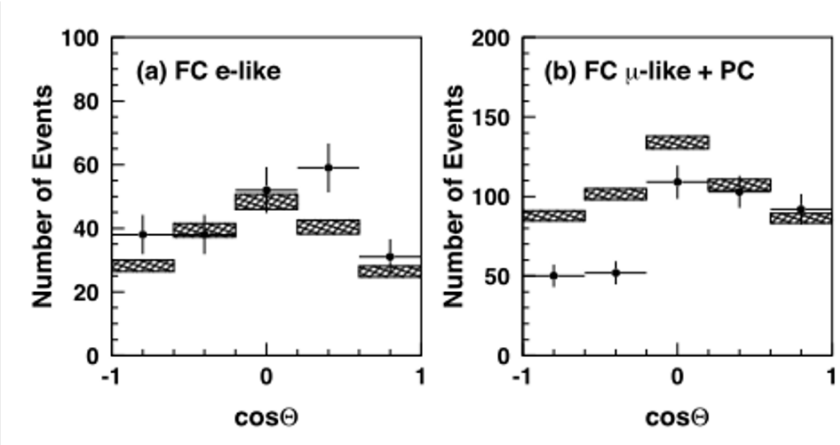

Figure 1.2: **Zenith angle distribution for multi-GeV full-contained (FC) and partially-contained (PC) events**, from the first 414 days of Super-Kamiokande data. Partially-contained events have a neutrino interaction in the fiducial volume with a final state particle exiting into the outer detector. The muon and electron final state particles that proceed from the CC neutrino interaction in the detector respectively refer to ν_μ and ν_e events. The markers represent the events counted by Super-Kamiokande, the boxes represent the expected event counts. For upward-going neutrinos coming from the opposite side of Earth (negative values of $\cos\Theta$), a deficit of μ-events is clearly visible. Source [30].

1.1.3 Measurements of oscillation parameters

Appearance and disappearance neutrino experiments, carried out with man-made neutrino sources, namely accelerator- or reactor-based experiments, allowed to measure with compelling accuracy the three mixing angles and the two (out of the three) mass-square splitting parameters.

$|\Delta m^2_{32}|$ and θ_{23}

The long-baseline accelerator experiments MINOS, NOνA and T2K [31] brought the most stringent constraints on the value of the $|\Delta m^2_{32}|$ and θ_{23} oscillation parameters. The basic design of a long-baseline accelerator neutrino experiment consists of a near detector, that allows to measure the characteristics of the neutrino beam (e.g. background estimate, neutrino flux and energy spectrum), and a far detector that allows for a relative rate comparison given a certain baseline, generally of the order of $\sim 100-1000$ km. The neutrino energy is at the GeV level. In such experiment, the neutrino beam is generated by means of an accelerated proton beam colliding a fixed target, and subsequently producing mesons that will decay in ν_μ or $\bar{\nu}_\mu$ (depending on the operating "mode" set by the direction of the magnetic horn current), with a small yet quantified contamination of ν_e. The measurement of the ν_μ (resp. $\bar{\nu}_\mu$) disappearance $\nu_\mu \to \nu_\mu$ (resp. $\bar{\nu}_\mu \to \bar{\nu}_\mu$) and the ν_e (resp. $\bar{\nu}_e$) appearance $\nu_\mu \to \nu_e$ (resp. $\bar{\nu}_\mu \to \bar{\nu}_e$) between the near and far detectors yield to $|\Delta m^2_{32}| \sim 2.4 \cdot 10^{-3}$ eV^2 and $\sin^2\theta_{23} \sim 0.4 - 0.5$. [32, 33, 34]. Due to being at least partially derived from the disappearance channel of ν_μ, that drives the atmospheric neutrino oscillation, these parameters are commonly referred to as the atmospheric oscillation parameters.

Δm^2_{21} and θ_{21}

Although the SNO data strongly hinted to the oscillation of electronic neutrinos towards other flavor states as the explanation of the solar neutrino puzzle, the final evidence was brought by the long-baseline reactor (anti)neutrino experiment KamLAND [35]. Located at an average baseline of ~ 180 km from a nuclear reactor, that emits neutrinos with typical energy of a few MeV, this experiment has a sensitivity to $\Delta m^2 \sim 10^{-5}$ eV^2, by investigating the $\bar{\nu}_e$ disappearance $\bar{\nu}_e \to \bar{\nu}_e$. Assuming CPT invariance, the survival probability of $\bar{\nu}_e$ equals the survival probability of ν_e: $\mathbb{P}(\bar{\nu}_e \to \bar{\nu}_e) = \mathbb{P}(\nu_e \to \nu_e)$, such that the experiment is sensitive to Δm^2_{12} and θ_{12} parameters, that drive the solar ν_e oscillation. Therefore, if this mechanism is to be the solution of the solar neutrino puzzle, KamLAND should observe reactor $\bar{\nu}_e$ disappearance. This result was indeed reported by the collaboration in [36], and the combined data of KamLAND and solar neutrinos allowed to set the value of the so-called solar neutrino oscillation parameters: $\Delta m^2_{12} \sim 7.4 \cdot 10^{-5}$ eV^2 and $\sin^2\theta_{12} \sim 0.30$.

θ_{13}

The measurement of θ_{13} was already investigated by the accelerator experiments, via the electron neutrino appearance channel, but the best and unambiguous experimental constraint was brought once again by reactor antineutrino experiments via the electron antineutrino disappearance channel. In such experiment, the energy resolution effects degrade the oscillation signal such that to have optimal sensitivity on the oscillation parameter, the detector must be placed at the first disappearance maximum of the oscillation. Approximately knowing the value of θ_{13} with the constraints from the accelerator experiments, and knowing that the reactor antineutrino spectrum peaks around $3 \sim 4$ MeV (see Section 1.2.1), one deduces that the reactor experiment should be located at a baseline of ~ 1 km. At this short baseline, the reactor $\bar{\nu}_e$ oscillations driven by the solar oscillation are negligible. The $\bar{\nu}_e$ survival probability then only depends, to a very good approximation, on $\sin^2\theta_{13}$ and Δm^2_{13}. From the analyses of the short-baseline reactor antineutrino experiments Double Chooz [37], Daya Bay [38] and RENO [39], the last mixing angle was found to be: $\sin^2(2\theta_{13}) \sim 0.09$.

All the oscillation parameter values are summarized in Table 1.1. As for the determination of the CP violating phase, the values returned by the T2K and NOνA analyses are found in sizeable tension [40]. Several other open issues remain, such as the determination of the mass hierarchy of the neutrinos − that cannot be thoroughly derived because the value of Δm^2_{32} is only known up to a $\pm$ sign. The mass ordering is said to be either normal ($m_1 < m_2 < m_3$) or inverted ($m_3 < m_1 < m_2$). On top of this, the absolute mass scale of neutrinos remains unknown, although some constraints exist from cosmology or oscillation experiments [41].

Besides, let's remark that θ_{13} turns out to be the smallest mixing angle, and at the same time the most accurately measured. This directly results from the strategy of the reactor antineutrino experiments (Double Chooz, Daya Bay and RENO) to use near and far detectors in order to alleviate the dominant systematic uncertainty of the absolute normalization of the antineutrino flux. Instead, they perform a relative comparison of the spectra measured in each detector. Furthermore, the near detectors provided in the process high statistics antineutrino data samples that motivated precision study on the accuracy of the predictions. From these studies arose the so-called reactor anomalies, that we discuss in the next section.

Parameter	best-fit	3σ
Δm^2_{21} $[10^{-5}$ eV $^2]$	7.37	$6.93 - 7.96$
$\Delta m^2_{31(23)}$ $[10^{-3}$ eV $^2]$	2.56 (2.54)	$2.45 - 2.69$ $(2.42 - 2.66)$
$\sin^2\theta_{12}$	0.297	$0.250 - 0.354$
$\sin^2\theta_{23}$, $\Delta m^2_{31(32)} > 0$	0.425	$0.381 - 0.615$
$\sin^2\theta_{23}$, $\Delta m^2_{32(31)} < 0$	0.589	$0.384 - 0.636$
$\sin^2\theta_{13}$, $\Delta m^2_{31(32)} > 0$	0.0215	$0.0190 - 0.0240$
$\sin^2\theta_{13}$, $\Delta m^2_{32(31)} < 0$	0.0216	$0.0190 - 0.0242$

Table 1.1: **Best-fit values and 3σ allowed ranges of the 3-neutrino oscillation parameters**. The values (values in brackets) correspond to normal (inverted) mass hierarchy. Source [42].

1.2 Reactor anomalies

As we saw in the previous section, long-baseline (KamLAND) and short-baseline (Daya Bay, Double Chooz, RENO) reactor experiments proved to be key ingredients in the accurate determination of neutrino oscillation parameters, as electronic neutrino disappearance experiments. Whereas several features remain to be addressed, reactor antineutrino physics still remains to-date a relevant probe to further investigate neutrino properties, with the so-called reactor anomalies.

1.2.1 Antineutrino spectrum predictions

In nuclear reactors, almost pure electron antineutrino flux is produced from the β^- decay of fission products, that proceed from the (thermal) neutron-induced nuclear fission of either four heavy isotopes ^{235}U, ^{238}U, ^{239}Pu, ^{241}Pu (in commercial or power reactors, lowly enriched in ^{235}U) or one heavy isotope ^{235}U (in research reactors highly enriched in ^{235}U). In a typical reactor experiment, reactor electron antineutrinos are detected via their Inverse Beta Decay (IBD) reaction with protons of a liquid scintillator. It will be detailed in Section 1.3.1. The detected event rate as a function of energy is given by the product of the IBD interaction cross section $\sigma(E_{\bar{\nu}})$ with the emitted antineutrino flux $S(E_{\bar{\nu}})$. The IBD cross section increases with energy whereas the emitted antineutrino flux decreases with energy, giving a typical "bell" shape to the detected antineutrino spectrum, as shown in Figure 1.3.

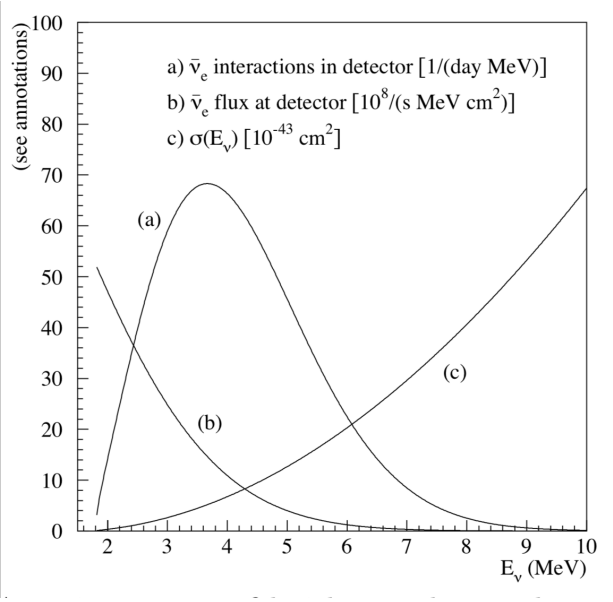

Figure 1.3: **Sketch of the detected/IBD $\bar{\nu}_e$ spectrum for a reactor antineutrino experiment**, assuming a 12-ton fiducial mass detector located 0.8 km from 12 GW_{th} power reactor. Source [17].

Several models exist for the IBD cross section, as discussed in [43]. Historically, the reference IBD cross section was that of Llewellyn Smith [44], that neglected contributions of order $(m_n - m_p)/E_{\bar{\nu}}$ (where m_n and m_p are respectively the neutron and proton masses), whose magnitude is $\sim 0.1 - 1$ for the typical few MeV energy of reactor antineutrinos, and is therefore not fully negligible. Later, Vogel and Beacom [45] included these contributions.

Yet, this IBD cross section proceed from a first order expansion in $E_{\bar{\nu}}/m_p$. The most recent Strumia-Vissani [46] cross section is then considered as the reference IBD cross section in this dissertation, as it was calculated without approximation in $(m_n - m_p)/E_{\bar{\nu}}$ and $E_{\bar{\nu}}/m_p$.

As for the emitted antineutrino flux as a function of the antineutrino energy, also called cumulative antineutrino spectrum, its prediction is not trivial, and to this day, two methods have been employed.

Summation method

The first method is an *ab initio* approach called the summation method. It consists of making use of all available information from nuclear databases, and to sum over all the ($\sim$ 10000) individual β-transition spectra for all the decaying fission fragments to obtain the cumulative antineutrino spectrum [47, 48]:

$$S(E_{\bar{\nu}}) = \sum_n Y_n(Z, A, t) \sum_i b_{n,i}(E_0^i) P(E_{\bar{\nu}}, E_0^i, Z) \tag{1.7}$$

where:

- $Y_n(Z, A, t)$ is the effective cumulative fission yield of the fragment nucleus (Z, A) after neutron exposure time t.
- $b_{n,i}(E_0^i)$ are the branching ratios for the ith branch with the maximal electron energy $E_0^i = Q_n + m_e c^2 - E_{\text{exc}}^i$, with Q_n the β decay Q-value of the fission fragment n, and E_{exc}^i the excitation energy in the daughter nucleus.
- $P(E_{\bar{\nu}}, E_0^i, Z)$ is based on the Fermi theory of beta-decay with correction terms for effects of the finite size of the nucleus, the radiative corrections and the form factors of forbidden transitions (when known).

The associated cumulative electron spectrum is obtained with the simple change of variable $E_\beta = E_0^i - E_{\bar{\nu}}$ in the branch-level spectral shape functions, that stems from the energy conservation law. Therefore, in this approach, electron and antineutrino spectra are calculated within the same theoretical framework, using the same inputs and preserving the symmetry of the two lepton spectra at the single-branch level [49]. However, the main drawback of this framework is that it suffers from the incompleteness and long-standing biases of nuclear databases, even in the most recent versions of this approach [50, 51].

Conversion method

To alleviate the limitations of the summation method, a more empirical approach, called conversion method, was developed. It relies on the cumulative electron spectra measured at the Institut Laue-Langevin for ^{235}U, ^{239}Pu and ^{241}Pu, by irradiation of target foils with thermal neutrons. Each electron spectrum is then fitted by the superposition of a set of virtual allowed β branches with different end points. Each branch is then converted in antineutrino energy, with the same argument as for the summation method, and summed up to provide the converted cumulative antineutrino spectra [52, 53, 54]. As for the ^{238}U cumulative antineutrino spectrum, it was historically deduced from the Vogel *et al.* summation method [48], such that the overall model was referred to as "ILL-Vogel" flux model. This model has been revised in 2011, yielding to improved summation prediction for the ^{238}U cumulative antineutrino spectrum by Mueller *et al.* [50], and conversion

predictions for ^{235}U, ^{239}Pu and ^{241}Pu cumulative antineutrino spectra by Mueller *et al.* [50] and then by Huber [55]. This "Huber-Mueller" model is the reference flux model, to be multiplied by the IBD interaction cross section for comparison with the spectra measured by reactor antineutrino experiments.

1.2.2 Rate anomaly

The measured IBD yields from short-baseline experiments ($L < 2$ km) were compared to the revised flux predictions in [56]. The ratio of the average measured yield with the predicted one was found to be: 0.943 ± 0.023, yielding to a systematic antineutrino deficit, with a 2.9σ significance. The authors of [56] called this discrepancy the "Reactor Antineutrino Anomaly" (RAA). This anomaly has been recently updated in [43] to be $0.936^{+0.024}_{-0.023}$. Therefore, the short-baseline data show indications for reactor $\bar{\nu}_e$ disappearance beyond the three-flavor oscillation pattern, hinting towards a potential very short baseline oscillation that would couple the three-flavor SM neutrinos with an additional eigenstate, that would necessarily not couple to matter via weak interaction. Such antineutrino is said to be "sterile". Its (hypothetical) existence is experimentally motivated by other very short baseline rate anomalies, namely the Gallium anomaly in ν_e disappearance channel of the GALLEX, SAGE and BEST experiments [57, 58], and the LNSD [59] and MiniBoone [60] anomaly in the $\nu_e/\bar{\nu}_e$ appearance channel from a $\nu_\mu/\bar{\nu}_\mu$ beam. On the theoretical point of view, sterile neutrinos can be part of models for the mass generation of neutrinos, that cannot be covered by the Higgs mechanism [61].

The most simple and natural extension of the oscillation analysis presented so far is to consider a 4×4 PMNS matrix, with the additional sterile flavor eigenstate ν_s and a supplemental mass eigenstate ν_4. The short baseline of the oscillations requires the new mass-square splitting parameter Δm^2_{41} to be about 1 eV^2, much larger than the two known parameters. Therefore, for very short distances of propagation, the $\bar{\nu}_e$ survival probability can be well described by the two-flavor oscillation approximation, such that:

$$P(\bar{\nu}_e \to \bar{\nu}_e) = 1 - \sin^2(2\theta_{14}) \sin\left(\frac{\Delta m^2_{41}}{4E} L\right) \tag{1.8}$$

At long distance from the reactor, the rate is then reduced by a factor $1 - \sin^2(2\theta_{14})$ $\cdot\langle \sin\left(\frac{\Delta m^2_{41}}{4E} L\right)\rangle \approx 1 - \sin^2(2\theta_{14})/2$, such that $\sin^2(2\theta_{14})/2$ must be consistent with the quoted RAA antineutrino deficit. The best fit point of the RAA is indeed found at: $\sin^2(2\theta_{14}) = 0.14$ and $\Delta m^2_{41} = 2.3$ eV^2 (see Figure 1.4).

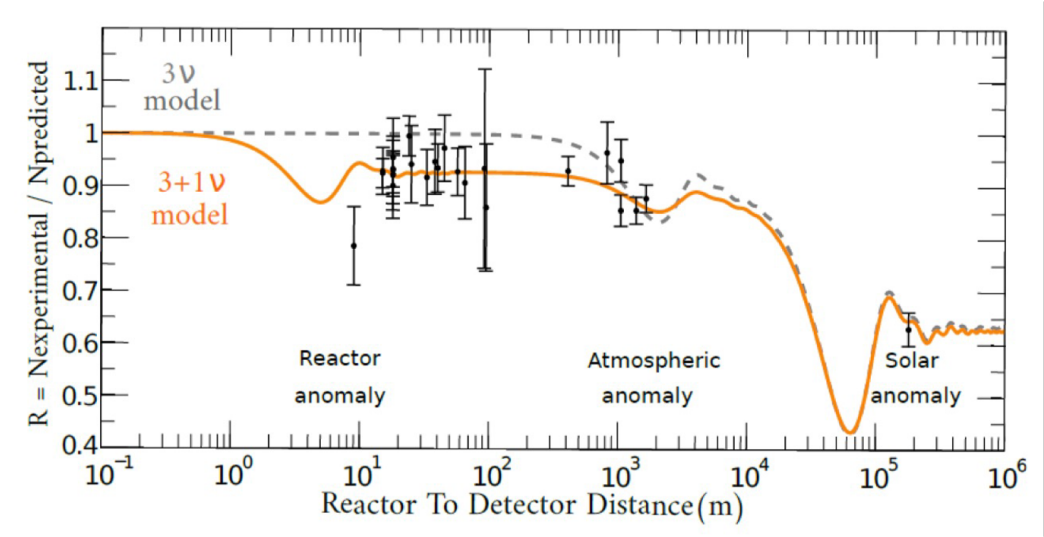

(a)

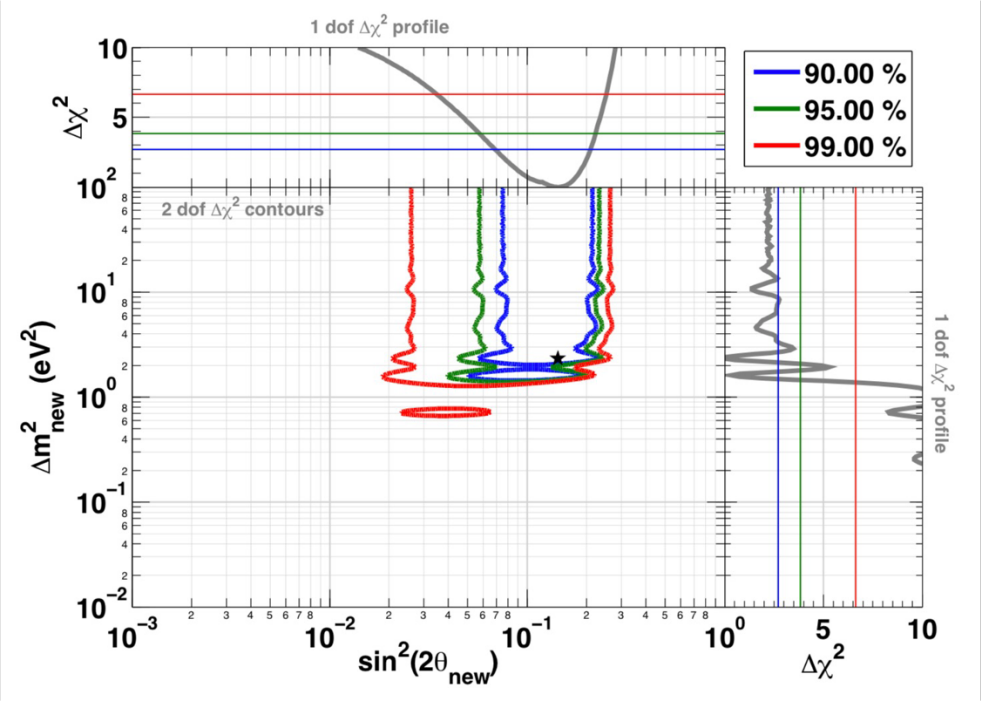

(b)

Figure 1.4: (a) Illustration of the electronic antineutrino flux reduction seen by reactor experiments, as a function of the baseline. The flux is normalized to the non-oscillated prediction. The different oscillation regimes are clearly visible and distinct from each other, stemming from the difference in magnitude of the mass-square splitting parameters. Most notably, the 3+1 flavor model with an eV-scale oscillation would allow to explain the deficit observed at very short baseline (RAA). (b) Allowed regions for the RAA in the two-flavor oscillation parameters plane. The RAA best-fit point is depicted as a black star. Source [56].

1.2.3 Shape anomaly

On top of the rate anomaly, Double Chooz [62], Daya Bay [63] and RENO [64] reported a spectral distortion with respect to the Huber-Mueller prediction, as clearly visible in Figure 1.5. A similar pattern was also highlighted in the data of the NEOS experiment [65]. It consists of a local event excess in the 4-6 MeV region in reconstructed energy, and is known as "5 MeV bump". Let's stress however that the energy considered here does not correspond to the antineutrino energy, as it will be sketched in the next section, and *a priori* includes the respective detection effects of each experiment.

All of these experiments operate near power reactors, with mixed nuclear fuel contents, such that it is not straightforward to disentangle the contributions to this event excess of each of the four main isotopes contributing to the total antineutrino flux (^{235}U, ^{238}U, ^{239}Pu, ^{241}Pu).

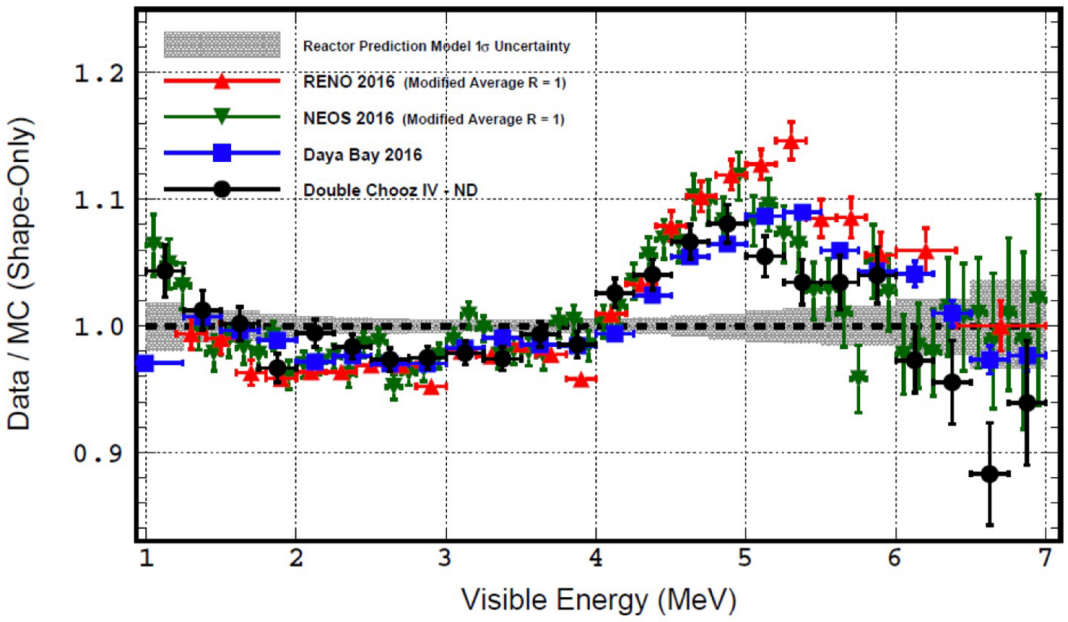

Figure 1.5: **Shape anomaly of reactor antineutrino spectra**, stemming from the (shape-only) comparison of Daya Bay, RENO, NEOS and Double Chooz measured spectra with the Huber-Mueller predicted spectra. All experiments exhibit a common pattern characterized by the 4-6 MeV excess, called "5 MeV bump". Source [37].

In this context, the STEREO experiment to which the main part of this doctoral work is dedicated will bring further information on both the rate and shape reactor antineutrino anomalies. By operating at a very short baseline ($\sim$ 10 m) from a research nuclear reactor, highly enriched in ^{235}U, it will be sensitive to an eV mass-scale oscillation of the electronic antineutrino flux, and will be able to accurately measure the pure-^{235}U induced antineutrino spectrum, allowing to shed light on the contribution of this one isotope to both reactor anomalies.

1.3 Interactions for reactor antineutrinos

The detection channel used in the STEREO experiment, as well as in all reactor experiments we discussed so far, is the IBD reaction. We discuss in this section the main features of this interaction. In a second time, we introduce the Coherent Elastic Neutrino-Nucleus Scattering (CEνNS) upon which several upcoming experiments are based. As we will see, this neutral current interaction channel features an enhanced interaction cross section with respect to the standard IBD channel, on top of opening up a new avenue for testing the Standard Model in the neutrino sector. This is the channel that the NUCLEUS experiment, on which part of this doctoral work is dedicated, aims at investigating.

1.3.1 A charged-current interaction: Inverse Beta Decay reaction

Threshold

The IBD reaction $\bar{\nu}_e + p \rightarrow e^+ + n$ is the basis detection channel used by reactor neutrino experiments since the experimental discovery of the neutrino by Cowan and Reines [2]. Given that the neutron mass is greater than the proton mass (with the neutrino mass being negligible), this reaction features an energy threshold. For the reaction to occur, kinematics impose that the square of the center-of-mass energy s is such that (in natural units):

$$s \geq (m_n + m_e)^2 \tag{1.9}$$

where m_n and m_e are respectively the neutron and electron masses. In the laboratory rest frame, s is given by:

$$s = (E_{\bar{\nu}} + E_p)^2 - (p_{\bar{\nu}} + p_p)^2 \tag{1.10}$$

with $E_{\bar{\nu}}$ and E_p (resp. $p_{\bar{\nu}}$ and p_p) are the energy (resp. the momentum) of the neutrino and the proton. Considering the proton at rest, and neglecting the neutrino mass, Equation 1.10 becomes:

$$s = 2E_{\bar{\nu}} m_p + m_p^2 \tag{1.11}$$

All in all, one then finds that:

$$E_{\bar{\nu}} \geq \frac{(m_n + m_e)^2 - m_p^2}{2m_p} \approx 1.806 \text{ MeV} \tag{1.12}$$

Reactor antineutrino experiments using the IBD reaction as a detection process are then only sensitive to neutrinos with energy greater than ~ 1.8 MeV.

Prompt and delayed signals

The IBD neutron kinetic energy is heavily suppressed by the proton mass, and reads at first order in $1/m_p$ [45]:

$$T_n \approx \frac{E_{\bar{\nu}}(E_{\bar{\nu}} - \Delta)}{m_p} \left(1 - \frac{p_e}{E_e} \cos\theta\right) + \frac{\Delta^2 - m_e^2}{2m_p} \tag{1.13}$$

with $\Delta = m_n - m_p \approx 1.293$ MeV and θ the angle between the impinging antineutrino and the outgoing positron. The neutron kinetic energy is therefore found to be ~ 10 keV and

can be neglected. Therefore, all the information on the antineutrino energy is encoded in the positron energy, that reads, at zeroth order in $1/m_p$ [45]:

$$E_{e^+} = E_{\bar{\nu}} - \Delta \tag{1.14}$$

Given that the IBD positron is expected to promptly[2] undergo a subsequent matter-antimatter annihilation in the detection apparatus, emitting two back-to-back 0.511 MeV γ in the process, the total visible energy experimentally accessible is:

$$\begin{aligned} E_{vis} &= T_{e^+} + 2m_e \\ &= E_{e^+} + m_e \\ &\approx E_{\bar{\nu}} + 0.782 \text{ [MeV]} \end{aligned} \tag{1.15}$$

In a typical reactor antineutrino experiment, the IBD neutron will thermalize by elastic scattering in the active detection volume and subsequently be captured, within a typical time of tens of μs. In general, the IBD neutron capture signal is then referred to as the IBD delayed signal, whereas the signal coming from the reconstruction of the visible energy, associated to the positron, is referred to as the IBD prompt signal. For this reason, E_{vis} is also called the prompt energy and labelled E_{pr}. The time and space correlation of the positron and neutron provides a distinctive signature for the IBD signal, that allows for a powerful discrimination against background events.

Interaction cross section

At zeroth order, the IBD interaction cross section can be expressed as [45]:

$$\sigma_{IBD} \approx \frac{2\pi^2}{m_e^5 f^R \tau_n} E_{e^+} \sqrt{E_{e^+}^2 - m_e^2} \tag{1.16}$$

where f^R is a phase-space factor and τ_n the neutron lifetime. This directly gives the following estimate:

$$\sigma_{IBD} \approx 9.62 \cdot E_{e^+} \sqrt{E_{e^+}^2 - m_e^2} \sim 10^{-44} \text{ cm}^2 \cdot \text{MeV}^{-2} \tag{1.17}$$

It corresponds to a tiny probability of interaction, and depends quadratically on the positron, and therefore on the antineutrino, energy.

1.3.2 A neutral-current interaction: CEνNS

Postulated soon after the discovery of weak neutral current [3], the Coherent Elastic Neutrino-Nucleus Scattering, or CEνNS, occurs when a neutrino or antineutrino interacts coherently with all nucleons within a given atomic nucleus ${}^A_Z\text{X}$:

$$\bar{\nu} + {}^A_Z\text{X} \rightarrow \bar{\nu} + {}^A_Z\text{X} \tag{1.18}$$

The scattering is said to be "coherent" if the transfer of momentum between the neutrino and the nucleus is smaller than the inverse of the nuclear De Broglie wavelength, which imposes the energy of the impinging neutrino not to exceed a few tens of MeV, which is a condition that is met by reactor antineutrinos (see Figure 1.3). In this regime, the nuclear

[2] At most in a few nanoseconds time scale.

structure of the target nucleus is unresolved, and the differential cross section of the process reads [66]:

$$\frac{d\sigma}{dT} = \frac{G_F^2}{4\pi} F^2(Q^2) \left(N - (1 - 4\sin^2\theta_W)Z\right)^2 M \left(1 - \frac{T}{T_{max}}\right) \tag{1.19}$$

where T is the nuclear recoil energy and T_{max} the maximum nuclear recoil energy, G_F the Fermi coupling constant, $F(Q^2)$ the nuclear form factor that can be approximated to 1 in the fully coherent regime, θ_W is the Weinberg angle, $N = A - Z$ is the number of neutrons in the target nucleus and M its mass.

In Equation 1.19, the so-called coherent regime of the interaction translates into the quadratic dependency of the cross section with the weak nuclear charge $N-(1-4\sin^2\theta_W)Z$, which stems from the fact that the amplitude of the process proceeds from the coherent sum of the nucleonic amplitudes, before squaring up to derive the cross section.

Given $\sin^2\theta_W \sim 0.22$, $1 - 4\sin^2\theta_W$ is coincidentally small, such that the weak nuclear charge can be approximated by the number of neutrons N and the differential cross section reads:

$$\frac{d\sigma}{dT} = \frac{G_F^2}{4\pi} N^2 M \left(1 - \frac{T}{T_{max}}\right)$$

Therefore, the remarkable feature of the CEνNS interaction is the boosting of the cross section by the target nuclear mass, with an enhancement factor proportional to the square of the number of neutrons. This allows the CEνNS cross section to be 1 to 3 orders of magnitude greater than the IBD cross section depending on the nature of the target nucleus (see Figure 1.6). Let's add as well that, contrary to the IBD process, the CEνNS process is thresholdless, and sensitive to all neutrino flavors as a neutral current interaction.

However, the maximum energy of the nuclear recoil, given by the subsequent relation, turns out to be in the sub-keV region, and suppressed with the target nucleus mass [66]:

$$T_{max} = \frac{E_{\bar{\nu}}}{1 + \frac{M}{2E_{\bar{\nu}}}} \sim \frac{2E_{\bar{\nu}}^2}{M} \tag{1.20}$$

Therefore, there is a trade-off to be found between the intensity of the CEνNS signal, given by the amplitude of the process, and the magnitude of the accessible output energy, which defines the experimental energy threshold. Due to technological limitations to go down to ultra-low threshold in recoil energy equivalent, CEνNS remained an elusive process for decades, until 2017 and the measurement performed by the COHERENT collaboration [4]. Operating with a beam of neutrinos and antineutrinos with $\sim 16 - 53$ MeV energy, they reported the measurement of the CEνNS process for CsI [4] and Ar [67] targets. However, in this neutrino energy range, their experiment lies at the limit of the coherent regime as we see sizeable deviations of their measurements with the form-factor-equals-unity assumption (see Figure 1.7). For reactor antineutrino experiments aiming at using CEνNS as a detection process such as NUCLEUS , we expect this deviation to be dwindled.

At last, let's note that the interests of CEνNS are numerous and go far beyond reactor neutrino physics. They have been compiled in [4]. Notably, on the theoretical point of view, this interaction channel allows to investigate a potential neutrino magnetic moment, Beyond the Standard Model (BSM) interactions mediated by new particles, and to improve constraints on the value of the weak nuclear charge. On an experimental point of view, it would allow to better characterize the so-called neutrino floor/fog [68] of Dark Matter

search experiments limited by an irreducible CEνNS background from solar and atmospheric neutrinos. Furthermore, on a technological aspect, the compactness of CEνNS based neutrino detectors may be of particular interest for non-intrusive nuclear reactor monitoring [69].

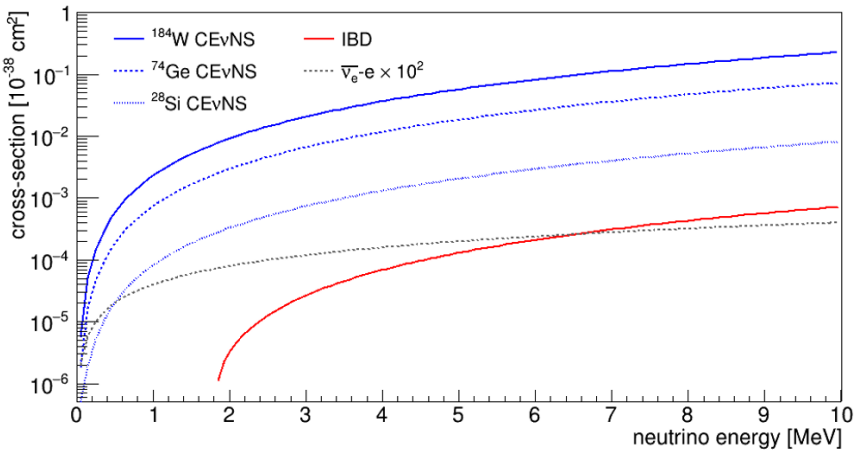

Figure 1.6: **Comparison of CEνNS and IBD cross sections**. Source [70].

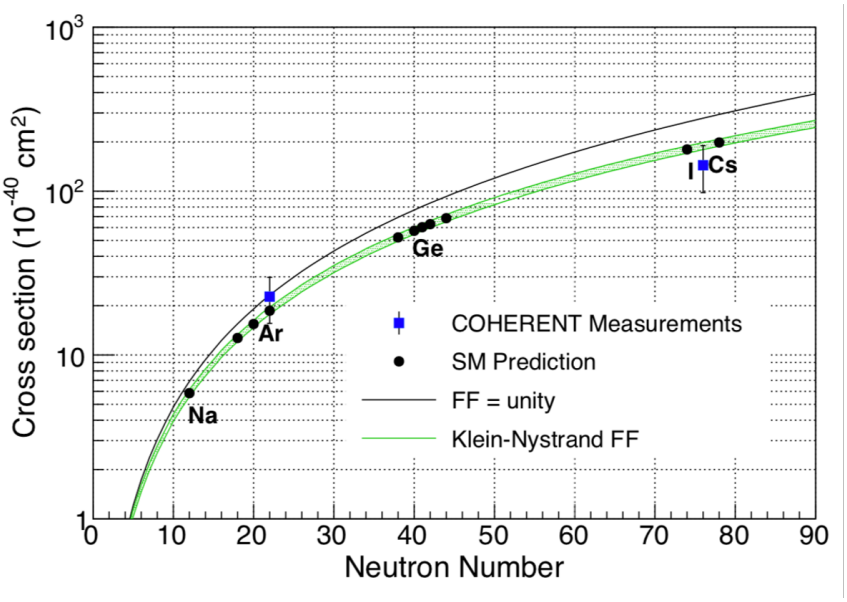

Figure 1.7: **CEνNS flux-weighted cross section** measured by COHERENT compared to the SM expectation as a function of neutron number. The form factor (FF) unity assumption is compared to the Klein-Nystrand value [71]. Source [67].

Chapter 2

The STEREO experiment

The STEREO experiment originates from the collaboration of five European research institutes: the "Institut de recherche sur les lois fondamentales de l'univers"(IRFU) of CEA Paris-Saclay (France), the "Laboratoire de Physique Subatomique et de Cosmologie" (LPSC) and "Institut Laue-Langevin" (ILL) from Grenoble (France), the "Laboratoire d'Annecy de Physique des Particules" (LAPP) from Annecy (France), and the "Max Planck Institute für Kernel physics" (MPIK) from Heidelberg (Germany).

STEREO can be described as a very short-baseline reactor antineutrino experiment, designed to test the hypothesis of a light sterile neutrino being the cause of the deficit of the observed antineutrino interaction rate at short baselines with respect to the predicted rate, known as the Reactor Antineutrino Anomaly (RAA), as detailed in Section 1.2. It also aims at providing a precise measurement of the antineutrino spectrum associated to the fission of ^{235}U, in both rate and shape. For these purposes, the STEREO experiment measures the antineutrino energy spectrum in six identical detector cells spanning baselines between 9 and 11 m from the compact core of the ILL research reactor highly enriched in ^{235}U.

This chapter is dedicated to the overall description of the experiment, from the experimental site to the detector in itself and its operation.

2.1 ILL experimental site

The Institut Laue-Langevin (ILL) is an international research center, located in Grenoble (France), at the cutting edge of neutron science and technology. The institute hosts about 600 experiments a year, run by 1400 scientists from all over the world. These experiments benefit from the world-leading thermal neutron flux emitted by the High Flux Reactor (HFR) feeding 40 high-technology instruments on-site. At nominal power, this nuclear fission reactor produces $1.5 \cdot 10^{15}$ neutrons/cm^2/s [72] in the moderator, allowing to probe matter in various research fields, e.g. biology, chemistry or nuclear physics.

In the STEREO case, the experiment detects the electronic antineutrinos that are emitted by the β^- decay of the neutron-rich fission products:

$$ {}^{A}_{Z}\mathrm{X} \rightarrow {}^{A}_{Z+1}\mathrm{Y} + e^- + \bar{\nu}_e \tag{2.1} $$

The HFR high neutron flux, representative of the high fission rate within the reactor, then translates into a high antineutrino flux, at the level of $\sim 10^{19}\bar{\nu}_e$/s at nominal reactor power [73]. As a result of the weak neutrino-matter interaction, all the HFR emitted antineutrinos escape the reactor in all directions and a tiny fraction of them can then be detected by a dedicated nearby experiment, such as STEREO. The specificity of the STEREO experiment is that it requires to be shielded against neutron beams as it only aims at detecting antineutrinos, and the dedicated detector is to be installed in the experimental site for the measurement.

2.1.1 Reactor core

As a research nuclear reactor aiming at providing a high thermal neutron flux, the design and operation of the HFR significantly differ from that of a commercial nuclear reactor.

First, the fuel element consists of 280 plates curved as involute, welded to two concentric aluminum tubes, forming a compact hollow cylinder with internal and external diameters of 26.08 cm and 41.36 cm respectively and a height of 80 cm for the fissile part of the plate. This part is made of dispersed UAI_x powders, which are 93%-enriched in ^{235}U [74]. This highly-enriched in ^{235}U (HEU) composition drastically differs from that of commercial reactors, lowly-enriched in ^{235}U (LEU), usually at the few percents level.

The HFR fuel arrangement is placed in an aluminum tank filled with heavy water (D_2O), acting as a moderator that thermalizes the neutrons induced by the fissions occurring within the nuclear core while minimizing the neutron capture rate. This tank is encapsulated in a pool of light water (H_2O) of dimensions $\varnothing$ 6 m $\times$ 14 m to absorb the residual thermal neutrons escaping the moderator. The thermal neutrons in the moderator are collected and collimated through dedicated aluminum beams, towards the neighboring experiments installed in the experimental hall, on level C of the reactor building.

In practice, the HFR is operated during $\sim$3 50-day long cycles per year, at constant power lying between 50 MW_{th} and 56 MW_{th}, slightly below the 58.3 MW_{th} nominal power. Such power is 2 orders of magnitude below the power of commercial nuclear reactors, usually at the few GW_{th} level. These reactor cycles are separated by shut-down periods dedicated to maintenance operations and fuel exchange.

The STEREO experiment takes full advantage of the special features of the HFR fuel composition and geometry to investigate the reactor anomalies.

The HEU fuel provides an antineutrino flux almost purely coming from the fissions of the ^{235}U isotope (at the 99.3% level), so that the experiment is able to measure a pure ^{235}U-induced antineutrino spectrum and shed light on the contribution of this one isotope to the anomalies. In practice, the total antineutrino flux measured by STEREO also includes antineutrinos emitted not-only from the beta-decay of the fission products, but also from the beta-decay of activated structural materials, in particular ^{27}Al. Nonetheless, these flux corrections are essentially low-energy corrections, impacting the very first bins of the measured antineutrino spectrum by few percents. They are discussed in Section 3.1.1.2.

Besides, as detailed in Section 1.2, the neutrino oscillation that STEREO aims to probe as a possible explanation to the flux anomaly is a short-baseline oscillation, unfolding over a few meters from the reactor core. In this respect, the uncertainty on the antineutrino emission vertices must be negligible in comparison to the baseline that is probed. This requirement is met with the compactness of the HFR fuel arrangement.

At last, the relatively low power at which the HFR is operated with respect to commercial reactors makes the experiment challenging in terms of signal-to-background ratio. In this regard, STEREO benefits from the alternance of reactor cycles and shut-down periods, allowing to accurately measure and study the background during the reactor-OFF periods in order to extract the antineutrino signal from the data taken during the reactor-ON periods.

2.1.2 Reactor hall

The STEREO detector is installed on level C of the reactor building, at (10.298 ± 0.028) m from the core (distance from the detector center to the core center). It is surrounded by two instruments: a thermal neutron diffractometer for single-crystal and fiber diffraction (D19) and a thermal three-axis spectrometer for inelastic scattering experiments (IN20) [72], fed with beams of thermal neutrons extracted from the reactor moderator. The vicinity of these instruments puts a two-fold constraint on the STEREO detector design. First, they limit the spatial extension of the experiment within the reactor hall. Second, they are a source of non-constant backgrounds, dependent upon the operating status of the instruments: γ rays and neutrons that may interact in the detector, as well as stray magnetic fields up to $\sim$ 1 mT (2 orders of magnitude above Earth's magnetic field), coming from high-field magnets inside the instruments, that may affect the operation of the detector photomultiplier tubes. Thus, a dedicated shielding assembly is mandatory to mitigate such background contamination. It is highlighted in Figure 2.1 and discussed in Section 2.2.

Finally, the STEREO detector is located below a 7m-deep water channel, used to transfer and store spent nuclear fuel. This adds another spatial constraint on top of the detector, but provides on the other hand a 15 meter water equivalent (m.w.e.) overburden against the vertical flux of cosmic rays, as it will be discussed in Section 2.2. To fully exploit the background reduction induced below the water channel, the detector is aligned with this channel, yielding to an angle of $(17.9 \pm 0.2)^\circ$ between the detector axis and the direction to the core [75].

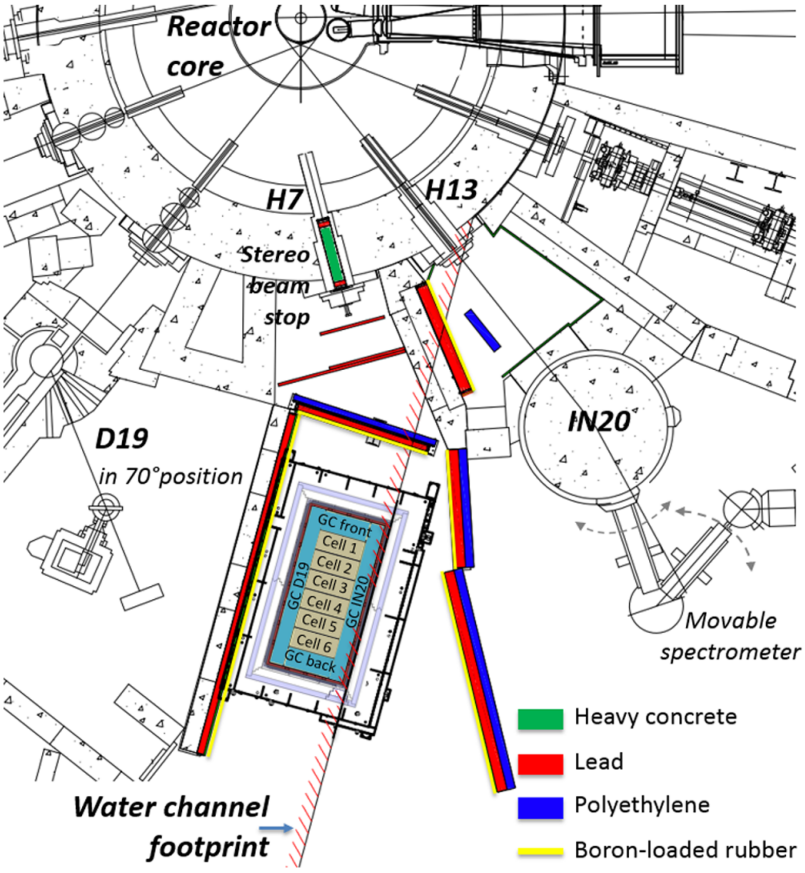

Figure 2.1: **Top view of the experimental site at level C of the ILL reactor building**. Reinforced shielding of the STEREO site is highlighted. The detector is aligned with the water channel, resulting in a slight deviation of the detector axis from the direction to the core. Taken from [75].

2.2 Detector description

2.2.1 Shielding

As it has been pointed out in the previous section, several background sources may be identified on the ILL experimental site. In this section, we propose to list out all these contributions and the associated design of the shielding assembly that has been chosen in order to mitigate them [73]. Each of them are sketched in Figure 2.2. The background contamination may be classified in 4 categories:

1. **the cosmic background**, coming from the cosmic rays (mostly muons) interacting in the detector and to which STEREO is particularly sensitive as a ground-level experiment with an overburden of only 15 m.w.e. below the water channel,

2. **the external neutronic background**, containing a reactogenic thermal component with an energy of ∼25 meV, and a cosmogenic and reactogenic fast component with a typical energy of several MeV. Such background can be mitigated by use of boron-loaded materials, that absorb thermal neutrons, coupled to polyethylene that allows to thermalize fast neutrons via (n, p) elastic scattering,

3. **the γ background**, coming either from the natural radioactivity for low-energy γ-rays (with energy up to 2.6 MeV, corresponding to the highest natural γ-line of ^{208}Tl) or, for high-energy γ-rays, from thermal neutron capture on the surrounding materials, such as ^{27}Al(n, γ) or ^{56}Fe(n, γ) (with energy up to 9 MeV), as well as from the activated water of primary loop circulating underneath STEREO with ^{16}N decay. These radiations are usually attenuated by use of appropriate lead shielding,

4. **the magnetic background**, coming from the neighboring instrument IN20.

Passive shielding

The passive shielding for the STEREO experiment is three-fold. It consists of:

- **localized shielding materials**, deployed in the H7 and H13 primary casemates, identified to be a significant source of fast neutron background. Consequently, an adapted plug has been designed for the H7 tube, consisting of 2 cm of Boral, 8 cm of lead and 1 m of heavy concrete whereas the H13 casemate bordering towards STEREO was reinforced by borated polyethylene, boron-loaded rubber and a 10 cm lead wall (see Figure 2.1).

- **reinforced walls** separating the detector site from the reactor and neighboring instruments. In this regard, the front wall contains 10 cm of polyethylene and 10 cm of lead, the wall on the D19 side, 10 cm of lead and 30 cm of heavy concrete, and the wall on the IN20 side 15 cm lead and 15 cm borated-polyethylene to mitigate the γ and neutron backgrounds (see Figure 2.1). For the last phase of the STEREO data-taking (cf. Section 2.3), a water wall was added in front of the detector. It consists of high-density polyethylene tanks filled with water and is 3.4 m high, 2.4 m wide and 40 cm thick,

- **a 65-ton shielding assembly** encapsulating the detector vessel. It is composed of borated polyethylene (29.7 cm on top, 14.7 cm on sides, and 20 cm below) and lead

(15 cm on top, 10 cm on sides, and 20 cm below). To shield the detector against magnetic background, the shielding structure has been enclosed in 10 mm thick walls of soft iron, with an additional 1.5 mm thick layer of μ-metal.

Active shielding

The last remaining background to be addressed is the cosmic ray induced background. It originates from the interaction of high energy primary cosmic rays (at ∼99%, protons and helium nuclei) with the nuclei of the upper atmosphere, generating a shower of secondary particles, among which are short-lived π mesons. These mesons will decay into muons that may reach the ground-level STEREO detector. These muon primary events constitute the bulk of the cosmic-ray background in the detector's active volume. However, the water channel below which the STEREO detector is aligned and the reactor building encompassing the experiment provide a 15 m.w.e. overburden, acting as a passive shielding and translating into a $\sim$ 2-to-4 attenuation factor of the muon flux, depending on the zenith angle [73]. The attenuation is maximal for the vertical part of the muon flux, which is the dominant one.

Besides, the high energy primary muons can also trigger spallation reactions, producing secondary gammas and fast neutrons inside and nearby the detector. Thus, the topology of the overall fast neutron background turns out to be rather complicated, as it is composed of very directional parts, coming either from the ILL's reactor core or the neighboring experiments, and an omni-directional muon-induced part.

In order to mitigate the primary and secondary muon-induced events and reach a signal-to-background ratio of $\sim$ 1, the passive shielding is not sufficient. The shielding strategy must then be coupled with active rejection technics, allowing to veto the muon-induced background events. For this purpose, a water Cherenkov detector was placed on top of the STEREO detector and used as an active muon veto. It is filled with deminaralized water doped with 4-methylumbeliferone, allowing to shift the wavelength of the emitted Cherenkov light in the optimal photo-efficiency domain of 20 photomultiplier tube (PMT) read-outs. A highly diffusive sheet of Tyvek 1059B covers the walls of the detector, so that a (99.5±0.1)% detection efficiency for vertical muons is achieved. Finally, to further reject the background, one complements this active shielding strategy with a particle discrimination analysis, taking advantage of the properties of the active detection volume, as it will be explained in Section 2.2.2.

2.2.2 Inner detector

The Target (TG) volume of the STEREO detector consists of an acrylic aquarium filled with gadolinium-loaded liquid scintillator (LS) and longitudinally segmented into 6 identical cells of dimensions $L \times l \times h = 0.369m \times 0.892m \times 0.918m$. The cells are optically separated with 4 mm thick inner walls, whereas the aquarium outer walls are 12 mm thick to properly seal the apparatus. The optical segmentation of the TG volume is a crucial point of the experiment to investigate the oscillation to a possible sterile neutrino state. This way, the antineutrino signal can be reconstructed at the cell level, and the oscillation signal can be tracked by a relative comparison between cells.

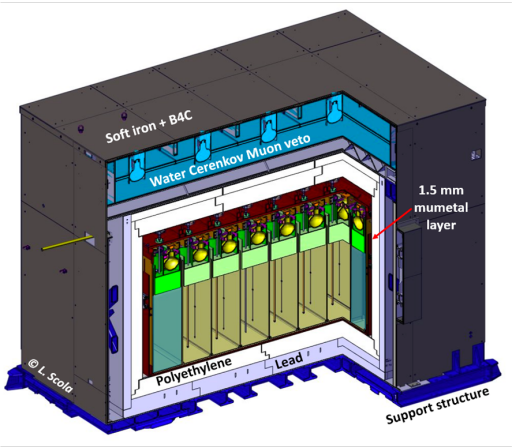

Figure 2.2: Cut view of the STEREO shielding assembly and detector.

The TG volume is enclosed within a larger stainless steel vessel of inner dimensions $L \times l \times h = 3.096m \times 1.536m \times 1.505m$, defining an outer crown filled with unloaded LS. The crown is designed to enhance the detection efficiency of the antineutrino signal. It is optically divided in 4 cells, known as Gamma-Catchers (GC) as they allow to detect escaping γ events from the TG. These γ-rays would either come from the e^+e^- annihilation of the IBD positron or from the de-excitation reaction following the capture of the thermalized IBD neutron. On the other hand, the GC can also be used as an active veto apparatus to reject external γ background that would enter the TG. The two cells intersecting the longitudinal continuation of the outer TG cells (GC front and back) have the same dimensions as the TG cells, whereas the cells placed at the sides of the TG (GC D19 and IN20) are 30 cm thick cells covering the full length of the TG volume.

In the TG and GC volumes, the LS converts the energy deposited by a crossing particle into light, throughout the scintillation process. This light is detected by means of 48 8-inch PMTs, model R5912-100 from Hamamatsu, placed on top of the overall detection volume (TG + GC) and isolated from the LS by 25 cm thick acrylic plates. Each PMT is enclosed in a μ-metal cylinder to further shield the read-outs against the magnetic background, and immersed in a bath of mineral oil to ensure the optical coupling with the acrylic blocks. A view of the overall inner detector is shown in Figure 2.3.

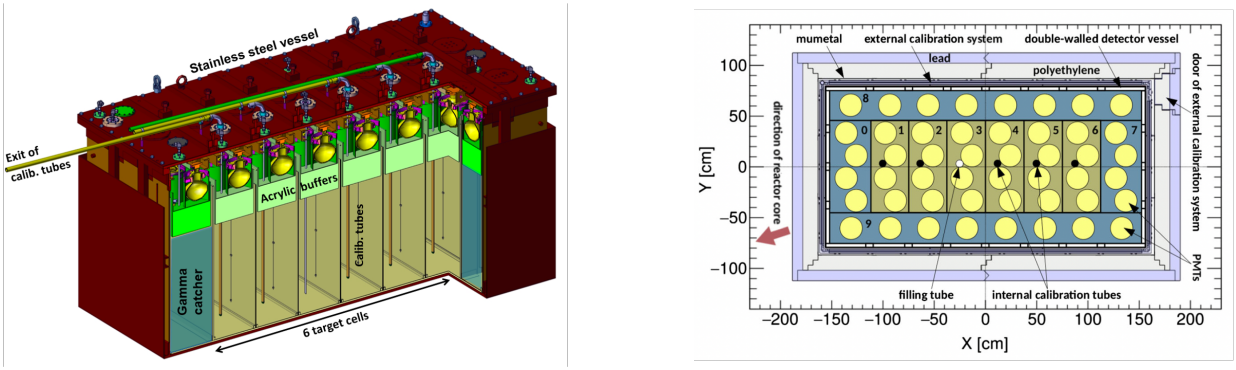

(a) (b)

Figure 2.3: **STEREO inner detector.** (a) Cut view. (b) Top view. TG cells are numbered from 1 to 6, whereas cells 0, 7–9 correspond to GC cells.

Reflective wall properties

The side walls and the bottom of all cells (TG and GC) are covered with highly reflective VM2000^{TM} Enhanced Specular Reflector (ESR) films, exhibiting a ∼98% reflectance in the range of emitted wavelength in the LS, typically around 400 nm [76]. The bottom reflective layer allows to reduce the top-bottom effect of the light collection within one given cell. This effect comes from the fact that the PMT read-outs are only placed on top of the active volume, so that the light emitted towards the bottom of the cells would be lost without these films. The side reflective layers in-between the cells ensure the optical segmentation of the detection volume. This allows to identify the interaction vertex of an event with a typical spatial resolution of about half the dimensions of the cell.

However, it has been shown that, when immersed in a liquid, the reflectivity of ESR films tends to drop above a critical incident angle dependent upon the light wavelength. To circumvent this effect, the films were placed in-between 2 mm thick acrylic plates. An air gap is ensured by means of a 100 μm thick nylon net, as seen in Figure 2.4. The impinging light on the separating wall can then either undergo a total reflection at the interface air-acrylic for angles greater than ∼42° or a reflection with a ∼98% reflectance index on the ESR film. Such design preserves optimal reflective properties for almost the entire surface of the separating walls, although edge effects remain at the level of the sealing of the air gap. Overall, the optical cross-talk between cells is limited to the few percent level, during the stable operation of the STEREO detector.

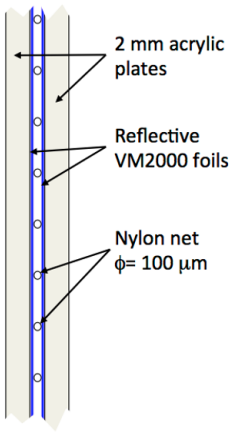

Figure 2.4: Schematic view of the separating wall of the STEREO detector.

Liquid Scintillator properties

The liquid scintillator plays a dual role in the STEREO detector. As a hydrogen-rich material, it acts as a target volume for impinging antineutrinos to trigger the IBD reaction, and as a scintillating material, it serves as an active volume, that converts the deposited energy of the IBD particles into light, to be collected in the PMT read-outs. In particular, it has to be transparent to the wavelength of the scintillated light, as shown in Figure 2.5.

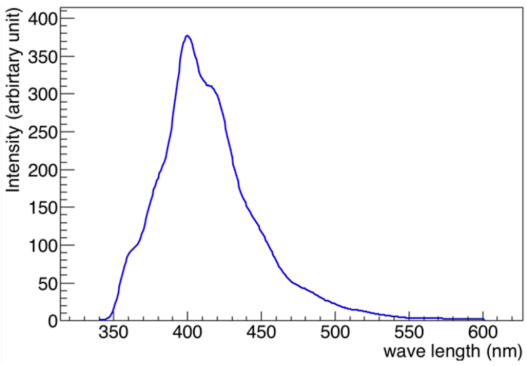

(a) Scintillation intensity

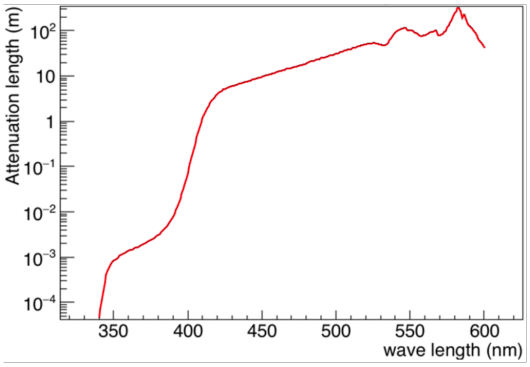

(b) Attenuation length

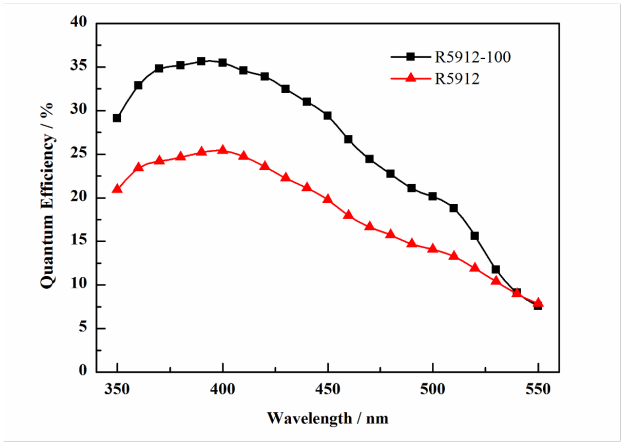

(c) PMT Photo-Detection efficiency (black curve)

Figure 2.5: **Optical properties of the STEREO liquid scintillator and PMTs.** The liquid is transparent to the scintillation light (Fig. b), as the dimensions of the cell ($\sim 1m$) are negligible with respect to the attenuation length in the wavelength range of interest ($\sim 10m$). Noticeably, the scintillation light (Fig. a) is also in the optimal sensitivity domain of the PMTs (Fig. c). Source [77, 78].

In the LS, the scintillation is based on the fluorescence mechanism. It originates from the prompt and delayed radiative transitions of molecules excited by the passage of charged particles [79]. A key point of this de-excitation process is that the overall transition scheme, given by the ratio of the prompt-to-delayed fluorescence, may differ depending on the type of the crossing ionizing particle, giving a sizeable difference in the pulse shape of the emitted light signal: the lower the prompt-to-delayed fluorescence ratio, the longer the tail of the signal. This feature can be utilized to discriminate particles and is known as Pulse Shape Discrimination (PSD).

In this approach, the classification of events is based on the tail-to-total PMT charge ratio observable: Q_{tail}/Q_{tot} (see Figure 2.6). For instance, positrons, that would come from the IBD reaction, and electrons, induce a light signal with a high prompt-to-delayed fluorescence ratio, and consequently a low tail-to-total PMT charge ratio. Such do the γ as they induce electron recoils in the liquid from Compton interaction or photo-electric effect. The PSD signal coming from these particles is then labelled as "electron-like" recoil. Fast neutrons, may they be cosmogenic or reactogenic, induce proton recoils from (n, p) elastic scattering, giving rise to a light signal with a low prompt-to-delayed fluorescence ratio, and thus a high tail-to-total PMT charge ratio. Consequently, the PSD signal of these particles is labelled as "proton-like" recoil.

Coupled to the aforementioned active and passive shielding strategy, the PSD capability of the LS turns out to be a key feature of the STEREO detector to boost the signal-to-background ratio of the experiment.

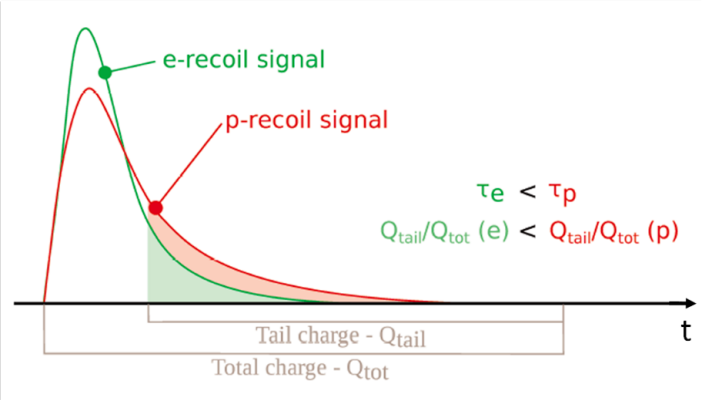

Figure 2.6: **Pulse Shape Discrimination of electron- and proton-like recoil signals.** The tail-to-total charge ratio Q_{tail}/Q_{tot} is higher for the proton-like recoil signal.

All these specifications led to a mix composition of the LS. In terms of mass fractions, the breakdown is as follows [80]:

- 73.0% is linear alkyl benzene (LAB), which is a solvent chemically compatible with detector materials, with a high flash point, fulfilling the safety requirements of the ILL experimental site. It is also highly transparent in the emission domain of the scintillation light, as shown in Figure 2.5.

- 24.4% is composed of ortho-phenyl-xylyl-ethane (PXE, 19.5%) and di-isopropyl-naphtalene (DIN, 4.9%), that proved to enhance the PSD capability of the liquid as well as its light yield, defined as the number of emitted photons per unit of deposited energy. It has been measured to be at least 6500 photons/MeV.

- 0.8% of diphenyloxazole (PPO) and 0.002% of bis-methylstyrylbenzene (bis-MSB) fluorescent molecules acting as wavelength shifters for the scintillated light.

- 0.9% of Gd-β-diketonate compound ($Gd(thd)_3$) dissolved in a proportion of 0.9% of tetrahydrofuran (THF) for the TG volume only, equivalent to a 0.2% gadolinium (Gd) loading. This complex fulfils the criteria of chemical stability and long time solubility of Gd molecules in the LS [81]. With thermal neutron capture cross sections $\sim 10^4 - 10^5$ higher than that of the hydrogen nuclei for the ^{155}Gd and ^{157}Gd isotope[1], the capture time of the thermalized IBD neutron then decreases[2] from 230 μs to 16 μs [82], which cuts by one order of magnitude the rate of accidental background events within the time window between the prompt positron signal and the delayed neutron signal. More details on the selection cuts applied in the analysis are given in Section 5.1. Finally, the Gd-loading of the TG liquid scintillator also results in a degradation of the liquid light yield, so that it is measured to be 6500 photons/MeV in the Gd-loaded TG liquid and 8400 photons/MeV in the unloaded GC liquid.

[1]The natural isotopic abundances of ^{155}Gd and ^{157}Gd are respectively 14.80% and 15.65%, that is, at a significant level.

[2]To be compared to the ~ 2 μs thermalization time.

2.2.3 Calibration systems

Calibration systems are necessary devices to extract the observables monitoring the detector response on a regular basis. In particular, the PMT charge that is recorded via the acquisition system discussed in the next section, and expressed in ADC units, has to be converted in a number of detected photons, and the dependence of the LS light yield upon the deposited energy and the type of the interacting particle is to be assessed, in order to properly relate the energy to a number of emitted photons.

The last remaining piece to complete the picture would be to relate the number of emitted photons in the LS to the number of detected photons in the PMTs, so that the PMT charge would be "convertible" into a deposited energy. Naturally, there is no one-to-one relationship between these two quantities, because of various detection effects (electronic noise, photo-statistical effects, resolution effects, detection efficiency, amongst others). Therefore, a refined modelling of the STEREO detector including a complete simulation of the particle propagation and interaction is critical to infer the detector response, at the cell- and target-level. This point will be discussed in detail in Section 3.1. The charge and energy calibration data will then serve as inputs of the simulation to constrain the free parameters of the detector modelling.

PMT Charge calibration

The PMT acts as an amplifier and a converter of a given light signal. When a photon reaches the PMT photocathode, it can generates an electron from photo-electric effect. This photo-electron (PE) signal is amplified into a macroscopic current flow, thereafter converted into an ADC charge.

To calibrate the PMT charge, one computes the gain of the PMT, that is the average number of ADC units per detected photon or, equivalently, the average number of ADC units per photo-electron. It is then expressed in ADC units per photo-electron [ADC/PE].

In this purpose, the TG and GC volumes are illuminated every 2 hours with 465 nm wavelength LED sources, operated at low intensity. More specifically, LEDs are placed within boxes outside the shielding and light is carried through optical fibers to diffusive teflon balls placed in the liquid scintillator. Such apparatus allows to measure the charge spectrum of the PMTs at the photo-electron level. In Figure 2.7, we show an example of such spectrum, where an amplification factor of 20 is applied on the PMT charge, corresponding to the X-axis of the graph. The measured spectrum is fitted with a model including the PMT response and various background processes [83]. The gain of the PMT is given by the fitted position of the first photo-electron peak Q_{PE}, corrected from the amplification factor of 20. As shown on the example spectrum of Figure 2.7, it is known with a typical 0.5% accuracy and the fitting procedure gives an overall satisfactory agreement between the model and the measured spectrum.

The computation of the gain to convert the ADC charge in a number of detected photons relies on the perfect linearity of the PMTs and associated electronics. This assumption has also been checked, by comparing the signal of several LEDs simultaneously switched on to the sum of the signals with each LED sequentially switched on, taken as a reference. The deviation from linearity was found to be at the sub-percent level over the dynamic range of interest.

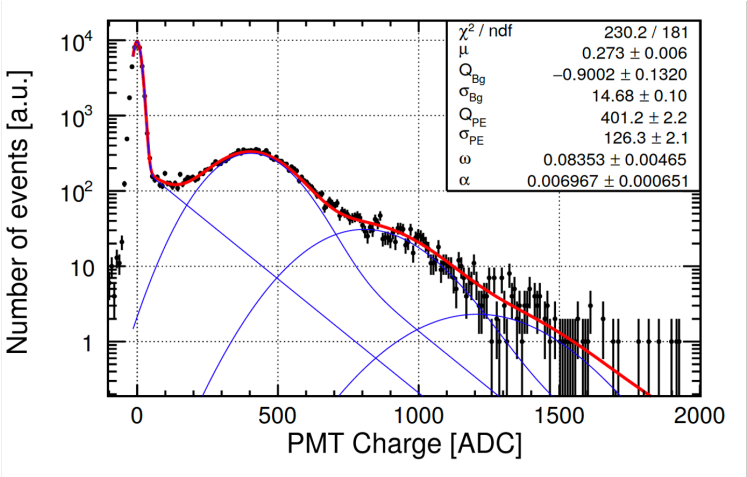

Figure 2.7: **Example of a PE spectrum measured for a PMT of a target cell.** The data are represented as black points, the overall fitted model as a red line, and the breakdown of the single PE signals as blue lines. An amplification factor of 20 has been applied on the PMT Charge X-axis. Source [73].

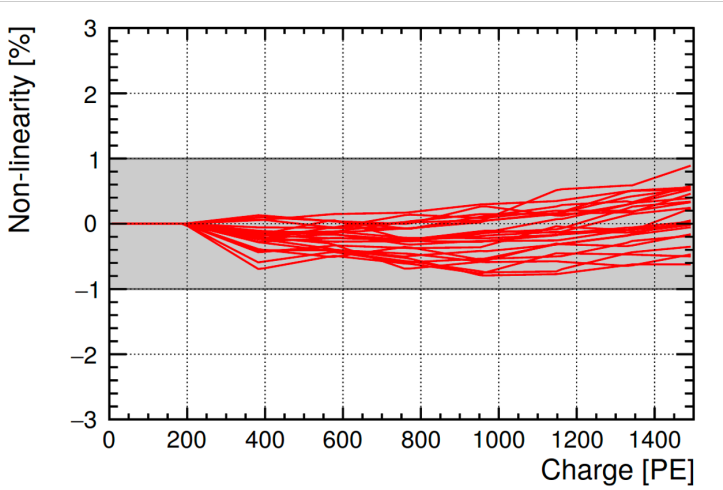

Figure 2.8: **Deviation from linearity for all TG PMTs.** Below 200 PE, the PMTs and electronics are assumed to be perfectly linear to ensure the convergence of the method [73]. At the cell level, the upper limit on the PE charge is equivalent to an energy of ∼25 MeV (see Section 3.2 for the correspondence between PE and MeV).

Energy calibration

The energy calibration is performed by deploying radioactive sources inside and around the STEREO detector, by means of 3 calibration systems, as displayed in Figure 2.9. The systems comprise: an external semi-automatized system beneath the detector, to deploy the sources below the cells along the central longitudinal axis ; an external semi-automatized system around the detector vessel, called the pantograph, that can be moved in the vertical direction at heights between 15 and 90 cm above the TG cell floor, while covering the whole perimeter of the detector volume ; internal Teflon-coated steel tubes inside all cells, except for cell 3, to deploy the sources at 5 different heights. The tubes are centered in the transverse direction and off-centered by about 12 cm in the longitudinal direction, towards the ILL reactor.

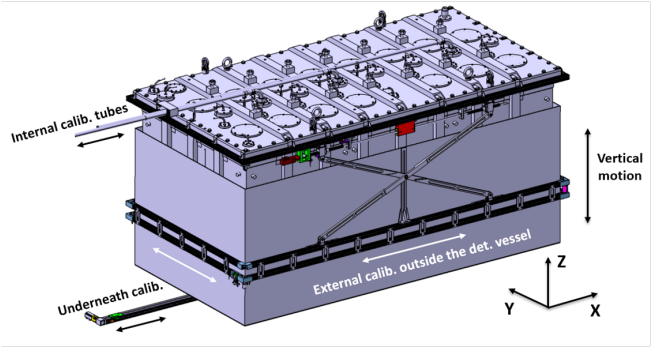

Figure 2.9: **STEREO calibration systems.** Source [73].

With such apparatus, it is then possible to study the detector response almost uniformly in the active detection volume. Two types of radioactive sources are used in this purpose: pure γ sources (^{68}Ge, ^{137}Cs, ^{54}Mn, ^{65}Zn, ^{42}K, ^{60}Co, ^{24}Na) and one neutron source (^{241}Am/^{9}Be). As we mentioned previously, the γ sources will induce electron-like PSD signal, akin to the signal given by the prompt IBD positron. As for the neutron source, it allows to study the PSD of proton-like recoil signals and to mimic the delayed IBD neutron signal, from its thermalization in the liquid to its capture on a hydrogen or gadolinium nucleus.

As noticeable in Table 2.1, the energy of the main γ-rays emitted by the radioactive sources are mostly below 2 MeV, where the dependence of the LS light yield upon the deposited energy significantly deviates from the pure linear regime. This is the so-called *quenching* effect, that will be described in Section 3.2.2.

Source	^{68}Ge	^{137}Cs	^{54}Mn	^{65}Zn	^{60}Co	^{42}K	^{24}Na	^{241}Am/^{9}Be
γ Energy [MeV]	0.511 ($\times$2)	0.662	0.835	1.11	1.17 1.33	1.52	1.37 2.75	4.43 (+ neutrons)
Activity [kBq]	90	37	90	2.8	50		5.9	$2.5 \cdot 10^5$ (^{241}Am) $\sim$10-20
Date	01 Oct. 2016	11 Oct. 2016	01 Oct. 2016	15 Dec. 2016	05 Oct. 2016		22 Feb. 2017	05 Oct. 2016

Table 2.1: Radioactive sources used for the energy calibration of the STEREO detector. Source [84].

Overall, during the operation of the detector, internal calibration campaigns are carried out on a weekly basis, and complete (i.e. internal + external) campaigns on a quarterly basis.

2.2.4 Acquisition systems

A specific data acquisition system (DAQ) has been developed for the STEREO experiment [85]. The charge signal coming from each of the 68 PMTs (20 for the Muon Veto and 48 for the active detection volume, TG + GC) is read-out, amplified and digitized with a 250MHz sampling frequency in a dedicated Front-End electronic card. The amplification factor depends on the operation mode of the PMTs: it is set to 20 in PE calibration mode, and 1 in standard acquisition mode. The digitized signals are then processed by a Field Programmable Gate Array (FPGA) card, where a numerical high-pass filter centers the baseline at 0 and a numerical Constant Fraction Discriminator (CFD) sets the trigger condition for an event signal to be processed, according to the following scheme: first, the CFD algorithm only selects events whose signal amplitude passes a given threshold value, set above noise, providing us with the start time of the pulse t_{CFD}. This trigger condition (T1) is checked on the summed up pulse of several PMT signals, coming e.g. from the 4 PMTs associated to the same TG cell. Second, the total charge of the event signal Q_{tot} is computed by a Riemann integration over a 240 ns time window, starting from t_{CFD} and encompassing the full pulse duration. Third, the tail charge of the event signal Q_{tail} is also computed by a Riemann integration, on a shifted time window that starts from $t = t_{CFD} + 65$ [ns]. The time shift has been optimized to maximize the Pulse Shape Discrimination power. The overall process is illustrated in Figure 2.10.

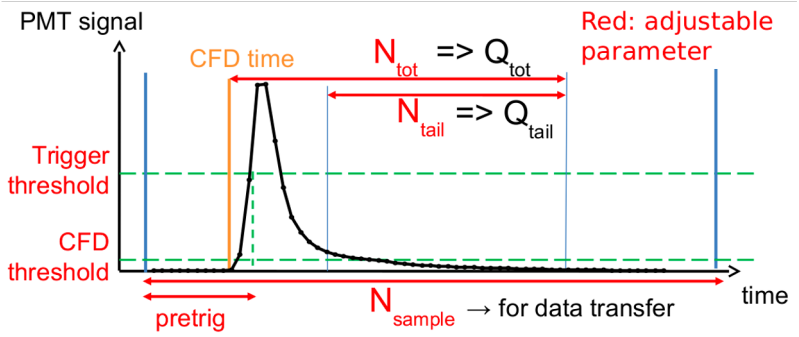

Figure 2.10: **Illustration of the processing of a PMT signal.** Source [85]

When the computation of $(t_{CFD}, Q_{tot}, Q_{tail})$ is done, a second set of selection rules can be applied. It consists on trigger conditions (T2) set on the minimal total charge collected in the TG, GC or muon veto. These additional selection conditions contribute to reduce the γ background contamination [86].

Only the observables $(t_{CFD}, Q_{tot}, Q_{tail})$ of the events passing the total selection scheme (T1 + T2) are written on disk, along with the event date. The induced deadtime of the procedure is less than 0.02% for trigger rates of the order of ~ 1 kHz in standard acquisition mode.

2.3 Detector operation

2.3.1 Monitoring

A variety of sensors deployed inside and around the STEREO detector allows a constant monitoring of the experiment. The observables that are measured can be split in the subsequent categories: electronics parameters, with the crates temperature, as well as PMTs voltage and current ; liquid scintillator parameters, such as the liquid temperature, pressure and level, and the light attenuation in the liquid (measured with LED); background parameters, such as the inner magnetic field, and the outer thermal neutron background, measured with He_3 and BF_3 neutron counters placed outside the detector; environmental parameters, such as the atmospheric pressure and temperature.

A refined study of the variations of the detector response or background contamination over a relevant subset of these parameters can then be carried out and the relevant corrections, when appropriate, can be implemented. As detailed in Section 5.2.1, this will specifically be the case of the PSD figure used to extract the antineutrino signal.

2.3.2 Data-taking periods

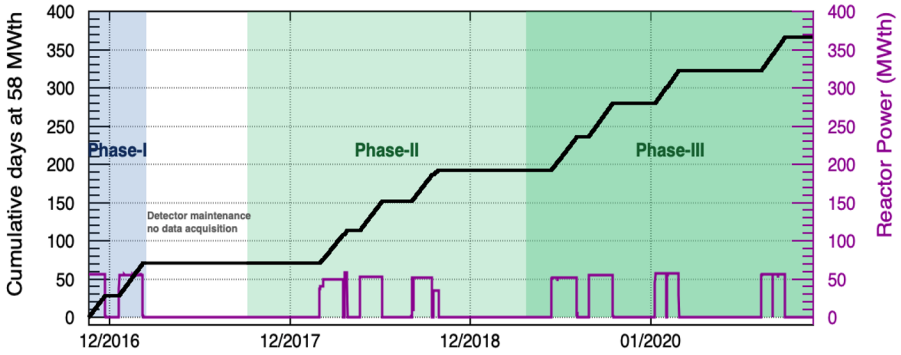

Figure 2.11: **Cumulative (black) and daily (purple) reactor power over calendar day.** The 3 phases of STEREO data-taking are highlighted. Source [84].

The STEREO experiment spans 4 years of data-taking, from November 2016 to November 2020. In this time frame, data were collected both during reactor-ON cycles and reactor-OFF periods. Three data-taking phases may be identified (cf. Figure 2.11):

- **Phase-I from November 2016 to March 2017**, when the detector had to be shut down for maintenance operations at the reactor site. This phase, corresponding to 66 days reactor-ON data and 28 days reactor-OFF data, turned out to be significantly impacted by several technical issues due to cracks in the acrylics. They resulted in a loss of the oil-bath on top of the TG cell 4 and the GC-front cell that leaked into the LS. Due to the subsequent loss of optical coupling between the PMTs and the LS, the collected light of these cells dropped by a factor 2.5. Furthermore, the optical isolation of TG cell 4 was also lost due to leaks of the LS in the air gap of the separating wall, such that its reflective properties were significantly affected and the optical cross-talk between cells increased from a typical few percent level to $\sim$15%.

- **Phase-II from October 2017 to April 2019**, corresponding to 137 days reactor-ON data and 247 days reactor-OFF data. In-between Phase-I and -II, maintenance operations on the detector to repair the defective acrylics allowed to fully restore the light collection and optical separation in and between TG cells. However, the separating walls between TG and GC cells could not be repaired. Also, in the reactor hall, the beam tube H7 and its beam-stop were removed and replaced by heavy water and a steel plug, thus changing the background conditions with respect to Phase-I.
- **Phase-III from April 2019 to November 2020**, when the detector were dismantled. It corresponds to 180 days reactor-ON data and 355 days reactor-OFF data. The Phase-II and -III transition is marked with the addition of the water wall in front of the detector in order to reduce the reactogenic fast neutron component of the background.

Chapter 3

STEREO Detector Response

The precise control of the STEREO detector response is a prerequisite to all analysis of the measured antineutrino spectrum and its comparison to a given prediction. In this chapter, we discuss the strategy consisting in comparing data and simulation at the level of the event reconstructed energy. Great care has been taken to properly implement and fine-tune the simulation of the detector and reproduce e.g. the volume effects, the imperfectness of the reflective wall, the optical cross-talk between cells, and achieve a percent level accuracy on the energy reconstruction, over the whole period of STEREO data-taking.

3.1 The STEREO simulation

The STEREO simulation is based on the version 10.5 of the GEANT4 Monte-Carlo simulation toolkit [87, 88], designed to simulate the passage of particle through matter by taking into account a variety of physical processes (e.g. electromagnetic, hadronic, optical) over a wide energy range, from hundreds of eV to a few TeV, fully covering our typical hundreds of keV to few MeV energy range. More specifically, STEREO utilizes the GLG4sim simulation package, that stands for Generic Liquid-scintillator Anti-Neutrino Detector (GenericLAND) Geant4 simulation [89]. It directly inherits from the Geant4-based Monte Carlo simulation used by the Kamioka Liquid-scintillator Anti-Neutrino Detector (KamLAND) experiment, a long-baseline reactor antineutrino experiment located in the Kamioka Mine (Japan), whose detection process is also based on scintillating liquid technology [36].

With these libraries, the entire detection process in a liquid scintillator-based antineutrino detector can be simulated, from the electromagnetic and hadronic interactions along the path of a crossing particle to the emission of light in the liquid scintillator and its propagation and collection in the photomultiplier tubes. For the simulation to specifically describe the behavior of the STEREO detector, all that remains is to implement its precise geometry and optical properties. This will be explained in detail in Section 3.1.2.

On top of this, one needs dedicated particle generators to properly simulate the propagation of particles (e.g. γ, muons, neutrinos) from their emission to their interaction in the detector, meaning that these generators must be reliable at reproducing the space-time distribution and energy spectrum of these particles. Overall, the distribution of particles that will be generated can be considered constant over time, so that only the spatial distribution and the energy spectrum are of interest in the implementation of the particle generators.

3.1.1 Particle Generators

3.1.1.1 Cosmic background

To simulate the cosmic background, the STEREO simulation made use of the CRY libraries [90]. It allows to generate the correlated showers of particles at sea level. The CRY libraries are based on precomputed input tables from full MCNPX simulations of primary cosmic rays on the atmosphere and have been benchmarked against published data, as shown in Figure 3.1 for the cosmic muon spectrum. Furthermore, given that the STEREO experiment is not located at sea level but at an altitude of 210 m, a relative multiplicative factor of 1.279 has been applied to the simulated flux. To account for the additional attenuation of the flux dependent upon the incident angle of impinging particles and the traversed materials, the water channel below which the STEREO detector is aligned (cf. Section 2.1), the reinforced walls shielding the detector against the environmental background as well as the main components of the reactor building are also implemented in the CRY simulation (see Figure 3.2).

Strictly speaking, the cosmic ray spectrum is not constant over time and is sensitive to the variations of atmospheric conditions directly impacting the way the flux is attenuated while traversing the atmosphere on top of the detector. Nonetheless, with smooth and slight variations of these conditions, this effect is tenuous and has not been included in the simulation.

Furthermore, due to a limited computational power, one cannot run a complete and comprehensive simulation of the background with a sufficient statistical accuracy by propagating all muon-induced events, e.g. muon capture triggering the production of ^{12}B that will be studied in Section 4.3 or spallation-induced fast neutrons emitted in and around the STEREO detector that will be used to study the stability of the n-H capture peak in Section 3.2.3. Instead, the simulation that has been developed provides us with the distribution of the interaction vertices (muon stop vertices, fast neutron emission vertices in particular) that can be used to study a subcategory of induced events.

3.1.1.2 Reactor antineutrinos

In the simulation, the sampling of the detected antineutrino events is done in two steps. First, one samples interaction and emission vertices in the detector and in the reactor core respectively. Secondly, one generates a neutron and a positron at the location of the interaction vertex, with energies sampled from the neutron and positron spectra derived from the predicted antineutrino spectrum. Angular correlations between the IBD generated particles, taken from [45], are also included.

Emission and interaction vertices

The emission vertices are sampled uniformly in a hollow cylinder of the same dimensions and placed at the same position from the detector as the fuel assembly (see Section 2.1.1). The compact dimensions of the core with respect to the reactor-to-detector baseline allows to neglect the spatial asymmetries of fission rates within the core, such that the spatial uniform distribution for the antineutrino production is a safe assumption. Moreover, the time evolution of the fuel composition is also neglected. This treatment was justified with the FISPACT code [92], that allowed to simulate this evolution over a typical reactor cycle,

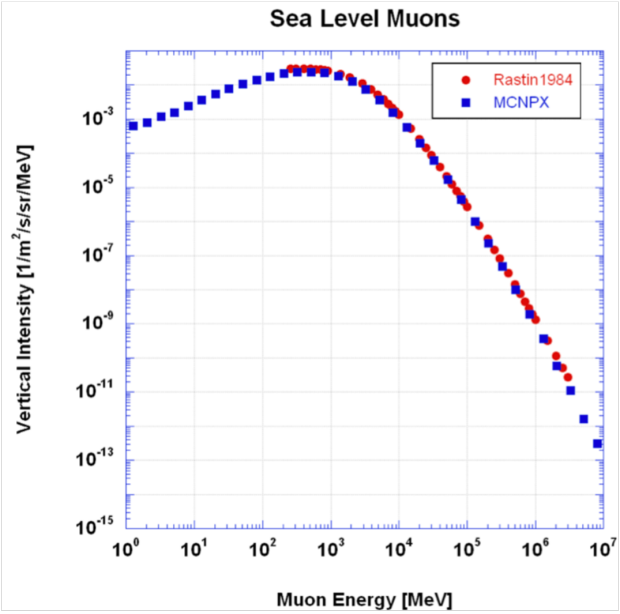

Figure 3.1: **Monte-Carlo generated muon spectrum and data measured at sea level.** Source [90].

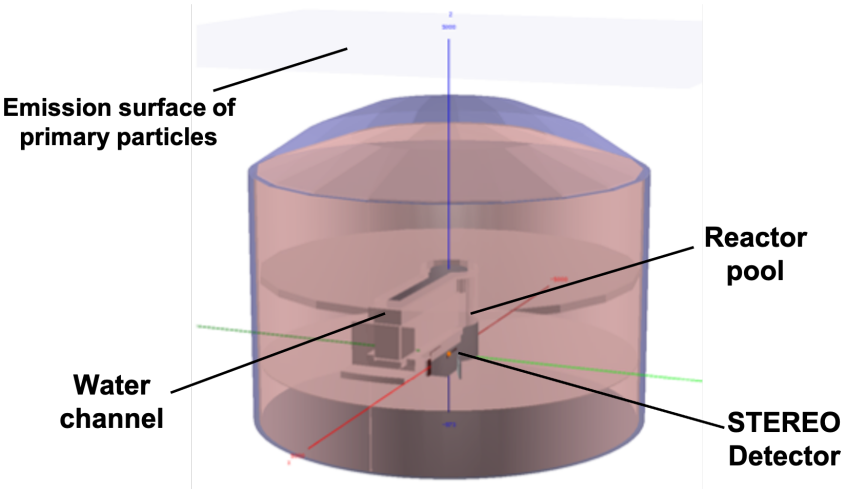

Figure 3.2: **ILL experimental site as implemented in the CRY simulation.** Source [91].

at nominal power. Thanks to the high enrichment in ^{235}U and the short cycle duration, it was shown that the contribution of other fissile isotopes (e.g. ^{239}Pu) to the overall antineutrino flux, averaged out over the cycle, is at the 0.7% level [75].

The interaction vertices are sampled in the entirety of the inner detector volume, including the separative walls and the support structure. The sampling is weighted by the proton number of each target material as well as a $1/L^2$ multiplicative factor, where L is the distance between the interaction and emission vertices, to account for the suppression of the flux with the distance of propagation.

Energy spectrum

As stated in Section 1.2, the detected antineutrino spectrum is given by the product between the emitted antineutrino flux spectrum and the IBD cross section, albeit some flux

corrections must be added to the pure ^{235}U emitted spectrum to get a consistent prediction. These corrections are threefold:

1. **aluminum corrections**, coming from the β-decay of ^{28}Al, whose end-point is at 2.86 MeV. This isotope is produced from neutron capture on ^{27}Al of structural materials,
2. **off-equilibrium corrections**, that make up for the fact that the ^{235}U prediction is given for short irradiation time and thus, do not include the contribution of long-lived fission products to the overall antineutrino flux over the typical cycle duration,
3. **spent-fuel corrections**, coming from the decay of long-lived fission products that accumulated in the spent fuel stored in the water channel above STEREO.

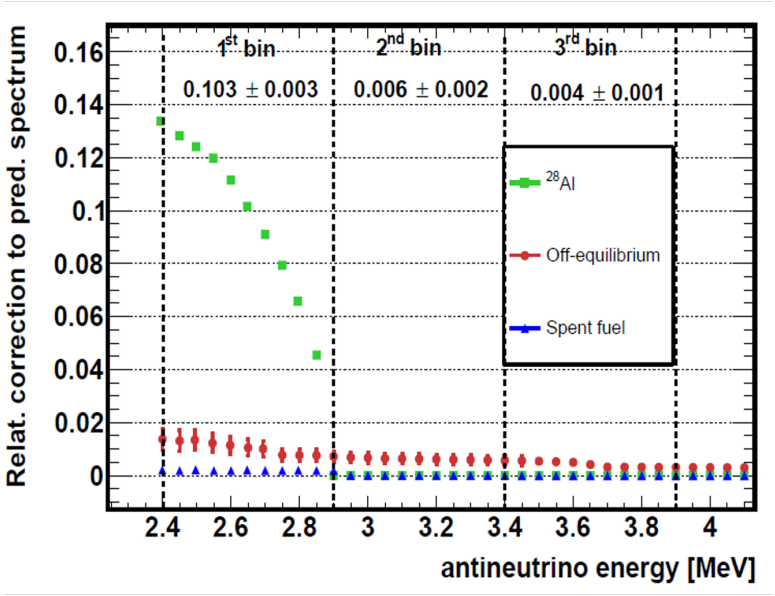

Figure 3.3: **Relative corrections to the predicted ^{235}U antineutrino spectrum.** The 1st, 2nd and 3rd bin labels correspond to the 500 keV-wide antineutrino energy bins of the predicted spectrum matching the reconstructed energy bins of the extracted antineutrino spectrum in STEREO sterile search analysis (see Section 6.1). Source [93].

The overall prediction for the detected antineutrino spectrum of the ILL reactor then reads:

$$\sigma(E_\nu) = S(E_\nu)\left(1 + \delta^{Al} + \delta^{off-equilibrium} + \delta^{spent-fuel}\right) \cdot \sigma_{IBD}(E_\nu) \tag{3.1}$$

where S is the antineutrino flux (expressed in fission$^{-1}\cdot$MeV^{-1}), σ_{IBD} is the IBD cross-section (expressed in cm^2), and δ^{Al}, $\delta^{off-equilibrium}$, $\delta^{spent-fuel}$ are the relative aluminum, off-equilibrium and spent-fuel corrections, displayed in Figure 3.3. The latter can be neglected, whereas the aluminum (resp. off-equilibrium) correction comes with a 5% (resp. 30%) normalization uncertainty, fully correlated between energy bins and phase.

The antineutrino energy is sampled from this predicted distribution. Then, the kinetic energy of the positron T_{e+} is thoroughly derived from the positron to antineutrino energy relation for the IBD reaction channel, whereas the kinetic energy of the neutron T_n is given by the relation [45]:

$$T_n \approx \frac{E_\nu E_{e^+} + \left((E_\nu - E_{e+})^2 - m_e^2\right)/2}{m_p} \tag{3.2}$$

3.1.1.3 Gd γ-cascade

As stated in Section 2.2.2, the loading of the liquid scintillator with gadolinium allows to reduce by one order of magnitude the capture time of the neutron delayed signal, especially with the ^{155}Gd and ^{157}Gd isotopes. After the neutron capture, ^{156}Gd and ^{158}Gd isotopes are formed in excited states, that decay to the ground state by emitting on average four gammas with a total energy of ~ 8 MeV[1]. At high excitation energy, the density of state is a continuum that is not known experimentally. At low excitation energy, the density of state is discrete and is increasingly constrained experimentally as lower energy states are considered.

The careful description of the nuclear energy level scheme is of key importance in the case of an experiment like STEREO. Indeed, the compactness as well as the segmented nature of the detector, that induce non-negligible energy leakage and cross-talk between cells, require the overall γ-cascade to be accurately described. High-energy gammas are more likely to escape and deposit only part of their energy in the liquid, populating the low energy tail of the n-Gd reconstructed energy peak, at the cell level and the detector level. As we will detail in Section 5.1, the selection of IBD candidates relies on the reconstruction of the n-Gd delayed signal, such that great attention has been paid to the accurate description of the Gd de-excitation process.

The standard GLG4sim package initially used to simulate the Gd γ-cascade is based on an effective treatment, that provides satisfactory results in the case of large detectors with limited energy leaks [94], but is no longer appropriate for the STEREO detector. This treatment was significantly improved by use of the dedicated nucleus de-excitation code FIFRELIN developed at CEA-Cadarache (France) [95]. In the FIFRELIN simulation, a set of nuclear level scheme is sampled from the most updated experimental data and recommended nuclear models and data evaluations. A Monte-Carlo Hauser-Feschbach framework allows to generate high-statistic samples of n-Gd de-excitation products that is thereby used in the STEREO simulation on an event-by-event basis [75, 96].

To compare the GLG4sim to the FIFRELIN treatment of the Gd γ-cascade, one deploys inside the detector the ^{241}Am/^{9}Be source that produce neutrons through the reaction:

$$\alpha + {}^{9}\mathrm{B}e \longrightarrow {}^{12}\mathrm{C} + n + \gamma \ (4.4 \text{ MeV}) \tag{3.3}$$

In most cases, the neutron emission goes with the emission of a 4.4 MeV γ coming from the de-excitation of the carbon nucleus. The output signal then exhibits the typical prompt/delayed structure of IBD candidate signals, with the 4.4 MeV γ as a prompt signal, and the delayed signal coming from neutron capture either on hydrogen or on gadolinium. To separate these events from the background events, one requires that the delayed signal lie in a time window of 100 μs after the prompt signal, in the data and simulation. The contributions from random coincidences, known as accidental background, are statistically subtracted [97].

The data-to-simulation comparison in the cases of GLG4sim and FIFRELIN is illustrated in Figure 3.4 for the ^{241}Am/^{9}Be source deployed in the central position of TG cell 4 and in a corner position of TG cell 1. The energy spectra of the delayed signal reconstructed at the detector level are shown for each case. The implementation of the STEREO

[1] 8.536 MeV for the ^{156}Gd isotope and 7.937 MeV for the ^{158}Gd isotope.

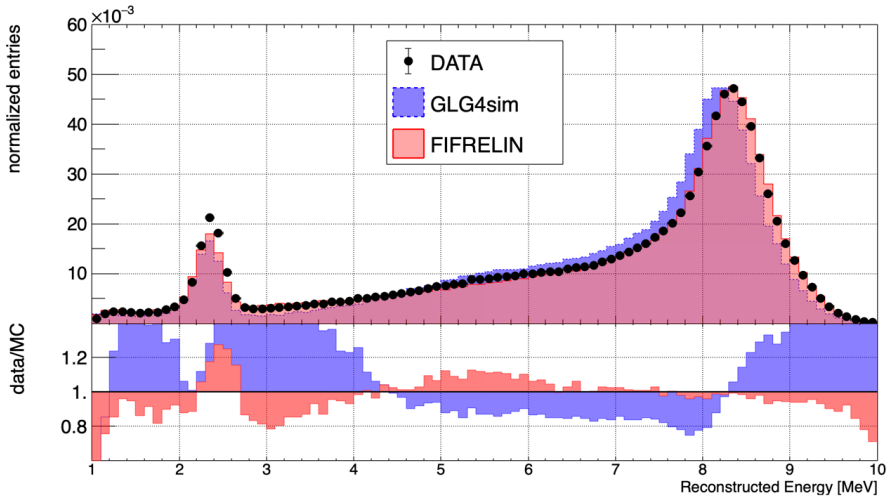

(a) TG cell 4 (center)

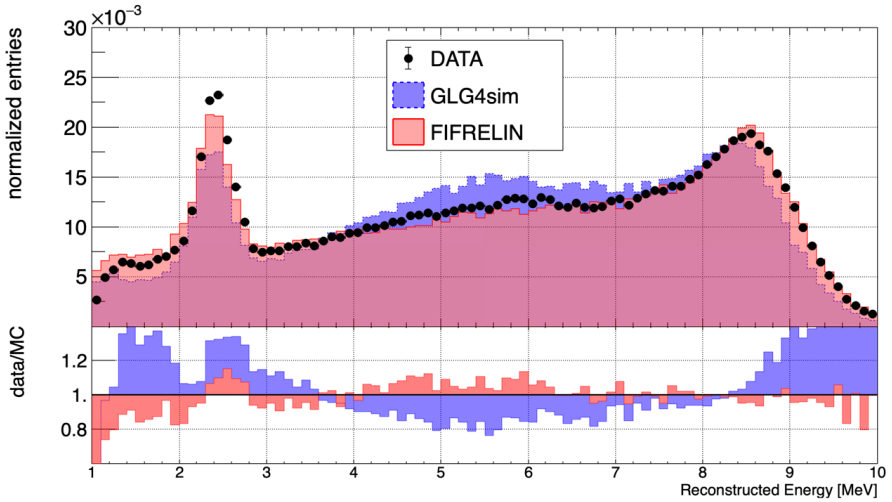

(b) TG cell 1 (corner)

Figure 3.4: **Reconstructed energy spectra from neutron captures from an AmBe source** deployed (a) in the center of TG cell 4 and (b) in the corner of TG cell 1.

detector as well as the energy reconstruction procedure will be laid out in detail in Sections 3.1.2 and 3.2.1. One may identify three regions. The 2 peak regions, corresponding to the n-H peak at low energy and the n-Gd peak at high energy. In-between these two peaks, lies the leak region of the n-Gd capture events consisting of gammas escaping the detector. As expected, the description of this region is improved in the FIFRELIN case with respect to the GLG4sim case, yielding an unprecedented quality of agreement between data and simulation.

3.1.2 Detector implementation

3.1.2.1 Geometry

A detailed description of the inner detector has been implemented in the simulation from technical drawings. Indeed, the acrylic buffers and separating plates, the photomultipliers, as well as the calibration source holders are all included in the detector simulation. Even the gray color of the calibration tubes (that may affect the reflectivity of the tubes, and as a consequence, locally alter the optical properties of the target volume) is encoded. A sketch of the inner detector structure is shown in Figure 3.5.

On top of this, the outer structure of the detector, consisting of the stainless steel vessel along with the various layers of passive shielding and the Cherenkov muon veto, has also been incorporated.

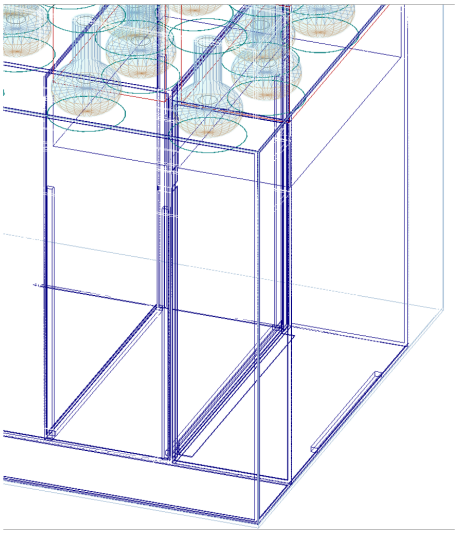

Figure 3.5: **Sketch of the inner structure of the STEREO detector, as implemented in the simulation.** PMTs and separative plates are clearly visible. Source [82].

3.1.2.2 Scintillation process

The scintillation light is propagated on a photon-by-photon basis, by converting the deposited energy of the interacting particle in the detector into light, with a wavelength-shifted emission spectrum coming from the addition of PPO and bis-MSB in the LS.

The propagation of the emitted photon is conducted through a series of absorption/re-emission processes, and eventually, the photon reaches a PMT and generates a photo-electron by photo-electric interaction, with a probability matching the quantum detection efficiency of the PMTs (cf. Figure 2.5), that is implemented in the simulation. There, it undergoes the PMT conversion and amplification process to give a pulse signal, that is converted into an ADC charge.

This way, the output of the simulation can be expressed in the same format as the data, and the same analysis chain can be applied to both sets.

3.1.2.3 Optical model for the separative plates

In order to cover the Phase-I scenario where leaks of the scintillating liquid into the separating walls resulted in a sizeable degradation of their reflective properties, a functional optical model of the separative plates was implemented.

Here, we focus on the case of a wall with a single ESR film to describe the optical model. The extension to the two films case will be derived subsequently. Two extreme cases, illustrated in Figure 3.6, must be studied when considering a wall with a *single* ESR film [98]:

1. the case where the ESR film of the reflective wall is immersed in the liquid. The optical model implemented in the simulation then defines three regions of different reflectivity r, parameterized by the incident angle θ and the wavelength λ of the impinging photon:

$$r(\theta,\lambda) = \begin{cases} 97\% & \text{, if } \theta \leq \theta_p(\lambda) \\ r_{inband} & \text{, if } \theta_p(\lambda) < \theta < \theta_s(\lambda) \\ 0\% & \text{, if } \theta \geq \theta_s(\lambda) \end{cases} \tag{3.4}$$

   where $\theta_p(\lambda)$ and $\theta_s(\lambda)$ refer to the critical angles for s- and p-polarized light that depend on the wavelength of the incident photon. r_{inband} is the probability for the photon to be reflected if its incident angle falls between $\theta_p(\lambda)$ and $\theta_s(\lambda)$. This parameter is a free parameter of the model, to be tuned.

2. the case where an air gap is maintained in the wall. The baseline reflective properties of the wall may then be parameterized as follows:

$$r(\theta,\lambda) = r(\theta) = \begin{cases} 98.5\% & \text{, if } \theta \leq \theta_c \\ 100\% & \text{, if } \theta > \theta_c \end{cases} \tag{3.5}$$

   where $\theta_c = arcsin(n_{air}/n_{acrylic}) \approx 42°$. If the incident angle of the photon is greater than θ_c, it undergoes a total reflection at the acrylic-air interface. Otherwise, it is reflected with a 98.5% probability on the ESR film.

The intermediate case where a certain proportion p of the wall is filled with liquid scintillator may be parameterized with a variable comprised between 0 and 1, corresponding respectively to the extreme cases 2. and 1. This parameter is a free parameter of the model.

At last, the presence of the nylon net (see Figure 2.4) as a potential photon absorber in the wall leads to considering the absorption process, on top of the reflection and transmission processes, to exhaustively describe the optical behavior of the wall. In the case of a *single* ESR film, one then defines the wall reflection probability R, transmission probability T, and absorption probability A as:

$$\left.\begin{array}{l} R = r \\ T = (1-r)(1-a) \\ A = (1-r)a = 1-R-T \end{array}\right\} \text{ for a separating wall with 1 ESR film} \tag{3.6}$$

where a is the nylon net absorption probability, that is also a free parameter of the model.

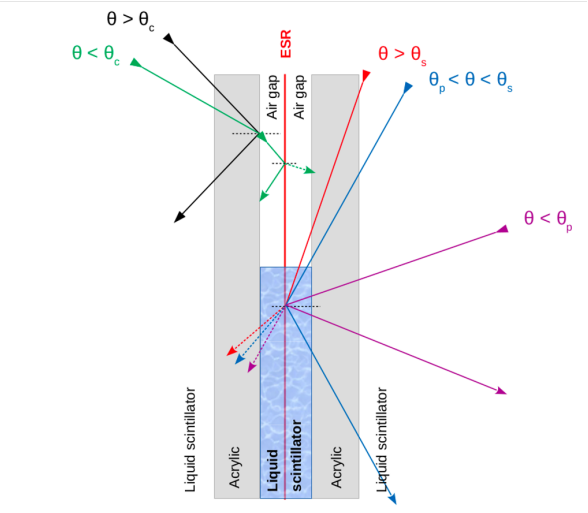

Figure 3.6: **Optical modelling of the separative plates.** The upper part of the scheme corresponds to the case where the air gap is maintained, whereas the lower part illustrates the case where the gap is filled with liquid scintillator. Source [98].

For a wall with *two* ESR films enclosed between the separating plates, these probabilities are significantly different since the photon can undergo a combination of reflection/transmission/absorption processes in-between the two films. Summing over the infinite number of possible scenarios, the reflection, transmission and absorption probabilities read:

$$\left.\begin{aligned} R &= r + \frac{rt^2(1-a)^2}{1-r^2(1-a)^2} \\ T &= \frac{t^2(1-a)}{1-r^2(1-a)^2} \\ A &= 1 - R - T \end{aligned}\right\} \text{ for a separating wall with 2 ESR films} \tag{3.7}$$

Overall, the comprehensive optical model of the separating walls has 3 free parameters:

1. r_{inband}: the probability for the photon to be reflected if its incident angle falls in the sub-critical region for the case where liquid scintillator leaked into the wall,
2. p: the proportion of the wall inner volume that is filled with liquid,
3. a: the nylon net absorption probability.

In order to have the most accurate description of the detector response, these parameters will be finely tuned, along with the liquid optical properties, using as primary inputs the laboratory measurements of these observables, measured once, and as constraints the calibration data, acquired during the real-time operation of the experiment [98].

3.1.3 Fine tuning of the simulation

Principle

The fine tuning procedure that has been developed in [98] is an iterative routine aiming at reaching the best simulation-to-data agreement at the raw PMT charge level for each cell, considering a given set of calibration spectra. To do so, the simulated charge spectra for a given calibration source is compared to the measured charge spectra, at the cell level. We remind that, for an event j, the total charge collected in a cell i is given by:

$$Q_i^j = \sum_{PMT_i} Q_{PMT_i}^j \tag{3.8}$$

where $\{PMT_i\}_i$ is the set of PMTs associated to cell i. To be fully consistent with the simulated charge spectra, it should be mentioned that the data charge spectra considered in the procedure are those obtained after subtraction of the background.

The free parameters to be tuned are those of the optical model of the separating walls (r_{inband}, p, a) and those encoding the LS optical properties (attenuation length, light yield in the TG and GC, and reflectivity of immersed calibration tubes).

The tuning of these optical parameters is performed only once per phase. It is done iteratively, with the parameters value set "by hand" at each step, in order to circumvent the computational cost of one simulation (∼24h). The tuning is based on the comparison of the simulation with the data for a reference calibration campaign, chosen in the middle of the considered phase. This way, the selected calibration data set is, at zeroth order, representative for the entire data-taking phase. The first order effect coming from the slowly evolving detector response over the phase time period will be taken into account in the energy reconstruction method, that will be described in Section 3.2.

For the Phase-I tuning, the optical parameters of the simulation were set as close as possible to the laboratory measurements. In the following, only the Phase-II and -III fine tuning procedure developed in [98] is sketched.

Procedure

The reference calibration runs used for the fine tuning are those of the ^{24}Na source measured on 26/04/2018 (resp. 29/02/2020) for Phase-II (resp. Phase-III). This radioactive source features two gamma lines at 1.38 and 2.76 MeV. The subsequent structure of the charge spectrum exhibits three peak regions, with two of them corresponding to the individual gamma lines whereas the third one is the full-energy peak corresponding to the simultaneous detection of the two gamma rays. This well-defined structure provides a good sensitivity to the tuning of the optical parameters.

The tuning utilizes as a constraint the ^{24}Na charge spectra measured in each cell in the configurations where the ^{24}Na source is successively deployed in each of the 5 heights of the TG cells equipped with a calibration tube (1, 2 and 4–6). The response of the source cell and its neighbors as well as the dependence on the Z position of the source spectra provide lever arm to disentangle the effects of the free parameters of the tuning.

Ultimately, a metric is necessary to compare the simulated and measured charge spectra at each iteration of the tuning of the parameters. To do so, the so-called simulation-to-data gain is computed [98]. It is defined as the multiplicative factor to apply to each simulated charge event to get the best agreement between the simulated and measured charge distributions, in the sense of the least-square method. This fitted gain value can then be interpreted as a correction on the linear calibration coefficient between the data and simulation charge scales. Therefore, a perfect agreement between measured and simulated charges is equivalent to a gain value of 1, so that the deviations to unity serve as a proxy for underlying mistuning of the parameters.

Results

In Figure 3.7, are shown the gain values computed from the comparison of the simulation fine-tuned on Phase-I with the Phase-II data, for each TG cell and each deployment height. The poor agreement that is obtained, with discrepancies reaching the 4% level, highlights the necessity of anchoring the simulation of each phase to representative data sets.

In Figure 3.8, we show for Phase-II and -III the gain values computed from the comparison of the data with the associated fine-tuned simulations. Almost all the values are contained within a $\pm 1\%$ band for every height of the TG cells. An example of data-to-simulation comparison before and after the fine tuning is given in Figure 3.9.

Finally, the robustness of the fine tuning was assessed by replacing in the aforementioned comparison the ^{24}Na with the ^{54}Mn source, which is of peculiar interest as this is the source on which the energy reconstruction procedure will be anchored (cf. Section 3.2.1). This comparison, done for Phase-II, yields to similar results as the ^{24}Na source comparison, as shown in Figure 3.10.

We may specify that, overall, the main parameter responsible for the evolution of the detector optical properties from one phase to another is the attenuation length, especially in the TG due to slow chemical kinetics induced by the Gd-loading of the LS. Subsequently, the attenuation length has been reduced by 33% in the TG liquid and by only 2% in the GC liquid, between Phase-II and -III reference dates.

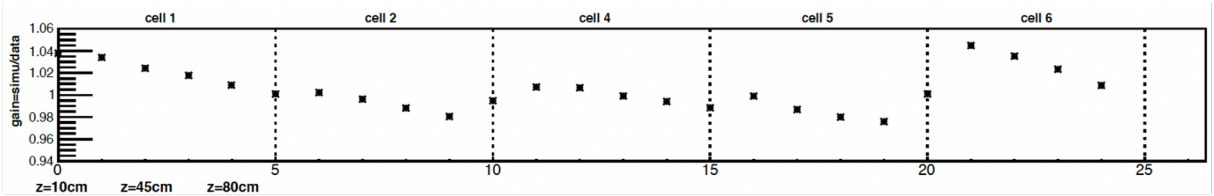

Figure 3.7: **Gain values obtained by comparing the simulation before the Phase-II tuning, with the representative data set of Phase-II, for the ^{24}Na source.** The columns indicate the cell in which the source is deployed at 5 different vertical positions. The gain values are obtained by fitting the two gamma peaks of the source when looking at the charge spectra inside the cell with the source. A noticeable feature is that the top-bottom light collection asymmetries are not well-described by the simulation. Source [98].

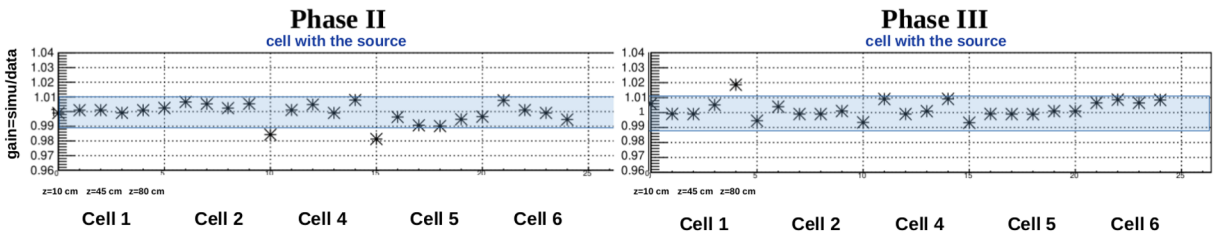

Figure 3.8: **Gain values obtained by comparing the fined-tuned simulation for Phase-II (resp. Phase-III), with the representative data set of Phase-II (resp. Phase-III), for the ^{24}Na source.** Overall, the values are contained in the ±1% blue band. Source [98].

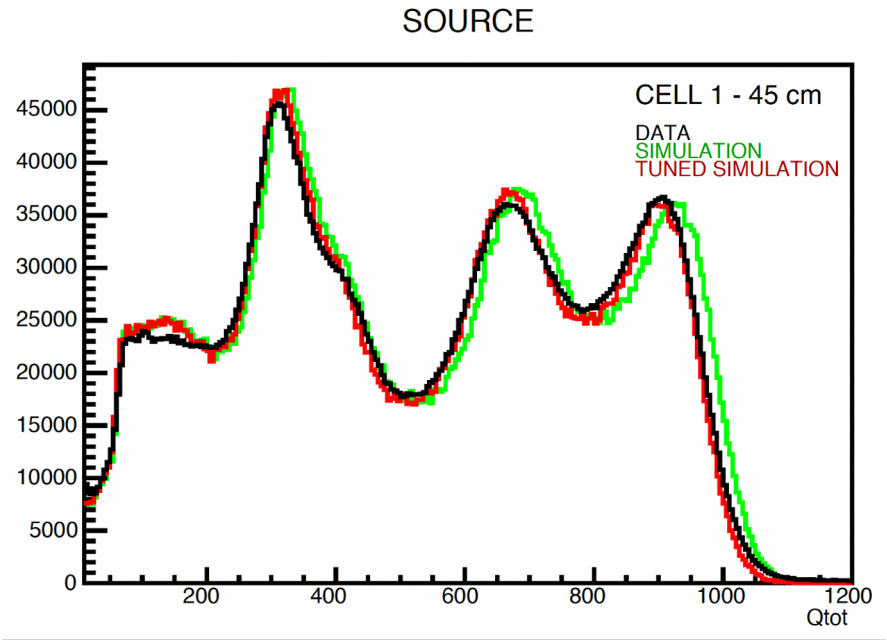

Figure 3.9: **Data-to-simulation comparison before and after the fine tuning**, from the ^{24}Na source deployed in TG cell 1 at a height of 45 cm from the bottom of the cell. The charged spectra are the ones measured/simulated in the source cell, that is cell 1. Source [98].

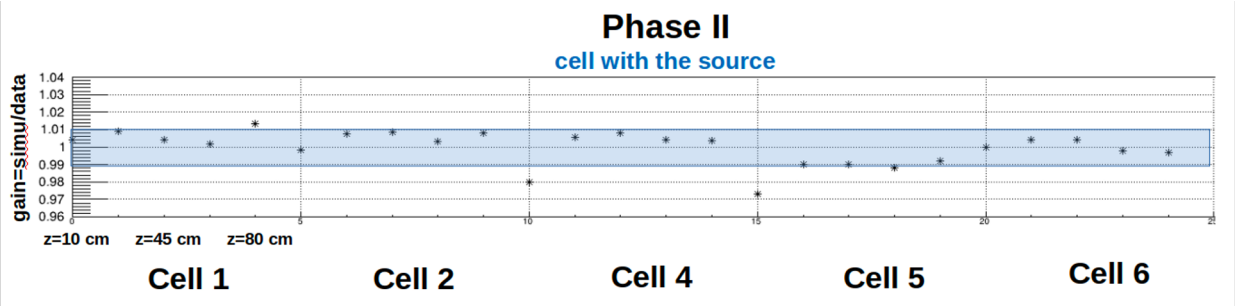

Figure 3.10: **Gain values obtained by comparing the fined-tuned simulation for Phase-II, with the representative data set of Phase-II, for the ^{54}Mn source.** Overall, the values are contained in the ±1% blue band. Source [98].

3.2 Energy reconstruction

In Section 3.1, we detailed the implementation of the STEREO detector, in terms of geometry, material composition and properties. When coupled to the GLG4sim libraries to describe the physical processes, these inputs provide a comprehensive simulation of the physical interaction chains of the detection process. In particular, the description of the optical properties of the detector was addressed with great care by means of an effective detector optical model, fine-tuned on the ^{24}Na measured charge spectra and cross-checked on the ^{54}Mn measured charge spectra.

What remains is to loop back to the actual energy deposited in the detector from the measured PMT charge. In other words, the energy calibration of the detector must be derived. In this section, we will briefly present the formalism that was developed in the STEREO collaboration to perform such calibration [77, 99], as well as the most recent refinements that were brought to further enhance the determination of the calibration coefficients. It will allow to reconstruct the deposited energy at the level of an individual cell, and by extension at the level of a group of cells (e.g. TG or GC volumes) and the entire detector.

3.2.1 Procedure

Principle

Let's consider a typical event depositing a certain amount of energy E in the detector. This energy can be split in a set $\vec{E} = (E_i)_{0\leq i\leq 9}$ of energies deposited in each detector cell. We denote $\vec{Q} = (Q_i)_{0\leq i\leq 9}$ the associated set of collected PMT charges in each cell, expressed here in photo-electrons.

The charge observable of a given cell i can be related to a set of deposited energies by:

$$Q_i = \sum_j L_{ij} \cdot C_j \cdot E_j \tag{3.9}$$

with

$$\begin{aligned} C_j &= LY_j \cdot \alpha_j \\ L_{ij} &= Q_i/Q_j \end{aligned} \tag{3.10}$$

where L_{ij} is the light leak coefficient that quantifies the optical cross-talk between cells i and j coming from the imperfectness of the separating walls, and C_i is the calibration coefficient for cell i, defined as the product of the cell light yield LY_i with the light collection efficiency α_i (averaged over the cell volume). The light leak coefficients are unitless whereas the calibration coefficients are expressed in PE/MeV. By definition, $L_{ii} = 1$.

Defining the calibration matrix element $M_{ij} = L_{ij} \cdot C_i$, we can derive the energy reconstructed from the collected charge as:

$$\vec{E}_{rec} = M^{-1}\vec{Q} \tag{3.11}$$

The energy reconstruction procedure then relies on the determination of the M matrix elements.

However, it should be noted that Equation 3.9, from which Equation 3.11 is derived, is an effective treatment that obfuscates several features. As already stated, the optical

response (i.e. the light yield) of the LS depends on the nature of the impinging particle. It also depends on the energy of the particle, because of the *quenching* effect (see Section 3.2.2). Moreover, the light collection efficiency, averaged out over all the possible directions of emission for the scintillation light, still depends on the position of the emission vertices. In principle, it is not expected to be constant in the entire volume of the cell. The procedure that is detailed so far then allows to implement only a first-order energy reconstruction procedure, in electron-equivalent energy. Discussions and refinements on the procedure will be presented further in the section.

Estimation of the light leak coefficients L_{ij}

The light leak coefficients are estimated from the cosmic muon background events depositing their energy in the detector. As particles at the minimum ionization power (depositing $\sim$ 2 MeV/cm in the liquid scintillator), they are the main background source capable to deposit at least 20 MeV of energy in the detector. Those events can then be selected merely with a lower cut applied on the charge collected in the entire detector (TG + GC). It is set to 4000 PE, corresponding roughly to 20 MeV when applying the calibration coefficients (see Section 3.2.3).

For given cells i and j, the light leak coefficient is then adjusted from a linear regression of the (Q_j, Q_i) 2D distribution.

Estimation of the calibration coefficients C_i

In order to get the calibration coefficient values, the ^{54}Mn 835 keV γ source is deployed at the 5 heights inside each TG cell equipped with an internal calibration tube. These γ deposit their energy in the liquid scintillator from the recoil electrons they induce from Compton interaction, so that using this source probes the detector optical response only for electron-like signals. In other words, the reconstructed energy derived from the STEREO calibration is, strictly speaking, an electron-equivalent energy.

The ^{54}Mn source was chosen to define the reference γ energy, because among the sources with long half-life at disposal, it is the single-γ source which has the highest γ energy being reliably separable from the reactogenic background of γ-rays of ^{41}Ar decays (1294 keV) and whose interaction length is comparable to the cell size [75].

As the calibration coefficient of a given cell relates the energy deposited in a given cell to the charge collected in this same cell, we would like to discard the events that would deposit their energy in a neighboring cell but would contribute to the collected charge in the considered cell via optical cross-talk. To do so, a cut on the light leak coefficient computed on an event-by-event basis is set as follows:

$$L_{ji} = \frac{Q_{j\neq i}}{Q_i} < \langle L_{ji} \rangle + k\Delta L_{ji} \tag{3.12}$$

where $\langle L_{ji} \rangle$ and ΔL_{ji} are respectively the light leak coefficient and its dispersion estimated from the cosmic muon study, and k is a coefficient adjusted so that the quantities $\langle Q_i \rangle$ and $\langle E_i \rangle$ defined below, in Equation 3.13, are weakly affected by a small perturbation

δk.

The calibration coefficient associated to a given source cell i is then computed as:

$$C_i \;=\; \langle \frac{Q_i}{E_i} \rangle \;\approx\; \frac{\langle Q_i \rangle}{\langle E_i \rangle} \tag{3.13}$$

where $\langle Q_i \rangle$ and $\langle E_i \rangle$ are respectively the average collected charge and average deposited energy in cell i, after applying the cut defined in Equation 3.12.

This procedure is applied on both the data and simulation. However, it should be noted that the value of $\langle E_i \rangle$ is naturally only accessible in the simulation. Consequently, this is this value that is used for the computation of the calibration coefficient in the data. This is equivalent to assuming that all the physical processes occurring in the liquid scintillator are accurately described by the simulation, which can be considered a safe assumption as the Geant4 libraries used in the STEREO simulation have been benchmarked on other independent data sets. In this picture, any sizeable discrepancy between the energy reconstructed in the data and the simulation is purely attributable to a misdescription of the optical properties of the detector. Given than the optical model of the overall detector has been carefully fine-tuned and cross-checked, the explanation could rather lie in the average treatment of the calibration and light leak quantities, that washes out volumic and edge effects. A finer adjustment of the calibration and light leak coefficients is then necessary and detailed below.

Refinement of the procedure

When setting the values of the elements of the calibration matrix M with the aforementioned procedure, one ends up with different reconstructed energy distributions in the data and in the simulation for the ^{54}Mn source. Therefore, an iterative procedure to correct for this effect has been developed in [99].

In this procedure, one computes from the simulation a reference energy distribution by convolving the distribution of deposited energies in a given cell with an effective energy response model of the cell using the values of calibration and light leak coefficients computed in the previous iteration. The reference energy E_{rec}^{ref} is set to be the most probable value of this distribution, extracted from a local gaussian fit in the vicinity of the maximum. The most probable values of the reconstructed energy in the data (E_{rec}^{data}) and in the simulation (E_{rec}^{simu}) are then corrected from the residual shift with this reference value. This correction is then propagated as a correction on the calibration matrix elements, that is, on the calibration and light leak coefficients. Then, the same process is repeated until convergence is reached on all calibration and light leak coefficients.

With this iterative procedure, one achieves a 0.2% agreement between E_{rec}^{data} and E_{rec}^{simu} in the case of the ^{54}Mn peak as seen in Figure 3.11. This constitutes the anchor point of the energy calibration of the STEREO experiment.

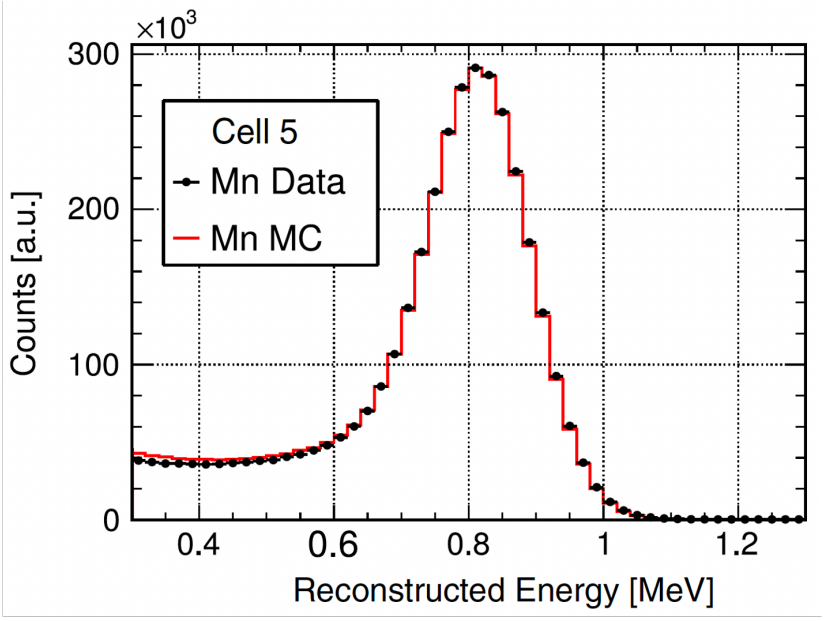

Figure 3.11: **Comparison of measured and simulated reconstructed energy spectra** in cell 5, for the average of the 5 vertical deployment positions of the ^{54}Mn source in cell 5 (Phase-II). Source [75].

Correction of the baseline effect

The procedure defined above allows to reach a 0.2% accuracy on the reconstruction on the ^{54}Mn peak, for all calibration data sets acquired during the 4-year operation of the STEREO experiment. However, it would not prevent a potential bias in the measurement of the peak, that would be propagated in the reconstructed energy. In particular, the high activity of the source operated during the energy calibration campaigns, typically at the few kBq-hBq level (see Table 2.1), can be in conflict with the typical recovery time of the baseline, resulting in a cross-talk between pulses that is not accounted for in the raw computation of the pulse charge.

To circumvent this effect, a time isolation cut of 10 μs between two successive pulse events has been implemented. In Figure 3.12, we show a comparison of the ^{54}Mn reconstructed energy peak with and without this time isolation cut, for all Phase-I, -II and -III data-taking periods. A sub-percent to percent level effect is highlighted, that can be fitted with an exponentially decreasing function over time whose half-life is $\tau = 312$ days, that is, the half-life of the ^{54}Mn radioactive source. In the case of the antineutrino events, the reconstructed energy is protected from this baseline effect by the applied time isolation cuts, that encompass the 10 μs cut (see Section 5.1).

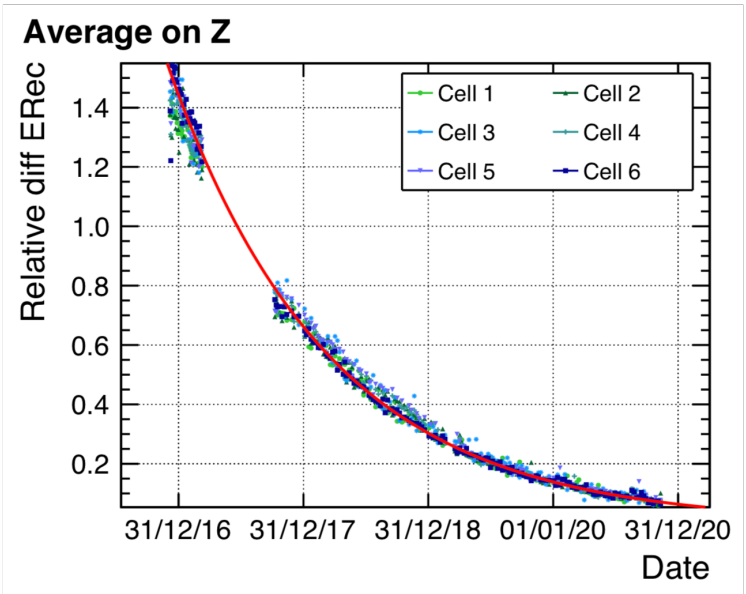

Figure 3.12: **Comparison of the reconstructed energy peak of ^{54}Mn source, with and without the time isolation cut of 10 μs**, for all STEREO data-taking periods. The model (red line) is an exponential decreasing function, with a half-life $\tau = 312$ days. Source [100].

3.2.2 Quenching effect

Description

In the previous section, we anchored the computation of the calibration matrix onto the ^{54}Mn energy peak, at 835 keV. Extending thoroughly this calibration onto the whole energy range would require the detector optical response to be linear with respect to the deposited energy. Most generally, this assumption does not hold for scintillating materials, due to the so-called *quenching* effect[2].

Indeed, two regimes for the optical response may be identified. First, a linear regime, corresponding to the light output being proportional to the deposited energy, provided the density of deposited energy $\frac{dE}{dx}$, expressed in energy per unit of path length, is low. Second, a non-linear regime corresponding to the saturation of the scintillation process induced by high density of energy deposit. This is known as the quenching effect. It has been first described by J. B. Birks, in the early 1950s, that proposed a phenomenological formula to relate the light yield $\frac{dL}{dE}$ with the density of deposited energy along the path length of a ionizing particle [101]. It reads:

$$\left(\frac{dL}{dE}\right)(E) = L_0 \cdot Q(E) \tag{3.14}$$

where L_0 is the light yield in the linear regime approximation, and $Q(E)$ is the Birks quenching function that writes:

$$Q(E) = \frac{1}{1 + kB \cdot \left(\frac{dE}{dx}\right)(E)} \tag{3.15}$$

[2]Another source of non-linearities for the scintillation process is the emission of Cherenkov light along the path of a charged particle traveling faster than light in a given dielectric medium. This effect is accounted for in the simulation.

In the linear regime approximation ($\frac{dE}{dx} \to 0$), $Q(E) \to 1$ and the light yield is constant, whereas in the quenched regime ($\frac{dE}{dx} \to \infty$), $Q(E) \propto \frac{1}{kB \cdot \left(\frac{dE}{dx}\right)(E)}$, corresponding to a suppression of the light yield as the density of the deposited energy increases.

In Equation 3.15, $B \cdot \left(\frac{dE}{dx}\right)(E)$ represents the fraction of excited molecules with respect to non-excited molecules due to the passage of the ionizing particle. It is assumed to be proportional to the density of deposited energy. k is the probability for non-radiative relaxation of these excited molecules, which then acts as quenching agents. Hence, the term $kB \cdot \left(\frac{dE}{dx}\right)(E)$ represents the fraction of light that is lost along the path of the ionizing particle.

Furthermore, since kB appears only as a product in Equation 3.15, it is in general treated as one coefficient k_B, called the Birks coefficient and expressed in unit of path length per unit of deposited energy. It depends on the scintillating material.

Other quenching models were developed since the 1950's, and some of them are summarized and discussed in [102]. Nonetheless, the original Birks model remains widely used and was chosen to implement the quenching effect in the STEREO simulation.

Adjustment of the Birks coefficient

To include the non-linearity induced by the quenching effect in the simulation of the STEREO detector, the Birks coefficient of the simulation must be tuned. To do so, one deploys the calibration γ source listed in Table 2.1 in the internal and external calibration systems, at all Z positions, to probe the overall detector response at different energies.

Three methods have been developed to perform such analysis [84, 99, 103]. They all rely on a relative comparison between data and simulation, carried out either in the collected charge space or in the reconstructed energy space, for all sources. They lead to consistent results and the final value for the Birks coefficient was set to be the mean of the coefficients derived from each method:

$$k_B = (9.63 \pm 0.69) \times 10^{-2} \text{ mm/MeV} \tag{3.16}$$

Figure 3.13 shows the result of the adjustment. For each source, one computes the calibration coefficient in the data and simulation, as defined in Equation 3.13. Each calibration coefficient has been normalized to the one derived for the ^{54}Mn. In the specific case of ^{54}Mn, the calibration coefficients extracted from the data and simulation are equal (at the 0.2% level – see Section 3.2.1), as it constitutes the calibration anchor point of the experiment. The quenching effect, responsible for a reduced light yield at low energy, is clearly visible on the top panel of Figure 3.13. On the bottom panel, the data-to-simulation comparison of the normalized calibration coefficients shows a sub-percent level agreement across the probed energy range, ensuring that the quenching effect is accurately described in the simulation after the tuning of the Birks coefficient.

It is worth mentioning that this additional tuning may be included in the global strategy of the fine tuning of the liquid scintillator parameters, as it encodes the intrinsic dependency of the LS light yield with the deposited (electron-equivalent) energy of the ionizing particle. The fine tuning as detailed in Section 3.1.3 actually only focused on the pure optical parameters of the LS, which deals with the propagation of the scintillation light.

In particular, once this effect is included in the simulation, it is not needed to compute the calibration matrix defined in the energy reconstruction routine for all the energies of the region of interest. Subsequently, it is computed and anchored, for the whole energy range, only once per calibration run with the ^{54}Mn data set.

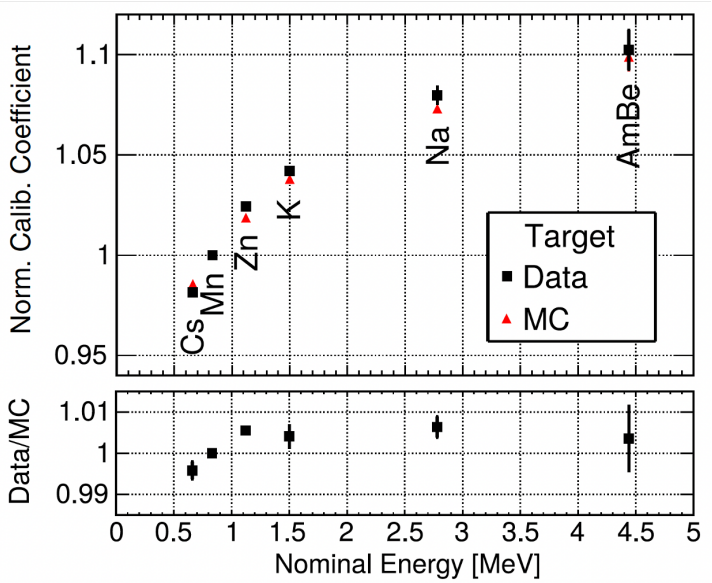

Figure 3.13: Top: calibration coefficients for various radioactive sources at mid-height, normalized to the ^{54}Mn point and averaged over all TG cells. The true deposited energy corresponding to the charge peak value is reported on the horizontal axis. For ^{24}Na, only the higher energy γ-ray is used. Bottom: ratio of data and MC curves, after tuning of the Birks coefficient k_B. Source [75].

3.2.3 Time stability

Detector response evolution

With the energy reconstruction procedure detailed in Section 3.2.1, one can monitor the evolution of the detector response, encompassed in the calibration matrix elements. As already stated, the fine tuning of the simulation carried out only once per phase allows to anchor, at zeroth order, the mean detector response of the considered phase, whereas the energy reconstruction procedure, performed for each ^{54}Mn calibration data set acquired on a weekly basis, encapsulates the first-order time evolution of the response within each phase[3].

In Figure 3.14, is shown the time evolution of the calibration coefficients (CC) extracted from the energy reconstruction procedure, for the 3 phases of STEREO data-taking. These coefficients reflect the evolution of the detector response over time.

During Phase-I (Nov. 2016 – Mar. 2017), the loss of optical coupling shows up as a reduced amount of collected light for TG cell 4 and GC-front (see Section 2.3).

During Phase-II and -III (Oct. 2017 – Nov. 2020), we notice that the detector response is more stable, although there is a slow decrease of the CC in the TG cells that is not present in the GC cells. As already stated, this is due to the slow chemical kinetics

[3]Yet, we remain dependent to effects beyond the average in the volume of a cell, such as the top-bottom light collection asymmetry due to the fact that PMTs are only situated on top of the detector.

induced by the Gd-loading of the TG liquid, resulting in a loss of transparency to the scintillation light over time.

Another illustration of the fast-evolving detector response during Phase-I data-taking period is given in Figure 3.15, where the evolution of some light leaks coefficients is shown in the cases of Phase-I and -II. One clearly sees that the light leaks, representative for the optical cross-talk between cells, increased during Phase-I. If considering only the optical cross-talk between TG cells, we note that they were brought back to their initial level for Phase-II, thanks to the repair of the detector that restored the optical segmentation of the TG volume, and are very stable during the entirety of the data-taking period. As for the optical cross-talk between TG and GC cells, they remain at the level they reached at the end of Phase-I as the walls separating TG and GC could not be repaired.

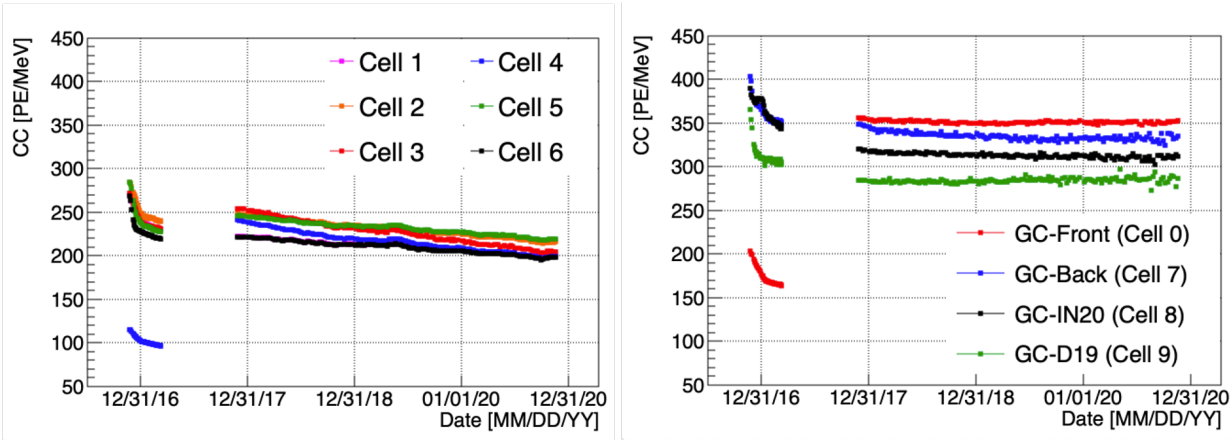

(a) Target (b) Gamma-catchers

Figure 3.14: **Evolution of the calibration coefficients (CC)** in the Target (a) and Gamma-Catcher (b) cells, for all STEREO data-taking periods.

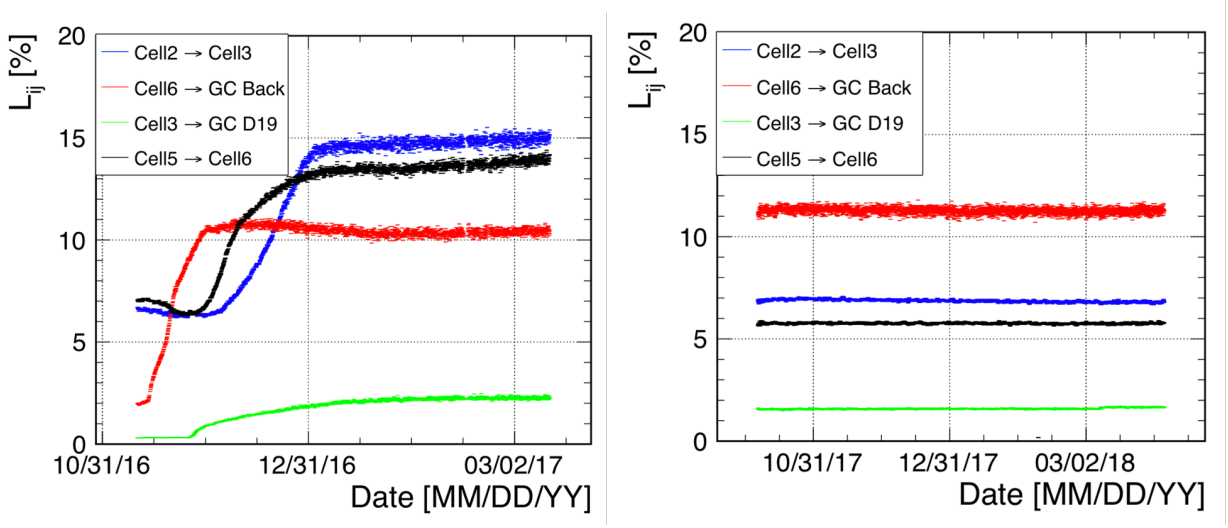

(a) Phase-I (b) Phase-II

Figure 3.15: **Evolution of some light leaks coefficients** during Phase-I (a) and Phase-II (b) data-taking periods. Source [73].

Stability of the energy reconstruction

As already stated, the key requisite of the energy reconstruction routine is to correct for the variations of the detector response. To investigate the time stability of the procedure, one can consider a set of backgrounds events, whose spatial distribution and energy are known to be stable over time.

These considerations led the STEREO collaboration to consider the capture of cosmic rays induced neutrons as a benchmark data set to probe the time stability of the energy reconstruction procedure. These neutrons are prominently generated from the spallation reaction of cosmic rays (mostly muons) with the lead shielding, such that the associated capture events are spatially distributed in the entire volume of the STEREO detector, similarly to the IBD events. Thus, they allow to span the response of the entire detector, as opposed to calibration sources whose exploratory potential is bounded by the limited deployment positions of the calibration systems and the interaction length of the γ-rays they emit ($\sim$ 0.1 m).

The cosmogenic neutron capture events also exhibit a similar signature than that of the IBD events, with a prompt (muon) and delayed (γ) signals. One can then isolate, for instance, the n-H capture peak in the data by looking for events around 2.2 MeV less than 300 μs after a muon signal in the veto or the detector. It will be explained in Section 5.1 how a signal is tagged as a muon signal.

Extracting the central value and standard deviation of the reconstructed energy peak from the Gaussian core portion of a Crystal Ball fit function, one can study the time evolution of the peak features, as shown in Figure 3.16. We may notice on the top panel that the mean reconstructed energy peak is $\sim$ 2.3 MeV, which is higher than the 2.2 MeV true deposited energy. This is due to the definition of the STEREO reconstructed energy scale, which is anchored at lower energy, at 0.835 MeV where the quenching is higher. As a consequence, the reconstructed energy above 0.835 MeV will systematically be higher than the true deposited energy (in electron-equivalent energy unit). The key point is that this shift is the same in the data and in the simulation. Overall, for the 4 years of data-taking, all points are contained within a $\pm$1% band, with a 0.25% associated uncertainty, which ensures the time stability of the energy reconstruction procedure. The remaining drifts being fully correlated across all cells, this uncertainty on the time stability is taken as fully correlated between cells. Moreover, the resolution of the peak, displayed in the bottom panel, exhibits a slowly increasing trend over time which is expected from the slow degradation of the liquid optical properties, as sketched in the evolution of the TG calibration coefficients (see Figure 3.14a). However, the degradation of the resolution is too pronounced to be fully explained with a loss of photo-statistics. It may also be explained by the increase in the top-bottom light collection asymmetry, induced by the loss of transparency of the liquid scintillator over time.

3.2.4 Energy resolution

To extract the energy resolution of the STEREO detector for each Phase (I, II or III), one merges the reconstructed energy peak signal of a variety of calibration sources over the whole data-taking period, and proceed to the same parameter extraction than for the n-H peak. The dependency of the resolution with the deposited energy is shown in Figure 3.17, for Phase-II. It follows a $1/\sqrt{E}$ at low energy and saturates around 5% at higher energies. This behavior is interpreted as the remaining smearing effect of the top-bottom

light collection asymmetry that becomes prominent at high energies in comparison to the pure statistical smearing.

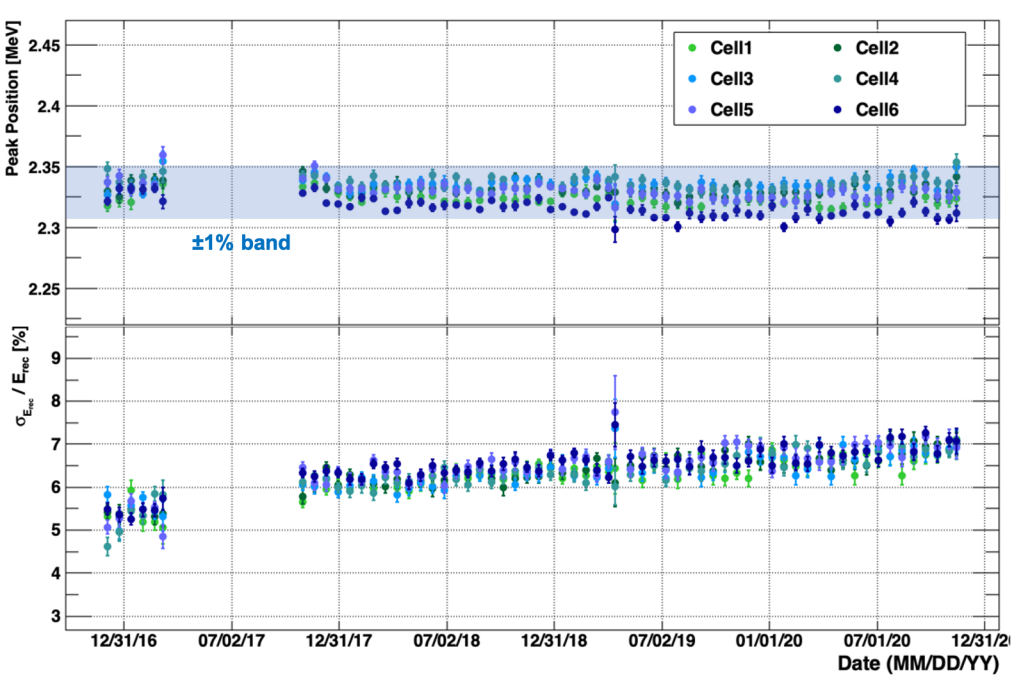

Figure 3.16: **Time-evolution of the n-H peak features during the overall STEREO data-taking.** (Top) Evolution of the reconstructed energy peak. All points are contained in the ±1% blue band. (Bottom) Evolution of the resolution of the peak. The slowly increasing trend over time is consistent with the slow degradation of the LS optical properties.

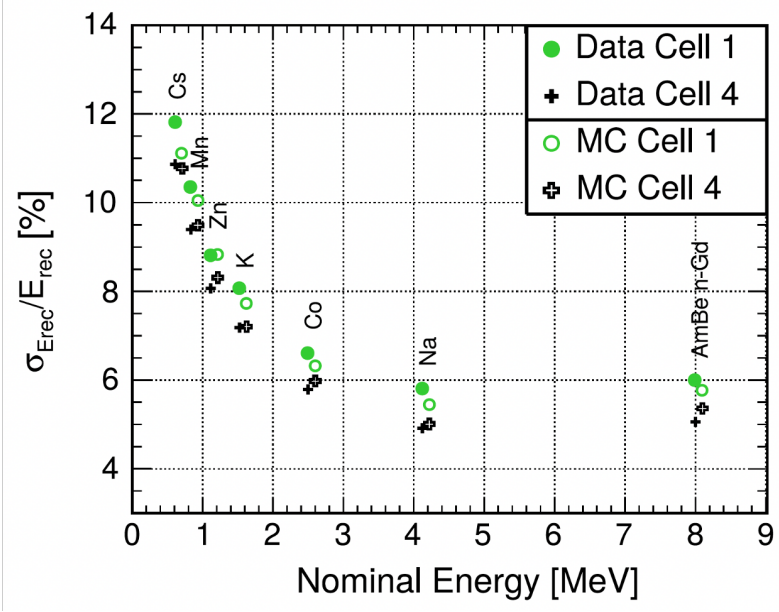

Figure 3.17: **Energy resolution for Phase-II as a function of the nominal energy of emitted γ-rays for the average of the 5 vertical deployment positions of the sources.** Filled (open) markers are for data (MC). When two γ-rays are emitted, the energy used here is the sum. Cell 4 is representative for the four inner TG cells, while cell 1 is representative for the two outer TG cells. Source [75].

Chapter 4

STEREO Energy scale study

Part of my contribution to the STEREO analysis effort was devoted to the control of the energy scale of the experiment, namely the relation between the reconstructed energy in the data and in the simulation. To that end, the collaboration made use of the set of radioactive sources of Table 2.1 as well as the cosmogenic ^{12}B reconstructed spectrum, as constraints on the residuals between the reconstructed energy in the data and simulation in the energy range of interest.

In my work, I implemented a formalism to constrain the residual non-linearity (RNL) of the energy scale with minimal assumptions on its expected shape. This study is based on a previous work done by G. Mention *et al.* in the context of the analysis of the Daya Bay measured antineutrino spectrum and its deviation in shape with respect to the Huber-Mueller predicted spectrum [104]. It consists in the minimization of a χ^2 that propagates the energy scale distortion in the calibration- and spectrum-like data space. The resulting global fit procedure will allow us to put final constraints on the STEREO energy scale.

Besides, we saw in Chapter 2 that, during Phase-I, the response of the detector was affected by several defects. Taking advantage of a long maintenance period of the reactor, the detector was repaired in-between Phase-I and -II such that the subsequent Phase-II and -III of data taking were shown to be far more stable with very similar responses, as shown in Chapter 3. Therefore, in the subsequent chapters, all analyses will be carried out with the high quality data from these last two phases.

4.1 Formalism

4.1.1 Generalities

The energy reconstruction procedure provides us with the reconstructed energy in the data, E_{rec}^{data}, and the reconstructed energy in the simulation, E_{rec}^{pred}. In this chapter, we decide to define the energy scale as the function ϕ that relates both reconstructed energy spaces, that is:

$$E_{rec}^{data} = \phi\left(E_{rec}^{pred}\right) \tag{4.1}$$

In the case of a perfect simulation and energy reconstruction, one would have $\frac{E_{rec}^{data}}{E_{rec}^{pred}} = \frac{\phi\left(E_{rec}^{pred}\right)}{E_{rec}^{pred}} = 1$. In the following, we denote δ the discrepancy with respect to the perfect energy scale case, also called residual non-linearity:

$$\frac{\phi\left(E_{rec}^{pred}\right)}{E_{rec}^{pred}} = 1 + \delta\left(E_{rec}^{pred}\right) \tag{4.2}$$

This distortion of the energy scale can be constrained with data-to-prediction ratios, derived either from the study of calibration radioactive sources or from the extraction of a given spectrum. To carry out such study, one has first to derive estimators of the data-to-prediction ratios, as functions of the RNL. In the subsequent section, E_{rec}^{data} and E_{rec}^{pred} will simply be denoted E_{data} and E_{pred}.

4.1.2 Estimators for the Data/Prediction ratios

Calibration-like data

For calibration-like data, one directly studies the ratios $R^{calib} = \frac{E_{data}}{E_{pred}}$ (where E_{data} and E_{pred} are fitted peak positions) as a function of the predicted energy for different calibration sources:

$$R^{calib}\left(E_{pred}\right) = \frac{E_{data}}{E_{pred}} \tag{4.3}$$

such that the estimator is:

$$\begin{aligned} R_{model}^{calib}(E) &= \frac{\phi(E)}{E} \\ &= 1 + \delta(E) \end{aligned} \tag{4.4}$$

Spectrum-like data

Implicit expression of the PDF ratios

For spectrum-like data, one considers the measured and predicted energy probability density functions: S_{data} and S_{pred}.

Given $E_{data} = \phi(E_{pred})$, the probability to have the data reconstructed energy in $[E_{data},\ E_{data} + dE_{data}] = [\phi(E_{pred}),\ \phi(E_{pred}) + d\phi(E_{pred})]$ would be equal to the probability to have the predicted reconstructed energy in $[E_{pred},\ E_{pred} + dE_{pred}]$, that is:

$$S_{data}(E_{data})\, dE_{data} = S_{pred}(E_{pred})\, dE_{pred} \tag{4.5}$$

With this assertion, we assume that the predicted and measured spectra would differ from each other only because of a distortion in the energy scale. In other words, we assume any discrepancy to be only due to this distortion.

We then infer:

$$\begin{aligned} S_{data}(\phi(E_{pred})) &= S_{pred}(E_{pred}) \frac{dE_{pred}}{dE_{data}} \\ &= \frac{S_{pred}(E_{pred})}{\phi'(E_{pred})} \end{aligned}$$

In fine:

$$S_{data}(E) = \frac{S_{pred} \circ \phi^{-1}(E)}{\phi' \circ \phi^{-1}(E)} \tag{4.6}$$

The ratios for spectrum-like data are then:

$$R^{spec}(E) = \frac{S_{data}(E)}{S_{pred}(E)}$$

i.e.:

$$R^{spec}_{model}(E) = \frac{1}{\phi' \circ \phi^{-1}(E)} \cdot \frac{S_{pred} \circ \phi^{-1}(E)}{S_{pred}(E)} \tag{4.7}$$

Explicit expression of the PDF ratios

The expression of the ratios above appears to depend implicitly on the energy scale distortion. One shall make this dependence explicit, by performing a Taylor expansion in δ, which we assume to be small. We decide to expand up to the 1^{st} order:

$$\begin{cases} \phi'(E) = 1 + \delta(E) + E\delta'(E) \\ \phi^{-1}(E) \approx E \cdot (1 - \delta(E)) \end{cases}$$

Hence:

$$\begin{aligned} \phi' \circ \phi^{-1}(E) &= 1 + \delta\left(\phi^{-1}(E)\right) + \phi^{-1}(E) \cdot \delta'\left(\phi^{-1}(E)\right) \\ &\approx 1 + \delta(E \cdot (1 - \delta(E))) \\ &\quad + E \cdot (1 - \delta(E)) \cdot \delta'(E \cdot (1 - \delta(E))) \\ &\approx 1 + \delta(E) - E\delta(E)\delta'(E) + E\delta'(E) - E^2\delta(E)\delta''(E) \\ &\quad - E\delta(E)\delta'(E) + E^2\delta(E)^2\delta''(E) \end{aligned}$$

We expect δ to be smooth enough to consider the cross-terms $E\delta(E)\delta'(E)$ and $E^2\delta(E)\delta''(E)$ as 2^{nd} order terms in the expansion. The expression above then reduces to:

$$\phi' \circ \phi^{-1}(E) \;\approx\; 1 \;+\; \delta(E) + \;E\delta'(E)$$

which gives immediately:

$$\frac{1}{\phi' \circ \phi^{-1}(E)} \;\approx\; 1 \;-\; \delta(E) \;-\; E\delta'(E) \tag{4.8}$$

Furthermore:

$$\begin{aligned} S_{pred} \circ \phi^{-1}(E) \quad &\approx \quad S_{pred}\left(E \cdot (1 \;-\; \delta(E))\right) \\ &\approx \quad S_{pred}(E) \;-\; E\delta(E)S'_{pred}(E) \end{aligned}$$

i.e.

$$\frac{S_{pred} \circ \phi^{-1}(E)}{S_{pred}(E)} \;\approx\; 1 \;-\; E\delta(E)\frac{S'_{pred}(E)}{S_{pred}(E)} \tag{4.9}$$

Combining Equations 4.8 and 4.9, one finds to 1^{st} order:

$$R^{spec}_{model,\ PDF}\ (E) \;=\; 1 \;-\; \delta(E) \;-\; E\delta'(E) \;-\; E\delta(E)\frac{S'_{pred}(E)}{S_{pred}(E)} \tag{4.10}$$

This formula displays two last terms worth the emphasis, that are not totally intuitive at first sight:

- the ratio is sensitive to local effects, that is, to the derivative of both the predicted spectrum and the energy scale distortion,
- these local effects scale as the energy and, consequently, could be dominant at high energy.

As a direct consequence, the parameterization of the δ function plays a crucial role in the study of the RNL of the energy scale. Setting a typical low order polynomial function encodes a smooth prior shape in the distortion that is derived, that could discard finer structures that would ultimately translates into significant deviations due to the derivative term in Equation 4.10. In Section 4.1.3, we show an alternate parameterization of the energy scale, that appears to be less stringent on the shape of the distortion.

Explicit expression of the CDF ratios (refinement)

Strictly speaking, the data provided by measurements do not directly give access to the PDF but to the CDF (cumulative distribution function), as histograms in which the spectra are reported are the integral of the PDF over each energy bin. Thus, one shall rather consider the quantity:

$$\begin{aligned} R^{spec}(E_i) &= \frac{\int_{E_i-\frac{\Delta E_i}{2}}^{E_i+\frac{\Delta E_i}{2}} f_{data}(E)dE}{\int_{E_i-\frac{\Delta E_i}{2}}^{E_i+\frac{\Delta E_i}{2}} f_{pred}(E)dE} \\ &= \frac{F_{data}\left(E_i+\frac{\Delta E_i}{2}\right) - F_{data}\left(E_i-\frac{\Delta E_i}{2}\right)}{F_{pred}\left(E_i+\frac{\Delta E_i}{2}\right) - F_{pred}\left(E_i-\frac{\Delta E_i}{2}\right)} \end{aligned} \tag{4.11}$$

where ΔE_i is the width of the bin centered in E_i, and F_{data} and F_{pred} are the CDF of S_{data} and S_{pred}.

Let's find the relation between F_{data} and F_{pred}. Equation 4.6 can be rewritten:

$$S_{data}(E) = S_{pred} \circ \phi^{-1}(E) \cdot \left(\phi^{-1}\right)'(E)$$

so that:

$$\begin{aligned} S_{data}(E)dE &= S_{pred} \circ \phi^{-1}(E) \cdot \left(\phi^{-1}\right)'(E)dE \\ &= S_{pred} \circ \phi^{-1}(E)d\phi^{-1}(E) \end{aligned}$$

from which, we infer:

$$F_{data}(E) = F_{pred} \circ \phi^{-1}(E) \tag{4.12}$$

Thus:

$$\begin{aligned} F_{data}(E) &\approx F_{pred}\left(E \cdot (1 - \delta(E))\right) \\ &\approx F_{pred}(E) - E\delta(E)S_{pred}(E) \end{aligned} \tag{4.13}$$

Combining Equations 4.11 and 4.13, one finds to 1^{st} order:

$$R^{spec}_{model,\ CDF}(E_i) = 1 - \frac{[E\delta(E)S_{pred}(E)]_{E_i-\frac{\Delta E_i}{2}}^{E_i+\frac{\Delta E_i}{2}}}{[F_{pred}(E)]_{E_i-\frac{\Delta E_i}{2}}^{E_i+\frac{\Delta E_i}{2}}} \tag{4.14}$$

4.1.3 Parameterization of the energy scale distortion

Now that we have quantified the impact of a distortion in the energy scale, we focus on the parameterization of this distortion. Two choices of parameterization are explored: the standard polynomial parameterization and the Kernel Density Estimation (KDE).

Polynomial estimator

A standard method to derive the energy scale consists in assuming that the reconstructed energy in the data can be expressed as a polynomial function of the reconstructed energy in the simulation:

$$E_{data} = \sum_{k=0}^{n} \alpha_k E_{pred}^k$$

Therefore, the distortion of the energy scale can be expressed as:

$$\delta(E) = \sum_{k=0}^{n} \omega_k E^{k-1} \tag{4.15}$$

where:

$$\begin{cases} \omega_k = \alpha_k - 1 & \text{if } k = 1 \\ \omega_k = \alpha_k & \text{otherwise} \end{cases}$$

Even if the expression 4.15 is not strictly speaking polynomial in the energy because of the E^{-1} term, it will always be referred to as the polynomial parameterization of the energy scale distortion in the subsequent sections.

Kernel Density estimator

Another prescription to parameterize δ is to use a so-called Kernel Density Estimation, such that:

$$\begin{aligned} \delta(E) &= \sum_{k=0}^{n} \omega_k \phi_k(E) \\ &= \sum_{k=0}^{n} \omega_k \phi \left(\frac{E - E_k}{h} \right) \end{aligned} \tag{4.16}$$

where:

- ϕ is the Kernel, chosen to be the standard normal distribution,
- h is the bandwidth parameter, that is fixed and is nothing but the common standard deviation of $(\phi_k)_k$,
- $(E_k)_k$ are a fixed set of equally-spaced sample points in energy, or knots, corresponding to the means of $(\phi_k)_k$,
- $(\omega_k)_k$ are a set of weights to be found.

The h parameter governs the overlapping of the $(\phi_k)_k$ and consequently the correlations of the $(\omega_k)_k$. It should typically be comparable to the energy bin width, and such should be the inter-knot distances $(|E_{k+1} - E_k|)_k$. An example of RNL estimated with a KDE approach is given in Figure 4.1.

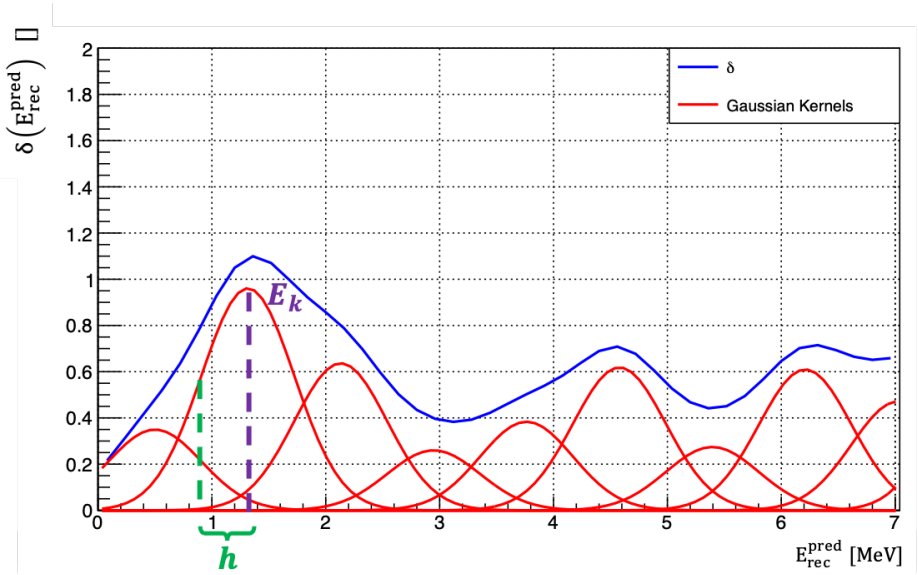

Figure 4.1: **Example of an energy scale distortion**, parameterized with a Gaussian Kernel Density Estimation.

Discussion and caveats

The polynomial parameterization of δ takes the same form as in Equation 4.16, up to the replacement of the (gaussian) kernel compact functions with non-compact (monomial) functions. The advantage of the KDE over the polynomial estimate lies in this distinction, which translates into a complete different pattern of correlations/anti-correlations on the fitted weights, as we will see further in the section. Due to the compactness and reasonable overlap between kernels, we expect to have mostly correlations between nearby weights, giving good sensitivity to fine structures of the RNL, whereas the polynomial estimate introduces significant correlations between all weights that balance the local agreement to potential fine structures with the overall agreement over the whole energy range.

However, due to the locality of the kernels in the KDE approach, a regularization or smoothing constraint is required in order to derive a reasonable shape for the energy scale distortion and to avoid overfitting the data. As we will see, this constraint only puts additional mid-range to short-range correlations, such that the KDE estimate would still remain a better probe than the polynomial estimate to investigate local distortions of the energy scale.

4.1.4 Writing of the χ^2

General form of the χ^2

In Section 4.1.2, every estimator of $\left(\frac{Data}{Prediction} - 1\right)$ that we have written are linear in the distortion δ because they were derived from a Taylor expansion. Furthermore, δ is linear in $(\omega_k)_k$. Those estimators are then linear in the weights to be fitted and can be rewritten as follows:

$$R_i^{model} - 1 = A_{ik}\omega_k \tag{4.17}$$

where A is a certain matrix and i the bin number. The matrix elements are determined using the formulae of the estimators of the vector of ratios derived in Section 4.1.2.

Let's suppose now that we have a set of ratios $R = (R_i)_i$, with an associated covariance matrix V. In the case where the polynomial estimator is chosen to parameterize the distortion, a standard method to find $\omega = (\omega_k)_k$ consists in minimizing:

$$\begin{aligned} \chi^2(\omega) &= ((R - 1) - A\omega)^T V^{-1} ((R - 1) - A\omega) \\ &:= \|(R - 1) - A\omega\|^2_{V^{-1}} \end{aligned}$$

However, in the KDE approach, this χ^2 would be irrelevant to minimize as it leads to overfitting the data. As already mentioned, a smoothing constraint must be added to the procedure. In the case of the Kernel Density estimation, we propose to minimize the aforementioned χ^2, completed with a regularization term:

$$\chi^2_\lambda(\omega) = \|(R - 1) - A\omega\|^2_{V^{-1}} + \lambda \int \delta''(E)^2 dE \tag{4.18}$$

The regularization term allows for smoothing the shape of the distortion that minimizes the χ^2 and depends on a hyperparameter $\lambda \geq 0$, called the regularization strength and that is to be tuned. This will be the subject of a further discussion (cf. Section 4.1.5). This parameter sets the balance between the sheer agreement of the model to the data and the smoothness of the model. In this sense, we may already notice that:

- if λ is small, their is little to no constraint set by the regularization and we might be overfitting the data,
- if λ is big, the constraint on the regularization becomes the dominant part of the χ^2 so that the minimization will tend to reach $\int \delta''(E)^2 dE = 0$, that is $\delta(E) = a \cdot E + b$. With the KDE estimate for δ, this would amount to $\delta(E) = 0$.

A compromise is then to be found between those two extreme cases. Developing the regularization term, we find:

$$\begin{aligned} \int \delta''(E)^2 dE &= \sum_{i,j} \omega_i \omega_j \int \phi_i''(E)\phi_j''(E) dE \\ &= \sum_{i,j} M_{ij}\omega_i\omega_j \\ &= \omega^T M \omega \\ &:= \|\omega\|^2_M \end{aligned} \tag{4.19}$$

where $M_{ij} = \int \phi_i''(E)\phi_j''(E)dE$ is the regularization matrix element.

The final writing for the χ^2 is:

$$\chi^2_\lambda(\omega) = \|(R - 1) - A\omega\|^2_{V^{-1}} + \lambda \|\omega\|^2_M \tag{4.20}$$

Such regularization is known as Tikhonov regularization [105] or Ridge regression. One shall need it as well in the chapter developing the unfolding of the antineutrino spectrum (see Chapter 6).

χ^2 of calibration-like data

Let's consider calibration-like data, so that we have:

- $(E_i)_i$ the energy values, corresponding to the γ-peaks of calibration sources,
- R^{calib} the vector of Data/Prediction ratios,
- V^{calib} the covariance matrix,
- A^{calib} the A matrix of Section 4.1.4 for calibration-like data.

Using Equation 4.4 of Section 4.1.2, we have:

$$R^{calib}_{model}(E_i) - 1 = \sum_k \phi_k(E_i)\,\omega_k$$

From which one infers:

$$A^{calib}_{ik} = \phi_k(E_i) \tag{4.21}$$

Finally:

$$\left(\chi^{calib}_\lambda\right)^2(\omega) = \left\|(R^{calib} - 1) - A^{calib}\omega\right\|^2_{(V^{calib})^{-1}} + \lambda \|\omega\|^2_M \tag{4.22}$$

χ^2 of spectrum-like data

Let's consider spectrum-like data, so that we have:

- $(E_i)_i$ the center values of the energy bins,
- R^{spec} the vector of Data/Prediction ratios,
- V^{spec} the covariance matrix,
- A^{spec} the A matrix of Section 4.1.4 for spectrum-like data.

If one takes the PDF model of Section 4.1.2 as an estimator, then Equation 4.10 gives:

$$R^{spec}_{model,\ PDF}\ (E_i)\ -\ 1\ = \sum_k -\left(\phi_k(E_i)\ +\ E_i\phi'_k(E_i)\ +\ E_i\phi_k(E_i)\frac{S'_{pred}(E_i)}{S_{pred}(E_i)}\right)\omega_k$$

So that:

$$A^{spec}_{ik}\ =\ -\left(\phi_k(E_i)\ +\ E_i\phi'_k(E_i)\ +\ E_i\phi_k(E_i)\frac{S'_{pred}\,(E_i)}{S_{pred}(E_i)}\right) \tag{4.23}$$

If one takes the CDF model of Section 4.1.2 as an estimator, then Equation 4.14 gives:

$$R^{spec}_{model,\ CDF}\ (E_i)\ -\ 1\ = \sum_k -\frac{\left[E\phi_k(E)S_{pred}(E)\right]^{E_i+\frac{\Delta E_i}{2}}_{E_i-\frac{\Delta E_i}{2}}}{\left[F_{pred}(E)\right]^{E_i+\frac{\Delta E_i}{2}}_{E_i-\frac{\Delta E_i}{2}}}\ \omega_k$$

So that:

$$A^{spec}_{ik}\ =\ -\frac{\left[E\phi_k(E)S_{pred}(E)\right]^{E_i+\frac{\Delta E_i}{2}}_{E_i-\frac{\Delta E_i}{2}}}{\left[F_{pred}(E)\right]^{E_i+\frac{\Delta E_i}{2}}_{E_i-\frac{\Delta E_i}{2}}} \tag{4.24}$$

In any case:

$$\left(\chi^{spec}_{\lambda}\right)^2(\omega)\ =\ \|(R^{spec}\ -\ 1) - A^{spec}\omega\|^2_{(V^{spec})^{-1}}\ +\ \lambda\,\|\omega\|^2_M \tag{4.25}$$

Global χ^2 of calibration- & spectrum-like data

Let's suppose now that we have a set of independent calibration- and spectrum-like data that we would jointly use to constrain the shape of the distortion in the energy scale. We can write a global χ^2 that has the same expression as in Equation 4.20.

To do so, R, A and V can be defined as follows:

$$\begin{cases} R\ =\ \begin{bmatrix} R^{calib} \\ R^{spec} \end{bmatrix} \\ \\ A\ =\ \begin{bmatrix} A^{calib} \\ A^{spec} \end{bmatrix} \\ \\ V\ =\ \begin{bmatrix} V^{calib} & 0 \\ 0 & V^{spec} \end{bmatrix} \end{cases} \tag{4.26}$$

This formalism remains valid with an arbitrary number of independent sets of data. The most general form for R, A and V is:

$$R = \begin{bmatrix} R^{(1)} \\ R^{(2)} \\ \vdots \\ \vdots \\ \vdots \\ R^{(n-1)} \\ R^{(n)} \end{bmatrix}$$

$$A = \begin{bmatrix} A^{(1)} \\ A^{(2)} \\ \vdots \\ \vdots \\ \vdots \\ A^{(n-1)} \\ A^{(n)} \end{bmatrix}$$

$$V = \begin{bmatrix} V^{(1)} & 0 & \dots & \dots & \dots & \dots & 0 \\ 0 & V^{(2)} & \ddots & & & & \vdots \\ \vdots & \ddots & \ddots & \ddots & & & \vdots \\ \vdots & & \ddots & \ddots & \ddots & & \vdots \\ \vdots & & & \ddots & \ddots & \ddots & \vdots \\ \vdots & & & & \ddots & V^{(n-1)} & 0 \\ 0 & \dots & \dots & \dots & \dots & 0 & V^{(n)} \end{bmatrix}$$

Minimization of the χ^2

As detailed in Appendix A, the χ^2 defined in Equation 4.20 can be minimized analytically. The solution of the inverse problem reads:

$$\begin{cases} \hat{\omega} = H(\lambda) \cdot (R - 1) \\ V^{\hat{\omega}} = H(\lambda) \cdot V \cdot H(\lambda)^T \end{cases} \tag{4.27}$$

where: $H(\lambda) = \left(A^T V^{-1} A + \lambda M\right)^{-1} A^T V^{-1}$.

As for the error band on the fitted distortion, it can be retrieved from the standard formula of error propagation to 1^{st} order:

$$\begin{aligned} \sigma_\delta(E) &= \left\| \frac{\partial \delta}{\partial \omega}(E) \right\|_{V^{\hat{\omega}}} \\ &= \sqrt{\sum_{i,j} V_{ij}^{\hat{\omega}} \frac{\partial \delta}{\partial \omega_i}(E) \frac{\partial \delta}{\partial \omega_j}(E)} \end{aligned} \tag{4.28}$$

Likewise, the error band on the fitted spectrum ratios is:

$$\sigma_{R^{spec}_{model}}(E) \;=\; \left\| \frac{\partial R^{spec}_{model}}{\partial \omega}(E) \right\|_{V^{\hat{\omega}}} \tag{4.29}$$

4.1.5 Regularization strength

With Equation 4.27, we showed that $\hat{\omega}$ is linear with respect to $R-1$. The fitted ratio $\hat{R}$ then reads:

$$\begin{aligned} \hat{R}-1 &= A\hat{\omega} \\ &= H_R(\lambda)\cdot(R-1) \end{aligned}$$

where $H_R(\lambda) \;=\; A \cdot H(\lambda)$. Therefore:

$$\begin{aligned} R-\hat{R} &= (R-1)-(\hat{R}-1) \\ &= (I-H_R(\lambda))\cdot(R-1) \end{aligned}$$

In 1979, Wahba et al. [106] provided a strong criterion to choose a "good" parameter λ. They proposed to minimize the so-called Generalized Cross-Validation (GCV) error function:

$$\begin{aligned} GCV(\lambda) &= \frac{\left\| R-\hat{R} \right\|^2_{V^{-1}}}{\left[Tr\left[I-H_R(\lambda)\right]\right]^2} \\ &= \frac{\left\| \left(I-H_R(\lambda)\right)\left(R\;-\;1\right) \right\|^2_{V^{-1}}}{\left[Tr\left[I-H_R(\lambda)\right]\right]^2} \end{aligned} \tag{4.30}$$

where Tr is the trace operator. In this expression, the parameter λ is only set to be a positive real number.

As detailed in Appendix B, one can derive an analytical expression for the denominator function $f : \lambda \rightarrow Tr\left[I-H_R(\lambda)\right]$ and show that f is an increasing function of the regularization strength that spans the interval $[N_R - N_\omega,\; N_R]$ when λ spans $[0, +\infty]$, where N_R and N_ω are respectively the dimensions of the vectors of ratios R and weights ω. The term $Tr\left[I-H_R(\lambda)\right]$ appearing in the denominator of Equation 4.30 can then be interpreted as an effective number of degrees of freedom. The GCV error then allows to encapsulate the predictive error of the fitted model, as a function of the regularization strength.

4.2 Case Study

To emphasize the sensitivity of the antineutrino spectrum data-to-prediction comparison to a small distortion of the energy scale, we propose to derive in this section the RNL from a global fit of calibration and antineutrino spectrum toy ratios, with the latter exhibiting sizeable distortions with respect to the calibration residuals. This will motivate, in a second time, the use of a complementary data set, namely the cosmogenic ^{12}B spectrum, to further constrain the energy scale.

We will then consider an example antineutrino spectrum that exhibits distortions at high energy with respect to the predicted spectrum. No emphasis is made on the STEREO antineutrino signal extraction procedure, that will be explained in Section 5.3. The question that will be addressed is whether or not the observed discrepancies may be explained by a mere distortion of the energy scale.

4.2.1 Data/Prediction ratios

Antineutrino spectrum

The ratio of measured/predicted antineutrino spectrum that will be used for this case study is displayed in Figure 4.2. Two discrepancies may be identified: a small event excess similar to the so-called 5 MeV-bump, and a twenty-ish percent deficit of events in the high energy end of the spectrum. The spectrum is reported in 250keV-wide energy bins, from 1.625 MeV (lower edge of first bin) to 7.125 MeV (upper edge of last bin).

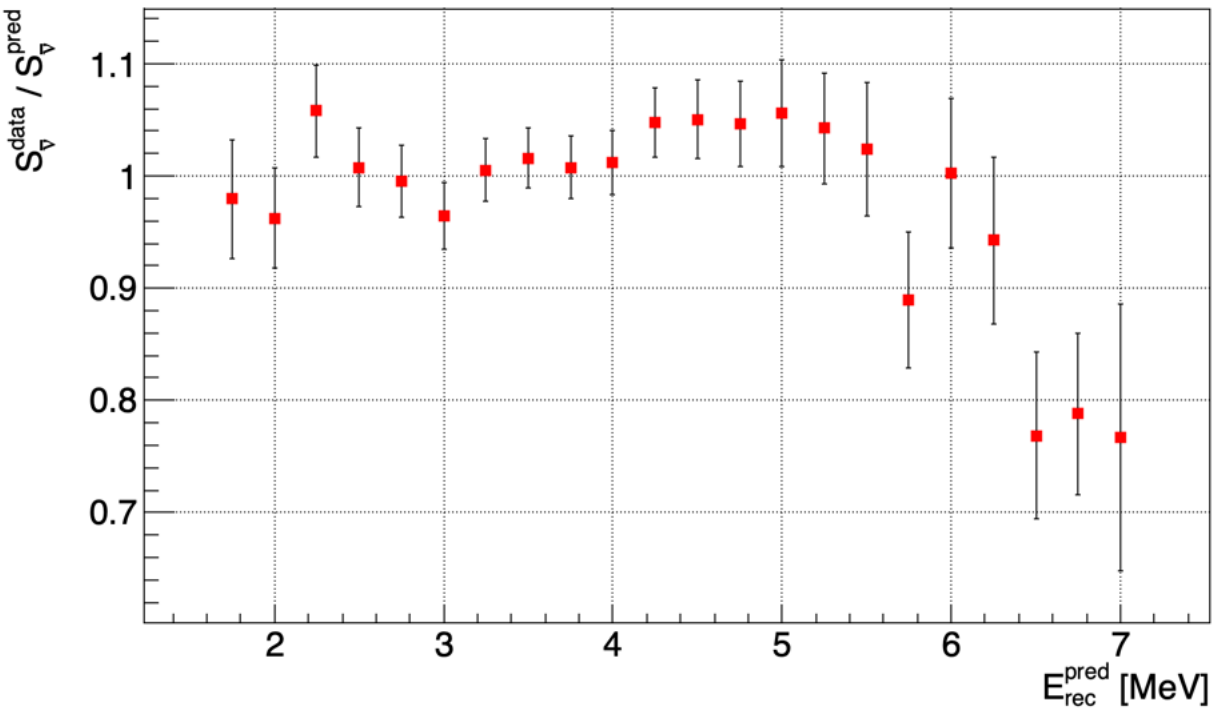

Figure 4.2: Example of Data/Prediction ratios for the antineutrino spectrum.

Calibration data

The set of calibration points used for the case study is displayed in Figure 4.3. Overall, one can see that the data-to-prediction residuals, that directly compares to the energy scale distortion δ, are compatible with 0.

However, the calibration constraints go up to 4.4 MeV and do not cover the high energy part of the spectrum where, on one hand, the data-to-prediction discrepancies are sizeable, and where, on the other hand, the impact of local distortions of the energy scale may become prominent as shown in Equation 4.10.

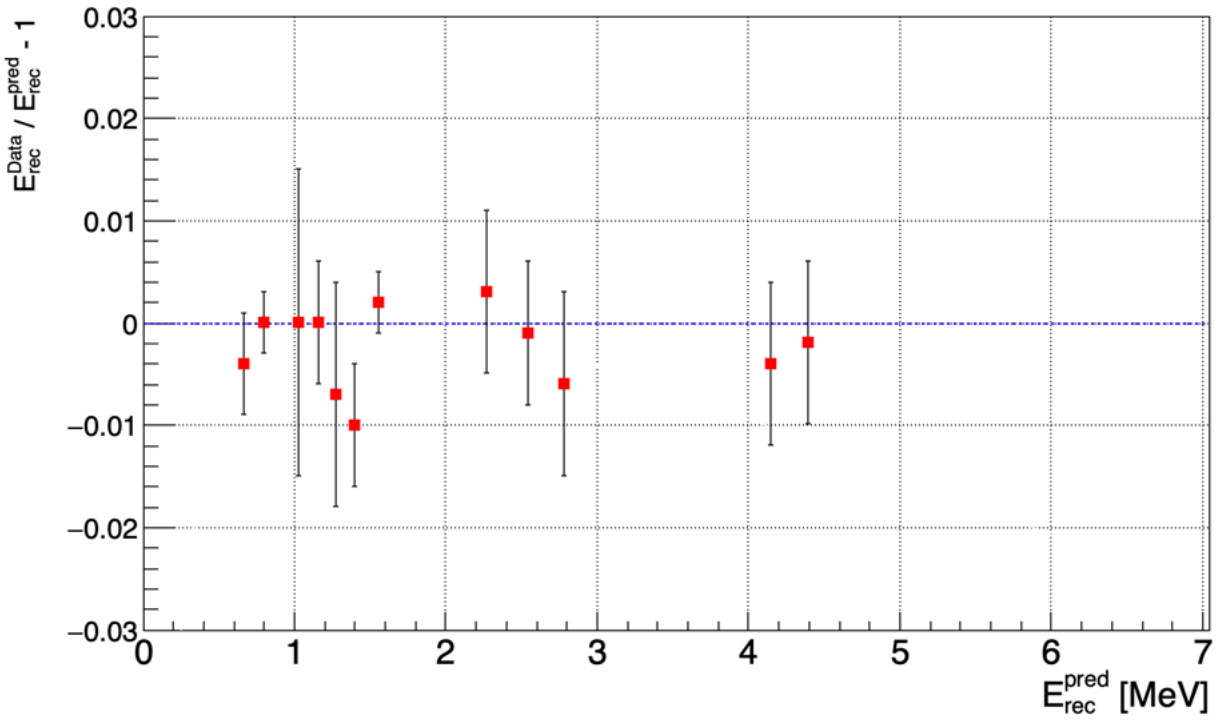

Figure 4.3: Example of Data/Prediction residuals for the calibration data set.

4.2.2 Derivation of the RNL

We seek to derive the distortion of the energy scale that would describe both the calibration residuals and the antineutrino spectrum distortions. To this end, both the polynomial and KDE estimates are compared.

For both approaches, the joint variables of calibration data and antineutrino spectrum, as defined in Equation 4.26, are used for the minimization of the χ^2. The model chosen for R is the most accurate CDF model, defined in Equation 4.14.

4.2.2.1 Polynomial estimate

Setting the Degree

In this approach, it is irrelevant to add a regularization term to the χ^2 of Equation 4.20. The regularization strength is then set to 0. However, to our knowledge, there is no *a priori* reason why one should take a low order polynomial. Even if it is most generally easier to give a physical interpretation to the coefficients of the polynomial parameterization[1], there is, to our knowledge, no assumption that could be made on the order where the expansion should be stopped.

Yet, when adding parameters to a model, one naturally increases the likelihood of the model and, even with a smooth parameterization, one may end up overfitting the data. To circumvent this issue, one should make use of the Akaike Information Criterion (AIC) for model selection. Proposed in 1973, this criterion tends to fulfill the principle of parsimony, which states in essence that data should be described with the least possible number of free parameters. Formally, it originates from the minimization of the Kullback-Leibler information quantity, that encapsulates the information that is lost when a model is used to approximate another one [107].

Akaike then proposed to penalize the log-likelihood function with the number of free parameters of the model [108]:

$$AIC \;=\; -2\,(log(\mathcal{L}) - N_\omega) \tag{4.31}$$

The model to be selected is the one that minimizes the AIC quantity. This criterion holds for "large samples" but may fail for small samples where the number of free model parameters (N_ω) gets close to the number of data to be fitted (N_R).

Later, Hurvich and Tsai derived an adjusted version of this criterion [109], known as the Corrected Akaike Information Criterion (AICc). The corrected criterion reads as:

$$AICc = AIC + \frac{2N_\omega(N_\omega+1)}{N_R - N_\omega - 1} \tag{4.32}$$

It tends to AIC in the large sample limit ($N_R \longrightarrow \infty$). This latter criterion is the one that we use to derive the degree of the polynomial to be used to fit the data.

In our case, the AICc then reads:

$$AICc\,(N_\omega) \;=\; \chi^2_{min} \;+\; 2N_\omega \left(1 + \frac{(N_\omega+1)}{N_R - N_\omega - 1}\right) \tag{4.33}$$

where χ^2_{min} is the minimum value of the χ^2 for the polynomial estimate:

$$\chi^2_{min} \;=\; \chi^2(\hat{\omega}) \;=\; \|(R \;-\; 1) - A\hat{\omega}\|^2_{V^{-1}}$$

with $\hat{\omega}$ the fitted weights.

[1]For instance, ω_0 may just be interpreted as a remaining shift in the energy reconstruction procedure, similarly to the 0.2% shift in the case of the reconstructed ^{54}Mn peak, whereas ω_1 is the deviation from unity of the linear calibration coefficient that would lead to reconstruct narrower or larger peak in the data with respect to the simulation.

We computed the values of χ^2_{min} and AICc for various polynomial degrees. They are reported in Figure 4.4. As expected, χ^2_{min} decreases as we increase the number of free parameters of the model. Yet, the AICc exhibits a minimum for a polynomial degree of 6, which sets the parameterization of δ for the polynomial approach of this case study.

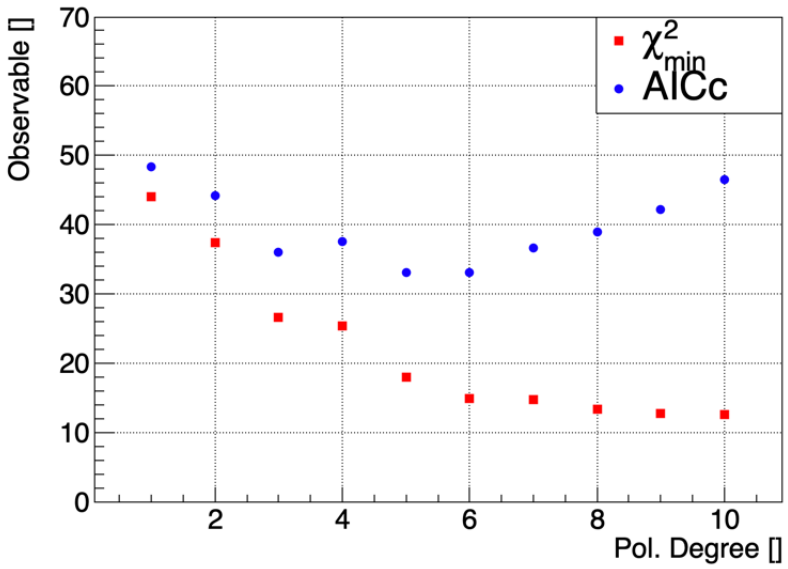

Figure 4.4: **Corrected Akaike Information Criterion**, for various polynomial parameterization of the energy scale distortion.

Results

The results of the global fit of the energy scale distortion are summarized in Figure 4.5.

First, let's note the good agreement between model and data, with a value of $\chi^2_{min}/ndf = 14.8/27$. The high degree of the polynomial parameterization allows for the RNL of the energy scale to be compatible with 0 below 4 MeV, where the calibration and antineutrino spectrum residuals show no hint for a distortion, and to exhibit a (small) 2% distortion beyond 4 MeV. Remarkably, when propagated to the shape of the antineutrino spectrum, this distortion fits both the 5% event excess around 5 MeV and the 20% event deficit at 7 MeV. Thus, despite the high quality of calibration residuals, large distortions of the $\bar{\nu}$ spectrum can be fitted. We will have a closer look on this result in Figure 4.7.

Also, the error band of the distortion seems to be an increasing function of the energy, as expected from the non-vanishing error of higher order fitted polynomial coefficients. Furthermore, as displayed in Figure 4.6, the fitted coefficients are strongly correlated and anti-correlated with each other, which finally makes difficult the physical interpretation of the terms of the expansion.

Finally, let's have a closer look on the fitted distortion in the antineutrino spectrum space. To this end, even if we used the more accurate CDF estimator (Equation 4.14) for the global fit, we show the breakdown of the contributions of the different terms written in the PDF formulation of the estimator (Equation 4.10). In Figure 4.7, the fitted ratios

using the CDF estimator are depicted as black dots whereas the fitted ratios using the PDF estimator are shown as a plain orange line: both give nigh identical results.

In the region of spectral distortions, one can notice the prominent role of the so-called local effects described in Section 4.1.2. These features explain the non-intuitive shape of the RNL between 4 and 7 MeV.

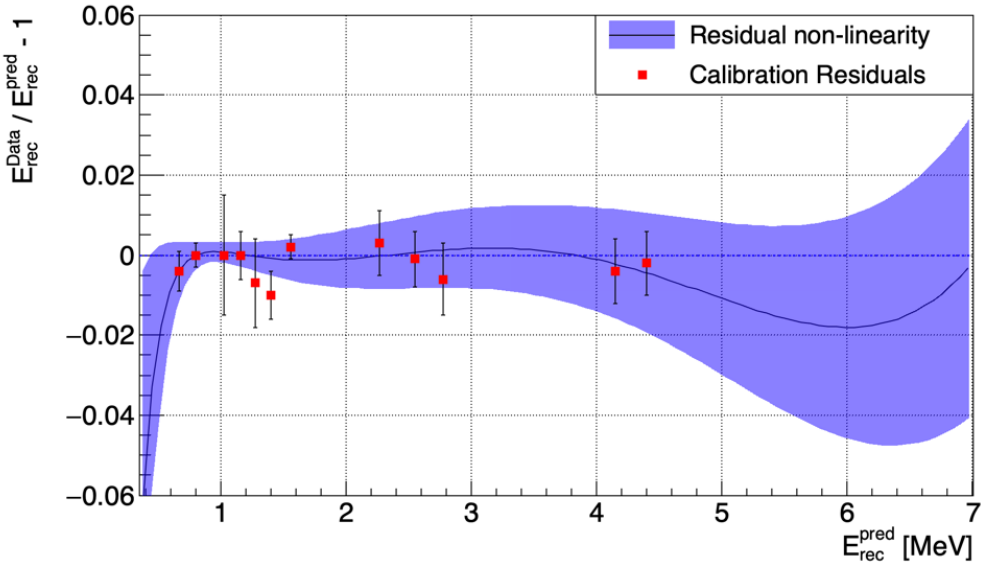

(a) Calibration data

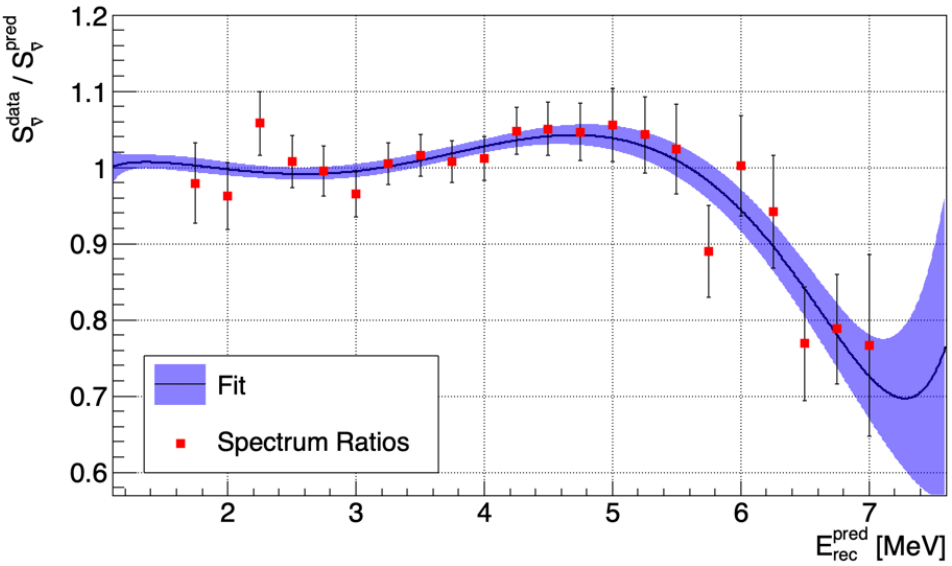

(b) Antineutrino spectrum data

Figure 4.5: **Global fit of an energy scale distortion in the (6^{th} order) polynomial approach**, constrained by calibration and antineutrino spectrum ratios.

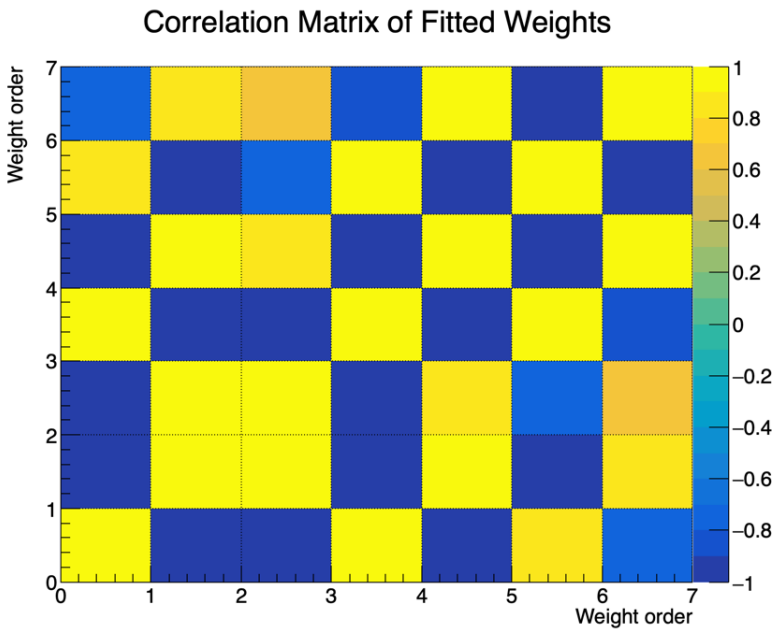

Figure 4.6: **Correlation matrix of the fitted weights, for the polynomial estimate.** The weight order corresponds to the k index in Equation 4.15.

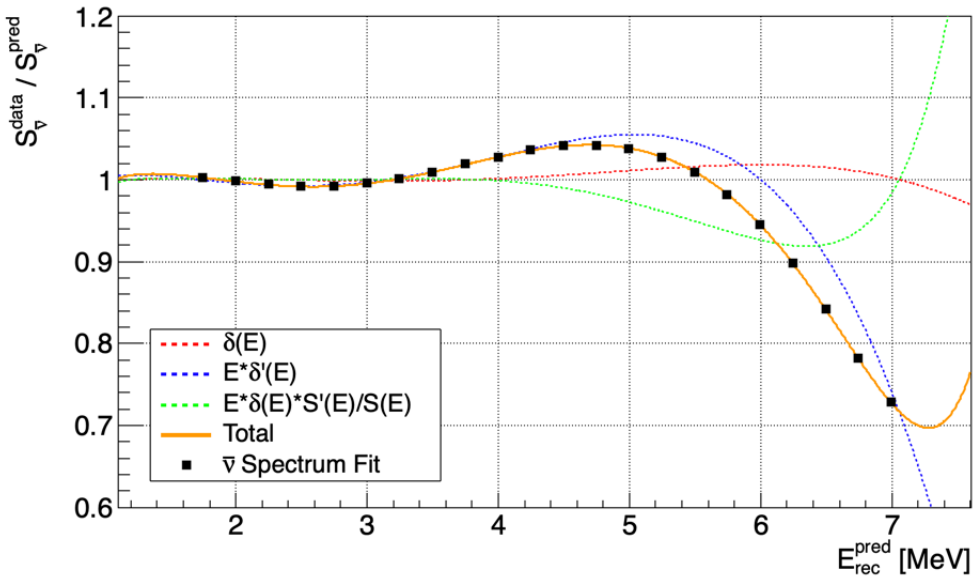

Figure 4.7: **Breakdown of the contributions for the antineutrino spectrum fit, for the polynomial estimate.** At high energy, the small amplitude of the energy scale distortion (dashed red line), plays a minor role, whereas the contribution coming from its derivative (dashed blue line), as well as from the derivative of the predicted spectrum (dashed green line), are the key inputs allowing to reproduce the observed discrepancies.

4.2.2.2 KDE approach

Setting the Regularization

We decide to parameterize the RNL with 10 equally spaced Gaussian Kernels, ranging from 0 MeV (mean of the first kernel) to 7 MeV (mean of the last kernel). The width of each kernel, which is set to be the constant inter-knot distance, is ~ 0.8 MeV, that is, about 3 energy bins of the antineutrino spectrum space.

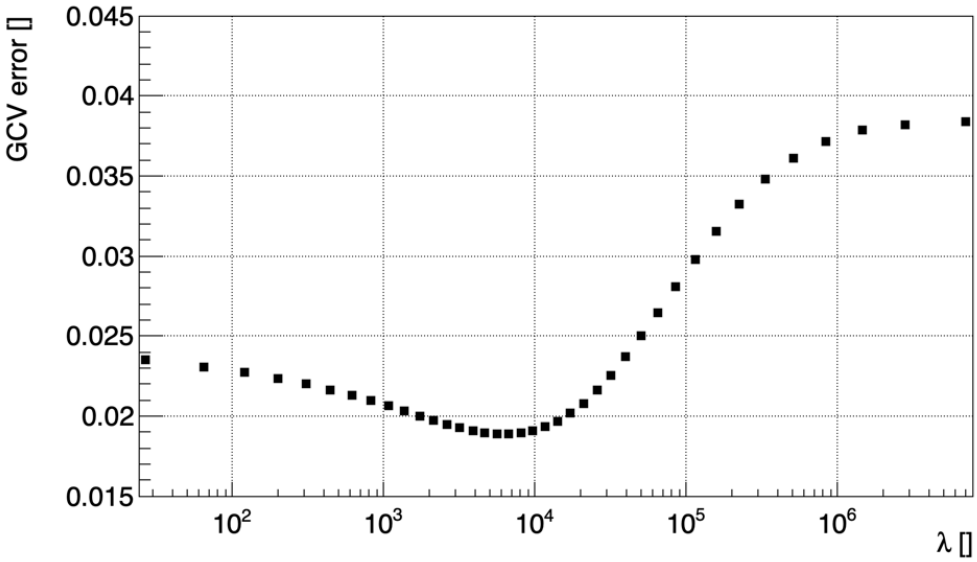

(a) GCV error

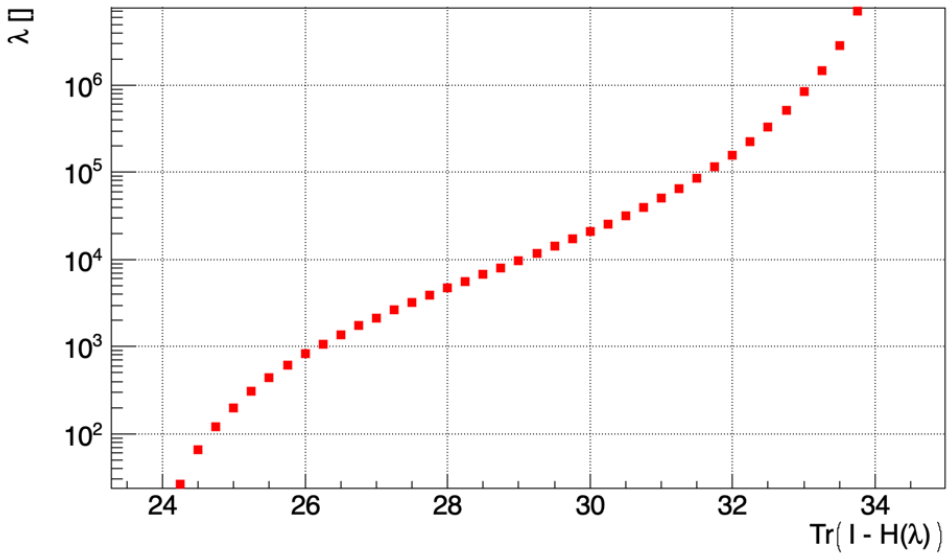

(b) Effective number of degrees of freedom

Figure 4.8: **Minimization of the Generalized Cross-Validation (GCV) error**, in the KDE approach. (a) The error is expressed as a function of the regularization strength λ. (b) It can be related to the effective number of degrees of freedom of the fitting procedure $\mathrm{Tr}\,(I - H(\lambda))$.

With this parameterization, we then minimize the GCV error to set the value of the regularization strength of the fit. The result of the procedure is shown in Figure 4.8. In

Figure 4.8b, we bring to view the regularization strength as a function of the effective number of degrees of freedom. In particular, it shows that the natural scale for λ is a logarithmic scale. The GCV error, displayed as a function of λ in Figure 4.8a, exhibits a well-defined minimum that allows to set non-ambiguously the value of the regularization strength. It approximately corresponds to a number of effective degrees of freedom of 29.

Results

The results of the global fit of the energy scale distortion in the KDE approach are summarized in Figure 4.9.

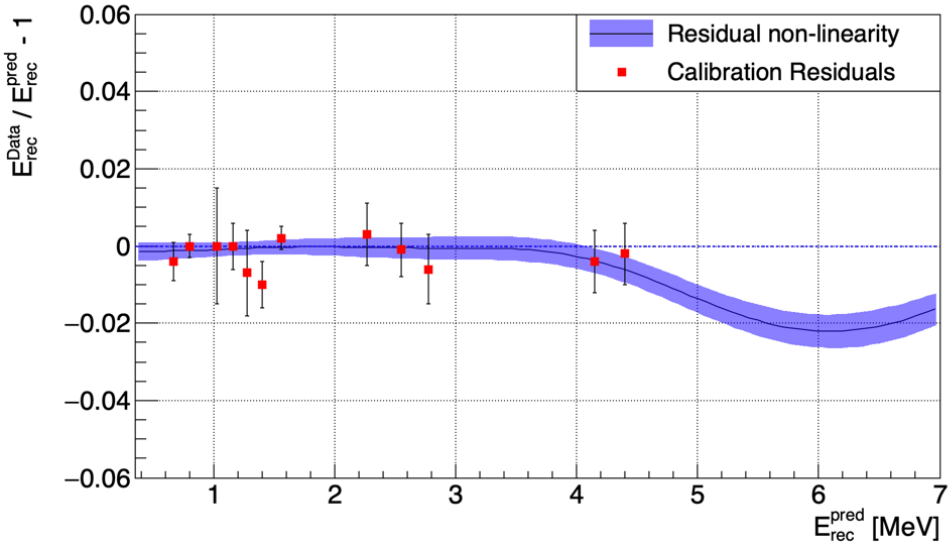

(a) Calibration data

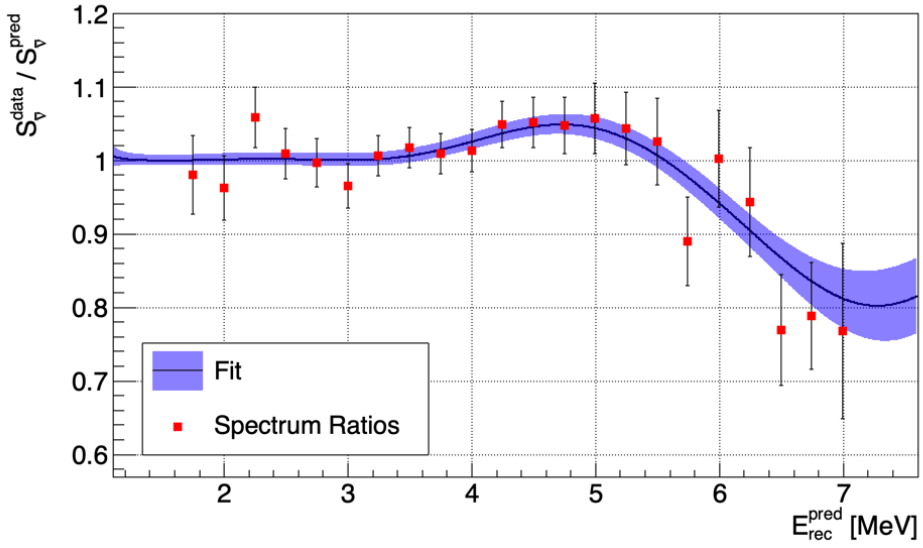

(b) Antineutrino spectrum data

Figure 4.9: **Global fit of an energy scale distortion in the KDE approach**, constrained by calibration and antineutrino spectrum ratios.

The overall shape of the distortion is very similar to the one we derived using the polynomial estimate, especially at high energy, where both distortions seem to describe

a "well" between 4 and 7 MeV. Yet, a closer look allows to realize that the KDE RNL is smoother, especially at low and high energy. It is due to the compact and non-diverging nature of the kernels, that also induce a complete different pattern of correlations for the fitted coefficients, as shown in Figure 4.10. Only the correlations and anti-correlations between nearby fitted weights are sizeable, which reflects the prominence of short-to-mid range correlations and anti-correlations in the KDE estimate. Moreover, contrary to the polynomial estimate, the error band of the fitted distortion is rather constant across all the energy range. These features endorse the enhanced local sensitivity of the KDE model to any energy scale distortion.

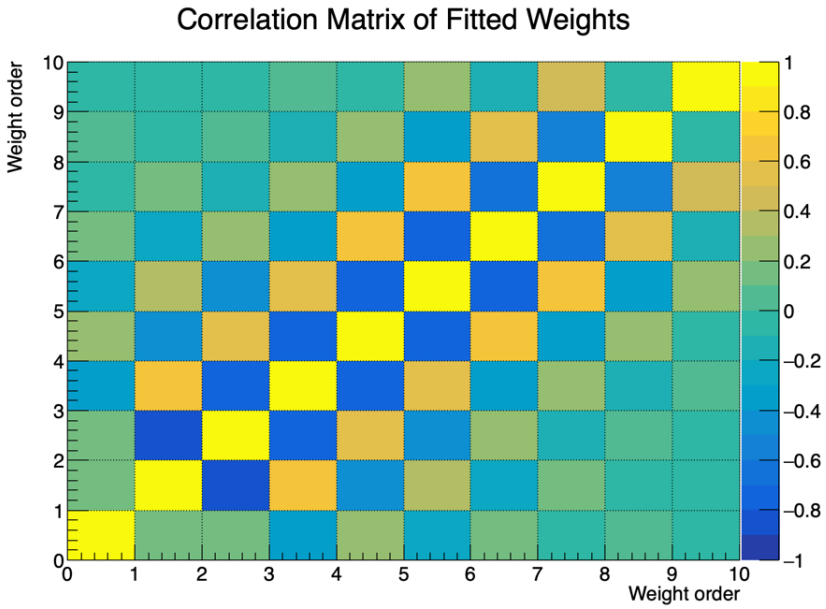

Figure 4.10: **Correlation matrix of the fitted weights, in the KDE approach.** The weight order corresponds to k index in Equation 4.16.

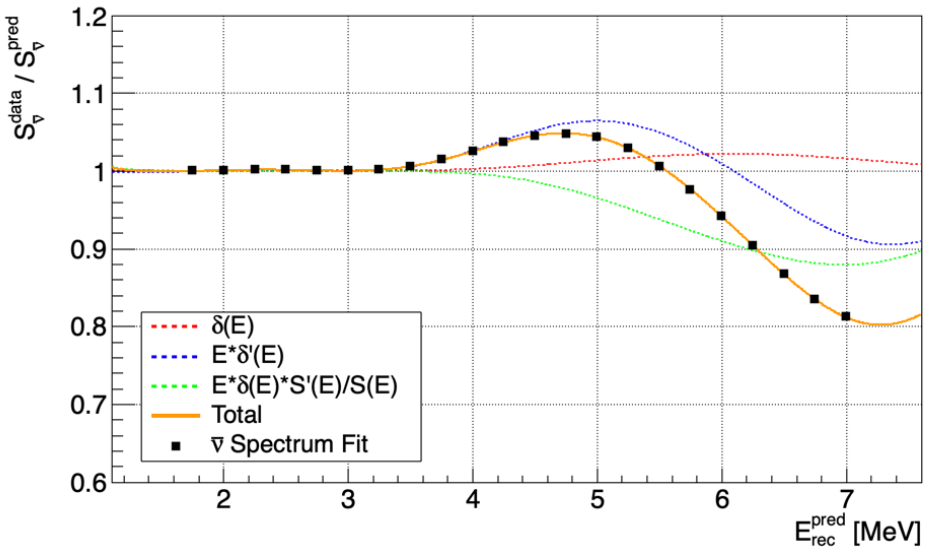

Figure 4.11: **Breakdown of the contributions for the antineutrino spectrum fit, in the KDE approach.**

At last, the breakdown of the different contributions to the KDE fit is shown in Figure 4.11. Similarly to the polynomial estimate, the effects induced by the derivatives of the distortion and the predicted spectrum are the key contributions allowing to fit the distortions at high energy.

4.2.3 Conclusions

With calibration and antineutrino spectrum toy data sets, we explored two strategies for the parameterization of the energy scale residual non-linearity. Both yield to similar results in terms of fitted shape for the RNL.

However, on one hand, it was shown that the flexibility of the KDE approach exhibits an enhanced sensitivity to local distortions of the energy scale, whereas, on the other hand, the high degree of the polynomial required to fit an arbitrary energy scale distortion makes the physical interpretation of the terms of the expansion quite non-intuitive in the end. Moreover, whereas the polynomial degree was imposed by the minimization of the Akaike criterion, the KDE parameterization is *a priori* unconstrained. Even if only one parameterization was tested for the sake of this case study, the Kernel Density Estimation offers a variety of scenarii to derive the energy scale distortion.

Therefore, in order to investigate potential energy scale non-linearities in the final of STEREO data sets, we will make use of the more flexible and effective KDE approach.

The case study also pointed out the necessity to constrain the energy scale in the high energy end of the spectrum. Experimentally, this is the region where we want to test a shape distortion of the antineutrino spectrum, namely the 5 MeV bump, and where the signal-to-background ratio drops due to the vanishing intensity of the spectrum. This is also the region where the local shape of the RNL takes over upon the amplitude of the RNL in inducing distortions in the measured antineutrino spectrum.

Yet, high energy calibration data are rather scarce so that the overall shape of the RNL cannot be well-constrained in this range. Instead, we would like to constrain the energy scale with a continuous data set to complement the punctual energy constraints of radioactive sources. To that end, we extract the cosmogenic ^{12}B spectrum and we use it as a supplemental data set. Such approach is not original and is widely used by several experiments (see for instance [110, 111, 112, 113, 114]). In the end, the energy scale distortion will be derived from a global fit to the boron spectrum ratios and the calibration residuals, independently of the antineutrino spectrum.

4.3 ^{12}B spectrum

^{12}B is produced inside the STEREO detector from the interaction with cosmic rays, via two channels. First, low energy muons, with typical energies lower than 120 MeV, may stop in the inner detector and induce a muon capture on a ^{12}C atom. In 1% of the cases, the captured μ^- reach the 1S orbital state, which favors the charged current interaction with the nucleus, therefore giving rise to a ^{12}B isotope [115]. The second production channel comes from the (n, p) reaction that transforms ^{12}C into ^{12}B, with the incoming neutron being produced from spallation reactions with high energy muons, of typical energies higher than 200 MeV.

The ^{12}B is an unstable isotope, with a half-time $\tau = 20.20$ ms, which undergoes a β^- decay with an end-point $Q_\beta = 13.37$ MeV. Thus, it fully covers the energy range of the antineutrino spectrum.

4.3.1 Experimental ^{12}B spectrum

The extraction of the experimental boron 12 spectrum relies on a correlated pair search algorithm [82], with a prompt muon signal and a delayed electron signal coming from the ^{12}B decay. As already pointed out in Section 3.1.1, the muon stop vertices are easier to simulate (with respect to induced spallation events) and to select in the data. Consequently, the pair search is based on the selection of the muon capture process, that can be thoroughly compared to the dedicated simulation detailed in the next subsection.

In the ^{12}B candidates selected by the pair search algorithm, there may be uncorrelated combinations of events that mimic the ^{12}B signature. These fake or accidental ^{12}B events are a source of background for the spectrum extraction. This accidental background depends on the rates of the single prompt and delayed events. A dedicated algorithm, based on the method of time-shifted gates [82], allows to extract the accidental background spectrum.

The extracted ^{12}B energy spectrum is then derived as the subtraction of the ^{12}B candidates spectrum obtained with the correlated pair search algorithm with the accidental spectrum.

Correlated pairs

Muon candidates are chosen in the [45, 120] MeV energy range (see Section 5.1 for the tagging of muon candidates), which corresponds to a distribution of stopping vertices covering a large fraction of the detector target volume and allows to reject crossing yet not-stopping muons and cosmic showers.

However, the selected stopping muons may decay via the channel $\mu^- \longrightarrow e^- + \nu_\mu + \bar{\nu}_e$, before being captured. The so-called Michel-electron [116] that is emitted acts as a signature of the muon decay process, that is to be rejected. Such process is then identified with a delayed Michel-electron signal coming shortly after the prompt muon signal, within a [0.25, 6] μs time window, and with an energy lying in the [5, 70] MeV range.

In the remaining stopping yet not-decaying muon candidates, the electron coming from the boron decay is searched in the same Target cell (defined as the cell with the maximal

reconstructed energy) as the prompt signal, within a [2, 35] ms time window. On top of this space-time correlation, we require that there is no muon event in 200 μs before the boron 12 delayed candidate in order to mitigate the contribution of spallation neutron events, that are an important source of fake ^{12}B events via their capture in the detector. Furthermore, a time isolation cut requiring no event in the previous 10 μs is applied on the delayed signal, to allow the recovery of the baseline, as already pointed out in Section 3.2.1.

Accidental pairs

The accidental background is assessed with ten off-time windows. In practice, for each correlated pair, the prompt event is virtually duplicated and shifted ten times far in the future, to prevent any correlations due to residual physical processes. The correlated pair search algorithm is applied to each of these virtual prompt signals. If a valid delayed candidate is identified, the formed pair is tagged as an accidental pair and populate the accidental distribution.

Result

The boron 12 spectrum is extracted at the TG cell level from the statistical subtraction of the accidental distribution. By merging the spectrum of each cell, one obtains the spectrum at the target level, displayed in Figure 4.12. Given that we do not have an absolute normalization of the predicted ^{12}B spectrum, the experimental ^{12}B spectrum is area-normalized.

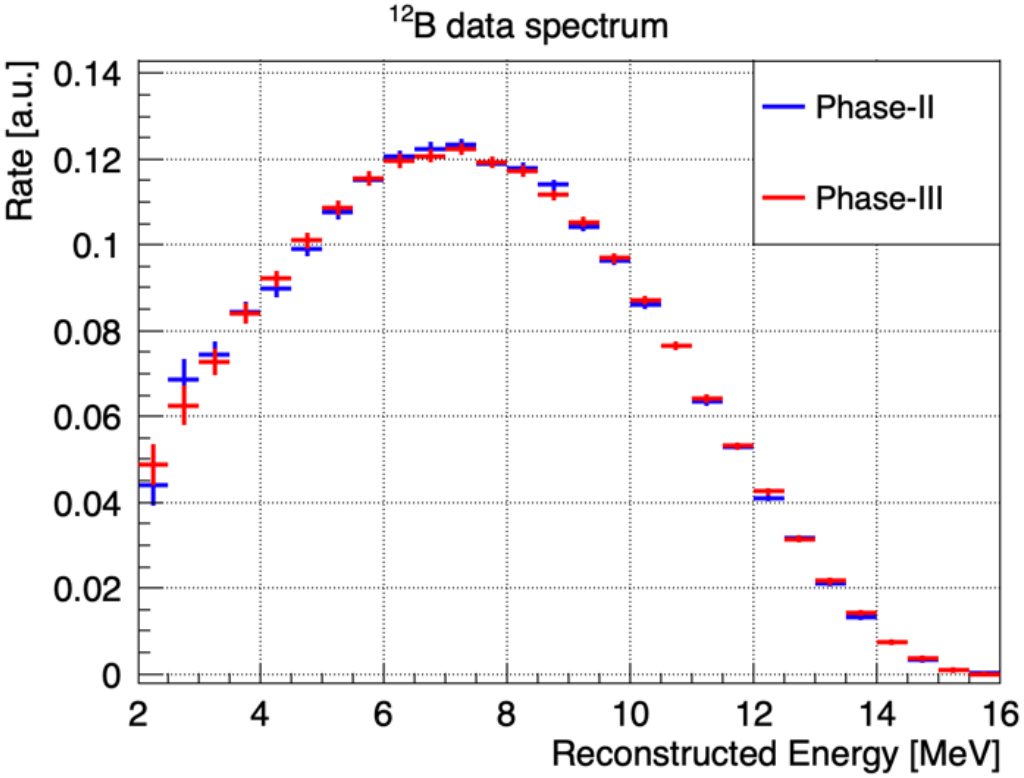

Figure 4.12: **Experimental ^{12}B spectrum**, for Phase-II and -III, reported in 500 keV-wide reconstructed energy bins.

4.3.2 Simulated ^{12}B spectrum

Distribution of muon stop vertices

The STEREO simulation provides us with the distribution of muon stop vertices in the whole detector, as well as the reconstructed energy at the target level and at the detector level on a muon event-by-event basis. We apply the same selection cuts as in the extraction of the experimental boron 12 spectrum, by selecting vertices from muons whose reconstructed energy at the detector level lies between 45 MeV and 120 MeV, and that deposited a majority of this energy in the target volume. The (X, Y, Z) distribution of the muon stop vertices is displayed in Figure 4.13. It is uniform in the horizontal plane, whereas there is a clear asymmetry on the Z-axis distribution that favors the stopping of the muons on the top of the detector. This comes from the overall decreasing shape of the muon flux energy spectrum such that the stopping muons reaching the bottom of the detector, that had an impinging energy greater than the muons stopping at the top of the detector, are fewer.

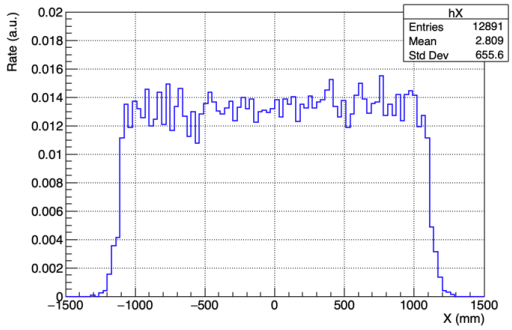

(a) X-axis distribution

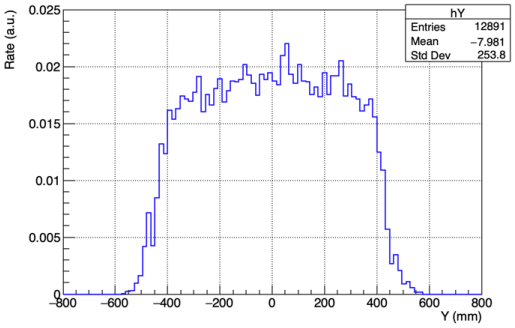

(b) Y-axis distribution

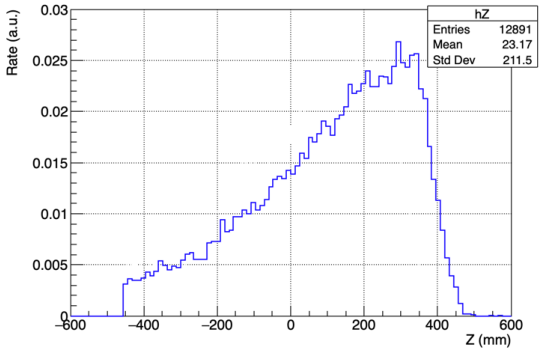

(c) Z-axis distribution

Figure 4.13: **Spatial distribution of muon stop vertices**. The Z-axis is ascending and the origin of coordinates is the center of the target volume, as defined in Figure 2.3b.

^{12}B predicted spectrum

In the ^{12}B Monte-Carlo event generator, I sample the emission vertices of the ^{12}B decay electron from the aforementioned spatial distribution of muon stop vertices. For such an event, the β transitions to the ground state of ^{12}C (98.22% branching ratio) and to the first two excited states have been included with their associated 4.4 MeV γ and α

particle emissions, accounting for a total branching ratio of 99.94 %. The prediction of the BetaShape code [117], shown in Figure 4.14, is chosen as a reference. The deviation of this spectrum with respect to the prediction given by the most recent version of the BESTIOLE code [118] is conservatively taken as a 1σ uncertainty on the shape of the spectrum fully-correlated between energy bins. It translates into a percent-level systematic across the spectrum energy range, much higher than the quoted uncertainties for the pure BetaShape model [119]. In a quite recent publication of the Daya Bay collaboration [120], it is argued that radiative corrections should not be applied to the simulated ^{12}B spectrum because the virtual loop corrections do not change the detected kinematics and the energy taken by the emitted real photons is actually deposited in the liquid scintillator. In the case of the smaller STEREO detector, real photons could escape the active volume. Therefore, the variations of the spectrum simulated without the radiative corrections was taken as a 1σ uncertainty on the shape of the spectrum fully-correlated between energy bins, translating into another percent-level systematic across the spectrum energy range. Another source of uncertainty is the distribution of muon stopping points given as input to the event generator, that may be affected by the level of the water channel on top of the STEREO detector. To check this assertion, the ^{12}B spectrum was simulated with the filled (resp. empty) water channel, with a 1 million events statistics. The ratio of the two obtained predictions being compatible with a constant fit within error bars, no systematic effects was identified.

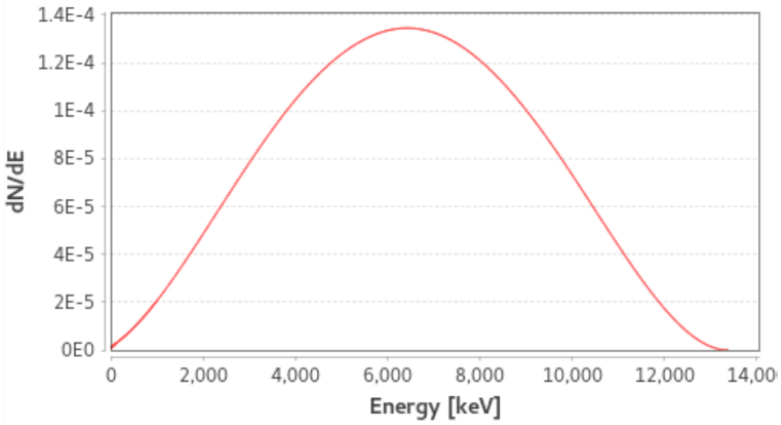

Figure 4.14: ^{12}B spectrum, as predicted by the BetaShape code [117].

^{12}N contamination

I also investigated a possible contribution of ^{12}N β-decays, with the ^{12}N β^+ spectrum prediction provided once again by the BetaShape code (see Figure 4.15). This isotope can be produced from ^{12}C nuclei either by charged-current interaction of an anti-muon on ^{12}C or charge exchange after proton production by a spallation process (although this last process should be suppressed by our selection cuts). The half-life of ^{12}N is 11 ms with an endpoint of 17.38 MeV, thus passing the boron selection cuts. The experimental spectrum is fitted with a weighted sum of the two β emitters, in a least-square approach. For Phase-II (resp. Phase-III) simulated spectrum at the target level, the ^{12}N contamination is found to be compatible with 0, amounting to $-0.5\% \pm 0.7\%$ (resp. $-0.4\% \pm 0.8\%$) of the total spectrum. Therefore, it is not taken into account in the overall ^{12}B simulated spectrum.

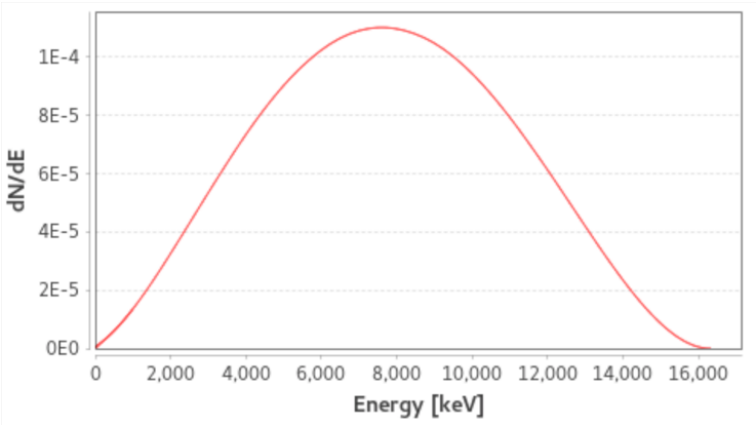

Figure 4.15: ^{12}N spectrum, as predicted by the BetaShape code [117].

4.4 Phase-II and -III energy scale

In this section, we make use of the final STEREO data sets for Phase-II and -III. Section 4.2 demonstrated the high sensitivity of the extracted antineutrino spectrum to a small energy scale distortion. The ^{12}B spectrum presented in Section 4.3 allows to complement the calibration data set and to put extra constraints on the energy scale, such that the RNL will now be derived from a global fit of the calibration and ^{12}B spectrum ratios, for each Phase, and the induced distortion on the antineutrino spectrum will be propagated as a systematic uncertainty on the antineutrino rates.

4.4.1 Calibration and ^{12}B residuals

In Figure 4.16, we show ^{12}B spectrum ratios reconstructed at the target level for Phase-II and -III. They are reported in 500-keV wide bins, between 2 MeV to 14.5 MeV. The ratios are found to be compatible with unity, and contained in a ±5% band.

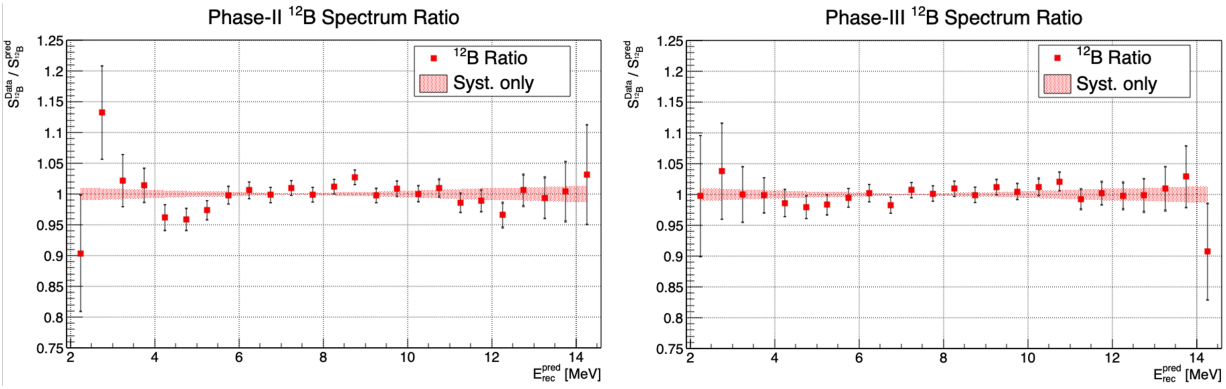

(a) Phase-II (b) Phase-III

Figure 4.16: **Targetwise ^{12}B ratios**, for (a) Phase-II and (b) Phase-III. They are both compatible with unity, with a $\chi^2/ndf = 29.2/23$ (resp. 10.3/23) for Phase-II (resp. Phase-III).

The cellwise and targetwise calibration residuals are shown in Figures 4.17 and 4.18, for Phase-II and -III, considering various radioactive sources (^{137}Cs, ^{54}Mn, ^{65}Zn, ^{42}K, ^{24}Na) and several neutron capture delayed signals obtained from the ^{241}Am/^{9}Be source (n-H, n-C and n-Gd peaks), averaged out over the 5-Z deployment positions in the cell of interest. They cover an energy range from 0.6 MeV to 8.3 MeV, thus fully encapsulating the energy range of interest for the antineutrino spectrum. At the target level and cell level, the residuals are contained in a ±1% band, although Cell 6 seems a bit more discrepant. This feature may be explained by the intensity of the light leaks between Cell 6 and the GC back (at the 11% level, see Figure 3.15b), due to the cracks in the acrylics during Phase-I that could not be repaired during the shutdown period of the experiment. This induces sizeable differences in the calibration matrix used for the energy reconstruction of this cell with respect to the other cells.

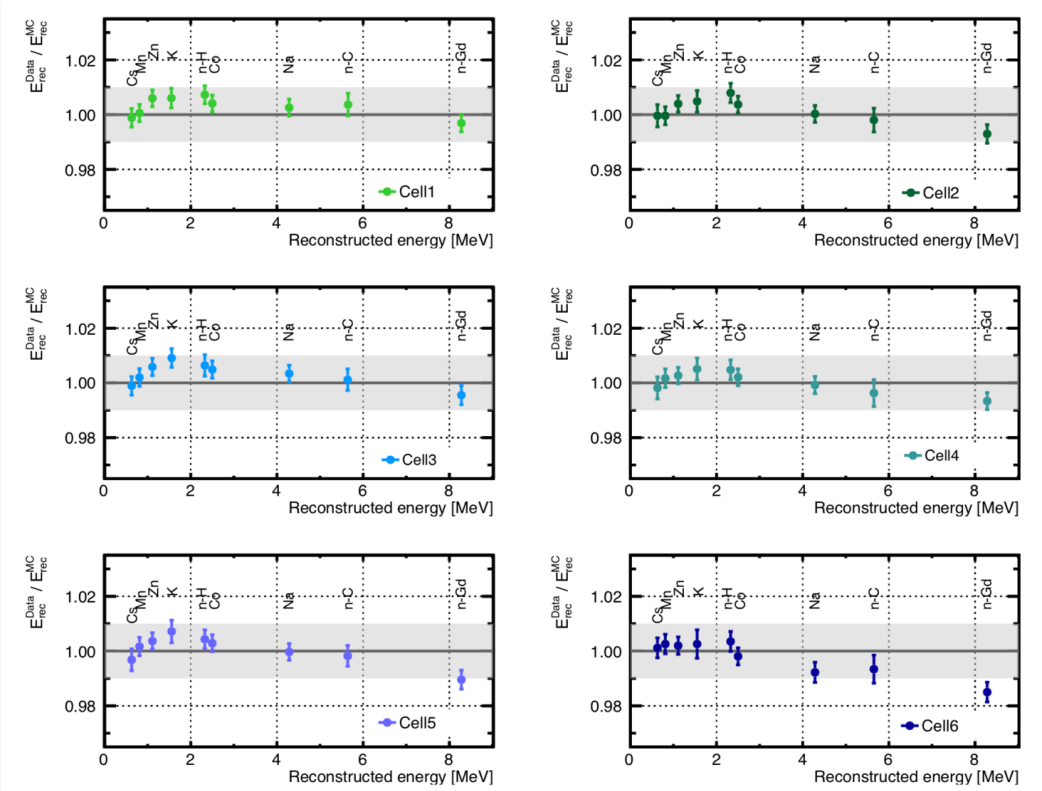

(a) Phase-II

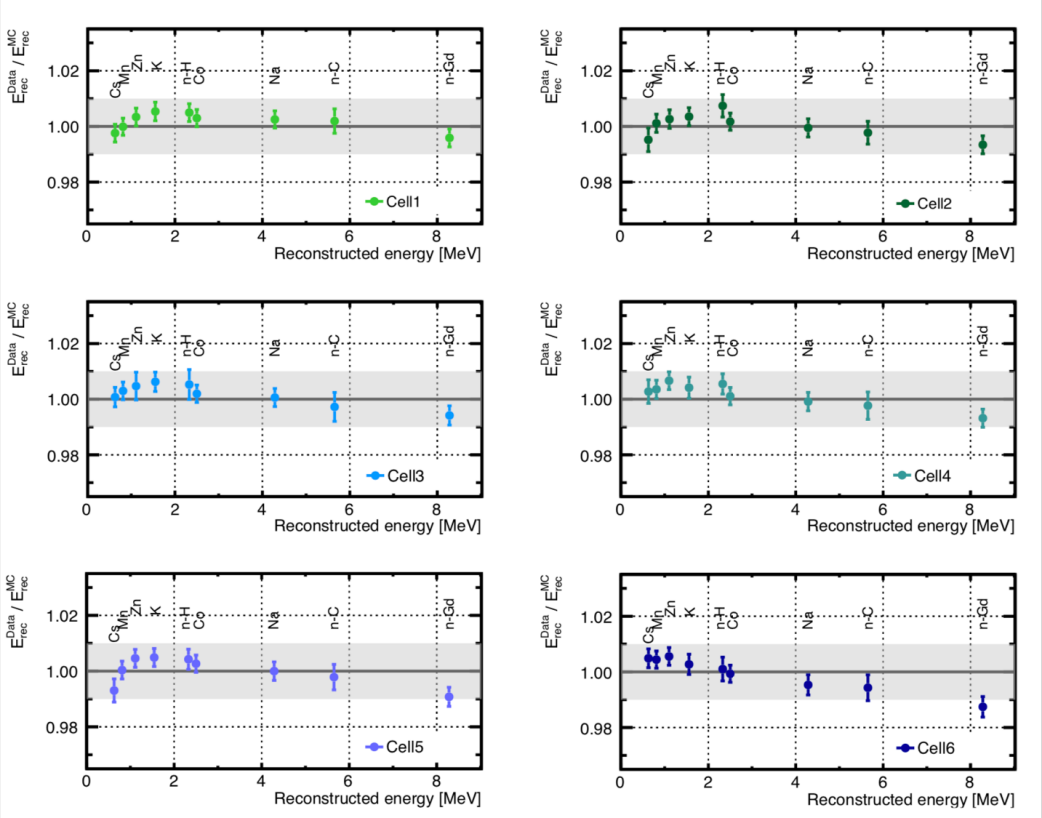

(b) Phase-III

Figure 4.17: **Cellwise calibration residuals**, for (a) Phase-II and (b) Phase-III. Source [121].

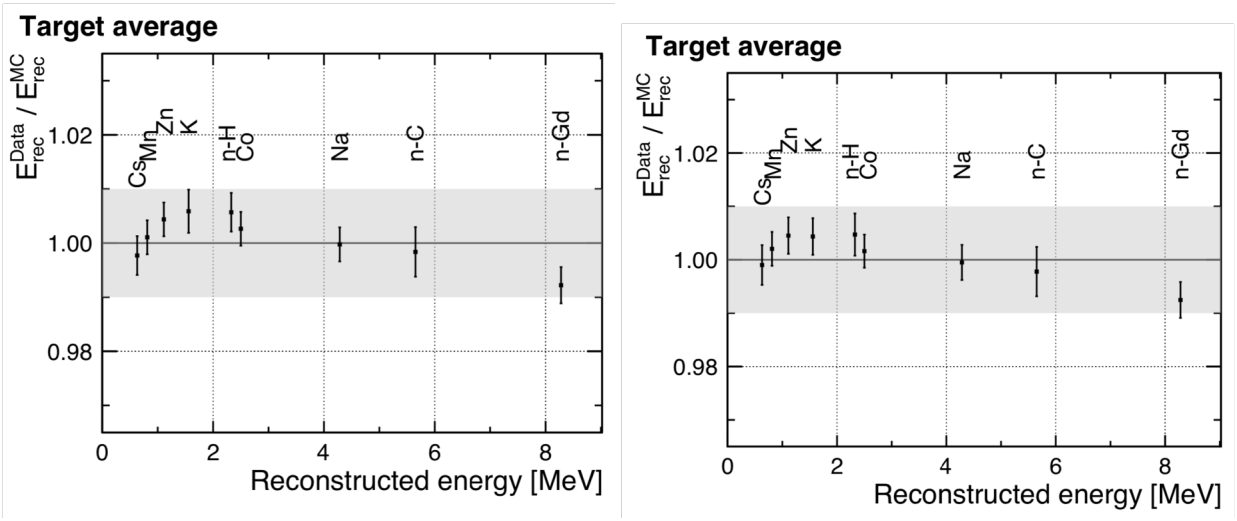

(a) Phase-II (b) Phase-III

Figure 4.18: **Targetwise calibration residuals**, for (a) Phase-II and (b) Phase-III. Source [121].

4.4.2 Global Fit of an energy scale distortion

The parameterization of the RNL is done in the KDE approach, with 10 equally spaced Gaussian Kernels, ranging from 0 MeV (mean of the first kernel) to 14 MeV (mean of the last kernel). The width of each kernel, which is also the constant inter-knot distance, is $\sim$ 1.6 MeV, that is, about 3 energy bins in the ^{12}B spectrum space. The distortion is then derived from a global fit of the ^{12}B spectrum ratios and the calibration residuals, by applying the exact same formalism as for the case study. For illustration, we only show the results of the procedure at the target level, for Phase-II (Figure 4.19) and -III (Figure 4.20) for this one KDE parameterization. Yet, the procedure has been run for each cell of the target volume, to derive the cell-dependent distortion, and for other KDE parameterizations, with 15/20/25 Gaussian Kernels. In order to set the energy scale related systematic uncertainty on the antineutrino rates, we compare the energy scale derived from the KDE approach with the energy scale resulting from a constant $\pm 1\%$ bias on the linear calibration coefficient cellwise, and $\pm 1\%/\sqrt{6}$ bias targetwise.

As shown in Figures 4.19 and 4.20, targetwise, the fitted RNL is well contained in a $\pm 1\%/\sqrt{6}$ bias on the linear calibration coefficient. We may notice as well that the RNL is smoother and flatter for Phase-III in comparison with Phase-II, due to the enhanced compatibility of the ^{12}B ratios with unity for Phase-III. Furthermore, we may add that similar results are obtained with polynomial estimates.

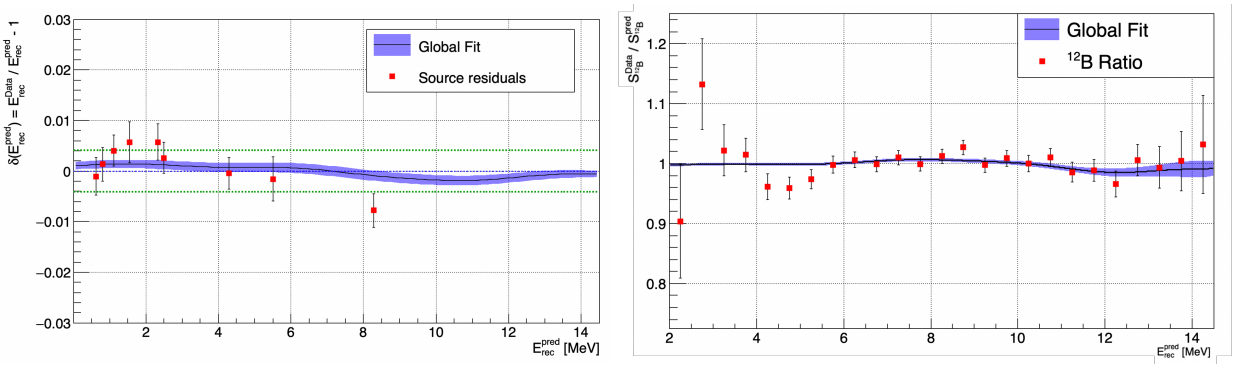

(a) Calibration data (b) ^{12}B spectrum data

Figure 4.19: **Target level Global fit for Phase-II**, constrained by (a) the calibration residuals and (b) the ^{12}B ratios. The dashed green lines represent a $\pm 1\%/\sqrt{6}$ bias on the linear calibration coefficient.

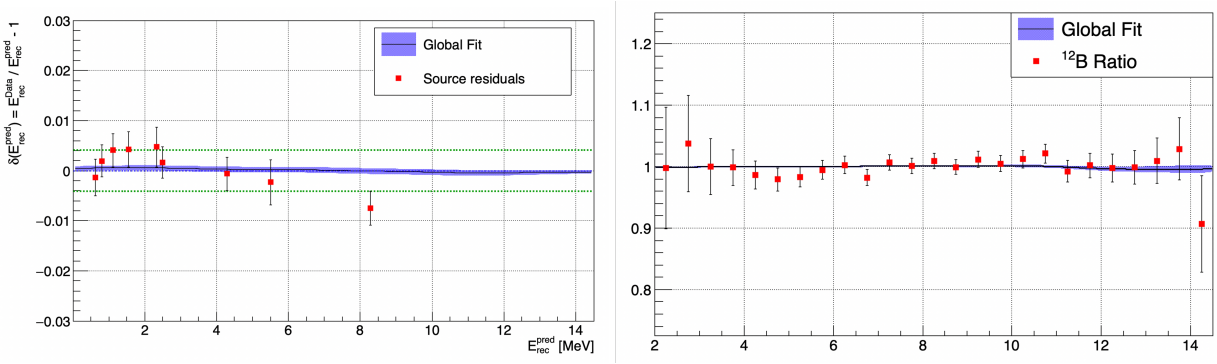

(a) Calibration data (b) ^{12}B spectrum data

Figure 4.20: **Target level Global fit for Phase-III**, constrained by (a) the calibration residuals and (b) the ^{12}B ratios. The dashed green lines represents a $\pm 1\%/\sqrt{6}$ bias on the linear calibration coefficient.

4.4.3 Energy scale systematic uncertainty on the $\bar{\nu}$ rates

We propose to compare, at the cell level and target level, the correction on the antineutrino rates induced by the fitted energy scale distortion to the correction induced by a mere bias on the linear calibration coefficient. In our framework, this corresponds to a polynomial parameterization of the RNL as: $\delta(E) = \frac{\omega_0}{E} + \omega_1$, with $\omega_0 = 0$ and $\omega_1 = \pm 1\%$ (cellwise) or $\pm 1\%/\sqrt{6}$ (targetwise).

Finally, the impact of the energy scale distortion from the KDE approach and from the baseline scenario of a bias on the linear calibration coefficient can be propagated on the antineutrino rates using the same formalism as for the case study. The results are shown in Figure 4.21.

As expected from the calibration residuals, we find the KDE fit results of cells 1 to 5 in rather good agreement among each other as compared to cell 6. With the other KDE parameterizations, the amplitude of the fitted distortion varies, but its shape remains similar for all fits and is, overall, contained within the aforementioned simple model of $\pm 1\%$ uncertainty on the linear calibration coefficient, at the cell level, and $\pm 1\%/\sqrt{6} \approx 0.41\%$, at the target level. Therefore, we take this envelope, mostly determined by the deviation

of cell 6, as a 1σ energy scale related uncertainty on the antineutrino rates with 100% energy-bin-to-energy-bin correlation and no cell-to-cell correlation.

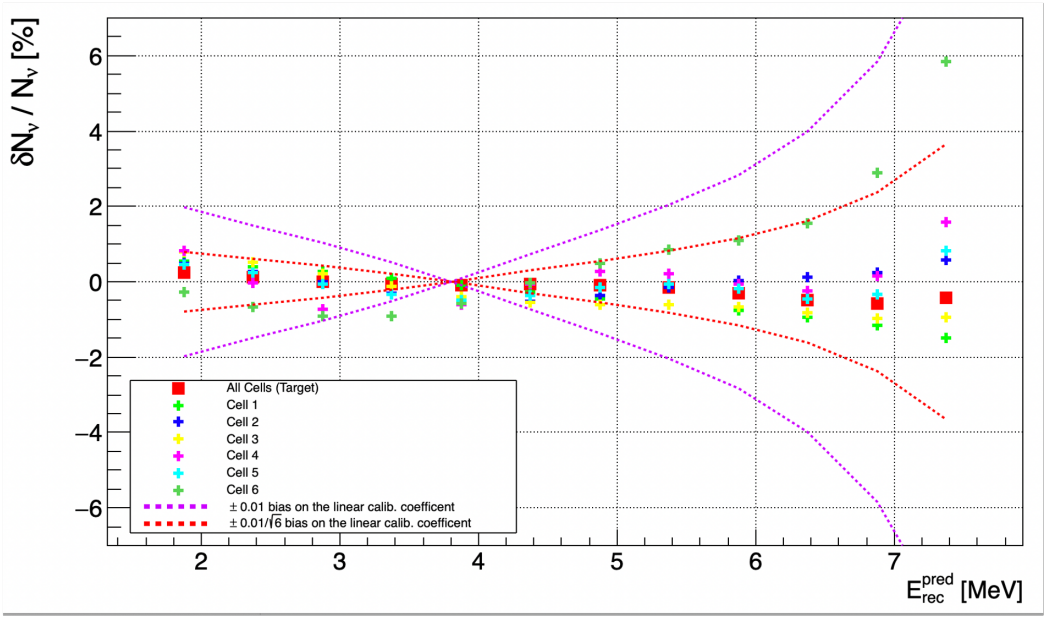

(a) Phase-II

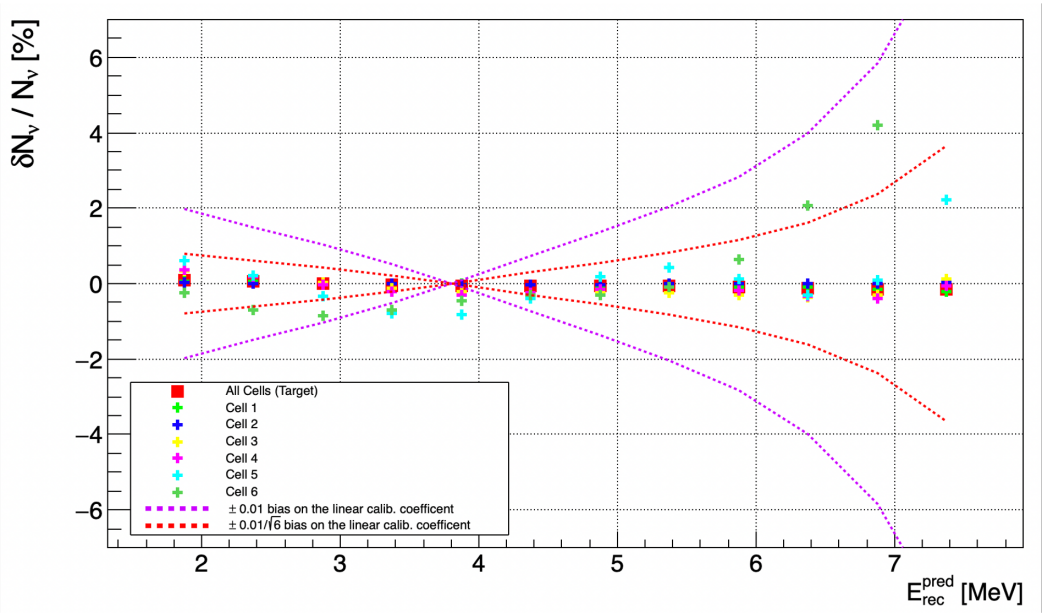

(b) Phase-III

Figure 4.21: **Energy scale induced correction on the antineutrino rates**, for (a) Phase-II and (b) Phase-III.

Chapter 5

Neutrino spectrum extraction in STEREO

As stated in the previous sections, the extraction of the IBD signal in the STEREO experiment relies on the dual signature of the IBD signal, with the prompt positron signal and the delayed neutron capture event. A set of selection cuts, based on the tagging of the prompt and delayed signal events as well as stringent constraints upon the time and space correlation between the two events, allows to select IBD-like events amongst those recorded during the operation of the STEREO detector. They will be presented in Section 5.1.

The selected events are labelled as "candidates" as they mimic the signature of the IBD signal, as defined by the selection cuts, and consist of "true" IBD events, i.e. the antineutrino signal events, and "fake" IBD events, i.e. background events that mimic the IBD signature. These last events can be categorized in two types: the accidental background events, consisting of pairs of uncorrelated events that pass the IBD selection cuts, and the correlated background events, composed of pairs of events with a common physical origin. Thus, the selection of IBD candidates constitutes only the first layer to the extraction of the antineutrino signal and must be completed by a procedure of background subtraction. The background signal is not known *a priori* on an event-by-event basis, but the correlated background distribution can be measured taking advantage of the reactor-OFF data, as sketched in Section 5.2, whereas the accidental background distribution can be measured during reactor-ON periods by the off-time windows method, as described in the case of the ^{12}B spectrum extraction (see Section 4.3). This allows to statistically subtract the total background distribution from the overall IBD candidates distribution and then extract the pure antineutrino signal distribution. This procedure will be detailed in Section 5.3.

At last, the normalization of the antineutrino extracted spectrum will be discussed in Section 5.4.

5.1 Event tagging

5.1.1 Muon candidates

The main source of correlated background is of cosmic origin and is mostly induced by the interaction of atmospheric muons with the liquid scintillator or neighboring structural materials. Muons constitute indeed the bulk of the flux of cosmic ray induced particles for the STEREO experiment, as shown in Figure 5.1. They can trigger spallation reactions and induce fast neutrons, giving rise to a prompt proton recoil signal via (n, p) elastic

scattering reaction and a delayed neutron capture signal, or multi-neutron events followed by two neutron captures closely correlated in time, that may mimic the prompt-delayed signature of the IBD signal.

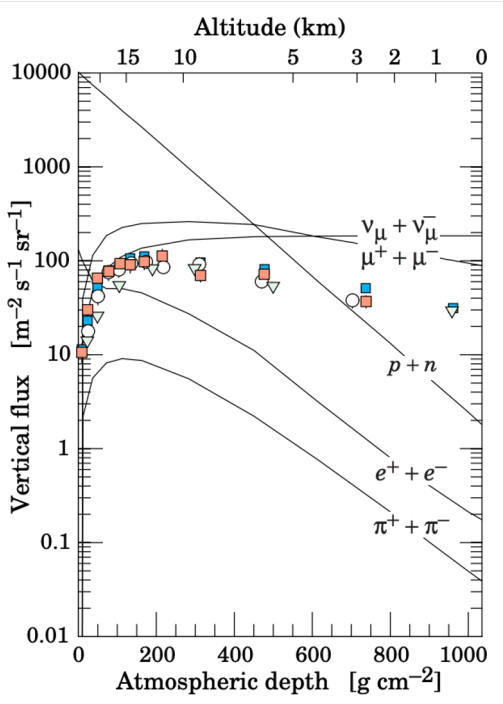

Figure 5.1: **Vertical flux of cosmic ray induced particles as a function of the atmospheric depth**. The lines correspond to particles with energy $E > 1$ GeV whose flux is estimated from a Monte-Carlo cosmic-ray shower simulation. The points show measurements of negative muons with $E_\mu > 1$ GeV. The altitude of the STEREO detector is 210 m, where muonic neutrinos and muons represent the overwhelming majority of the flux. Source [17].

Therefore, the proper tagging of muons is of key importance for the signal extraction procedure. Exploiting the fact that muons are highly energetic ionizing particles that can exceed the dynamic range of the PMTs by traversing several centimeters of the liquid scintillator, an arbitrary cut can be set to tag the muons depositing their energy in the detector:

$$E^{det}_{muon} > 20 \text{ MeV} \tag{5.1}$$

where E^{det}_{muon} corresponds to the reconstructed energy at the detector level.

This argument was used in Section 3.2.1 to tag muon events in the evaluation of the light leaks for the energy reconstruction procedure. This supplemental selection cut complements the tagging power of the muon veto, whose criterion is set on the total collected charge in the veto PMTs:

$$Q^{veto}_{muon} > 70 \text{ PE} \tag{5.2}$$

This condition is actually part of the T2 trigger scheme for event selection (see Section 2.2.4). Other secondary conditions related to the asymmetry of the collected charges or the PSD figure of the muon signal seen by the veto have also been added [122, 123]. Their main function is to further discriminate the muon signal from the γ and neutron background contamination mostly coming from the neighboring instruments.

In the following, a muon event will be an event tagged as such either in the detector, from Equation 5.1, or in the muon veto. The rate of tagged muons is found to be $\sim$ 900 Hz.

5.1.2 IBD candidates

The selection of IBD candidate events is done by a dedicated correlated pair search algorithm that applies a set of time-, space- and energy-related cuts to a sliding memory window containing four successive recorded events such that an optimal compromise between signal acceptance and background rejection as well as the stability of the extracted signal under small cut variations are achieved [82]. It is worth mentioning that the energy observable of the cuts refers to the reconstructed energy, as given by the procedure detailed in Section 3.2, may it be at the cell, target or detector level. Each of these cases will be referred to by a dedicated superscript. In particular, these energies cannot be thoroughly interpreted as true deposited energies due to the non-linearity of the energy reconstruction.

All IBD selection cuts are summarized in Table 5.1. In the following, the vertex cell of an event will designate the TG or GC cell exhibiting the largest reconstructed energy for the prompt signal.

Type	#	Requirement for passing cut
Total	1	$1.625 \text{ MeV} < E^{\text{detector}}_{\text{prompt}} < 7.125 \text{ MeV}$
Energy	2	$4.5 \text{ MeV} < E^{\text{detector}}_{\text{delayed}} < 10.0 \text{ MeV}$
Topology	3	$E^{\text{cell}}_{\text{prompt}} < \begin{cases} 1.0 \text{ MeV (Ph-II) / } 1.1 \text{ MeV (Ph-III), neighbour cell} \\ 0.4 \text{ MeV, other cell} \end{cases}$
	4	
	5	$E^{\text{target}}_{\text{delayed}} > 1.0 \text{ MeV}$
Coincidence	6	$2\ \mu s < \Delta T_{\text{prompt-delayed}} < 70\ \mu s$
	7	$\Delta X_{\text{prompt-delayed}} < 600 \text{ mm}$
Rejection of muon-induced background	8	$\Delta T^{\text{veto}}_{\text{muon-prompt}} > 100\ \mu s$
	9	$\Delta T^{\text{detector}}_{\text{muon-prompt}} > 200\ \mu s$
	10	for all events with $E^{\text{detector}}_{\text{event}} > 1.5 \text{ MeV}$: $\begin{cases} \Delta T_{\text{before prompt}} > 100\ \mu s \\ \Delta T_{\text{after delayed}} > 100\ \mu s \end{cases}$
	11	$\frac{Q_{\text{PMT max, prompt}}}{Q_{\text{cell, prompt}}} < 0.5$

Table 5.1: Selection cuts for IBD candidates.

The energy-related cuts set on the energy reconstructed at the detector level allow to tag an event as a prompt (#1) or a delayed (#2) candidate. For the prompt positron signal, the total reconstructed energy should lie between 1.625 and 7.125 MeV. The lower cut is set to mitigate the contribution from the time-evolving reactogenic background induced by neutron-activated ^{41}Ar in ambient air, whereas the setting of the upper cut is done by requiring (arbitrarily) a signal-to-background > 0.2 ratio in the high energy end of the reconstructed spectrum. For the delayed signal, only the neutron capture events on gadolinium are selected by the cut as they offer greater separation potential from the

background than the 2.2 MeV gamma-line of the hydrogen capture events.

Then come the topological cuts on the prompt (#3/4) and delayed (#5) signals. They are set on the energy reconstructed in a portion of the detector, cellwise (#3/4) or target-wise (#5), and thus constrain the topology of the energy deposition for both signals.

As the two 511 keV γ rays coming from the annihilation of the IBD prompt positron signal are emitted back-to-back, it is therefore very unlikely for them to be detected in the same cell if they escape the vertex cell. Moreover, with the interaction length of these gammas at the $\sim$ 10 cm level, comparable to the dimension of a cell, escaping gammas are expected to deposit most of their energy in the closest volumes neighboring the vertex cell. Cuts #3/4 then set upper limits on the prompt signal reconstructed energies in cells other than the vertex cell to allow for the detection of only one escaping 511 keV gamma in a given neighboring cell. When setting these cuts, one has to consider potential bias on the reconstructed energy leaks of prompt events, due to the imperfect modelling of the cell-to-cell optical cross-talk. This is the reason why cut #3 includes a margin of $\sim$ 0.5 MeV with respect to the 511 keV nominal energy. Furthermore, due to the small degradation of the detector resolution between Phase-II and -III caused by the slow deterioration of the optical properties of the liquid scintillator, the upper limit set for cut #3 is slightly less stringent for Phase-III signal extraction.

By requiring the reconstructed energy in the target to be larger than 1.0 MeV for the delayed signal, cut #5 allows to reject the high-energy background events depositing most of their energy in the GC. As the delayed signal that is selected is only generated in the TG, which is the only active volume loaded with gadolinium, most of its deposited energy is expected to lie in the TG volume, up to inevitable edge effects at the TG borders.

Cuts #6 and #7 implement the space-time correlation between the signals tagged as prompt and delayed. The lower limit of cut #6 allows to reject the decay of stopping muons, when a prompt muon signal and a delayed Michel electron signal may fall into the respective energy ranges of cut #1 and #2. The upper limit of cut #6 encompasses most of the time distribution of the delayed neutron capture signal, whose time constant is 16 μs (+ 2 μs thermalization time). After 70 μs, the contribution of accidental coincidences becomes dominant over physically correlated events. Cut #7 is set on the distance between prompt and delayed vertices along the detector X-axis (see Figure 2.3b), calculated from the barycenters of the two vertices. The barycenters are determined by weighting the positions of all PMTs j within a cell l by their charges Q_j, and within the entire detector by the reconstructed energy E_l in their cell l [75].

Cuts #8-11 aims at rejecting the muon-induced background. To this end, one requires (cut #8-9) any muon event to stand at least 100 μs (resp. 200 μs) before the prompt signal if it is detected in the muon veto (resp. the detector). Cut #10 mitigates the detection of multi-neutron events, that could be induced by e.g. an undetected muon. Such neutrons are expected to be closely correlated in time. The cut then requires any event of energy $>$ 1.5 MeV to stand at least 100 μs away from the tagged correlated pair. At last, by limiting the charge collection asymmetry at the vertex cell level, cut #11 further rejects stopping muon events as prompt candidates. As already shown in the ^{12}B study (see Section 4.3), such events mostly occur at the top of the detector, close to the PMTs location, causing an asymmetric distribution of light collection with respect to events occurring in the bulk of the detector.

5.2 Background distribution

As already mentioned, selection cuts certainly allow to drastically reduce the background contamination, but cannot completely eliminate it. Both the accidental and correlated background distributions must be accurately estimated in order to extract the antineutrino signal from the periods when the reactor is turned on.

The accidental background can be derived along the data flow irrespective of the reactor status. The method of time-shifted gates, sketched in Section 4.3 for the ^{12}B signal extraction, is also used to obtain the accidental background distribution in the case of the antineutrino signal extraction.

As for the correlated background, its distribution is characterized from the periods where the reactor is turned off, such that it is mandatory that the combination of the detector shielding and the selection cuts presented in Section 5.1 suppress all correlated background originating from the reactor. An upper limit of the reactogenic component of the correlated background will thereupon be set in Section 5.3.

Furthermore, to enhance the capability of background rejection and achieve a signal-to-background ratio of ~ 1, we fully exploit the PSD capability of the liquid scintillator and add a supplemental dimension to the set of cuts presented in the previous section. Bearing in mind that all the information on the antineutrino energy is embedded in the reconstructed energy of the prompt signal, an IBD prompt candidate will then be described by its vertex cell, its reconstructed energy at the detector level and its PSD observable Q_{tail}/Q_{tot}.

5.2.1 Pulse shape discrimination

As described in Section 2.2.2, the ratio Q_{tail}/Q_{tot} allows to discriminate between electron-like and proton-like recoil signals. The prompt IBD signal, consisting of a positron and 2 annihilation γ, can be fully categorized as an electron-like signal, such that any prompt proton-like signal can be unambiguously tagged as background.

The top panel of Figure 5.2 shows a PSD distribution of the prompt signal for correlated and accidental background events, from reactor-OFF data whose reconstructed prompt energy lies in [2.125, 2.625] MeV. The correlated background distribution, depicted in black, clearly exhibits an electron (resp. proton) recoil region at low (resp. high) Q_{tail}/Q_{tot}. The proper separation between electron recoils from proton recoils is done from the high-statistics sample of single events in the detector, without any selection cuts applied. The PSD figure of such sample is displayed in the bottom panel of Figure 5.2 and is dominated by electron recoils. The mean (μ_γ) and width (σ_γ) of this distribution are extracted from a gaussian fit, such that a recoil signal is tagged as electron recoil if its PSD observable is lower than $\mu_\gamma + 2\sigma_\gamma$, and as proton recoil if its PSD observable is greater than $\mu_\gamma + 2.5\sigma_\gamma$.

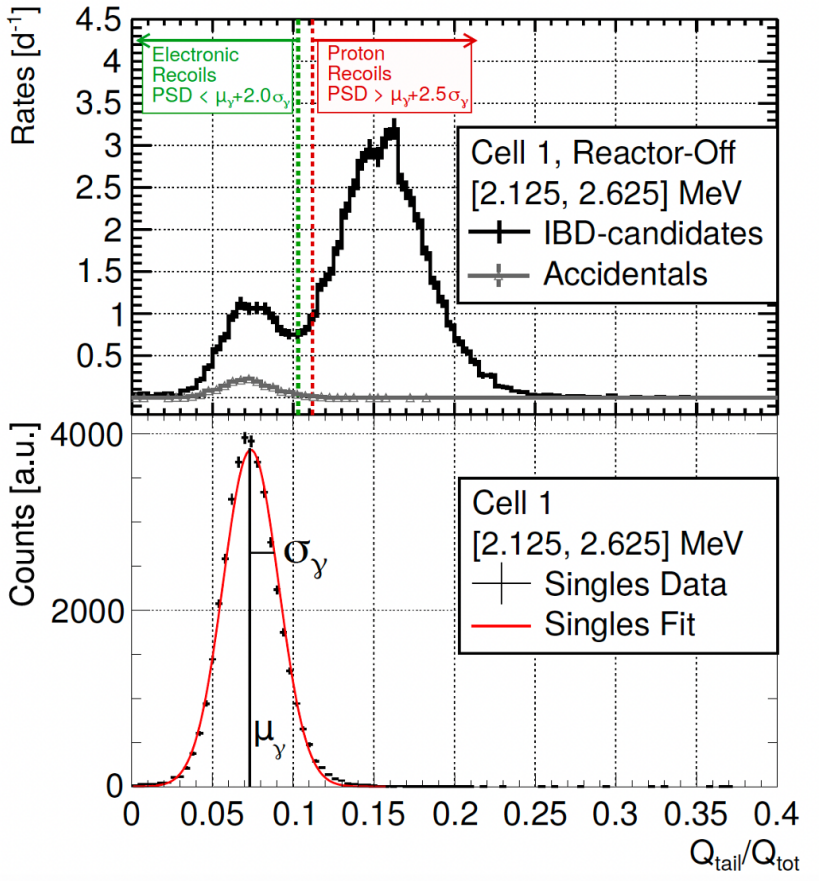

Figure 5.2: **PSD distribution of background prompt signals**, for the reactor-OFF periods of Phase-II, in TG cell 1, and for a prompt reconstructed energy in [2.125, 2.625] MeV. (Top) PSD distribution of correlated (black) and accidental (grey) background. (Bottom) One-day PSD distribution of single events, dominated by electron recoils. The extracted parameters μ_γ and σ_γ allow to define a PSD cut to separate electron recoils from proton recoils. Source [75].

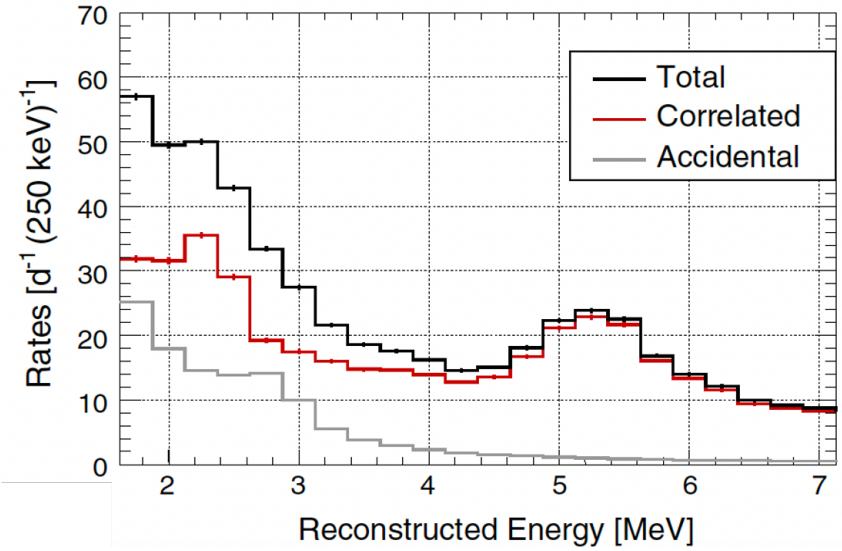

Figure 5.3: **Prompt energy spectrum of correlated and accidental background contributions**, for Phase-II, for events in the target volume. Source [75].

At last, for each TG vertex cell and each bin of reconstructed energy at the detector level, the background event rate can be thoroughly computed as the integral of the electron recoil region of the PSD spectrum of this energy bin, ranging from 0 up to $\mu_\gamma + 2\sigma_\gamma$. Estimating the accidental background from the time-shifted gate method during reactor-ON periods and the correlated background from the application of selection cuts during reactor-OFF periods, one can derive the overall background spectrum, as shown in Figure 5.3. For the correlated background, the peak around 2.2 MeV originates from neutron cascades surviving the selection cuts, that result in a neutron capture prompt signal on hydrogen (and gadolinium, around 8 MeV, not shown). The peak around 5.4 MeV arises from the neutron inelastic scattering on ^{12}C nuclei, that gives rise to a prompt signal that comprises a dominant electron-like recoil part with the emission of a 4.4 MeV γ and a proton-like recoil part from the neutron scattering on protons.

5.2.2 Model of correlated background

As mentioned in Section 3.1, the simulation package of STEREO does not allow to run a complete and comprehensive simulation of all correlated background events generated in the STEREO detector. However, this is not prohibitive with respect to the signal extraction procedure provided one can measure the correlated background and extract a model that we can demonstrate to be stable over time. In this purpose, one has to correct the PSD spectrum of the correlated background from any time-dependent variations that could affect the extracted rate of correlated background events with respect to the antineutrino events rates.

PSD stability

The underlying assumption supporting the extraction procedure that will be detailed in Section 5.3.1 is the time-stability of the Q_{tail}/Q_{tot} scale. Similarly to the energy scale study carried out in Chapter 4, a distortion in the scale of the PSD observable would change the PSD spectrum, hence possibly impacting the extracted rates of IBD events.

Due to the slow degradation of the liquid optical properties, the separation between the populations of electron-like and proton-like recoils comes to be reduced over time. Moreover, a change in the liquid scintillator temperature may dilate or contract the liquid and change the effective density of energy deposition, shifting the PSD variable to lower or higher values. Such changes may be sizeable, as shown in Figure 5.4, and cannot be neglected. Therefore, a dedicated correction has been implemented [84]. It is based on the n+γ Am-Be source, that has a PSD spectrum comparable to that of antineutrinos.

The distortion of the PSD at date t with respect to the reference date t_{ref}, May 28th, 2019 (middle of the data-taking), is expressed with a scaling factor f and a shift S:

$$\text{PSD}(t) = f \times \text{PSD}(t_{\text{ref}}) + S. \tag{5.3}$$

The quantities f and S are determined for each Am-Be calibration run of each target cell, every 1-2 months, from a least-square fit. In order to obtain the correction to be applied on a daily basis, for each acquisition run, one has to derive their continuous evolution over time and temperature. To this end, this evolution is parameterized by a polynomial

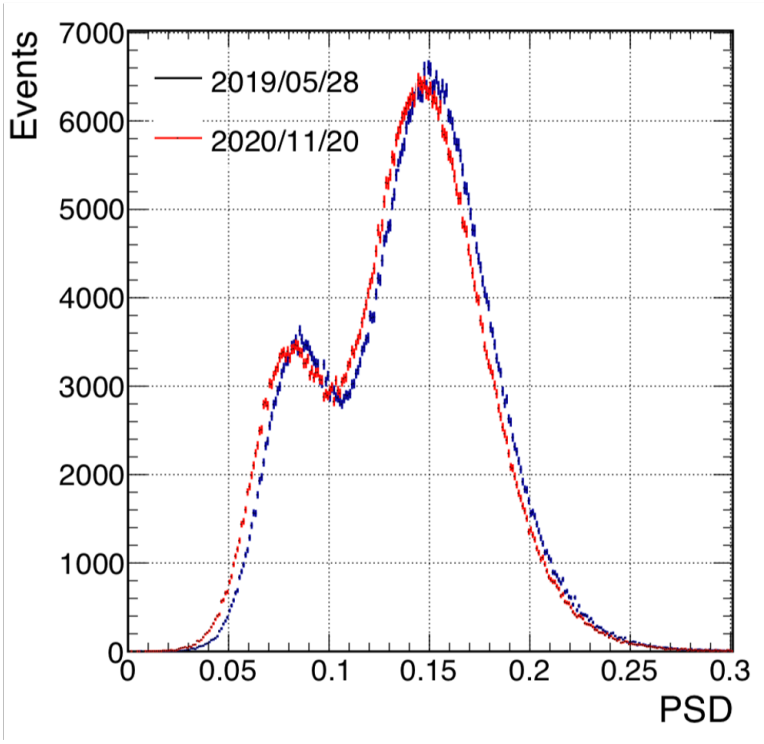

Figure 5.4: **PSD distributions of Am-Be events** from a run in May 2019 (reference date for the correction) and a run in November 2020 (end of the data-taking), showing the PSD distortion.

function of time (second order) and temperature (first order) as follows:

$$\begin{cases} f(t,T) = a_f t + b_f t^2 + c_f T + d_f \\ S(t,T) = a_s t + b_s t^2 + c_s T + d_s \end{cases} . \tag{5.4}$$

The polynomial parameterization was set to be as simple as possible and proved to be successful in encapsulating the time and temperature dependence of f and S for the entire Phase-II and -III data-taking periods, as illustrated in Figure 5.5 for the case of the PSD shift parameterization $S(t,T)$.

The fitted coefficients (a_f, b_f, c_f, d_f) and (a_s, b_s, c_s, d_s) were found to be quite independent of the height of the source in the calibration tube or the energy of the events. Therefore, the correction was built with calibration runs in the center of each cell, combining events from a wide energy range: from 1.625 to 4.125 MeV.

For each reactor-ON and -OFF run at date t, with detector temperature T, the PSD variable is corrected based on the fitted $f(t,T)$ and $S(t,T)$. The extraction procedure detailed in Section 5.3.1 is then applied on the corrected PSD spectrum.

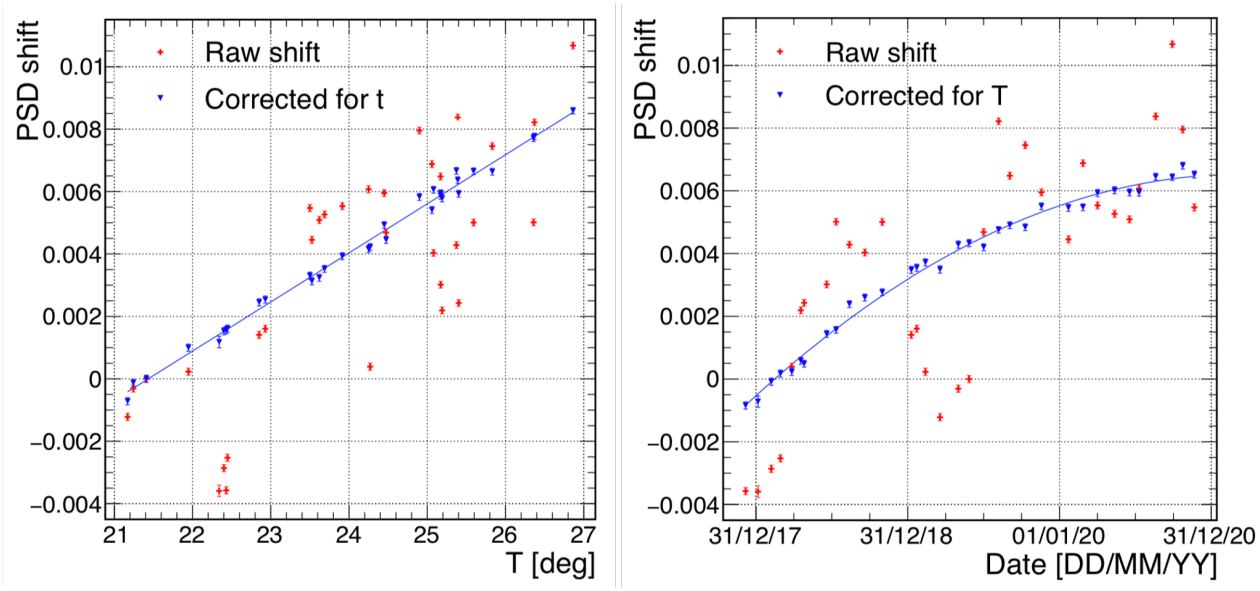

(a) Temperature correction (b) Time correction

Figure 5.5: **Correction of the PSD shift S, for Phase-II and -III data-taking periods**. (a) Temperature-evolution, following a first order polynomial provided the time dependence is corrected. (b) Time-evolution, following a second order polynomial provided the temperature dependence is corrected.

Correlated background and environmental parameters

As expected from its cosmic-induced origin, the correlated background rates showed to be sensitive to environmental parameters. As shown in Figure 5.6, both the rates of electron and proton recoil events are found to be linearly (anti-)correlated to the atmospheric pressure, with compatible linear correlation coefficients between the two populations. A mild dependence on the filling level of the water pool above the reactor core was also observed. However, it turned out to be one order of magnitude lower than the typical atmospheric pressure variations, below our statistical accuracy.

To study the influence of these changes on the PSD distribution of the correlated background, the reactor-OFF data set is divided into subsets of data, classified by atmospheric pressure and reactor pool level. The shape of the PSD distributions remains very stable in all conditions such that the fit of a single normalization parameter is enough to correct from the observed discrepancy of the PSD spectra, as shown in the example of Figure 5.7. The fitted value of this parameter is anti-correlated with the atmospheric pressure. Correcting each subset of reactor-OFF data, for Phase-II and -III, with the appropriate normalization factor amounts to reducing to one reference distribution for the correlated background model, anchored on fixed values of atmospheric pressure and reactor pool level. This is only meaningful because the reactor antineutrino event rate is not expected to depend on environmental parameters, due to its pure reactogenic origin.

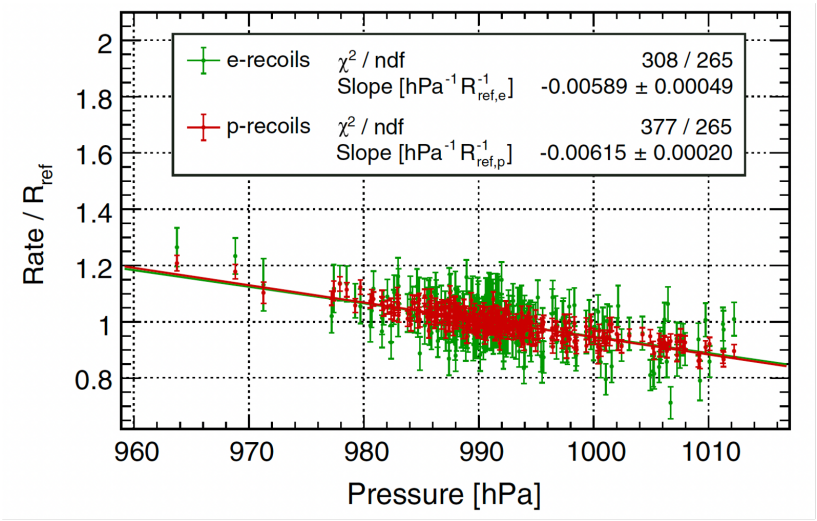

Figure 5.6: **Relative rates of IBD candidates from reactor-OFF periods of Phase-II as a function of the atmospheric pressure**, in the electron-like (green) and proton-like (red) recoil regions. Compatible relative dependencies are found in the two regions. Source [75].

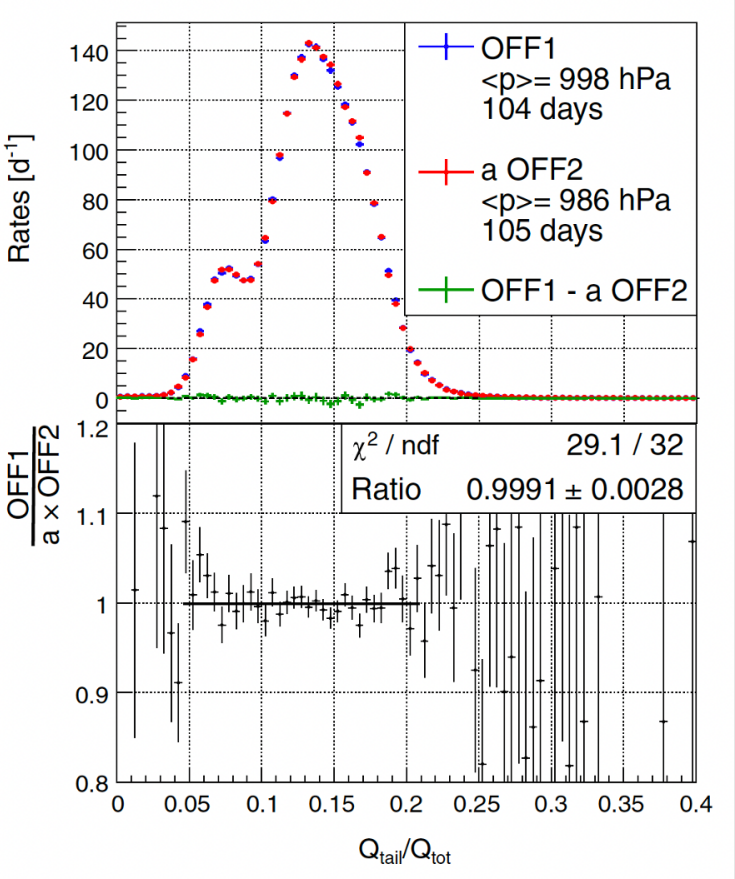

Figure 5.7: **PSD comparison for the Phase-II reactor-OFF data set**, split into two bins of high and low atmospheric pressure. The spectra are normalized to their acquisition times, while the OFF2 spectrum is additionally scaled by a parameter a, fitted to the OFF1 spectrum. a accounts for the mean atmospheric pressure difference between the data sets. The residuals between the two OFF distributions shown in the bottom plot demonstrate the very good stability of the shape of the PSD spectrum achieved in the STEREO experiment. Source [75].

5.3 Antineutrino signal

5.3.1 Extraction principle

For a given bin of energy i, we denote ON_i and OFF_i the PSD distributions of IBD candidates obtained from reactor-ON and -OFF data-taking periods by applying the selection cuts of Section 5.1, and ON_i^{acc} and OFF_i^{acc} the PSD distributions of the accidental events obtained from the time-shifted gate method.

ON_i^{acc} and OFF_i^{acc} are modelled with a set of parameters, one per PSD bin p: $m_{i,p}^{acc,ON}$ and $m_{i,p}^{acc,OFF}$. Similarly, the correlated background component of OFF_i PSD distribution is described by a set of parameters $m_{i,p}^{corr,OFF}$. The PSD distribution of IBD events is given by a scaled normal distribution $\mathcal{G}_p(A_i, \mu_i, \sigma_i)$, with $\{A_i, \mu_i, \sigma_i\}$ as free parameters. The IBD event rate for the considered energy bin is then given by the integral of the gaussian function.

Therefore, the overall model $\mathcal{M}_i^{OFF}$ for the OFF_i distribution writes:

$$\mathcal{M}_{i,p}^{OFF} = m_{i,p}^{corr,OFF} + f^{acc,OFF} m_{i,p}^{acc,OFF} \tag{5.5}$$

where $f^{acc,OFF}$ is a fixed normalization factor that accounts for the number of time-shifted gates used in the accidental extraction method for the OFF-period.

Taking full advantage of the time-stability in shape of the OFF distribution of the correlated background, and in the absence of any reactor-induced correlated background, the overall model $\mathcal{M}_i^{OFF}$ for the ON_i distribution reads:

$$\mathcal{M}_{i,p}^{ON} = a \cdot m_{i,p}^{corr,OFF} + f^{acc,ON} m_{i,p}^{acc,ON} + \mathcal{G}_p(A_i, \mu_i, \sigma_i) \tag{5.6}$$

where a is a free normalization parameter, encapsulating the difference in mean atmospheric pressure and reactor pool level as well as the run time difference between the ON and OFF periods. It may also compensate potential imperfections of the dead-time corrections.

Finally, all parameters of the PSD distribution models $(m_{i,p}^{acc,ON})_p$, $(m_{i,p}^{acc,OFF})_p$, $(m_{i,p}^{corr,OFF})_p$, a, A_i, μ_i, σ_i are fitted to ON_i^{acc}, OFF_i^{acc}, ON_i and OFF_i extracted PSD distributions, from a binned-likelihood maximization framework, implemented by considering the PSD bins statistics to be described by Poisson law, more appropriate to deal with bins with a low event rate. The extraction procedure is illustrated in Figure 5.8.

At last, let's note that no PSD cut to separate the electron- from the proton-recoils is used in the antineutrino signal extraction. Such cut only intervenes in the estimation of the background spectrum. Instead, for the signal extraction, it is replaced by constrained models describing the different contributions (signal and background) to the overall PSD spectrum.

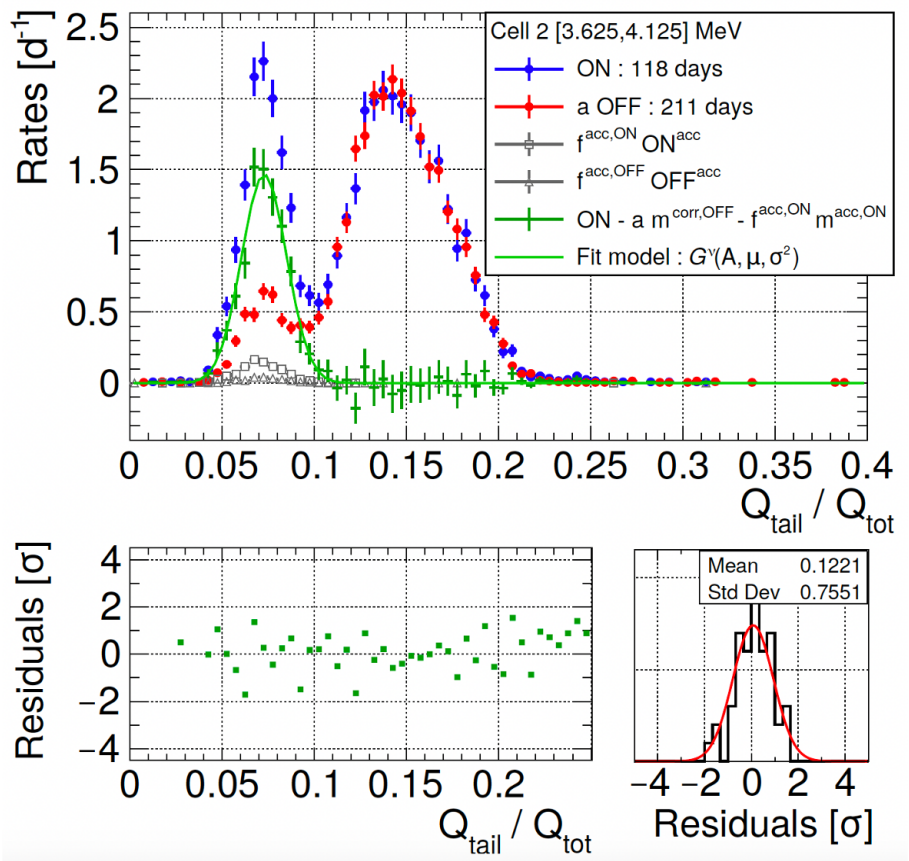

Figure 5.8: **Illustration of the IBD signal extraction, for TG cell 2 and Phase-II**. (Top) The ON pair rate (blue) is the sum of: correlated background pairs (red, rescaled from OFF data), accidental pairs (grey squares) and the IBD signal (green, modelled by a gaussian distribution whose integral gives the IBD rate). (Bottom) Residuals of the IBD signal fit (left) and their distribution (right). Source [75].

5.3.2 Reactogenic background

As already mentioned, the signal extraction method relies on the assumption of the pure cosmogenic origin for the correlated background, which is to be checked. To investigate a potential reactogenic component for the correlated background for Phase-II and -III, one compares the ON and OFF PSD distributions in the proton-recoil region, corrected for the atmospheric pressure and water pool level instead of fitting a relative normalization parameter.

Hints for an excess of events are found at low energy for the two phases, as shown in Figure 5.9. This excess is fitted by a power law which is used to correct the antineutrino rates for each reconstructed energy bin. The correction is at the few percents level, essentially below 3 MeV. Yet, the origin of this reactogenic background remains unclear. It may be produced by fast neutrons, inducing prompt proton recoils that would not fall in the electron recoil region of the IBD signal and therefore should not affect the extracted IBD rate. Consequently, a conservative 100% uncertainty is set on the correction of the extracted IBD rates coming from the evaluation of the reactogenic correlated background. It amounts to an energy-dependent systematic uncertainty on the extracted antineutrino

spectrum, with a few percents correction in the first energy bin then decreasing as a power law across the energy range.

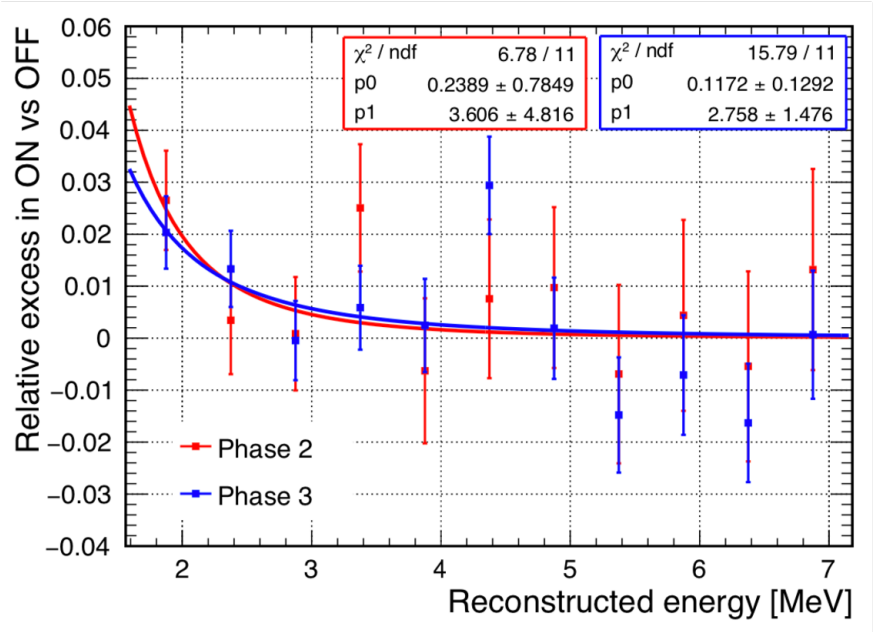

Figure 5.9: **Reactogenic component of correlated background**, evaluated from the proton-recoil regions of ON and OFF PSD distributions. A low-energy event excess is hinted below 3 MeV. The correction and uncertainty on the cellwise or targetwise antineutrino rates are propagated by taking into account the associated signal-to-background ratio.

5.3.3 Stability of the extracted antineutrino spectrum

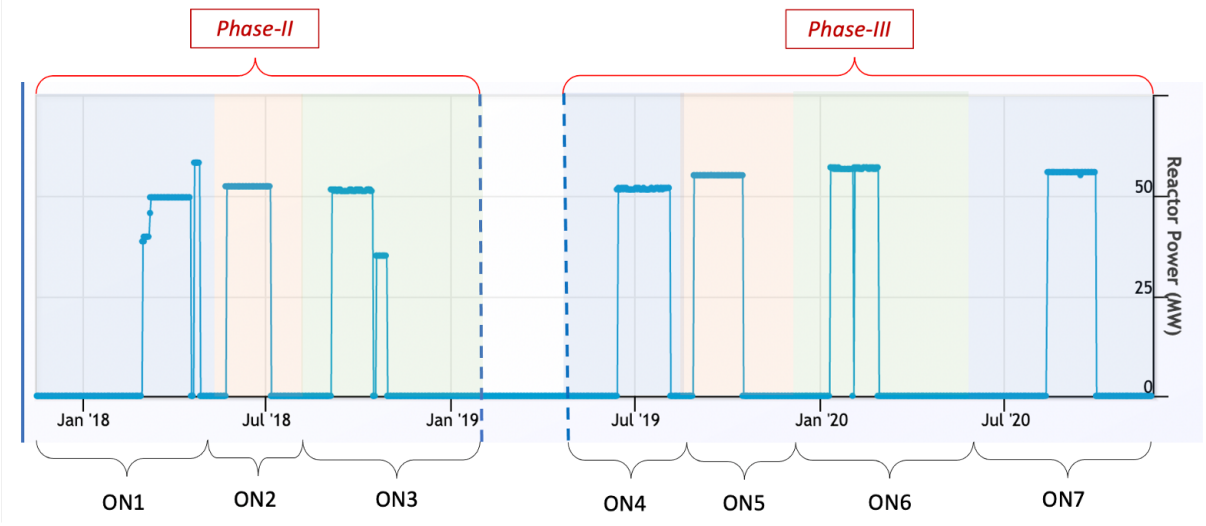

Figure 5.10: **Phase-II and -III reactor-ON periods**, consisting of 7 reactor cycles (3 for Phase-II and 4 for Phase-III).

To assess the stability of the extracted antineutrino spectrum, one merges the PSD spectrum of all TG cells, which allows to extract the spectrum at the target level for every reactor-ON period of Phase-II and Phase-III (see Figure 5.10), using for each the

closest reactor-OFF data sets. The observed fluctuations of the 7 spectra are found to be compatible with pure statistics, as shown in Figure 5.11, such that no time evolution systematic uncertainty is to be considered.

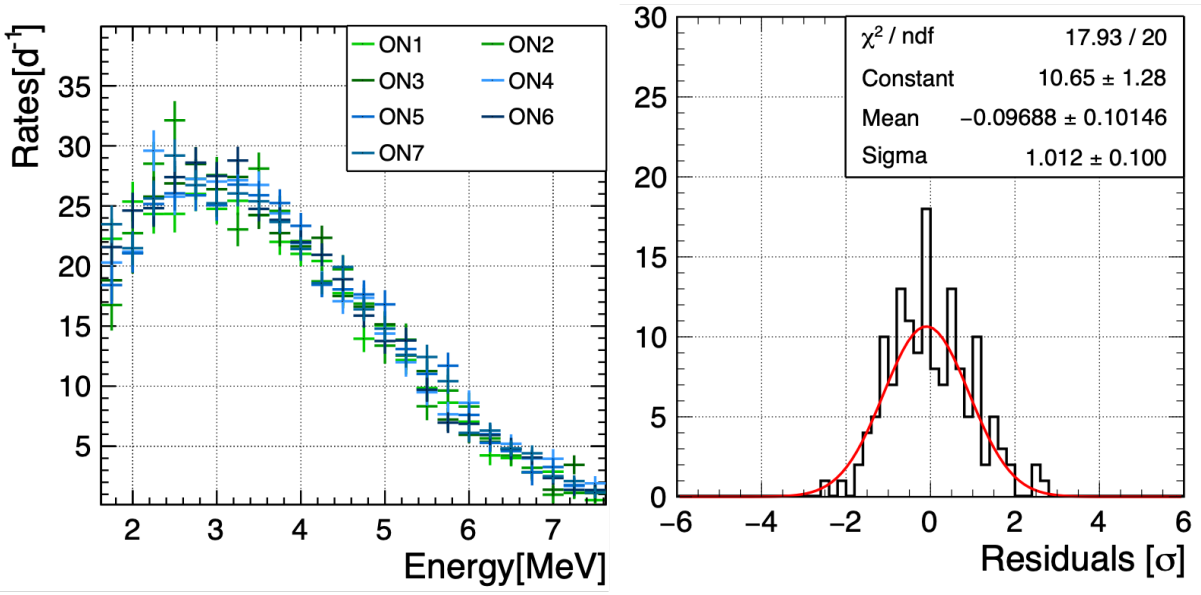

(a) (b)

Figure 5.11: **Time stability of the antineutrino spectrum**. (a) Target level antineutrino spectrum extracted for the 7 ON periods. (b) Residuals of the spectra with respect to the mean spectrum of Phase II+III, for all energy bins. Their are compatible with pure statistical fluctuations.

5.3.4 Signal-to-background ratio

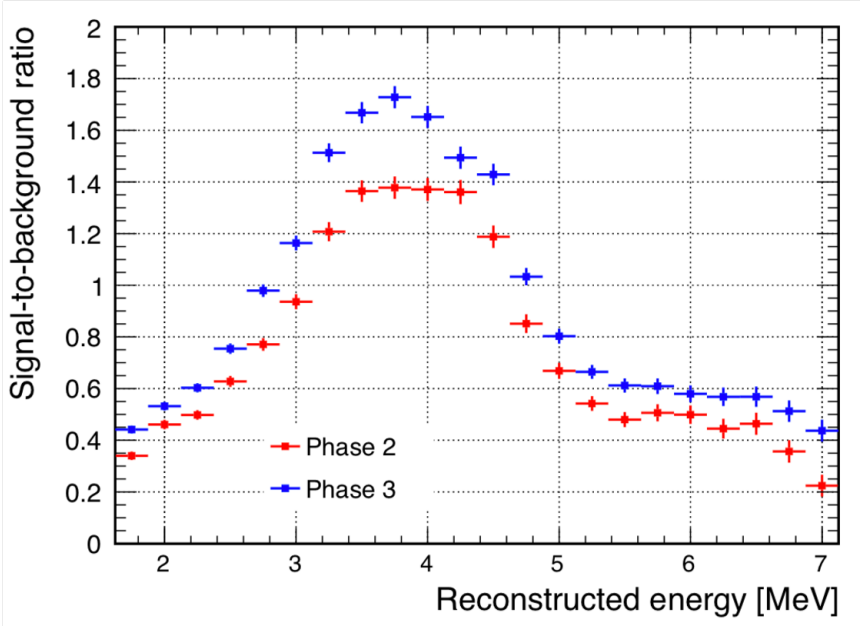

Figure 5.12: **Signal-to-background ratio**, at the target level for Phase-II and -III.

The target level signal-to-background ratio is displayed in Figure 5.12 for each phase. It is limited by the accidental background at low energy and by the vanishing intensity of the antineutrino signal at high energy. The average ratio is found to be 0.8 for Phase-II and 1.0 for Phase-III, the discrepancy being due to the difference in mean reactor powers between the two phases.

5.3.5 Selection cuts related systematic uncertainty

The systematic uncertainty induced by the selection cuts have been evaluated by a dedicated simulation across the reconstructed energy range for each TG cell [124]. To do so, one evaluates first the error of each selection cut observable. The error on the reconstructed energy can be obtained from the simulation as the difference between the true deposited energy and the energy that is effectively reconstructed. The error on the reconstructed barycenter X, calculated from the PMTs charge and the cell reconstructed energy, can be inferred by fluctuating the cell reconstructed energy within their uncertainties (neglecting the error in the PMTs charge). The error on the time of an event T is simply 4 ns, given by the DAQ sampling frequency.

Then, one compares the antineutrino spectrum obtained from the simulation with the spectrum obtained when varying the values of the selection cut observables within their uncertainties on an antineutrino event-by-event basis. The discrepancy between the two spectra is set to be the selection cuts related systematic uncertainty. Parameterized with a third order polynomial $p_0 + p_2(E_{rec} - 1.625)^2 + p_3(E_{rec} - 1.625)^3$, this uncertainty exhibits an increasing trend with energy up to $\sim 2\%$ in the last energy bin (see Figure 5.13). It is fully correlated between cells and phases.

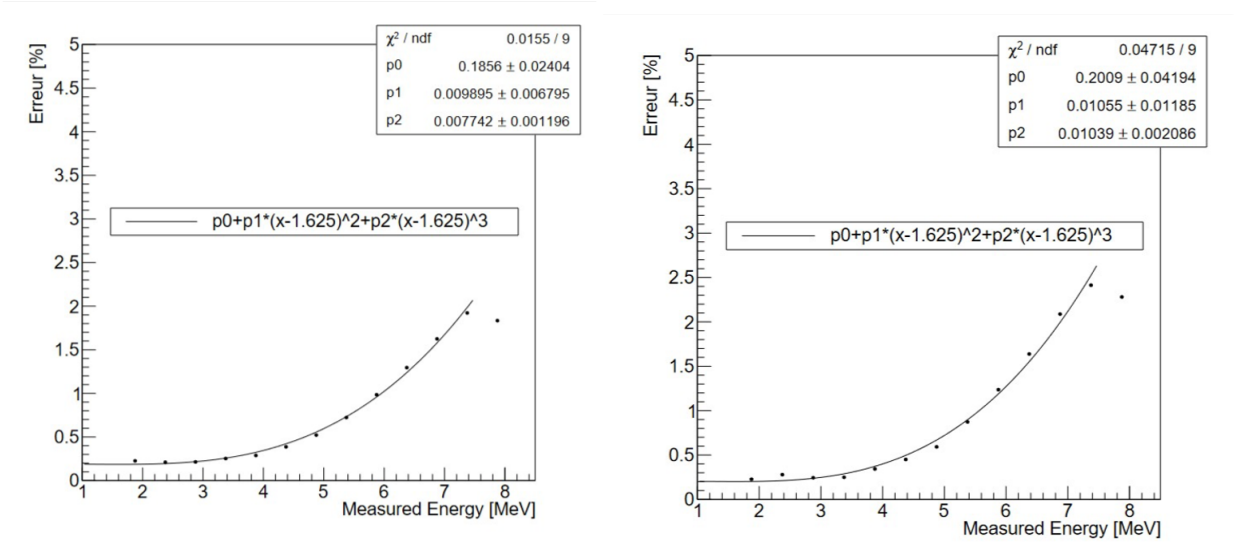

(a) Phase-II (b) Phase-III

Figure 5.13: **Selection cuts related systematic uncertainty**, for Phase-II and -III.

5.4 Spectrum normalization

As the detection channel used by STEREO is the IBD reaction, the absolute number of detected antineutrinos in the detector TG volume is directly proportional to the proton number of the target liquid scintillator n_p, and to the detection efficiency of the delayed neutron signal used to tag the IBD candidates ε_d. We discuss first the corrections that were derived to account for the measurement-to-simulation discrepancies of these two quantities in order to accurately normalize the STEREO antineutrino spectrum to cm^2/fission units. The normalization factor to be applied to the spectrum will then be laid out.

5.4.1 Proton number

n_p depends on the target liquid mass m, the hydrogen fraction f_H and the hydrogen mass m_H:

$$n_p = \frac{f_H \cdot m}{m_H} \tag{5.7}$$

The liquid mass and hydrogen fraction have been measured to be: $m = (1602 \pm 2)$ kg and $f_H = (11.45 \pm 0.11)\%$ [73], whereas the hydrogen mass reads $m_H = 1.673533 \cdot 10^{-27}$g, with a fully negligible uncertainty with respect to the others. Therefore, the total proton number as given by the measurement is: $n_p = (1.096 \pm 0.011) \cdot 10^{29}$, with a 1% associated uncertainty.

In the simulation, n_p is calculated from the vessel volumes, the densities of the solvents and the chemical composition of all the liquid scintillator components. However, the main component (LAB solvent at 73%, see Section 2.2.2) does not have a well-defined molecular formula, such that approximated values are used for the number of hydrogen and carbon atoms per molecule in the Monte-Carlo to match the average molecular mass specified by the supplier. Moreover, the cell volumes are known with an uncertainty of 0.83%, uncorrelated between cells. Taking all factors into account, a correction factor $c_p = 0.983 \pm 0.010$ is applied in the normalization of the simulated antineutrino spectrum [75].

5.4.2 Detection efficiency of the delayed neutron

To evaluate the detection efficiency of the delayed neutron, the ^{241}Am-^{9}Be source, producing correlated (γ, n) pairs mimicking IBD events, is deployed at five different heights in each the target cell.

All selection cuts of the delayed signal described in Table 5.1 are applied, except the 600 mm distance between the prompt and delayed vertices, not relevant for this study. The resulting amount of (γ, n) pairs is then compared to a sample without these cuts, giving the detection efficiency of the delayed neutron for measured and simulated events.

The (X, Z) spatial dependence of the efficiency is well reproduced in the simulation up to a $\sim$1.5% data-to-simulation discrepancy, as visible in Figure 5.14. Assuming the same behaviour in the two horizontal dimensions (X and Y), a 3D spatial model of the efficiency $\varepsilon_{\mathrm{n}}(X, Y, Z)$ is built by fitting the Am-Be points in data or simulation. The position-dependent correction coefficient of the efficiency may then be calculated as:

$$c_{\mathrm{n}}(X, Y, Z) = \frac{\varepsilon_{\mathrm{n}}^{\mathrm{data}}(X, Y, Z)}{\varepsilon_{\mathrm{n}}^{\mathrm{MC}}(X, Y, Z)} \tag{5.8}$$

Integrating $c_{\mathrm{n}}(X,Y,Z)$ over each cell volume, one derives the correction coefficient associated to the normalization of the spectrum of each target cell. For Phase-II and -III, the cell-averaged coefficients $\overline{c_{\mathrm{n}}}$ and their uncertainties read:

$$\overline{c_{\mathrm{n}}} = \begin{array}{c} 0.9824 \pm 0.0063\ [\mathrm{uncorr}] \pm 0.0019\ [\mathrm{corr}]\ (\mathrm{Phase\text{-}II}) \\ 0.9847 \pm 0.0063\ [\mathrm{uncorr}] \pm 0.0027\ [\mathrm{corr}]\ (\mathrm{Phase\text{-}III}) \end{array} \tag{5.9}$$

where part of the uncertainty is correlated [corr] between cells (change in $\varepsilon_{\mathrm{n}}^{\mathrm{MC}}$ due to quality of subtraction of accidental pairs, discrepancies on $\overline{c_{\mathrm{n}}}$ due to the choice of the 3D spatial model) and part is uncorrelated [uncorr] between cells (statistical error on ε_{n} measurements, uncertainty on the positions of the Am-Be source in each calibration tube). Almost all cellwise uncertainties are fully correlated between phases, except for the statistical uncertainties of the fits, leading to a correlation coefficient of 0.92 between Phase-II and -III.

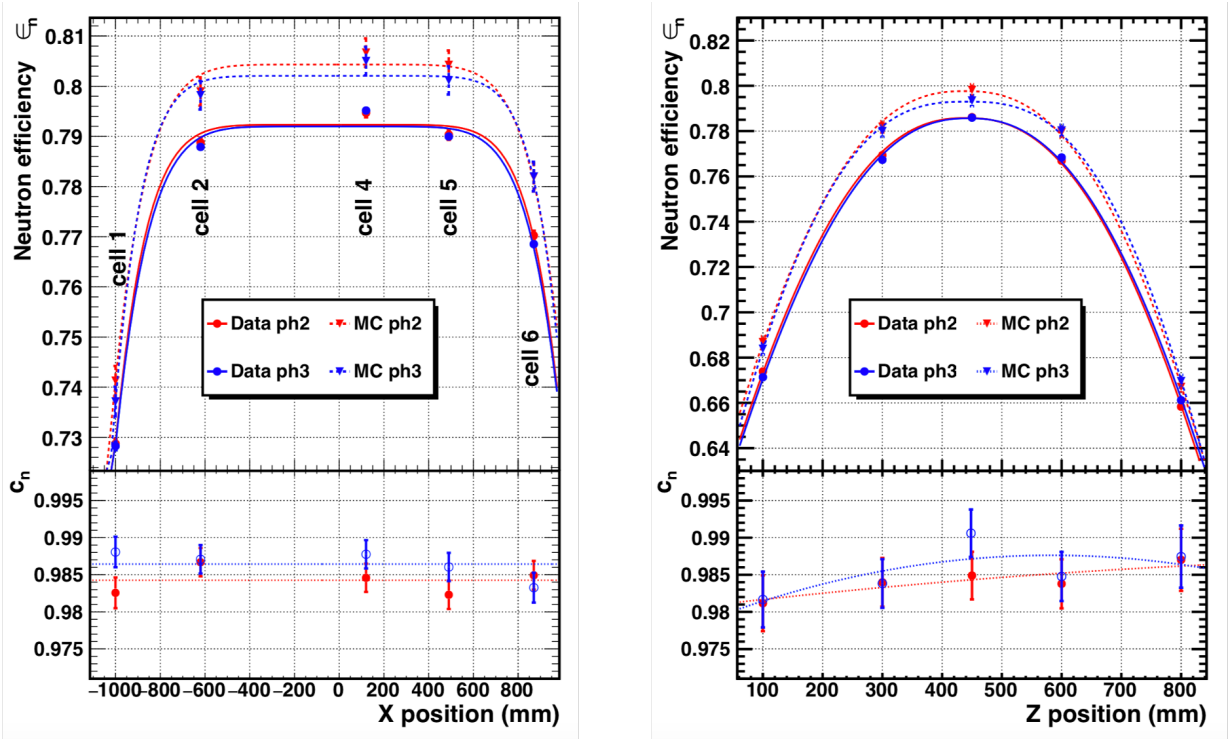

(a) (b)

Figure 5.14: **Delayed neutron detection efficiency**. Top panels: ε_{n} obtained with the Am-Be source as function of (a) horizontal and (b) vertical position for Phase-II (red) and Phase-III (blue). Measured efficiencies are shown as circles and simulated values as triangles. A fitted 3D spatial model gives a continuous description of the efficiency in the detector for data $\varepsilon_{\mathrm{n}}^{\mathrm{data}}(X,Y,Z)$ (solid lines) and simulation $\varepsilon_{\mathrm{n}}^{\mathrm{MC}}(X,Y,Z)$ (dashed lines). Bottom panels: coefficient $c_{\mathrm{n}} = \varepsilon_{\mathrm{n}}^{\mathrm{data}}/\varepsilon_{\mathrm{n}}^{\mathrm{MC}}$ used to correct for efficiency biases. It is consistent with a constant function of X and a second order polynomial in Z; the difference in the integrated $\overline{c_{\mathrm{n}}}$ coming from the choice of a (X,Y,Z) model for c_{n} is propagated as a systematic uncertainty.

5.4.3 Normalization factor

It can be shown [125, 126] that the normalization factor to be applied to the detected antineutrino spectrum expressed in day^{-1} can be written as:

$$\mathcal{N} = \frac{\langle E_f \rangle}{\langle P_{th} \rangle} \times \frac{\langle \sigma_{IBD} \rangle}{\tau_{int}} \times \frac{1}{c_p \cdot c_n} \tag{5.10}$$

where:

- $\langle E_f \rangle = (203.41 \pm 0.26)$ MeV/fission is the mean energy released per fission,
- $\langle P_{th} \rangle = 2.65 \cdot 10^{25}$ (Phase-II) / $2.92 \cdot 10^{25}$ (Phase-III) MeV/day is the mean reactor thermal power for Phase-II and -III,
- $\langle \sigma_{IBD} \rangle = 3.657 \cdot 10^{-43}$ cm^2 is the averaged IBD cross section, weighted by the total flux model of the ILL reactor (see Equation 3.1) normalized to unity,
- $\tau_{int} = 8.10 \cdot 10^{-21}$ [unitless] is the fraction of antineutrinos interacting in the whole detector, accounting for solid angle and detector proton number in particular,
- c_p and c_n [unitless] are respectively the corrections to the proton number and delayed neutron detection efficiency.

A quick dimensional analysis shows that $\mathcal{N}$ has units of cm$^2 \cdot$ day/fission, as expected.

The associated uncertainty on the reactor power has been evaluated to be 1.44% [127], partially correlated between phases with a correlation coefficient of 0.46. The uncorrelated part comes from calibration uncertainties that were derived from dedicated calibration campaigns during both phases and, therefore, are not correlated.

The uncertainty on τ_{int} mainly comes from the solid angle uncertainty, assessed at the 0.50% level, fully correlated between phases.

Chapter 6

STEREO lights on the reactor anomalies

In this Chapter, the extracted antineutrino spectrum for each target cell will be used to investigate the oscillation to a sterile neutrino as an explanation to the Reactor Antineutrino Anomaly. In a second time, the antineutrino spectrum reconstructed at the detector level will provide the measurement of the ^{235}U fission induced antineutrino spectrum, that is to be expressed in true antineutrino energy instead of reconstructed energy. In this purpose, we present the unfolding framework that has been developed during this doctoral thesis. It allows to deconvolve the measured antineutrino spectrum and to perform unbiased shape comparison of the unfolded spectrum with any prediction, a relevant feature for the accurate investigation of the shape anomaly.

6.1 Sterile neutrino search

6.1.1 Principle

The principle of the oscillation analysis for the sterile neutrino search relies on a relative comparison of the antineutrino spectra reconstructed in the different target cells of the STEREO detector. They directly provide a measurement of the (electronic) antineutrino spectrum at different baselines from the reactor core, therefore allowing to probe an oscillation signal from the distortions induced on the spectra, cellwise. As already shown in the introductory chapter, the expression of the survival probability P_{ee} of the electronic antineutrino as a function of its energy E and the distance between the emission and detection vertices L reads:

$$P_{ee} = 1 - \sin^2(2\theta_{ee}) \sin\left(\frac{\Delta m^2_{41}}{4E} L\right) \tag{6.1}$$

This expression is only valid at short baseline from the reactor core (which is the case of STEREO) where the atmospheric and solar oscillations can be neglected. $\sin^2(2\theta_{ee})$ is the amplitude of the mixing, that drives the value of the observed deficit of electronic antineutrinos at short baseline, and Δm^2_{41} is the mass-square splitting parameter between sterile and standard neutrino states. $\frac{\Delta m^2_{41}}{4E}$ can be interpreted as an energy-dependent oscillation frequency.

In an oscillation scenario, i.e. $(\sin^2(2\theta_{ee}), \Delta m^2_{41}) \neq (0, 0)$, the measured (electronic) antineutrino spectrum will exhibit a global deficit shared between cells with respect to the no-oscillation scenario due to the non-zero value of $\sin^2(2\theta_{ee})$, as well as cell-to-cell relative

spectral distortions due to the non-zero value of the energy-dependent oscillation frequency $\frac{\Delta m^2_{41}}{4E}$. These features are illustrated in the example Figure 6.1.

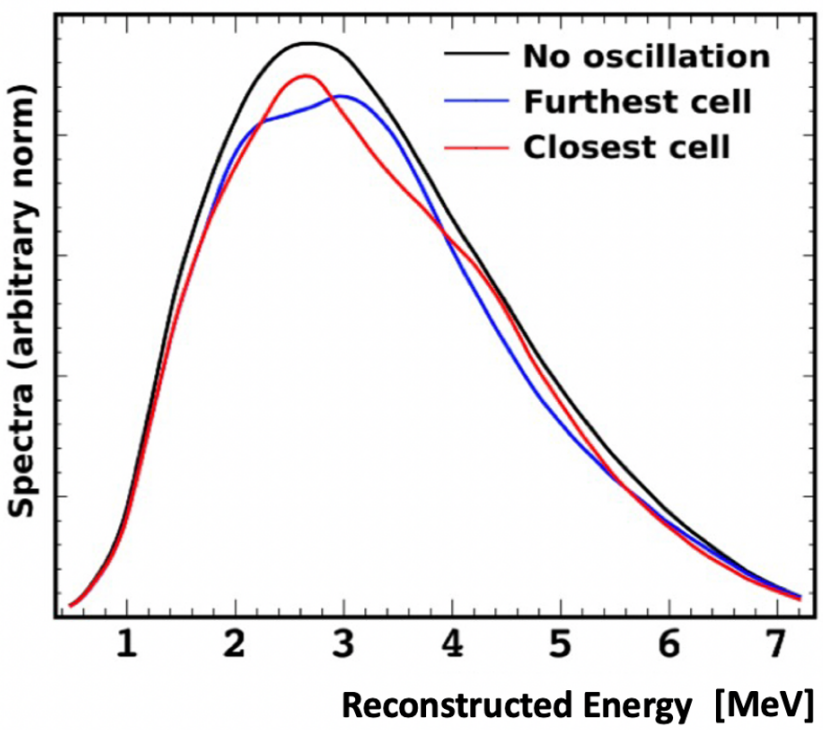

Figure 6.1: **Example of the distortion in the cellwise antineutrino spectra, induced by the RAA best-fit oscillation parameters**. Cell-to-cell relative spectral distortions, as well as an overall deficit, similar to that of the RAA, are the signature of an oscillation signal.

In the practical case of the STEREO experiment, the antineutrino spectra extracted for the 6 detector TG cells are binned in 11 500 keV-wide energy bins ranging from 1.625 to 7.125 MeV in reconstructed energy, for Phase-II and -III respectively. They are fitted to the spectra predicted by an oscillation scenario by minimizing the following χ^2:

$$\begin{aligned}
&\chi^2\left(D|\sin^2(2\theta_{ee}),\Delta m^2_{41};\phi_i,\alpha_j\right) = \\
&\sum_{p=\mathrm{II}}^{\mathrm{III}}\sum_{l=1}^{6}\sum_{i=1}^{11}\left(\frac{D_{p,l,i}-\phi_i\,M_{p,l,i}(\sin^2(2\theta_{ee}),\Delta m^2_{41};\alpha_j)}{\sigma_{p,l,i}}\right)^2 \\
&\quad+\sum_{l=1}^{6}\left(\frac{\alpha_l^{\mathrm{EscaleU}}}{\sigma_l^{\mathrm{EscaleU}}}\right)^2+\left(\frac{\alpha_l^{\mathrm{NormU}}}{\sigma_l^{\mathrm{NormU}}}\right)^2+\left(\frac{\alpha_l^{\mathrm{ReactBg}}}{\sigma_l^{\mathrm{ReactBg}}}\right)^2 \\
&\quad+\left(\frac{\alpha^{\mathrm{EscaleC}}}{\sigma^{\mathrm{EscaleC}}}\right)^2+\left(\frac{\alpha^{\mathrm{Cuts}}}{\sigma^{\mathrm{Cuts}}}\right)^2+\left(\frac{\alpha^{\mathrm{II\ VS\ III\ norm}}}{\sigma^{\mathrm{II\ VS\ III\ norm}}}\right)^2
\end{aligned} \tag{6.2}$$

where $D_{p,l,i}$ stands for the measured IBD rate in the i-th energy bin of cell number l for Phase p, $M_{p,l,i}(\sin^2(2\theta_{ee}),\Delta m^2_{41},\alpha_j)$ is the predicted IBD rate in the corresponding bin for the sterile neutrino oscillation parameters $(\sin^2(2\theta_{ee}),\Delta m^2_{41})$, and α_j are the nuisance parameters encoding the systematic uncertainties on the spectra. The amplitude of these uncertainties have all been discussed in previous sections. They are encoded in the σ_j and were found to be at the percent or sub-percent level. Some are uncorrelated between cells: uncertainty on the energy scale $\alpha_l^{\mathrm{EscaleC}}$ (Section 4.4.3), uncorrelated part of the normalization uncertainty $\alpha_l^{\mathrm{NormU}}$ originating from deviations of the cells' volume from the

design geometry as well as from variations of the neutron detection efficiency (Section 5.4), reactogenic background uncertainty $\alpha_l^{\text{ReactorBg}}$ (Section 5.3.2). The remaining part is correlated between cells: time stability of the energy scale α^{EscaleU} (Section 3.2.3), selection cuts α^{Cuts} (Section 5.3.5), relative normalization of phases $\alpha^{\text{II vs III norm}}$ driven by the difference in reactor thermal power (Section 5.4.3). All systematic uncertainties are summarized in Table 6.1.

The ϕ_i variables, one per each energy bin, apply a cell-independent correction to the predicted spectra of each cell $M_{p,l,i}$, thus absorbing all absolute rate information per energy bin i and making the analysis independent of the spectrum prediction.

The statistical uncertainty $\sigma_{p,l,i}$ is parameterized as a function of the expected number of signal events (and not the number of measured events). According to Equation 6.2, this number depends on the values of ϕ_i and the oscillation parameters. It is estimated from simulation under real conditions of background rate and spectral shape [99].

Type	Source	Nuisance parameter	Uncertainty	Correlations		
				Energy	Cell	Phase
Energy scale	Energy reconstruction	$\alpha_l^{\text{EscaleC}}$	1%	1	0	1
	Time stability	α^{EscaleU}	0.25%	1	1	0
Signal	Selection cuts	α^{Cuts}	0% to 2%	1	1	1
	Reactor background	$\alpha_l^{\text{ReactorBg}}$	5% to 0%	1	0	1
Normalization	Relative cell volume	α_l^{NormU}	0.83%	1	0	1
	Neutron efficiency		0.63%	1	0	0.92
	Relative norm ph-2/ph-3	$\alpha^{\text{II vs III norm}}$	1.5%	1	1	-

Table 6.1: **Systematic uncertainties for the oscillation analysis.** The two values reported for the selection cuts and the reactor background related systematics correspond to the extremal values of the systematic uncertainties over the entire reconstructed energy range. The values reported in the three last columns are the correlation coefficients associated to each systematic uncertainty, respectively between reconstructed energy bins, between target cells and between phases.

6.1.2 Test statistic

The goal of the oscillation analysis is to discriminate between various oscillation scenarii. For instance, let's consider for a given data set D a reference or null hypothesis, say $H_0 = \left\{\sin^2(2\theta^0_{ee}), \Delta^0 m^2_{41}\right\}$, that is to be tested against an alternative hypothesis $H_\alpha = \left\{\sin^2(2\theta^\alpha_{ee}), \Delta^\alpha m^2_{41}\right\}$. We briefly present here two statistical analyses that have been implemented within the STEREO collaboration for the sterile neutrino search [84].

2D Feldman-Cousins approach

One defines the type-I error as the error of rejecting H_0 whereas it should have not been rejected, and the type-II error as the error of failing to reject H_0 whereas it should have been rejected. The latter is typically the error that is to be minimized in the analysis.

According to Neyman–Pearson lemma [128], the likelihood ratio test statistic is the one that minimizes the type-II error probability. In terms of χ^2, it amounts to computing the subsequent quantity, which is nothing but twice the log of the likelihood ratio:

$$\Delta\chi^2(D) = \chi^2(D|H_0) - \chi^2(D|H_\alpha) \tag{6.3}$$

where $\chi^2(D|H_0)$ and $\chi^2(D|H_\alpha)$ are the values of the χ^2 of Equation 6.2 minimized over $\{\phi_i, \alpha_j\}$, at fixed oscillation parameters.

The Feldman-Cousins prescription suggests to take as an alternative hypothesis the oscillation scenario that minimizes the χ^2 in the 2D $\left\{\sin^2(2\theta_{ee}), \Delta m^2_{41}\right\}$ plan [129]: $H_\alpha = H_{bestfit}$. Should the Wilks theorem [130] apply, the $\Delta\chi^2$ defined in Equation 6.3 would converge, in the large sample limit, to a χ^2-distribution if the null hypothesis happens to be true.

However, as discussed in [131, 132, 133], the regularity conditions required by the Wilks theorem are not *a priori* met in regular sterile neutrino search analysis. First, there is a physical boundary for the mixing angle, which is set to be positive. Second, the mass-square splitting parameter becomes undefined and unphysical when the mixing angle tends to 0 and vice-versa. Third, the cosine dependence on the mass-square splitting of the oscillation probability leads to a strong non-linear behavior.

In a note written with the PROSPECT collaboration [134], STEREO reported significant deviations to the Wilks theorem, by comparing the $\Delta\chi^2$ distribution obtained by a Monte-Carlo simulation of Phase-II pseudo-data generated under the no-oscillation hypothesis with the Wilks-predicted χ^2 distribution (see Figure 6.2). The pseudo-experiments were produced by taking the non-oscillated predicted spectrum in each cell and independently fluctuating each energy bin according to a normal distribution whose standard deviation is the statistical uncertainty of the bin $\sigma_{p=II,l,i}$. Variations within the systematic uncertainties were also included. For this test case, the median $\Delta\chi^2$ of simulated MC distribution happened to correspond to a 90% confidence level under Wilks theorem assumption. In other words, in absence of oscillation, data interpreted through Wilks theorem would disfavor the null oscillation hypothesis at 90% C.L. half of the time, thus providing a strong signature of biased results due to improper statistical treatment.

Consequently, the $\Delta\chi^2$ distribution required for the statistical analysis of a given hypothesis $\{\sin^2(2\theta_{ee}), \Delta m^2_{41}\}$ is systematically computed by generating a set of Phase II+III 10^4 pseudo-data. Denoting $\Delta\chi^2_{obs}$ the value of Equation 6.3 observed in data, the oscillation hypothesis is excluded at the α confidence level if $\mathbb{P}\left(\Delta\chi^2 \geq \Delta\chi^2_{obs}|H_0\right) \leq 1-\alpha$.

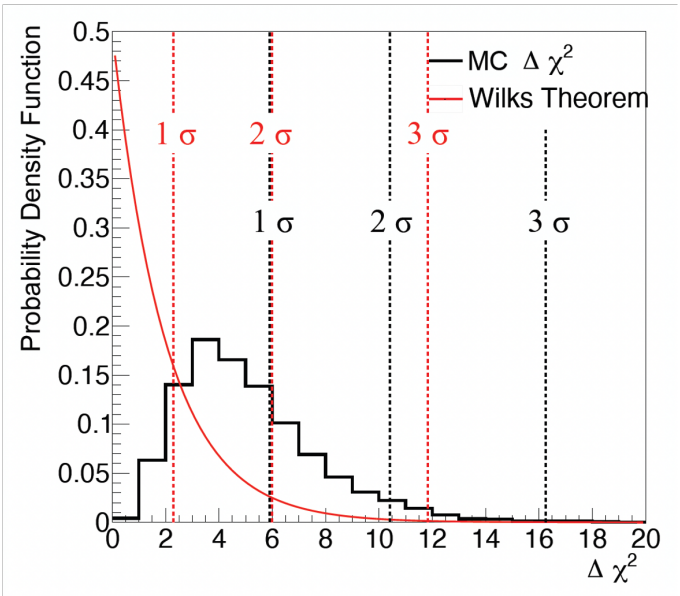

Figure 6.2: **Phase-II Monte-Carlo generated $\Delta\chi^2$ distribution compared to the Wilks theorem predicted values for the no-oscillation hypothesis.** Also shown, as red and black vertical dashed lines, are 1, 2, and 3σ values for the standard χ^2 and data-generated $\Delta\chi^2$ respectively. Assigning significance based on standard χ^2 leads to significantly biased results. Source [134].

CLs approach

In the signal confidence level (CL_s) approach [135, 136], the alternative hypothesis for the $\Delta\chi^2$ statistics is merely a reference hypothesis to be chosen. This is a more favorable case as far as computational cost is concerned, given that it does not require to find the global minimum in the 2D oscillation parameters plane for each pseudo-experiment that is generated. In the case of sterile neutrino search, the natural reference is the no-oscillation hypothesis H_{NoOsc}, such that the test statistic now reads:

$$\Delta\chi^2(D) = \chi^2(D|H_0) - \chi^2(D|H_{NoOsc}) \tag{6.4}$$

One then generates the probability density function (p.d.f.) of $\Delta\chi^2$ under the assumption that the oscillation (resp. no-oscillation) hypothesis is true. Denoting $\Delta\chi^2_{obs}$ the value of Equation 6.4 observed in data, one computes the CL_s observable as:

$$CL_s = \frac{CL_{s+b}}{CL_b} \tag{6.5}$$

where:

$$\begin{cases} CL_{s+b} = \mathbb{P}\left(\Delta\chi^2 \geq \Delta\chi^2_{obs}|H_0\right) \\ CL_b = \mathbb{P}\left(\Delta\chi^2 \geq \Delta\chi^2_{obs}|H_{NoOsc}\right) \end{cases}$$

CL_b (resp. CL_{s+b}) measures the consistency with the no-oscillation hypothesis (resp. oscillation hypothesis that is tested).

The oscillation hypothesis is excluded at the α confidence level if $CL_s \leq 1-\alpha$. The construction of CL_s ensures that even if CL_{s+b} is small, indicating disagreement with the four-flavor hypothesis, this hypothesis can only be excluded when CL_b is large, indicating consistency with the three-flavor hypothesis. Thus, the CL_s construction ensures that the four-flavor hypothesis can only be excluded if the experiment is sensitive to it [137].

6.1.3 Exclusion limits

The 95% confidence level (C.L.) exclusion contour derived from the two frameworks for Phase-II and -III data are displayed in Figure 6.3. In both approaches, the exclusion sensitivity contour is obtained by replacing the data with the non-oscillated prediction. As expected, the exclusion contours oscillate around the sensitivity.

A significant part of the favoured region for the RAA is rejected by STEREO data. Additionally, we find that the best-fit point of the oscillation signal reported by the Neutrino-4 collaboration [138] is excluded with 3.3σ significance. We also observe that our data are compatible with the no-oscillation hypothesis with a p-value of 0.52. Thus, a few eV mass sterile neutrino explanation to the Reactor Antineutrino Anomaly is ruled out by STEREO data. Other experiments reach the same conclusion [114, 139].

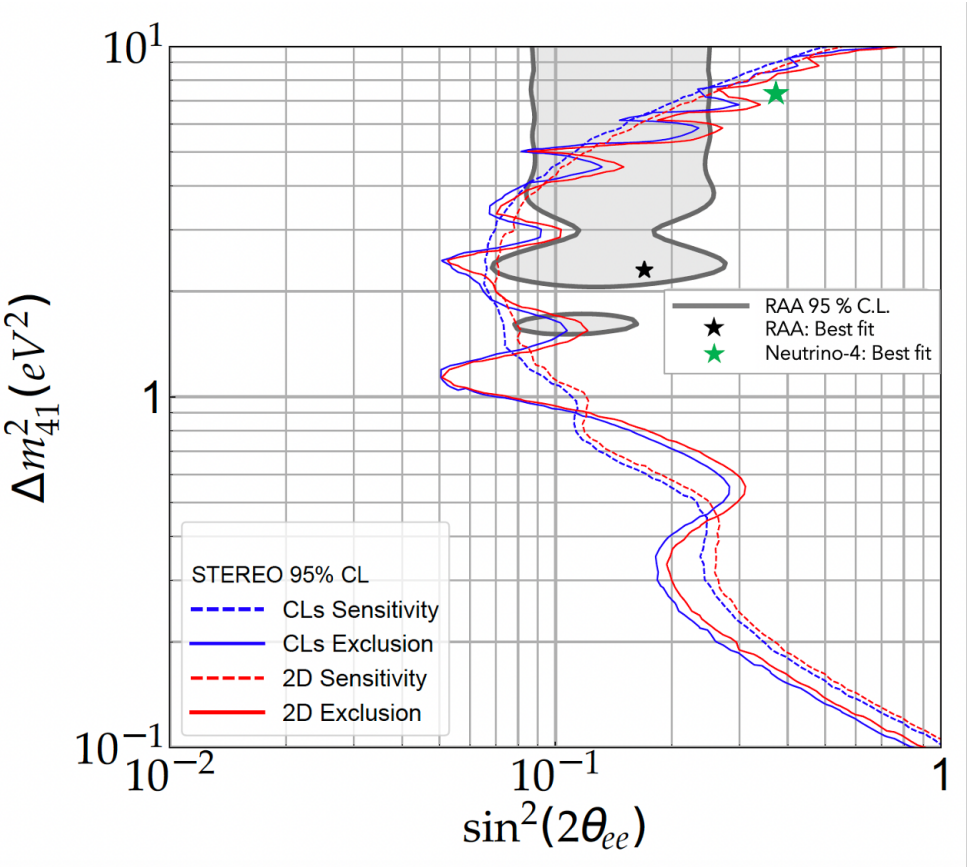

Figure 6.3: **2σ exclusion contour for the STEREO oscillation analysis, in the 2D Feldman-Cousins (red) and CL_s (blue) approaches**. Both frameworks yield consistent exclusion contours (solid lines) and sensitivity contours (dashed lines). High values of $\sin^2(2\theta_{ee})$ are excluded (right of the exclusion curve). The 95% C.L. parameter space regions of the sterile neutrino as an explanation of the RAA (grey area) is rejected by STEREO below mass splittings of 4 eV^2. The initial RAA best fit point, marked by a black star, is rejected with very high confidence level (p-value $< 10^{-4}$). The Neutrino-4 best-fit point [138], marked by a green star, is excluded at the 3.3σ level.

6.2 Unfolding of STEREO ^{235}U spectrum

The rejection of the oscillation hypothesis in the previous section justifies the merging of the IBD signal of all TG cells and opens the door to the measurement of the ^{235}U fission induced antineutrino spectrum, with optimal statistical accuracy. In the subsequent sections, we will then work with the TG level antineutrino spectrum and aim at unfolding this spectrum from reconstructed energy space to true antineutrino energy space. The latter is the only energy space that is common to all measurements and predictions.

6.2.1 Inputs

6.2.1.1 Predicted spectrum

As laid out in the introductory chapter, several methods exist to predict the ^{235}U antineutrino spectrum, that can be categorized in either conversion method or summation method. In the following, the prediction that will be used is the Huber ^{235}U model, derived from Huber's conversion method. To this end, one parameterizes the ^{235}U fission induced antineutrino flux [fission^{-1} · MeV^{-1}] with the fifth order polynomial reported in Huber's publication [55]. To derive the prediction for the detected ^{235}U antineutrino spectrum, we multiply this flux with the finely-binned IBD cross-section [cm^2] derived by Strumia and Vissani [46, 140]. The resulting Huber ^{235}U predicted spectrum is reported in Figure 6.4, in 50 keV-wide energy bins, ranging from 1.875 MeV (lower edge of first bin) to 8.125 MeV (upper edge of last bin) in antineutrino energy space. It is expressed in cm^2/fission/MeV.

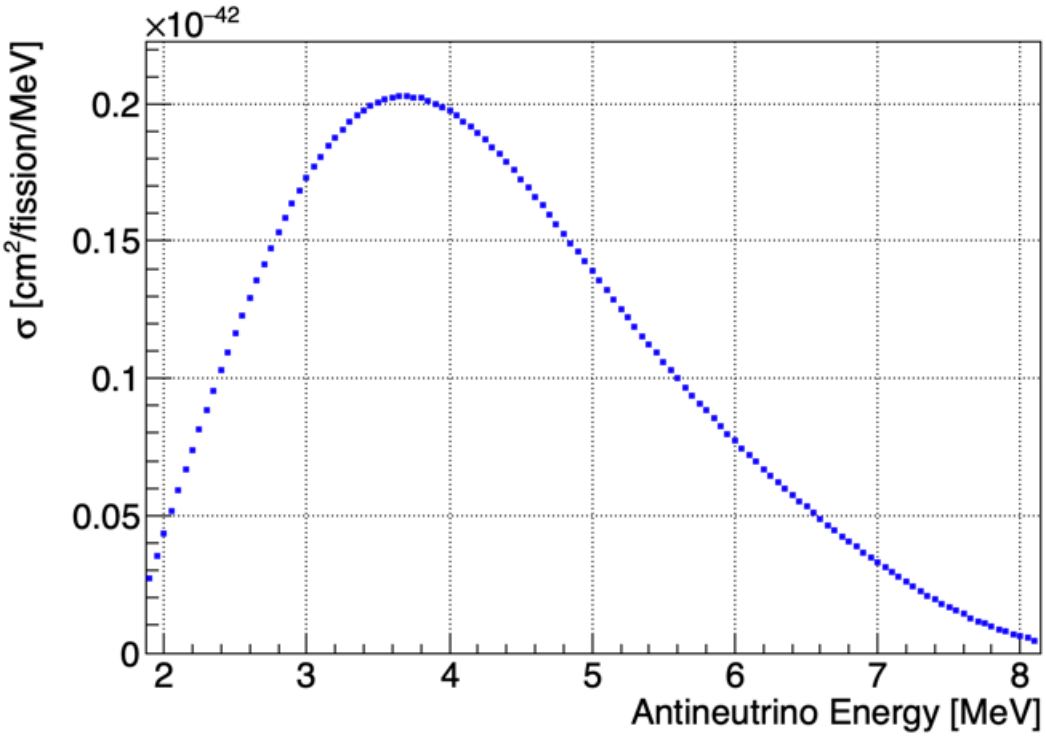

Figure 6.4: **Huber ^{235}U predicted antineutrino spectrum**, reported in 50-keV wide antineutrino energy bins spanning [1.875, 8.125]MeV.

6.2.1.2 Response matrix

Definition

To unfold the measured antineutrino spectrum from reconstructed energy to antineutrino energy space, we need to connect the two spaces via a detector response model for Phase-II and -III. To this end, we build the so-called detector response matrices as follows: one generates reactor antineutrino events, distributed according to a flat antineutrino energy spectrum, in the STEREO detector simulation corresponding to each phase (see Section 3.1.1.2) and apply the IBD selection cuts (see Section 5.1). The simulation provides us with the reconstructed energy on an event-by-event basis, such that, for each phase, one can build the acceptance response matrix element $\mathcal{R}_p^{ij}$ as the fraction of antineutrinos events with energy $E_{\bar{\nu}}$ in a given true energy bin $[E_{\bar{\nu}}^j - \frac{\Delta E_{\bar{\nu}}^j}{2}, E_{\bar{\nu}}^j + \frac{\Delta E_{\bar{\nu}}^j}{2}]$ that effectively passed the selection cuts and gave a reconstructed energy $E_{rec,p}$ in a certain reconstructed energy bin $[E_{rec,p}^i - \frac{\Delta E_{rec,p}^i}{2}, E_{rec,p}^i + \frac{\Delta E_{rec,p}^i}{2}]$. It is nothing but the transition probability to get the reconstructed energy given an incident antineutrino energy:

$$\mathcal{R}_p^{ij} = \mathbb{P}\left(E_{rec} \in \left[E_{rec,p}^i - \frac{\Delta E_{rec,p}^i}{2}, E_{rec,p}^i + \frac{\Delta E_{rec,p}^i}{2}\right] \;\middle|\; E_{\bar{\nu}} \in \left[E_{\bar{\nu}}^j - \frac{\Delta E_{\bar{\nu}}^j}{2}, E_{\bar{\nu}}^j + \frac{\Delta E_{\bar{\nu}}^j}{2}\right]\right) \tag{6.6}$$

where p stands for the phase number (II or III). Each column of the response matrix encodes the energy-dependent smearing due to the detection process. Furthermore, for each antineutrino energy bin, one can extract the reconstructed energy most probable value E_{rec}^{MPV}, from a local second order polynomial fit in the vicinity of the maximum of the reconstructed energy probability distribution encoded in each response matrix column. Comparing this value to the true prompt energy $E_{pr} = E_{\bar{\nu}} - 0.782[\text{MeV}]$ as a function of the antineutrino energy $E_{\bar{\nu}}$, one retrieves the typical trend of the quenching effect (see Figure 6.5). This shows that all detection effects (e.g. resolution, non-linearity of the energy reconstruction) are included in the response matrix.

Selection efficiency

Noticeably, with the definition of Equation 6.6, the columns of the acceptance response matrix are by construction normalized to the selection efficiency:

$$\varepsilon_p^j = \mathbb{P}\left(E_{rec} \in [1.625, 7.125]\,\text{MeV} \mid E_{\bar{\nu}} \in \left[E_{\bar{\nu}}^j - \frac{\Delta E_{\bar{\nu}}^j}{2}, E_{\bar{\nu}}^j + \frac{\Delta E_{\bar{\nu}}^j}{2}\right]\right) = \sum_i \mathcal{R}_p^{ij} \tag{6.7}$$

It is smaller than 1 given that there is a chance that an interacting antineutrino with given energy $E_{\bar{\nu}}$ is rejected by selection cuts. With this choice of normalization, all selection related effects are encapsulated in the response matrix, on top of detection effects.

The acceptance response matrices of Phase-II and -III are generated in the fine true antineutrino energy binning of the predicted spectrum and in the coarse reconstructed energy binning of the measured spectrum. The selection efficiencies of Phase-II and -III are displayed in Figure 6.6. They are nigh-identical, as expected from the stability of the energy reconstruction procedure during Phase-II and -III.

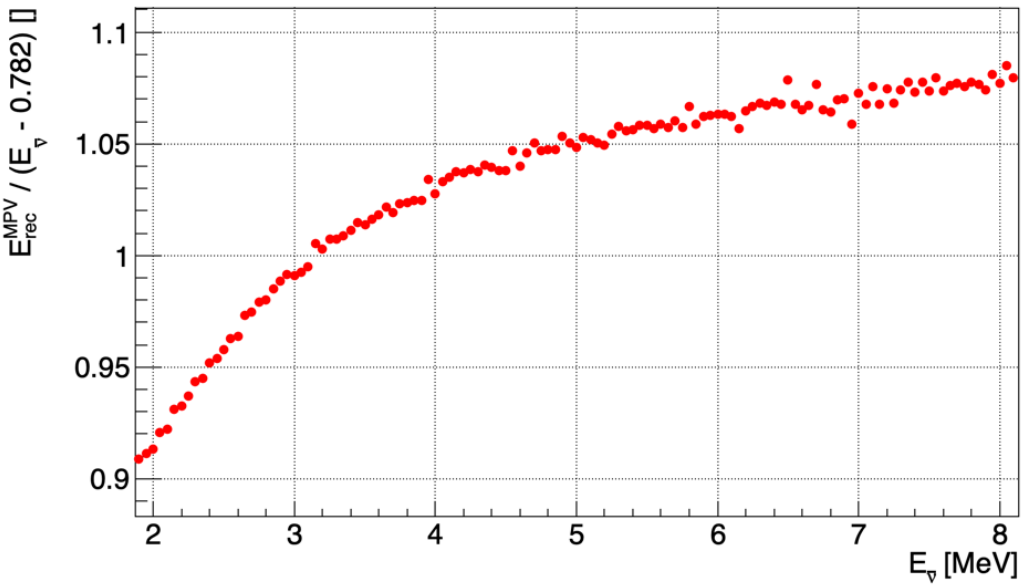

Figure 6.5: **Quenching effect as encapsulated in the Phase-II response**, and reported in 50-keV wide antineutrino energy bins. For each antineutrino energy $E_{\bar{\nu}}$, one extracts the most probable value (MPV) of the reconstructed energy E_{rec}^{MPV}. This value, when compared to the true prompt energy $E_{pr} = E_{\bar{\nu}} - 0.782$[MeV], exhibits the typical trend of the quenching effect described in Section 3.2.2.

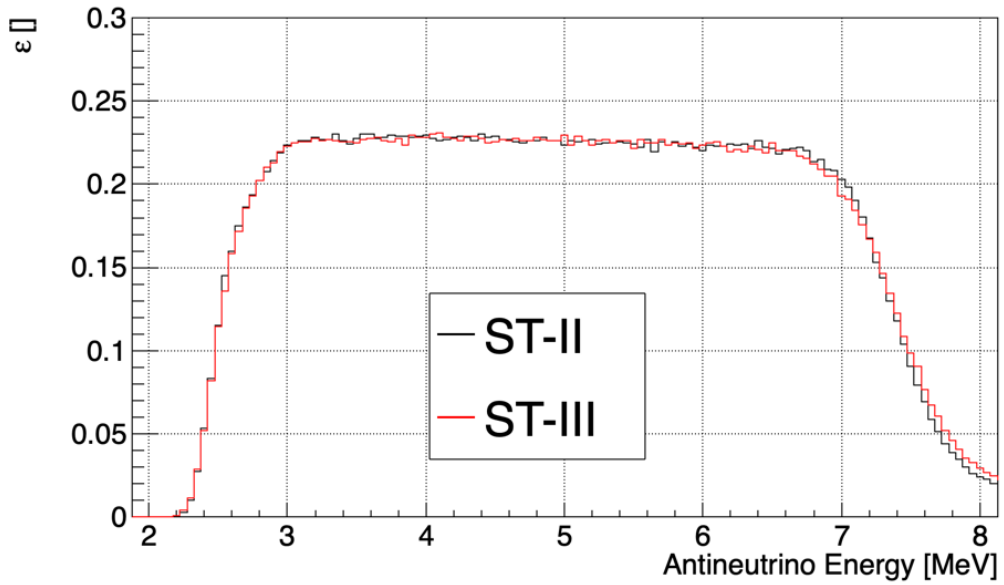

Figure 6.6: **Selection efficiency for Phase-II and -III**, reported in 50-keV wide antineutrino energy bins. The evanescent trend at low and high antineutrino energy comes from the lower and upper cuts set on the reconstructed energy of the antineutrino events, respectively 1.625 and 7.125 MeV.

Prior spectrum

For the unfolding procedure that will be detailed further, we will need to rebin the acceptance response matrix into a coarser true antineutrino energy binning. Whereas the

rebinning procedure is straight-forward when it comes to the reconstructed energy space as it only amounts to summing up the lines of the acceptance response matrix, such method would be nonsensical in terms of probability interpretation for the rebinning of the columns in antineutrino energy space and thus cannot be transposed to this case. Alternatively, one weights the columns by a number of events following a prior distribution, e.g. a flat distribution which is the one that was used to generate the response in the first place, or the Huber distribution. The raw response matrix element then reads:

$$\mathfrak{R}_p^{ij} = N^j \mathcal{R}_p^{ij} \tag{6.8}$$

where N^j is the antineutrino event rate for a true energy E_ν^j following a given prior distribution. The columns of $\mathfrak{R}^{ij}$, corresponding to raw event rates, may then be summed up such that, for a coarser true energy bin J, we have:

$$\mathfrak{R}_p^{iJ} = \sum_{j \in J} \mathfrak{R}_p^{ij} \tag{6.9}$$

The selection efficiency can then be rebinned as follows:

$$\varepsilon_p^J = \frac{N_{selected}^J}{N_{generated}^J} = \frac{\sum_{j \in J} N^j}{\sum_{j \in J} N^j / \varepsilon_p^j} \tag{6.10}$$

Finally, the rebinned acceptance response matrix is computed by normalizing the columns of the rebinned raw response matrix to the values of the rebinned efficiency:

$$\mathcal{R}_p^{iJ} = \frac{\mathfrak{R}_p^{iJ}}{\sum_i \mathfrak{R}_p^{iJ}} \cdot \varepsilon_p^J \tag{6.11}$$

The reasoning above shows that the response matrix is sensitive to the choice of a prior spectrum in antineutrino energy space. To study the sensitivity to this choice, the acceptance response matrix is rebinned to a coarser 250-keV wide antineutrino energy binning with alternatively a: 1/ flat prior, 2/ Huber model prior, 3/ Huber model prior to which we add a local 10% gaussian event excess around 5.5MeV to mimic in antineutrino energy space the spectral distortion observed between data and prediction. The rebinned nominal Huber prediction is folded in reconstructed energy space through the 3 response matrices and all folded predictions are compared to each other. The unbiased reconstructed energy spectrum is the one obtained from the response built out of the Huber model prior. Any deviation to this spectrum is to be interpreted as a remaining bias on the construction of the response originating from the discrepancies between the real antineutrino energy spectrum and the prior spectrum used to derive the response. The comparison is reported in Figure 6.7. In both cases, one gets sub-percent level biases, even reaching the permil level for local and moderate distortions such as the 10% gaussian excess. This allows us to generate the acceptance response matrices with the Huber model as a prior spectrum for the unfolding analysis, which is expected to fairly describe the real antineutrino spectrum shapewise, without concern of introducing sizeable biases.

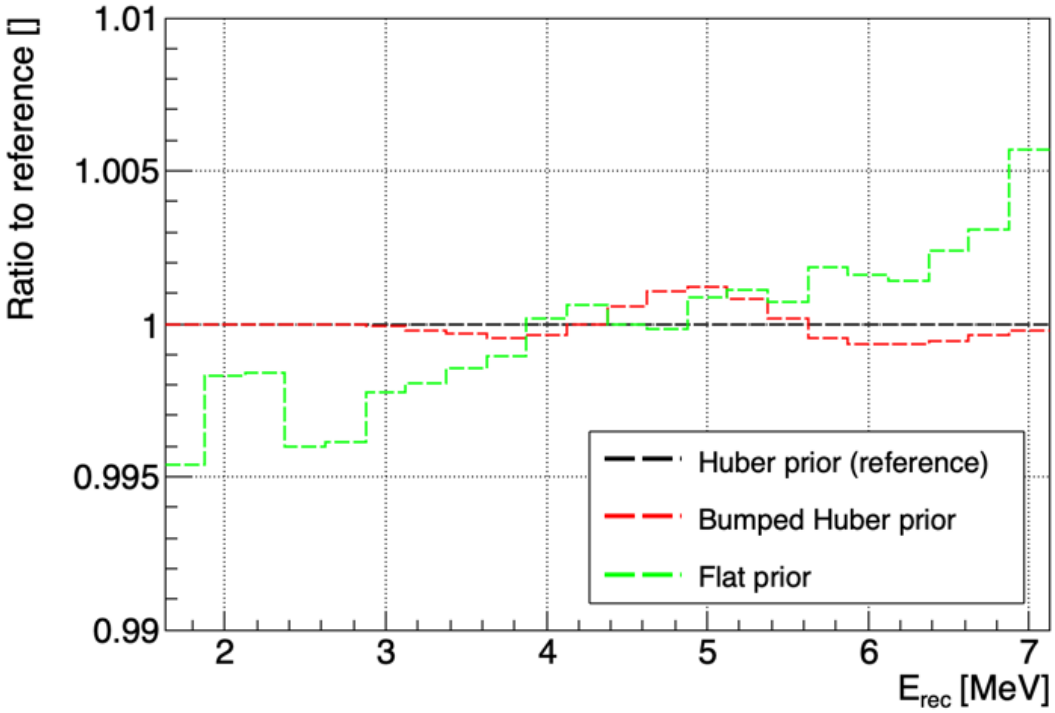

Figure 6.7: **Biases induced by the prior choice for the (Phase-III) response matrix generation**. The Huber true prediction is folded in reconstructed energy space through the response, generated alternatively with the Huber prior spectrum (reference case), a bumped Huber prior spectrum (with a 10% gaussian event excess around 5.5 MeV in $E_{\bar{\nu}}$ space) and a flat prior spectrum. We display in the figure all folded predictions as a ratio to the reference folded prediction, exhibiting only sub-percent level biases. The moderate biases that are obtained for the flat prior case originate from the flatness of the selection efficiency, such that the rebinned response is rather insensitive to the relative statistical weight of the fine energy bins of the prior.

Phase-II and -III responses

The acceptance response matrices for Phase-II and -III are displayed in Figure 6.8. They are reported in 22 250keV-wide reconstructed energy bins spanning [1.625, 7.125]MeV to match the energy binning of the measured spectra presented below, and in 22 antineutrino energy bins spanning [1.875, 8.125]MeV, and defined as follows: 20 250keV-wide $E_{\bar{\nu}}$ bins for [2.375, 7.125]MeV and [7.875, 8.125]MeV, 1 500keV-wide $E_{\bar{\nu}}$ bin for [1.875, 2.375]MeV, and 1 750keV-wide $E_{\bar{\nu}}$ bin for [7.125, 7.875]MeV. The analysis range for the antineutrino spectrum is set to be [2.375, 7.875]MeV, such that the [1.875, 2.375]MeV and [7.875, 8.125]MeV are considered as edge bins, absorbing the edge effects of the unfolding procedure in the lower and upper end of the antineutrino spectrum.

At last, all spectra reported in reconstructed or antineutrino energy space are expressed in cm^2/fission/MeV units and therefore, each energy bin content is corrected for the energy bin width. This is not taken into account in the derivation of the acceptance response matrix. The response matrix for the two phases of STEREO is then defined by correcting the acceptance response matrix from the reconstructed (resp. antineutrino) energy bin width $\left\{\Delta E^i_{rec,p}\right\}_i$ (resp. $\left\{\Delta E^j_{\bar{\nu}}\right\}_j$). It is shown in Figure 6.9 and its matrix element R^{ij}_p

reads:

$$R_p^{ij} = \frac{\Delta E_{\bar{\nu}}^j}{\Delta E_{rec,p}^i} \cdot \mathcal{R}_p^{ij} \tag{6.12}$$

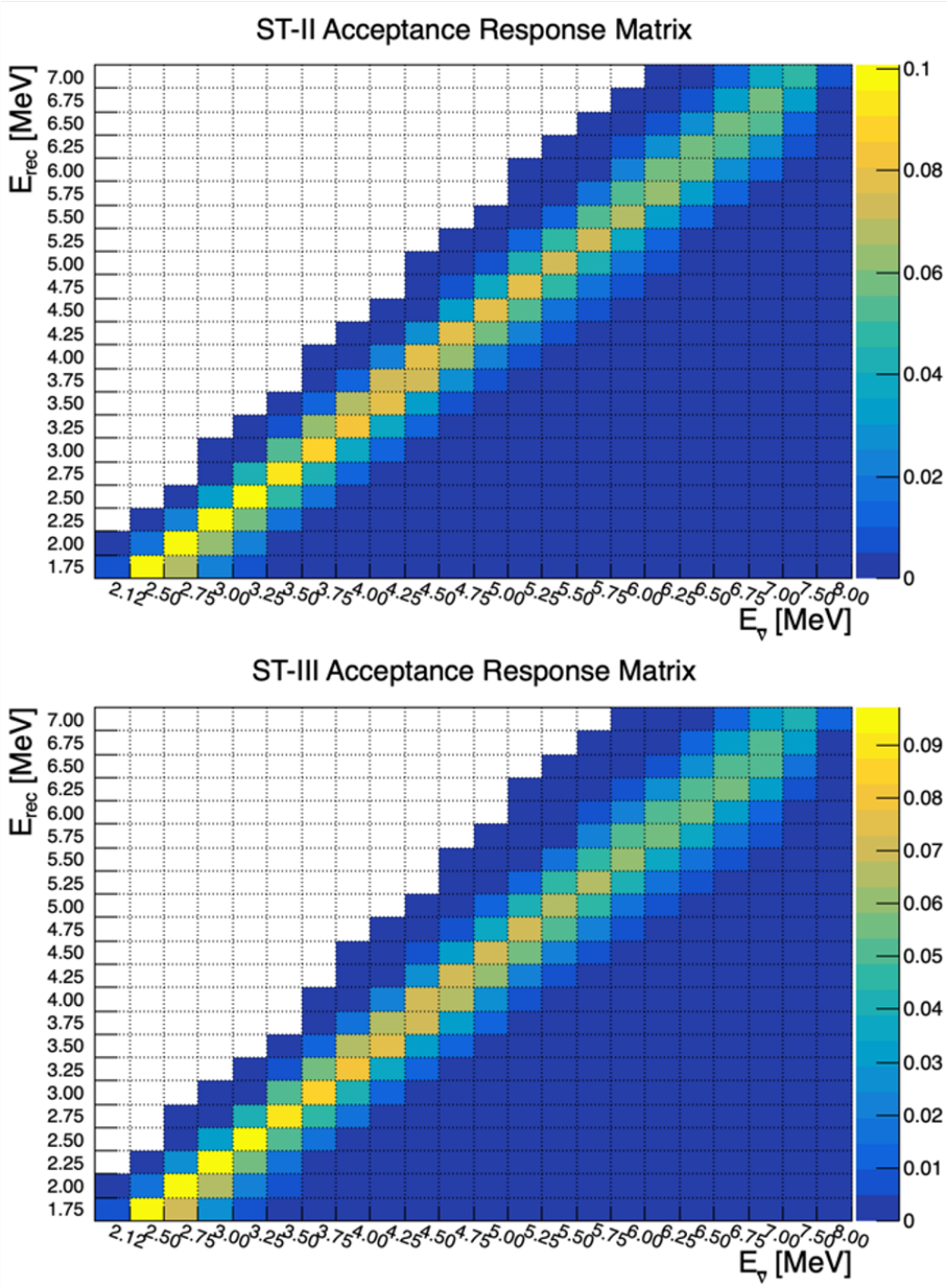

Figure 6.8: **Stereo Acceptance Response Matrices, for Phase-II and -III**. They span [1.625, 7.125]MeV in reconstructed energy space (lines) and [1.875, 8.125]MeV in antineutrino energy space (columns). The matrix elements represent the probability to get a certain reconstructed energy given an incident antineutrino energy, for an antineutrino interacting in the Stereo detector.

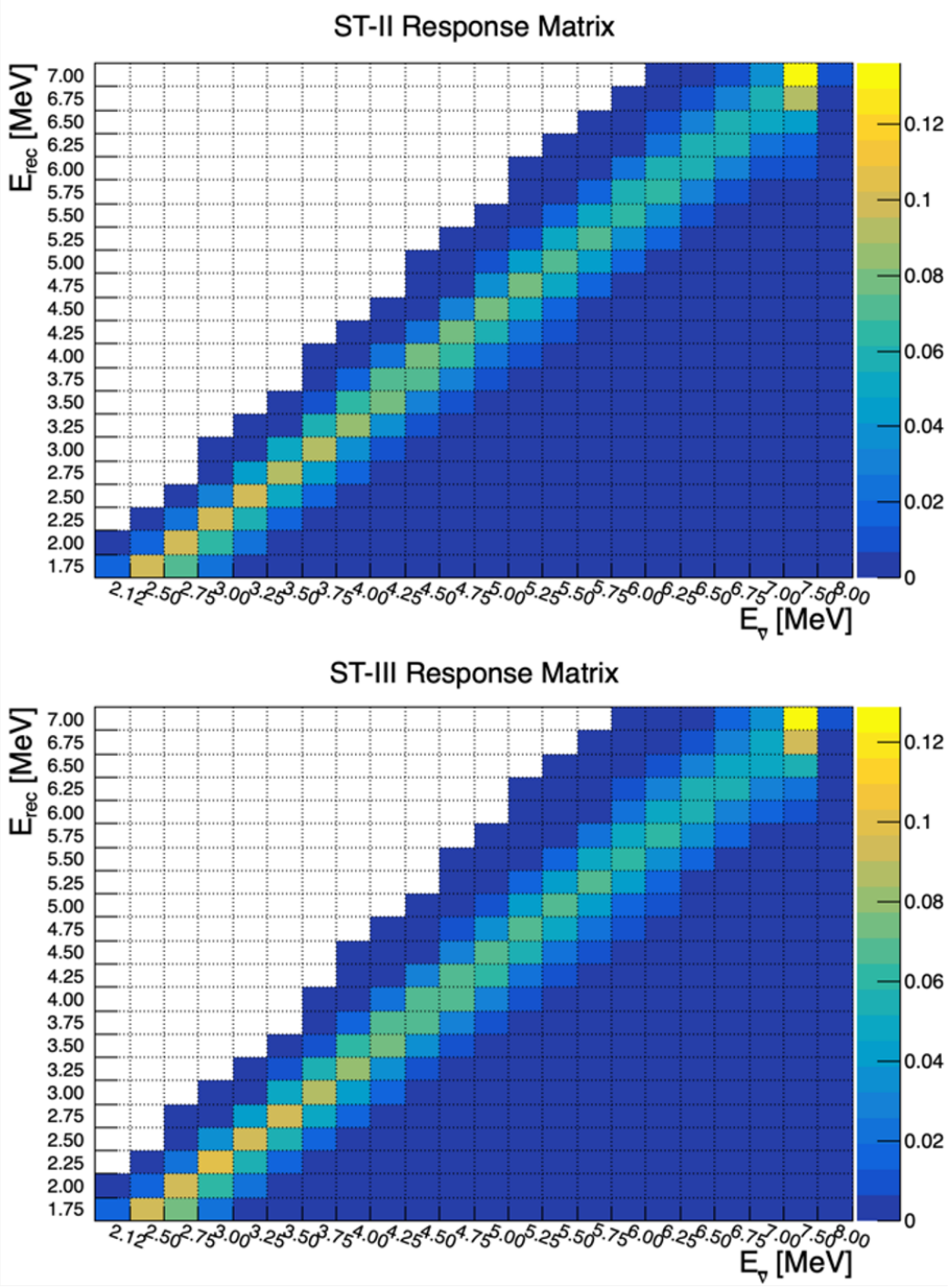

Figure 6.9: **Stereo Response Matrices, for Phase-II and -III**. They correspond to the acceptance response matrices, corrected from the reconstructed energy and antineutrino energy bin widths. These are the ones that will be used in the unfolding algorithm.

6.2.1.3 ^{235}U measured spectrum

The TG level measured spectra for Phase-II and -III are extracted in 250keV-wide reconstructed energy bins, ranging from 1.625 MeV (lower edge of first bin) to 7.125 MeV (upper edge of last bin). They correspond to an overall statistics of $\sim$ 100k antineutrino events ($\sim$ 40k for Phase-II and $\sim$ 60k for Phase-III). To isolate the pure ^{235}U fission induced antineutrino spectrum, the relative flux corrections must be subtracted from the overall

antineutrino spectrum. To this end, the relative corrections of Figure 3.3, expressed in antineutrino energy space, are folded in reconstructed energy space via the response matrix of each phase. They are subsequently removed from the overall measured spectra. The measured ^{235}U spectra for Phase-II and -III can then be displayed in absolute (Figure 6.10) and relative (Figure 6.11) values with respect to the corresponding predictions, which are nothing but the folded ^{235}U Huber predictions. The overall antineutrino deficit as well as the local event excess around 5 MeV are clearly visible.

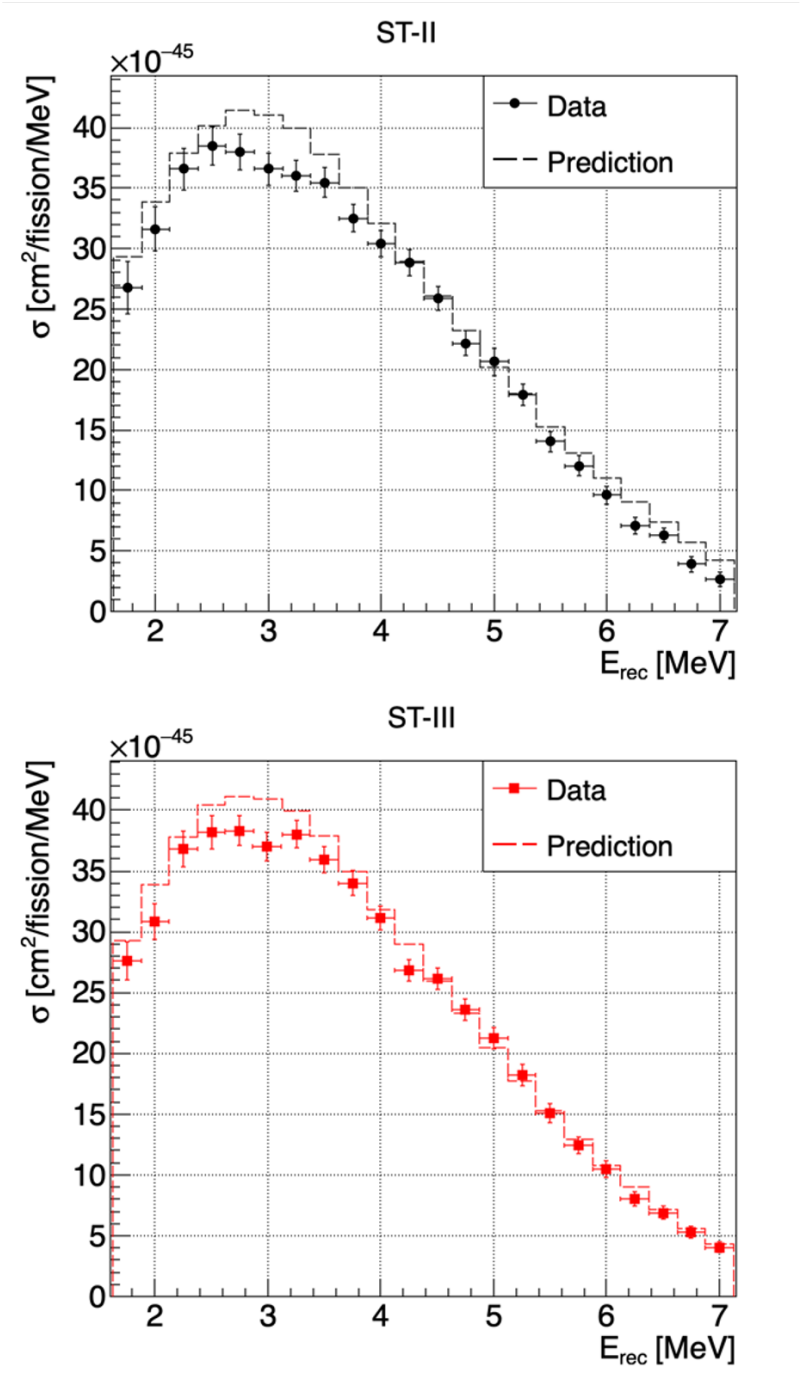

Figure 6.10: **Stereo measured and predicted ^{235}U antineutrino spectrum, for Phase-II and -III**, reported in 250-keV wide reconstructed energy bins spanning [1.625, 7.125]MeV. The overall deficit of antineutrinos between the data and the prediction is clearly visible for both phases.

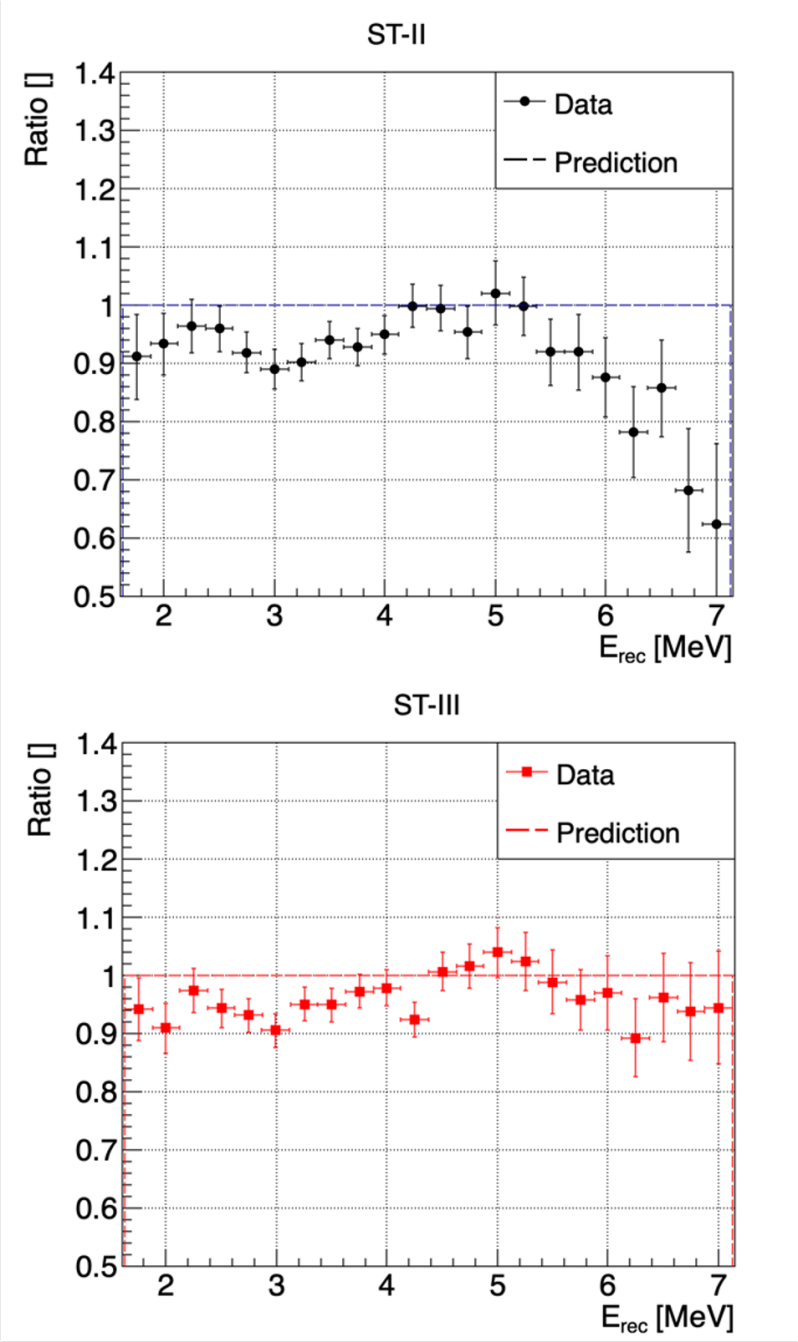

Figure 6.11: **STEREO measured ^{235}U antineutrino spectrum relatively to the predicted ^{235}U antineutrino spectrum, for Phase-II and -III**. The overall deficit of antineutrinos between the data and the prediction translates into a global shift of the ratio towards values lower than 1. The spectral distortion around 5 MeV, or "5 MeV bump", is clearly visible for both phases.

6.2.1.4 Experimental covariance matrix

The uncertainties on the measured ^{235}U antineutrino spectrum have already been discussed in previous sections and are summarized in Figure 6.12. All systematic uncertainties are fully correlated between energy bins. The systematic uncertainties related to selection cuts, reactor-induced background correction and flux corrections are fully correlated between phases, whereas the energy scale and normalization systematic uncertainties are

partially correlated between phases, as already seen in the oscillation analysis (Section 6.1). One then builds the experimental covariance that encapsulates all statistical and systematic uncertainties on the measured ^{235}U antineutrino spectrum, as well as all bin-to-bin and phase-to-phase correlations, as shown in Figure 6.13.

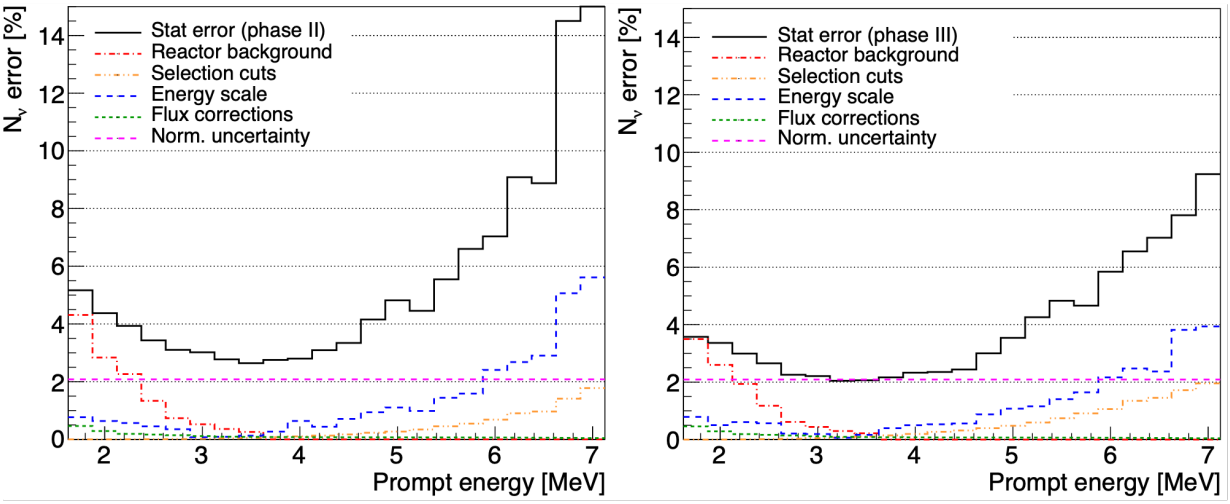

Figure 6.12: **Uncertainty budget on the measured ^{235}U antineutrino spectrum, for Phase-II and -III**.

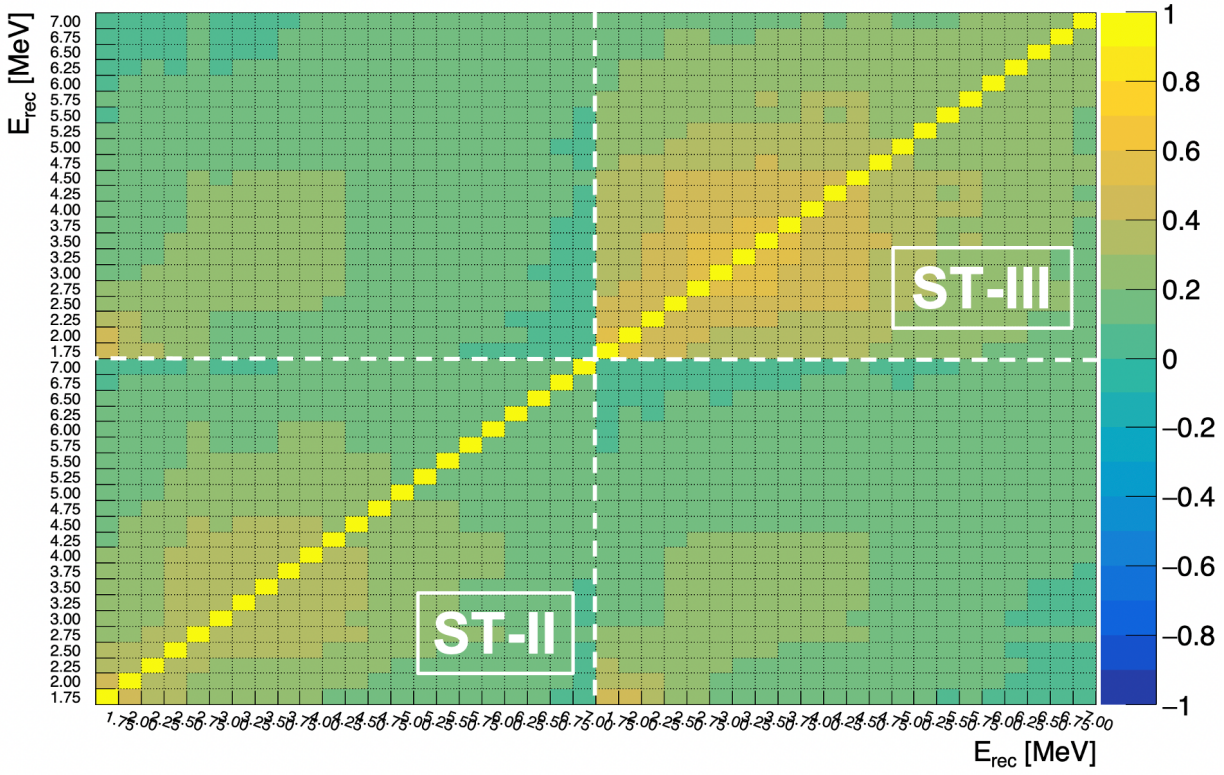

Figure 6.13: **Joint correlation matrix of Phase-II and -III measured ^{235}U antineutrino spectra**. The Phase-III correlations are stronger than for Phase-II due to decreased statistical uncertainties, thanks to higher reactor thermal power and 1 supplemental reactor-ON cycle (see Figure 5.10).

6.2.2 Unfolding framework

6.2.2.1 Notations

The main notations that will be used are briefly summarized in Figure 6.14 illustrating the forward-folding procedure. In this scheme, one propagates the antineutrino energy spectrum in the reconstructed energy space using the response matrix.

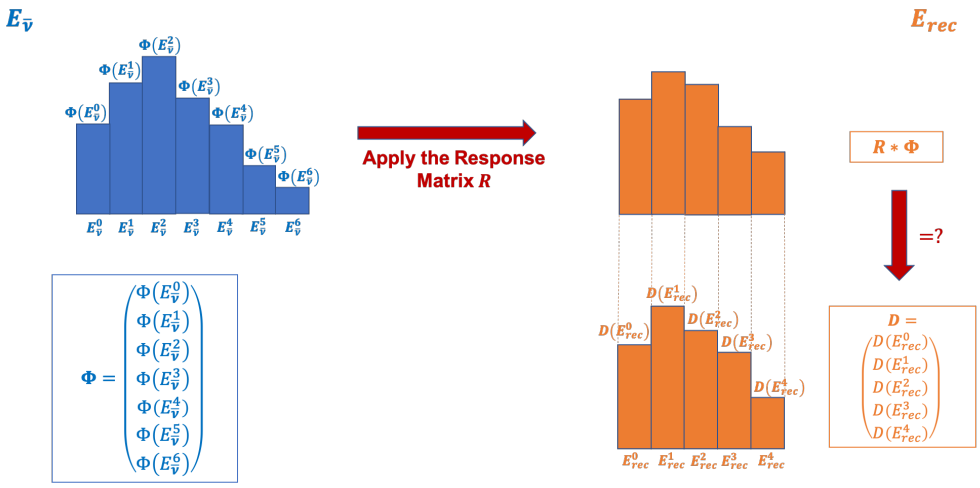

Figure 6.14: Scheme of the forward-folding procedure.

For the unfolding, we do the opposite and, starting from a measured spectrum in reconstructed energy space, one seeks for the underlying spectrum in true antineutrino energy space. However, the deconvolution of the noise inherent to experimental data may result in large fluctuations in the unfolded spectrum, possibly leading to non-physical results, e.g. negative numbers of unfolded events, as discussed for instance in [141, 142]. These well-known features, arising from ill-conditioned inverse problems, call for regularized unfolding technique. The framework that will be presented here is very similar to the formalism that was presented in Chapter 4. It relies on a Tikhonov regularization approach, written in a matricial formalism. However, on the road to provide a reference ^{235}U antineutrino spectrum, greater attention will be paid to the bias introduced by the regularization term. In the following, we then denote:

- $R_p = \left[R_p\left(E^i_{rec,p}, E^j_{\bar{\nu}}\right)\right]_{i,j}$ the $N_D \times N_\Phi$ response matrix, with $N_D = 22$ and $N_\Phi = 22$,
- $D_p = \left[D_p\left(E^i_{rec,p}\right)\right]_i$ the $N_D \times 1$ vector of the measured spectrum in reconstructed energy space,
- $V_p = \left[V_p\left(E^i_{rec,p}, E^{i'}_{rec,p}\right)\right]_{i,i'}$ the $N_D \times N_D$ experimental covariance matrix,
- $\Phi = \left[\Phi\left(E^j_{\bar{\nu}}\right)\right]_j$ the $N_\Phi \times 1$ vector of the unfolded/deconvolved spectrum in antineutrino energy space.

with $p =$ ST-II/ST-III referring to the considered STEREO phase.

6.2.2.2 χ^2 writing and minimization

In the following, we set the regularization on the first order discrete derivative of the unfolded spectrum. The expression for the χ^2 to be minimized reads:

$$\begin{aligned}
\left(\chi_p^{\lambda}\right)^2 &= \|D_p - R_p\Phi\|^2_{V_p^{-1}} + \lambda \sum_j \left(\frac{\Phi^{j+1}}{\Phi^{j+1}_{\mathrm{HM}}} - \frac{\Phi_j}{\Phi^j_{\mathrm{HM}}}\right)^2 \\
&= \|D_p - R_p\Phi\|^2_{V_p^{-1}} + \lambda \sum_j \left(\left[\frac{\Phi^j}{\Phi^j_{\mathrm{HM}}}\right]^{(1)}\right)^2 \\
&= \|D_p - R_p\Phi\|^2_{V_p^{-1}} + \lambda \sum_j \left(\left[C_{\mathrm{HM}}\Phi\right]^{(1)}_j\right)^2 \\
&= \|D_p - R_p\Phi\|^2_{V_p^{-1}} + \lambda \sum_j \left(\left[C_{(1)}C_{\mathrm{HM}}\Phi\right]_j\right)^2 \\
&= \|D_p - R_p\Phi\|^2_{V_p^{-1}} + \lambda \left\|C_{(1)}C_{\mathrm{HM}}\Phi\right\|^2 \\
&= \|D_p - R_p\Phi\|^2_{V_p^{-1}} + \lambda \|\Phi\|^2_M
\end{aligned} \tag{6.13}$$

where we denote $M := \left(C_{(1)}C_{\mathrm{HM}}\right)^T \left(C_{(1)}C_{\mathrm{HM}}\right)$ the global regularization matrix, set to mitigate the bin-to-bin fluctuations in the unfolded spectrum given the prior spectrum Φ_{HM}, set to be, again, the Huber ^{235}U spectrum. It is built out of:

- $C_{(1)}$ the $N_\Phi \times N_\Phi$ first order discrete derivative matrix:

$$C_{(1)} = \begin{bmatrix}
1 & -1 & 0 & \dots & \dots & \dots & 0 \\
0 & 1 & -1 & \ddots & & & \vdots \\
0 & \ddots & \ddots & \ddots & \ddots & & \vdots \\
\vdots & \ddots & \ddots & \ddots & \ddots & \ddots & \vdots \\
\vdots & & \ddots & \ddots & \ddots & \ddots & 0 \\
\vdots & & & \ddots & 0 & 1 & -1 \\
0 & \dots & \dots & \dots & 0 & 0 & 0
\end{bmatrix} \tag{6.14}$$

- C_{HM} the $N_\Phi \times N_\Phi$ prior matrix:

$$C_{\mathrm{HM}} = \begin{bmatrix}
\frac{1}{\Phi^0_{\mathrm{HM}}} & 0 & \dots & \dots & \dots & \dots & 0 \\
0 & \frac{1}{\Phi^1_{\mathrm{HM}}} & \ddots & & & & \vdots \\
\vdots & \ddots & \ddots & \ddots & & & \vdots \\
\vdots & & \ddots & \ddots & \ddots & & \vdots \\
\vdots & & & \ddots & \ddots & \ddots & \vdots \\
\vdots & & & & \ddots & \frac{1}{\Phi^{N_\Phi-1}_{\mathrm{HM}}} & 0 \\
0 & \dots & \dots & \dots & \dots & 0 & \frac{1}{\Phi^{N_\Phi}_{\mathrm{HM}}}
\end{bmatrix} \tag{6.15}$$

Let's note that the regularization term is totally insensitive to the normalization of the prior spectrum and encodes only the prior shape information. A change in the prior normalization would indeed be absorbed by the tuning of the regularization strength: multiplying

the prior spectrum by a global normalization factor α would translate into a change of the regularization strength from λ to $\alpha^2\lambda$, such that the overall value of the regularization term $\lambda \|\Phi\|^2_M$ would remain unchanged.

The expression in Equation 6.13 is in essence the same as in Equation 4.20[1]. Therefore, the formula of Equation 4.27 still holds, such that, for each phase p, the unfolded spectrum $\hat{\Phi}_p$ and its corresponding covariance matrix $V_{\hat{\Phi}_p}$ are given by:

$$\begin{cases} \hat{\Phi}_p &= H_p(\lambda) \cdot D_p \\ V_{\hat{\Phi}_p} &= H_p(\lambda) \cdot V_p \cdot H_p(\lambda)^T \end{cases} \tag{6.16}$$

where:

$$H_p(\lambda) = \left(R_p^T V_p^{-1} R_p + \lambda M\right)^{-1} R_p^T V_p^{-1} \tag{6.17}$$

Besides, let's note that, applying the same reasoning as in Equation 4.26, the formulae still hold for the joint unfolding of Phase-II and -III data provided we define the joint experimental spectrum, response and covariance as follows:

$$\begin{cases} D_{\text{ST-II+III}} &= \begin{bmatrix} D_{\text{ST-II}} \\ D_{\text{ST-III}} \end{bmatrix} \\ R_{\text{ST-II+III}} &= \begin{bmatrix} R_{\text{ST-II}} \\ R_{\text{ST-III}} \end{bmatrix} \\ V_{\text{ST-II+III}} &= \begin{bmatrix} V_{\text{ST-II}} & V_{\text{ST-II/III}} \\ V^T_{\text{ST-II/III}} & V_{\text{ST-III}} \end{bmatrix} \end{cases} \tag{6.18}$$

where $V_{\text{ST-II/III}}$ is the Phase-II/Phase-III cross-covariance matrix.

6.2.2.3 Filter matrix

In the Tikhonov approach, the regularization term induces a bias with respect to the standard linear least square (LLS) solution, that would be given by $\hat{\Phi}_{\text{LLS}} = H(0) \cdot D$.

Let's first briefly remind that the LLS estimator is unbiased. Let's consider the true ^{235}U antineutrino spectrum Φ_0, that we fold in reconstructed energy space via the response matrix R, providing us with the prediction $D_0 = R \cdot \Phi_0$. Still assuming that all spectrum uncertainties encoded in the experimental covariance matrix V are gaussian-distributed, one can fluctuate the prediction D_0 to generate a set of pseudo-data D distributed under the null hypothesis that the underlying antineutrino spectrum is Φ_0. The pseudo-data then writes $D = D_0 + \varepsilon$, where $\varepsilon \sim \mathcal{G}(0, V)$ is a random variable encoding the experimental noise. The unfolded spectrum $\hat{\Phi}$, namely the estimator for the true antineutrino spectrum

[1]Nonetheless, let's note that the regularization matrix M defined for the unfolding is singular, for $C_{(1)}$ is not invertible. Therefore, as a symmetric positive matrix, it only defines a semi-norm, that cancels out only for vectors equal to the prior spectrum Φ_{HM} up to a global normalization factor.

Φ_0, is given in the LLS approach by:

$$\begin{aligned}
\hat{\Phi}_{\text{LLS}} &= H(0) \cdot D \\
&= \left(R^T V^{-1} R\right)^{-1} R^T V^{-1} \cdot D \\
&= \left(R^T V^{-1} R\right)^{-1} R^T V^{-1} \cdot (D_0 + \varepsilon) \\
&= \left(R^T V^{-1} R\right)^{-1} R^T V^{-1} \cdot (R\Phi_0 + \varepsilon) \\
&= \left(R^T V^{-1} R\right)^{-1} \left(R^T V^{-1} R\right) \cdot \Phi_0 + \left(R^T V^{-1} R\right)^{-1} R^T V^{-1} \cdot \varepsilon \\
&= \Phi_0 + \left(R^T V^{-1} R\right)^{-1} R^T V^{-1} \cdot \varepsilon
\end{aligned} \tag{6.19}$$

such that, we have on average:

$$\begin{aligned}
\mathbb{E}\left(\hat{\Phi}_{\text{LLS}}\right) &= \underbrace{\mathbb{E}\left(\Phi_0\right)}_{=\,\Phi_0} + \left(R^T V^{-1} R\right)^{-1} R^T V^{-1} \cdot \underbrace{\mathbb{E}\left(\varepsilon\right)}_{=\,0} \\
&= \Phi_0
\end{aligned}$$

which proves that the standard LLS estimator is unbiased.

It is worth noting that Equation 6.19 is actually defined if and only if (iif) $R^T V^{-1} R$ is invertible. This holds iif the response matrix R is injective, which requires to have at least as many constraints (number of reconstructed energy bins) as free parameters (number of antineutrino energy bins). This is the case for Phase-II and -III data sets and unfolding ranges, given $N_D = N_\Phi = 22$.

Now, let's remark that the LLS matrix $H(0)$ can be factorized out of the Tikhonov matrix $H(\lambda)$ as follows:

$$\begin{aligned}
H(\lambda) &= \left(R^T V^{-1} R + \lambda M\right)^{-1} R^T V^{-1} \\
&= \left(\left(R^T V^{-1} R\right)\left(I_{N_\Phi} + \lambda \left(R^T V^{-1} R\right)^{-1} M\right)\right)^{-1} R^T V^{-1} \\
&= \left(I_{N_\Phi} + \lambda \left(R^T V^{-1} R\right)^{-1} M\right)^{-1} \cdot \left(R^T V^{-1} R\right)^{-1} R^T V^{-1} \\
&= \underbrace{\left(I_{N_\Phi} + \lambda \left(R^T V^{-1} R\right)^{-1} M\right)^{-1}}_{:=A_c(\lambda)} \cdot H(0)
\end{aligned} \tag{6.20}$$

where I_{N_Φ} is the $N_\Phi \times N_\Phi$ identity matrix. We denote:

$$A_c(\lambda) = \left(I_{N_\Phi} + \lambda \left(R^T V^{-1} R\right)^{-1} M\right)^{-1} \tag{6.21}$$

Comparing the Tikhonov and LLS unfoldings, we then have $\hat{\Phi}_{\text{Tikhonov}}(\lambda) = A_c(\lambda) \cdot \hat{\Phi}_{\text{LLS}}$, such that:

$$\begin{aligned}
\mathbb{E}\left(\hat{\Phi}_{\text{Tikhonov}}(\lambda)\right) &= \mathbb{E}\left(A_c(\lambda) \cdot \hat{\Phi}_{\text{LLS}}\right) \\
&= A_c(\lambda) \cdot \mathbb{E}\left(\hat{\Phi}_{\text{LLS}}\right) \\
&= A_c(\lambda) \cdot \Phi_0
\end{aligned} \tag{6.22}$$

Thus, $A_c(\lambda)$ encodes the bias of the Tikhonov regularized unfolding. In the limit where $\lambda = 0$, the Tikhonov result coincides with the LLS estimate which directly translates into the fact that $A_c(0)$ is the identity matrix.

By analogy with the Wiener-SVD regularized unfolding [142], we call A_c the filter matrix of the Tikhonov regularized unfolding. In the Wiener-SVD approach, no regularization strength is needed as the framework aims at maximizing the signal-to-noise ratio in the effective frequency domain, given a prior spectrum for the expected signal. The so-called Wiener filter, A_c^{Wiener}, that is derived from this criterion is then applied to the LLS estimator as:

$$\hat{\Phi}_{\text{Wiener}} \;=\; A_c^{Wiener} \cdot \hat{\Phi}_{\text{LLS}} \tag{6.23}$$

Noticeably, this framework has been used by the Daya Bay collaboration to unfold their uranium and plutonium separated spectra [143].

6.2.2.4 Bias study

In order to thoroughly assess the dependency of the bias with respect to the regularization strength λ, we apply the filter matrix $A_c(\lambda)$ for various values of λ to a modified Huber ^{235}U prediction Φ_0, built as follows:

$$\Phi_0\left(E_{\bar{\nu}}\right) = \Phi_{\text{HM}}\left(E_{\bar{\nu}}\right) \cdot \left(1 + A_0 \cdot \exp - \frac{\left(E_{\bar{\nu}} - \mu_0\right)^2}{2\sigma_0^2}\right) \tag{6.24}$$

with $A_0 = 10\%$, $\mu_0 = 5.5$ MeV, $\sigma_0 = 0.5$ MeV. This way, we add a 10% gaussian event excess to the nominal Huber prediction in order to mimic the reactor spectral anomaly in antineutrino energy space.

Filter-induced bias

Due to the smoothing introduced by the regularization term in Equation 6.13, we expect a flattening of the filtered/unfolded bump as the regularization strength increases, meaning a decrease in its amplitude and an increase in its width. This is the typical trend that is illustrated in the case study of Figure 6.15, for which the response and experimental covariance matrices of Phase-II, -III and -II+III data sets were alternatively used to define the filter matrix associated to the unfolding of each data set. Several features may be emphasized from this study.

First, for high values of λ, it can be seen that the flattening of the bump is not symmetrical and becomes more pronounced at high energy. This trend is explained by the expression of the regularization matrix M, which is $\propto 1/\Phi_{\text{HM}}$ such that in the high energy end of the antineutrino spectrum where the signal vanishes, the smoothing induced by the regularization is greater. This feature becomes more patent in the filtered spectrum as the weight of the regularization increases, i.e. as the regularization strength increases.

Second, in the region outside the bump range, below 4 MeV and above 7 MeV, where Φ_0 coincides with Φ_{HM}, let's note that the ratio Φ_0/Φ_{HM} is flat. This is expected given the expression of the filter matrix (Equation 6.21). Indeed, the prior spectrum Φ_{HM} used for the regularization cancels out the regularization matrix M: $M \cdot \Phi_{\text{HM}} = 0$, such that

$A_c(\lambda) \cdot \Phi_{\text{HM}} = \Phi_{\text{HM}}$, whatever λ used. In other words, as we would expect, there is no bias in shape induced on the regularization prior spectrum.

Third, in the limit where $\lambda \longrightarrow \infty$, the ratio $(A_c(\lambda) \cdot \Phi_0) / \Phi_{\text{HM}}$ converges to a flat ratio over the whole energy range. This is consistent with the fact that, in the high λ limit, the filtered/unfolded spectrum is no longer constrained by the data but fully determined by the regularization term of Equation 6.13. Therefore, the minimization of the Tikhonov χ^2 leads, in the high λ limit, to the cancellation of the regularization matrix M by the unfolded spectrum. However, this matrix defines a semi-norm only cancelled out by spectra proportional to the prior spectrum. Therefore, in this limit, the filtered spectrum $A_c(\lambda) \cdot \Phi_0$ is set to be the prior spectrum Φ_{HM} up to a normalization factor. In this case study, the normalization factor is merely unity corrected from the percent level total event excess originating from the 10% bump added on top the prior spectrum.

Fourth, in the high statistics limit, the filtered/unfolded spectrum is expected to be fully constrained by the data and no longer by the regularization term. Mathematically, this regime translates into the fact that the experimental covariance matrix V tends to 0, so that $V^{-1} \longrightarrow \infty$ (neglecting in this reasoning possible non-vanishing systematic uncertainties). As a consequence, the term $R^T V^{-1} R$ that encapsulates the experimental constraints in Equation 6.17 becomes dominant over the regularization term λM. In the expression of the filter matrix in Equation 6.21, this translates into the mitigation of the term $\left(R^T V^{-1} R\right)^{-1} \cdot (\lambda M)$ which is to be interpreted as the "ratio" of regularization constraints with respect to experimental constraints. Thus, for equal regularization strength λ between two different data sets, one can have different effective *regularization power*, defined by $\left(R^T V^{-1} R\right)^{-1} \cdot (\lambda M)$, depending on the statistics of the data sets. At fixed regularization strength, the regularization power is expected to decrease as the statistics increases. This is exactly what we see in Figure 6.15, where the filtered-induced bias on the spectral distortion decreases from Phase-II to Phase-III, and from Phase-III to Phase-II+III.

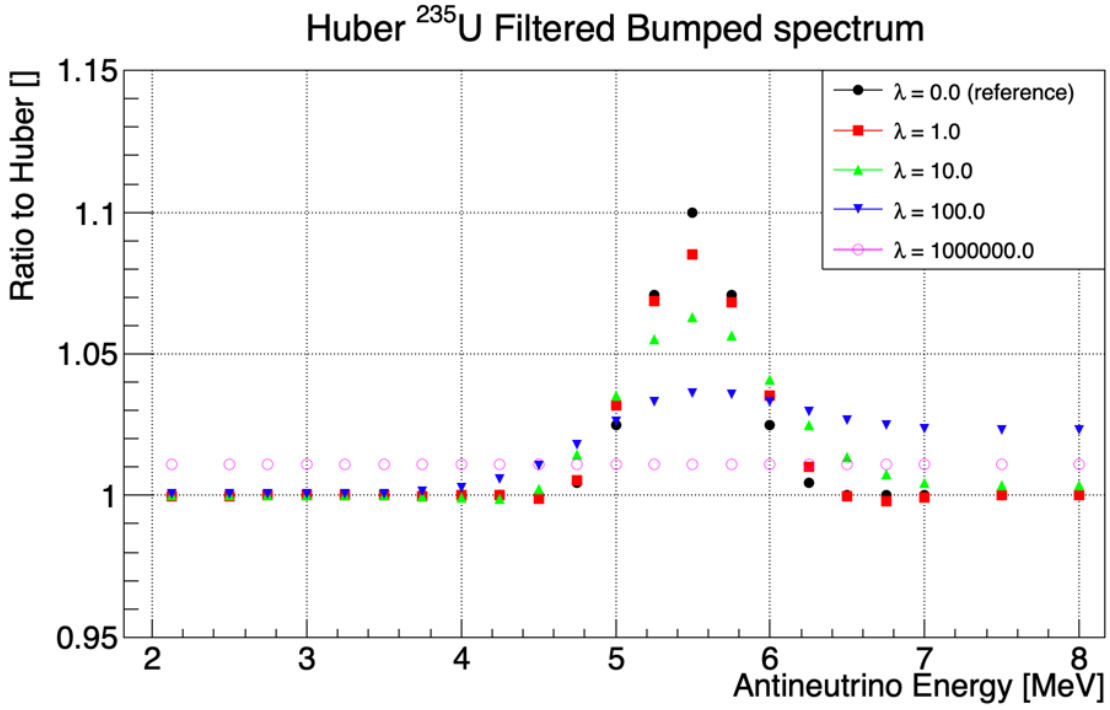

(a) Phase-II data set

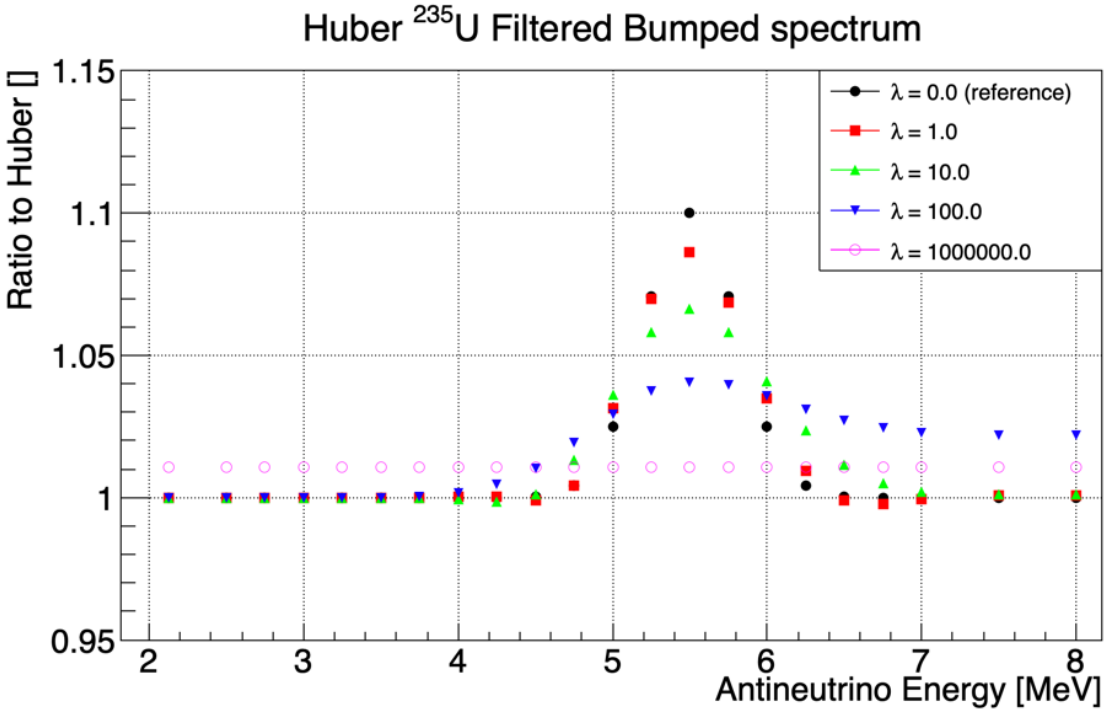

(b) Phase-III data set

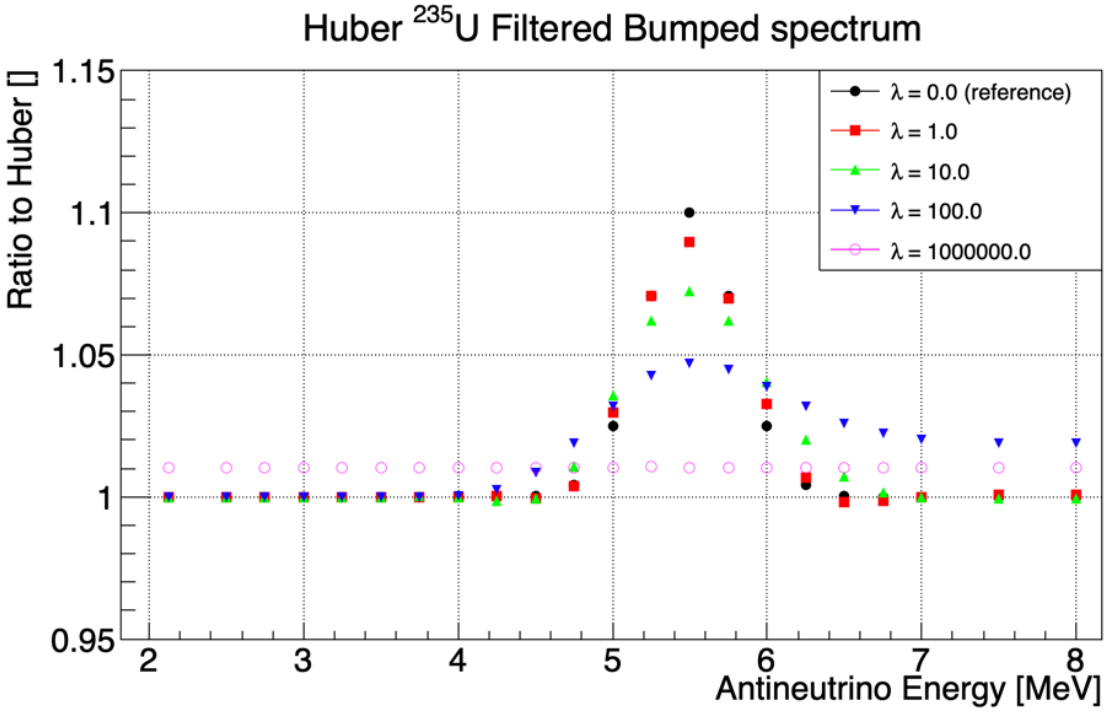

(c) Phase-II+III data set

Figure 6.15: **Filter-induced bias on a bumped Huber ^{235}U prior spectrum, for Phase-II, -III and -II+III data sets**. The nominal bumped Huber spectrum, exhibiting a 10% local event excess around 5.5 MeV, coincides with the case of vanishing regularization strength ($\lambda = 0$) where the filter matrix is merely the identity matrix. It is displayed in black dots. As the regularization strength increases, the nominal spectral distortion is flattened when applying the filter matrix of the associated Tikhonov unfolding. See text for further details.

Bias-variance trade-off

For various values of regularization strength λ, one now computes the arithmetic average bias of the filtered bumped Huber prior spectrum, over the whole antineutrino energy range. It is defined in relative values as:

$$\langle \text{Bias} \rangle_{E_{\bar{\nu}}}(\lambda) = \left\langle \left| \frac{\left(A_c(\lambda) \cdot \Phi_0\right)\left(E_{\bar{\nu}}^j\right)}{\Phi_0\left(E_{\bar{\nu}}^j\right)} - 1 \right| \right\rangle_{E_{\bar{\nu}}} \tag{6.25}$$

Knowing the expression of the covariance matrix of the filtered/unfolded spectrum, one can similarly computes the arithmetic average error of the filtered bumped Huber prior spectrum. It is defined in relative values as:

$$\langle \text{Error} \rangle_{E_{\bar{\nu}}}(\lambda) = \left\langle \left| \frac{\sqrt{V_{A_c(\lambda)\cdot\Phi_0}\left(E_{\bar{\nu}}^j, E_{\bar{\nu}}^j\right)}}{\left(A_c(\lambda) \cdot \Phi_0\right)\left(E_{\bar{\nu}}^j\right)} \right| \right\rangle_{E_{\bar{\nu}}} \tag{6.26}$$

where $V_{A_c(\lambda)\cdot\Phi_0}$ is the covariance matrix of the filtered/unfolded spectrum which, according to Equations 6.16, 6.20, is given by $V_{A_c(\lambda)\cdot\Phi_0} = (A_c(\lambda)H(0))^T \cdot V \cdot (A_c(\lambda)H(0))$.

For Phase-II, -III and -II+III data sets, we plot in Figure 6.16 the dependence of the afore-defined unfolded spectrum relative bias and error upon the value of the regularization strength. For each data set, we show as a vertical green line the tuned value of the regularization strength obtained from the minimization of the GCV error. In horizontal red line, we display the relative error of the experimental spectrum which is to be compared to the regularization strength dependent relative error of the unfolded spectrum. It is defined as:

$$\langle \text{Error} \rangle_{E_{rec}}(\lambda) = \left\langle \left| \frac{\sqrt{V\left(E_{rec}^i, E_{rec}^i\right)}}{D\left(E_{rec}^i\right)} \right| \right\rangle_{E_{rec}} \tag{6.27}$$

Again, several remarkable features may be identified in this Figure.

First, for each data set, the bias and the error of the unfolded spectrum are respectively increasing and decreasing functions of the regularization strength. This is a well-known feature of regularized unfolding, known as bias-variance trade-off [144], where one reduces the high variance of the estimator that reflects the ill-conditioning of the inverse problem at the expense of a reasonable bias.

Indeed, one deduces from Equation 6.22 that the bias of the Tikhonov unfolding is encoded in the $I_{N_\Phi} - A_c(\lambda)$ matrix:

$$\begin{aligned}
I_{N_\Phi} - A_c(\lambda) &= I_{N_\Phi} - \left(I_{N_\Phi} + \lambda \left(R^T V^{-1} R\right)^{-1} M\right)^{-1} \\
&= \left(I_{N_\Phi} + \lambda \left(R^T V^{-1} R\right)^{-1} M\right) \cdot \left(I_{N_\Phi} + \lambda \left(R^T V^{-1} R\right)^{-1} M\right)^{-1} \\
&\quad - \left(I_{N_\Phi} + \lambda \left(R^T V^{-1} R\right)^{-1} M\right)^{-1} \\
&= \left(I_{N_\Phi} + \lambda \left(R^T V^{-1} R\right)^{-1} M - I_{N_\Phi}\right) \cdot \left(I_{N_\Phi} + \lambda \left(R^T V^{-1} R\right)^{-1} M\right)^{-1} \\
&= \left(\lambda \left(R^T V^{-1} R\right)^{-1} M\right) \cdot \left(I_{N_\Phi} + \lambda \left(R^T V^{-1} R\right)^{-1} M\right)^{-1}
\end{aligned}$$

The unfolding bias is found to roughly scale as $\frac{\lambda}{1+\alpha\cdot\lambda}$ and thus increases with respect to λ, yet saturating in the high λ limit.

On the other hand, from Equation 6.16, the error in the unfolded spectrum is found to roughly scale as $\frac{1}{1+\alpha\cdot\lambda}$ and decreases with respect to λ. Noticeably, the non-vanishing trend of the error in the high λ limit, that we can observe for all data sets in Figure 6.16, originates from the singularity of the regularization matrix. As already explained, it comes from the fact that the normalization of the filtered spectrum is completely unconstrained by the regularization if this spectrum happens to coincide with the prior spectrum. In the regime $\lambda \longrightarrow \infty$ where the regularization becomes dominant, this degeneracy translates into a residual and non-vanishing error on the filtered spectrum. Also let's add that the convergence of the error and bias towards a common value is purely coincidental. For different values of the gaussian spectral distortion, this feature disappears.

Second, for Phase-II and -II+III data sets, one observes that the order of magnitude of the regularization strength obtained from the minimization of the GCV error, λ_{GCV}, is close to unity. It corresponds to a small permil level average bias across all the energy range according to Figures 6.16a and 6.16c, and to a reasonable percent level bias on the amplitude of the filtered distortion according to Figure 6.15. Furthermore, let's note that, with $\lambda = \lambda_{\mathrm{GCV}}$, the average error of the unfolded spectrum is brought to a level comparable to the average error of the data spectra for Phase-II and -II+III data sets, which is a sound result.

Third, we may be surprised by the fact that the λ_{GCV} value for Phase-III data set is almost two orders of magnitude lower than for Phase-II and-II+III, translating into a one order of magnitude greater average error in Phase-III unfolded spectrum and high and non-physical bin-to-bin fluctuations as illustrated in Figure 6.17. As shown in the next subsection, such regularization originates from the degeneracy of the GCV error function for Phase-III data set, that exhibits more than one local minimum.

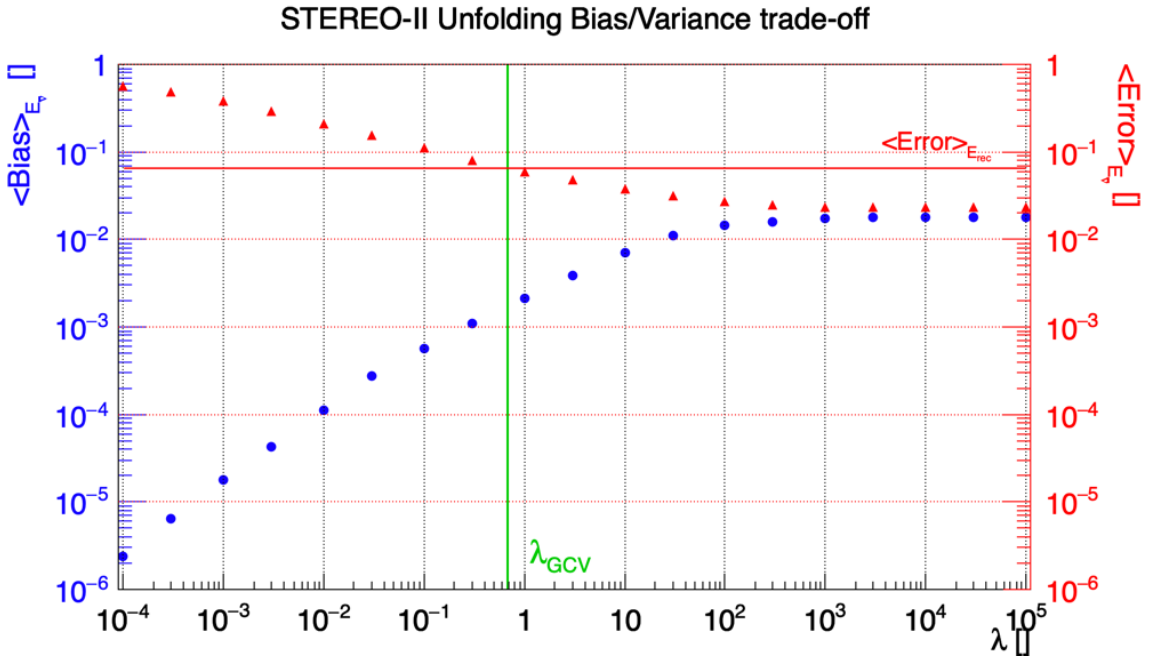

(a) Phase-II data set

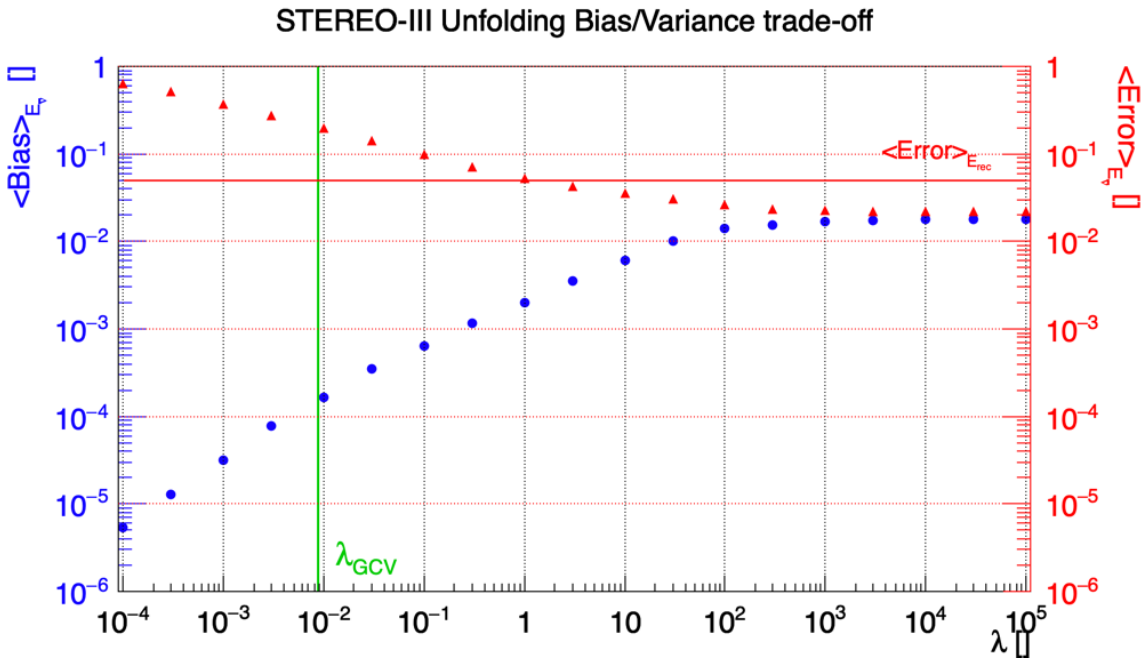

(b) Phase-III data set

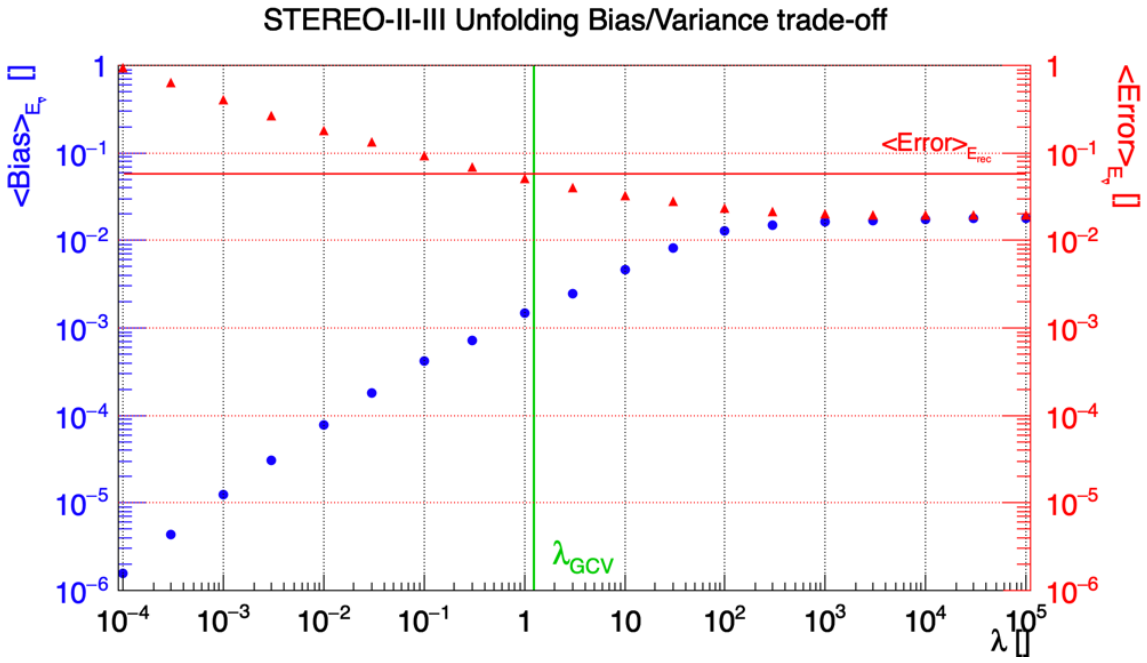

(c) Phase-II+III data set

Figure 6.16: **Bias-variance trade-off for Phase-II, -III and -II+III data sets**. The vertical green line represents the value of the regularization strength obtained from the GCV prescription. The horizontal red line illustrates the error contained in the data spectrum, that is to be compared to the regularization strength dependent error in the unfolded spectrum. See text for further details.

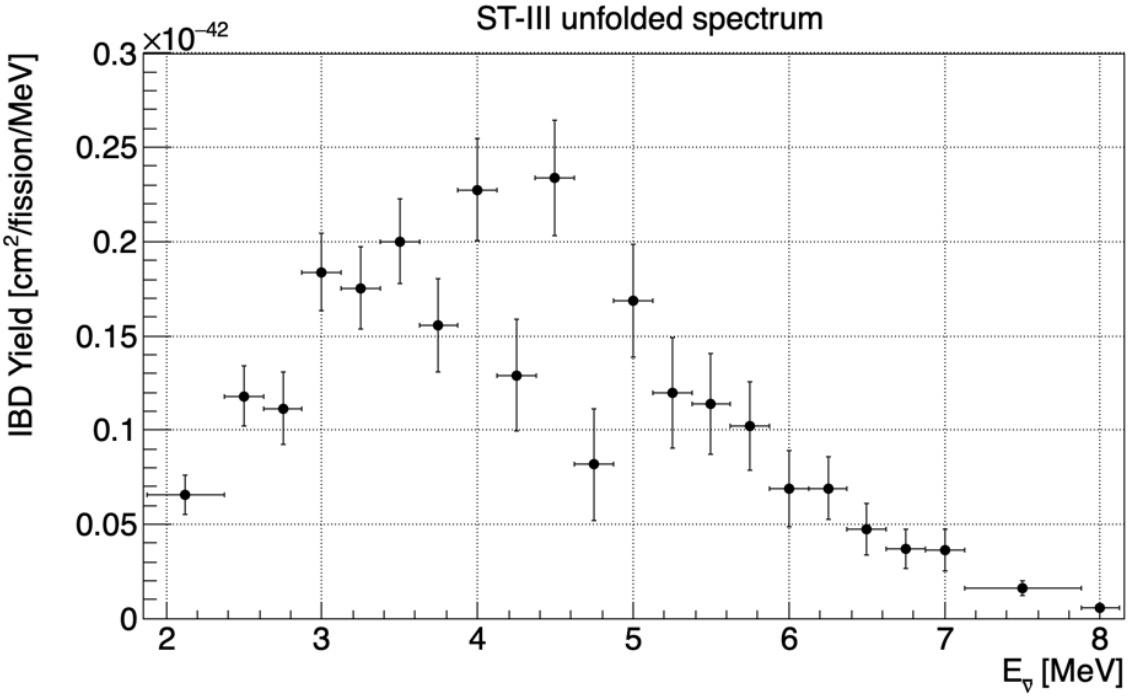

Figure 6.17: **Phase-III ^{235}U unfolded spectrum with the standard GCV prescription**, yielding to high bin-to-bin fluctuations. This hints towards an underestimation of the required regularization strength.

Modified GCV prescription

We show in Figure 6.18 the GCV error profile for Phase-II, -III and -II+III data sets. Whereas the error exhibits a unique and well-defined minimum close to unity for Phase-II and -II+III, two close local minima are found for Phase III. Noticeably, the higher minimum is found to be close to unity. To lift the degeneracy that may arise in the GCV error profile, we decide to slightly change the prescription and to choose as a regularization strength the highest local minimum of the GCV error instead of the global minimum.

(a) Phase-II data set

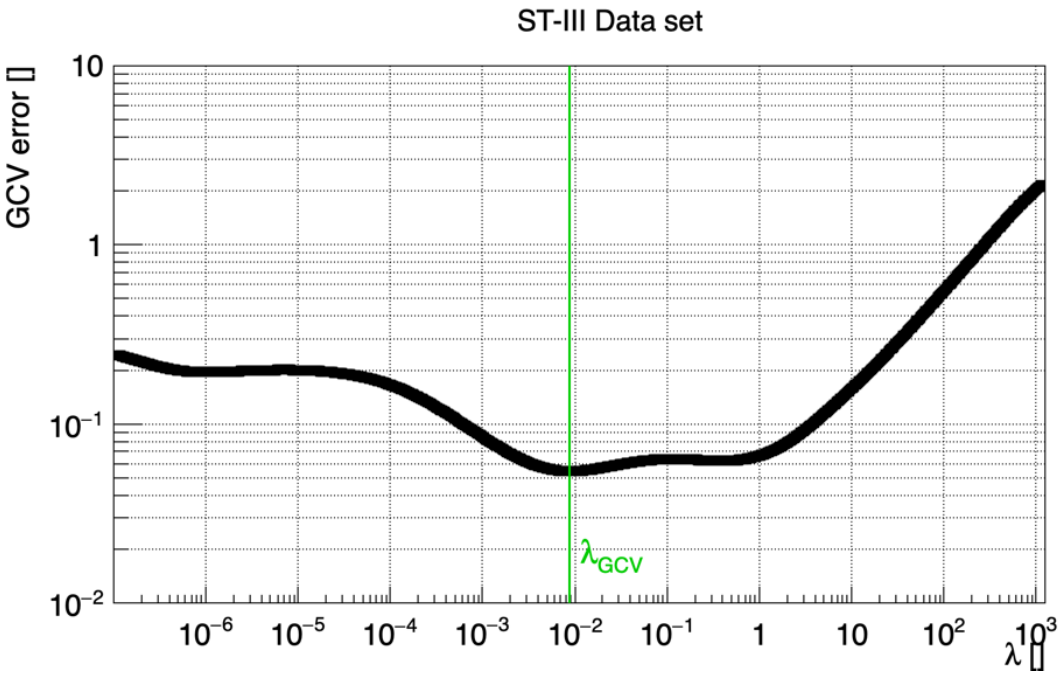

(b) Phase-III data set

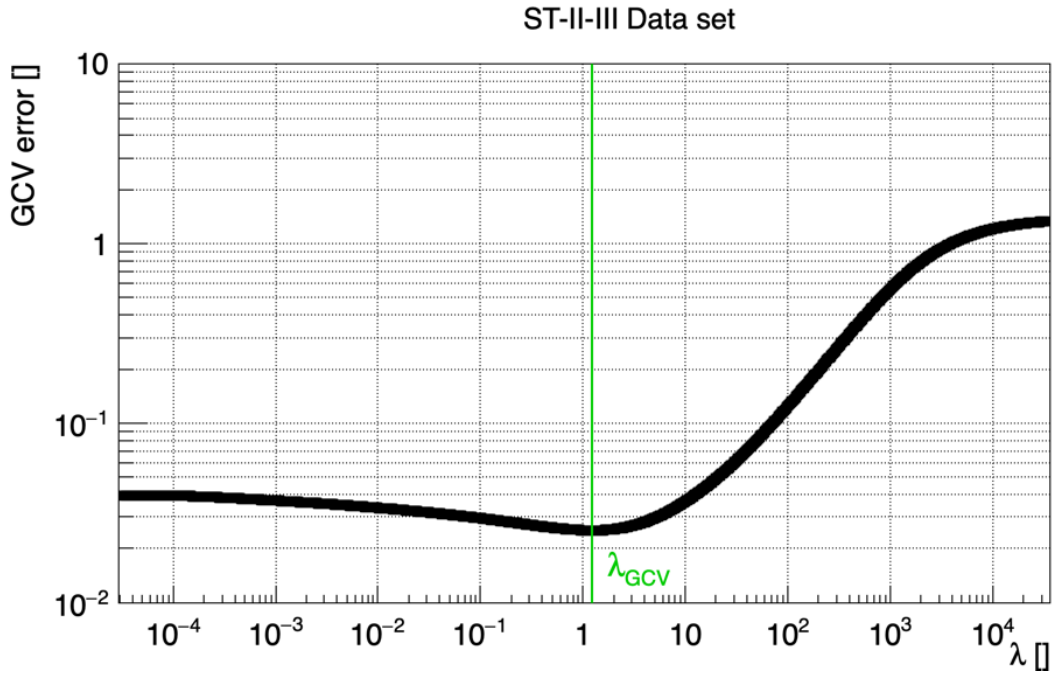

(c) Phase-II+III data set

Figure 6.18: **GCV error profile**, for Phase-II, III and II+III data sets. The green line represents the global minimum of the GCV error, which is nothing but the tuned value of the regularization strength λ_{GCV}.

To study the impact of this change in the prescription, we generate 10^4 pseudo-data, for Phase-II, -III and -II+III respectively around the nominal Huber predicted reconstructed energy spectrum normalized to the data spectrum of each phase. For each pseudo-data, we derive $\lambda^{\mathrm{old}}_{\mathrm{GCV}}$ and $\lambda^{\mathrm{new}}_{\mathrm{GCV}}$ from the old and new criterion respectively. This allows to plot the dispersion of λ_{GCV} for both criteria and each Phase. The result is displayed in Figure 6.19. The change in criterion has no impact on the dispersion of the tuned regularization strength for Phase-II+III pseudo-data set (Figure 6.19c). Yet, it translates into a sizeable narrowing of the distribution for Phase-II (Figure 6.19a) and -III (Figure 6.19b) pseudo-data set, which shows that the degeneracy of the GCV error profile preferably comes out for the data sets associated to these phases. In particular, the tail of the dispersion at the lowest values of λ is cut in the new approach, for both Phase-II and -III, as expected from the modified criterion. Furthermore, the regularization strength derived for Phase-III data set when applying the new criterion, displayed in plain red line in Figure 6.19b, seems fully consistent with the expected statistical distribution of regularization strengths. It also yields, *a posteriori*, to bias and error comparable to Phase-II and Phase-II+III unfoldings.

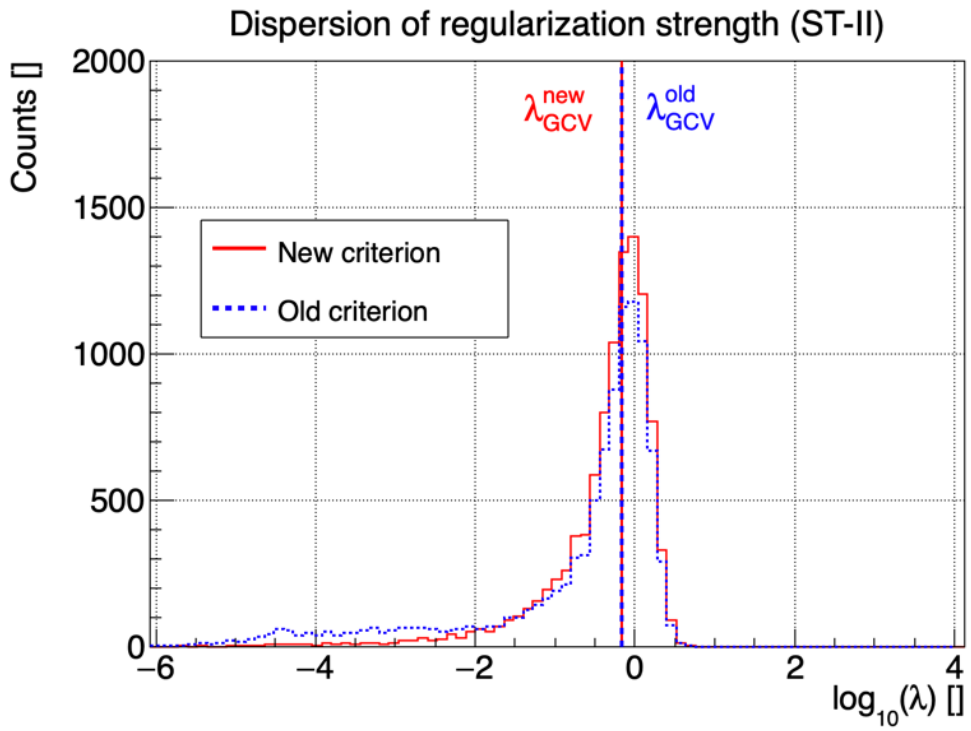

(a) Phase-II data set

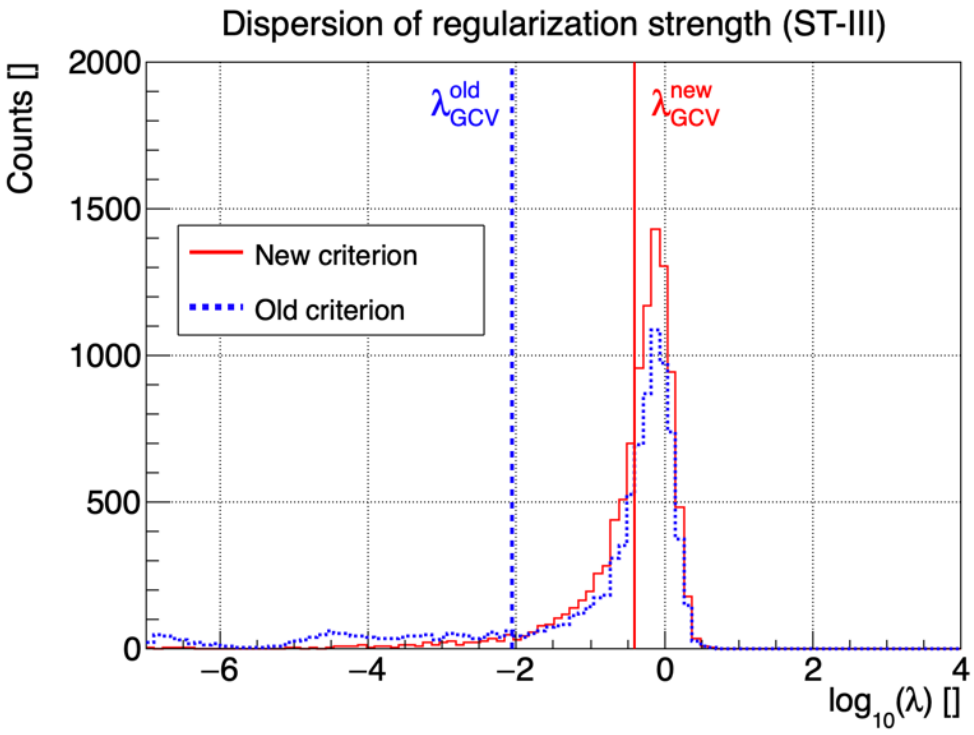

(b) Phase-III data set

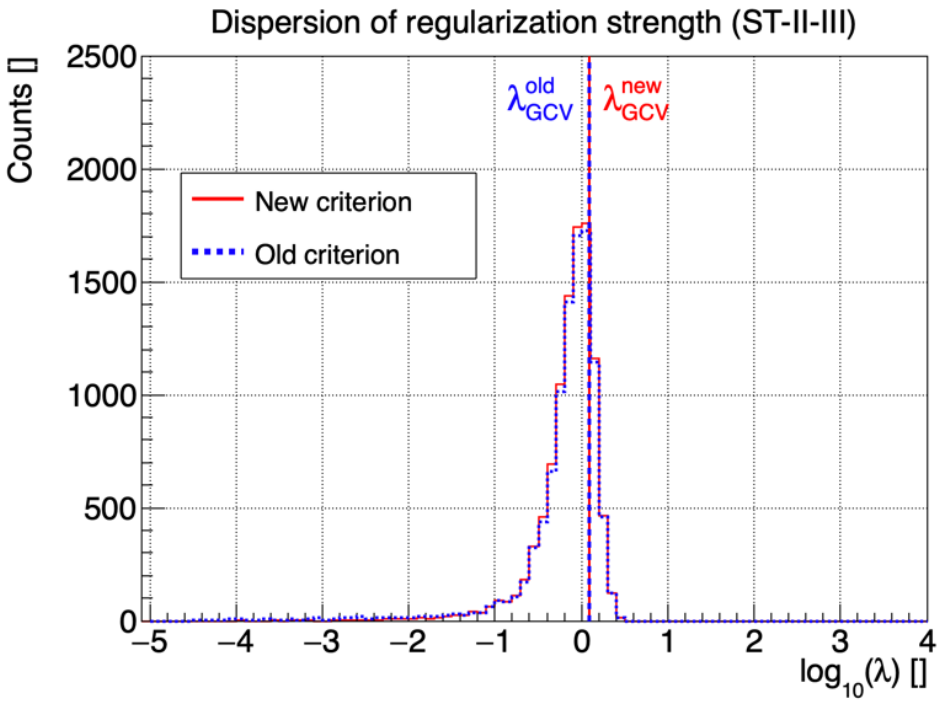

(c) Phase-II+III data set

Figure 6.19: **Statistical dispersion of the tuned regularization strength**, for the standard/old (dashed blue) and modified/new (plain red) GCV prescription. For each phase, the histograms were generated with 10^4 pseudo-data. For each phase, also shown in plain red (resp. dashed blue) line the regularization strength obtained for the true data set from the new (resp. old) prescription. See text for further details.

6.2.3 Unfolding results

6.2.3.1 STEREO unfolded spectra

Setting the regularization strength with the modified GCV prescription, we unfold the data of Phase-II, -III and -II+III respectively. The result is displayed in Figure 6.20 and is expressed in cm^2/fission/MeV. All spectra exhibit a smooth dependency over the whole energy range, thanks to the regularization. From the bias study that we carried out, we expect only sub-percent to percent level biases on the spectrum shape. At last, let's note that Phase-II+III unfolded spectrum lies between the Phase-II and -III separately unfolded spectra, as we would have anticipated.

The reference ^{235}U spectrum for the STEREO experiment is naturally the Phase-II+III unfolded spectrum, where the overall deficit and the local event excess around 5.5 MeV are blatant.

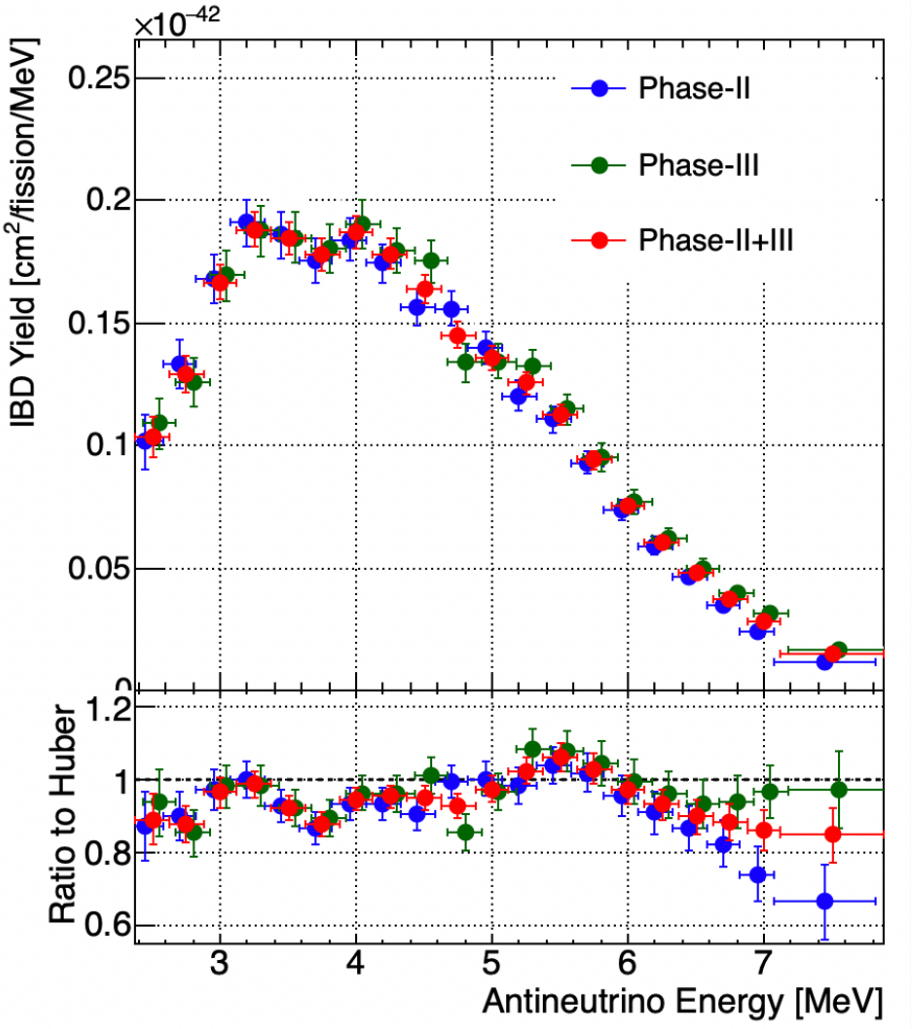

Figure 6.20: **STEREO ^{235}U unfolded spectra**, for Phase-II, -III and -II+III data. The energy bin centers of Phase-II (resp. -III) spectrum has been downwards- (resp. upwards-) shifted for display purposes. As expected, the Phase-II+III (red) spectrum lies between the Phase-II (blue) and -III (green) spectra. We retrieve both the flux and shape anomalies in the spectrum. For each spectrum, the reported uncertainties are the (square root of) diagonal elements of their associated covariance matrix.

6.2.3.2 Phase-II+III spectrum analysis

The overall unfolding result is actually threefold and consists of the unfolded spectrum $\hat{\Phi}$, its covariance matrix $V_{\hat{\Phi}}$, and the filter matrix A_c. In this subsection, we compare the Phase-II+III unfolded spectrum with the predictions from the Huber conversion model Φ_{HM} [55] and the Estienne, Fallot *et al.* (EF) summation model Φ_{SM} [51]. Both predicted spectra are obtained from the convolution of the predicted flux with the Strumia-Vissani IBD cross-section [46]. Following the prescription in [55], the reported uncertainties on the Huber predicted spectrum have been symmetrized in order to be included in a global covariance matrix $V_{\Phi_{\text{HM}}}$.

Rate analysis

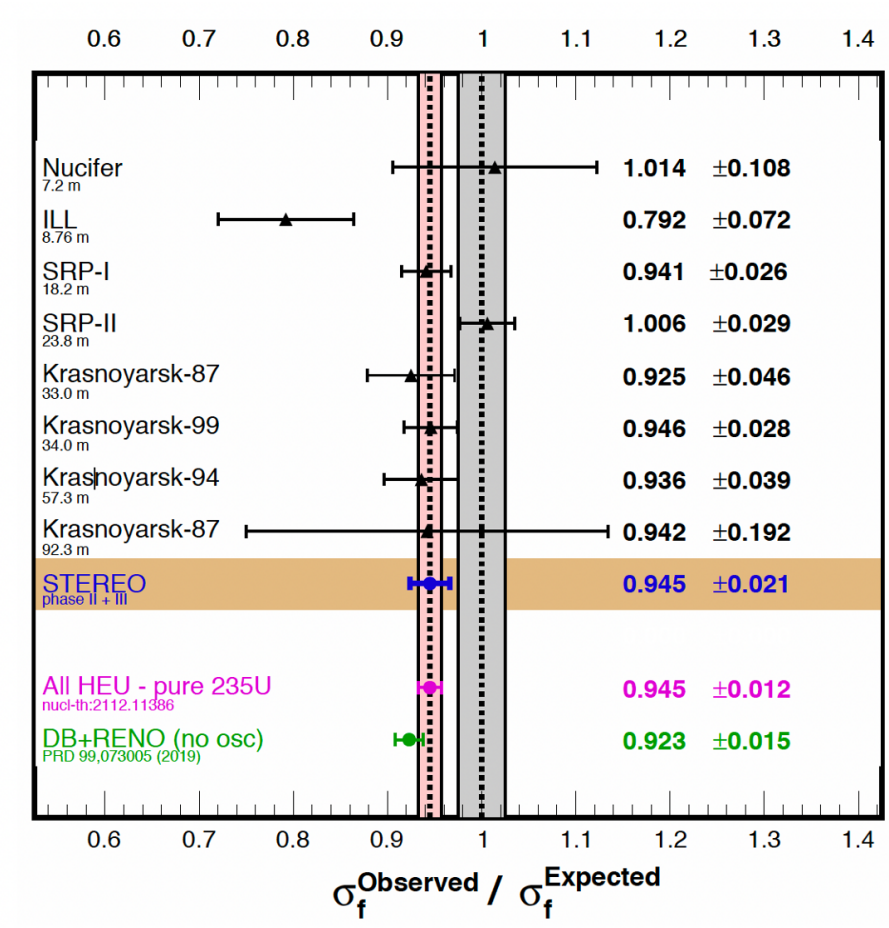

Figure 6.21: **IBD yield of ^{235}U fission**. Overview of the ratio of measured antineutrino flux from highly enriched in ^{235}U, or HEU, nuclear fuel relative to the Huber model. The grey band represents the model uncertainty on the ratios, that is common to all experiments. It is not propagated in the reported ratio uncertainties, that only account for experimental uncertainties. The STEREO measurement (in blue) turns out to be the most accurate to date and is found in excellent agreement with the world average (represented in magenta, with its error band). For comparison, we also display the measurement from Daya Bay and RENO with commercial reactors (in green), operated with lowly enriched in ^{235}U, or LEU, nuclear fuel. Contrary to direct measurements of ^{235}U fission yield, this value obtained from LEU experiments relies on reactor evolution simulations to separate the contribution of ^{235}U from other isotopes.

Integrating the Phase-II+III unfolded spectrum in antineutrino energy space in the [2.375, 7.875] MeV analysis range, one ends up with an IBD yield σ_f of $(5.96 \pm 0.13) \cdot 10^{-43}$ cm^2/fission/MeV, to be compared with the $(6.30 \pm 0.14) \cdot 10^{-43}$ (resp. $5.91 \cdot 10^{-43}$) cm^2/fission/MeV of the Huber (resp. EF) prediction for ^{235}U. We note that the EF model yields to a value of the predicted antineutrino flux consistent with the data, as opposed to the Huber model. Still, evaluating the deficit with respect to the standard Huber prediction yields to a value of: (5.5±2.1 [exp.]±2.2 [model])%. This measurement is the most accurate to date and is in agreement with the world average, as illustrated in Figure 6.21.

Shape analysis

Now, we investigate the shape anomaly and aims at quantifying the significance of the local event excess around 5.5 MeV with respect to the Huber prediction.

Bias correction

The filter matrix of Phase-II+III unfolding is displayed in Figure 6.22. The non-vanishing sub- and super-diagonal elements are the signature of the short-range correlations induced by the regularization.

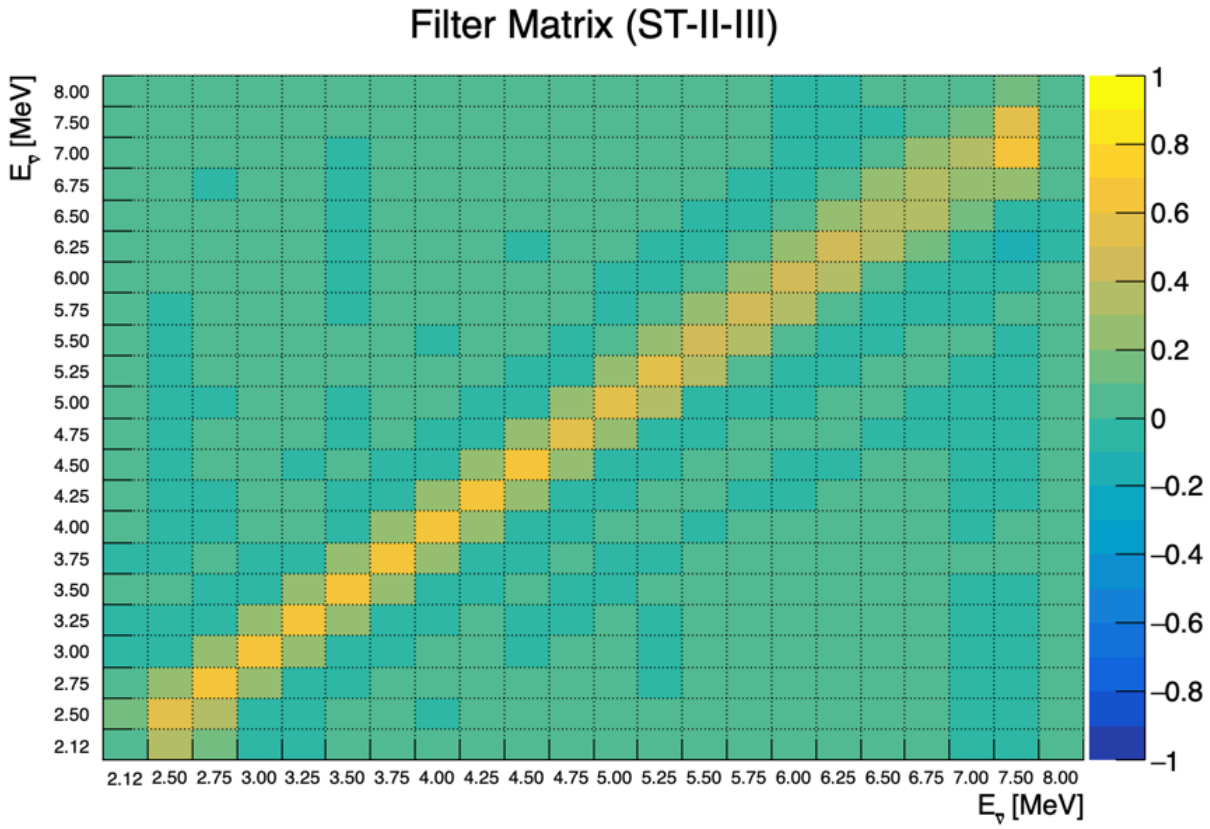

Figure 6.22: **Filter matrix of Phase-II+III unfolding**. The non-vanishing matrix elements are close to the diagonal, as they reflect the short-range bin-to-bin correlations induced by the regularization.

In order to render the data-to-prediction comparison free of unfolding bias, the unfolded spectrum should be compared to the filtered prediction instead of the nominal prediction.

Whereas the bias induced on the Huber prior spectrum is 0 as already demonstrated, small biases are expected in the case of the ^{235}U summation model spectrum. They are found to be at the sub-percent to percent level (see Figure 6.23), mostly in the high energy end of the spectrum, and consistent with the bias study that we carried out in Section 6.2.2.4.

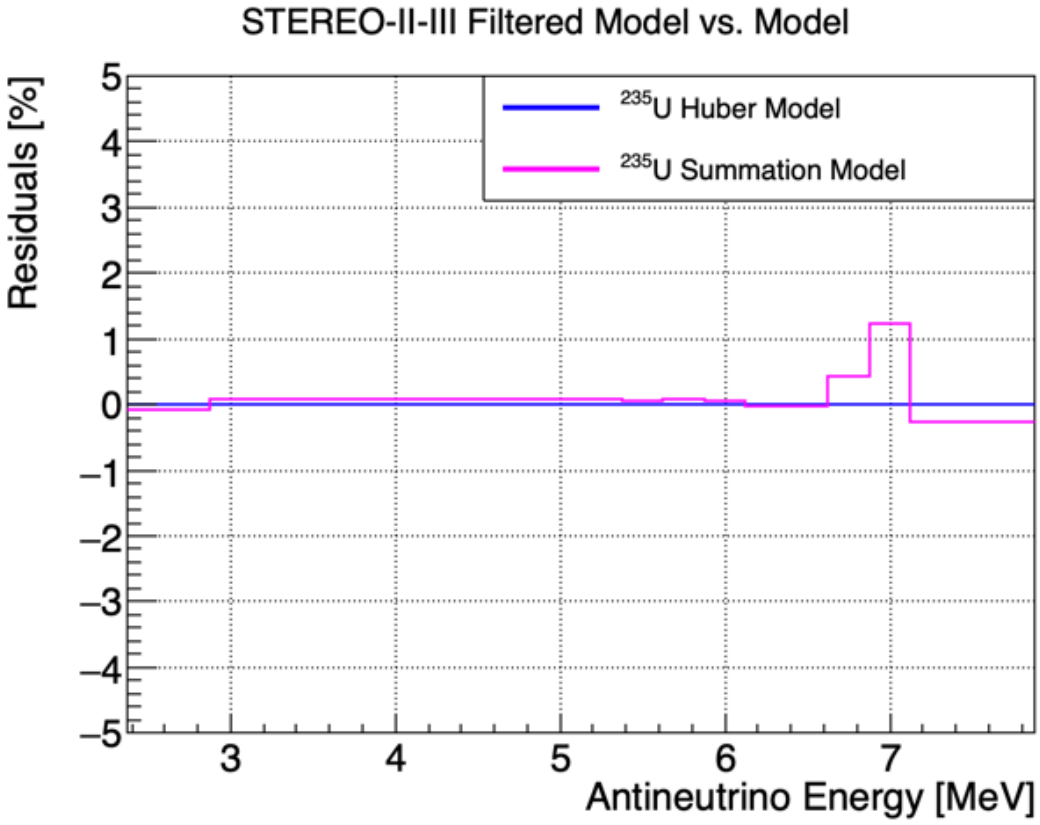

Figure 6.23: **Comparison of the filtered and unfiltered predictions**. As expected, the residuals are 0 for the Huber model spectrum used as a prior for the regularization, whereas small biases are highlighted for the summation model spectrum.

Test statistics for model comparison

The prediction that we use to fit the unfolded spectrum writes as follows:

$$\Phi_{\alpha,A,\mu,\sigma}\left(E_{\bar{\nu}}\right) = \Phi_{\mathrm{HM}}\left(E_{\bar{\nu}}\right) \cdot \alpha \left(1 + A \cdot \exp - \frac{\left(E_{\bar{\nu}} - \mu\right)^2}{2\sigma^2}\right) \tag{6.28}$$

where α is meant to absorb the overall rate discrepancy whereas A, μ and σ ought to describe the gaussian-shaped distortion with respect to the nominal Huber prediction. We use the likelihood ratio as a test statistic to quantify the significance of this distortion.

In this picture, the naive approach would consist in computing the following $\Delta\chi^2$ quantity:

$$\Delta\chi^2_{\hat{\Phi}} = \chi^2\left(\hat{\alpha}, A = 0, \mu = 0, \sigma = 0 | \hat{\Phi}\right) - \chi^2\left(\hat{\alpha}, \hat{A}, \hat{\mu}, \hat{\sigma} | \hat{\Phi}\right) \tag{6.29}$$

where:

$$\begin{aligned}\chi^2\left(\alpha, A, \mu, \sigma|\hat{\Phi}\right) &= \chi^2_{\text{unfiltered}}\left(\alpha, A, \mu, \sigma|\hat{\Phi}\right) \\ &= \left\|\hat{\Phi} - \Phi_{\alpha,A,\mu,\sigma}\right\|^2_{\left(V_{\hat{\Phi}}+\alpha^2 V_{\Phi_{\text{HM}}}\right)^{-1}}\end{aligned} \tag{6.30}$$

and the hat parameters $\{\hat{\alpha}, \hat{A}, \hat{\mu}, \hat{\sigma}\}$ denote the best-fit parameters that minimize the χ^2.

However, such reasoning leads to compare the biased unfolded spectrum with an unbiased nominal prediction. In order to render the comparison insensitive to unfolding bias, one would rather compare the unfolded spectrum to the filtered prediction, such that the χ^2 now writes:

$$\begin{aligned}\chi^2\left(\alpha, A, \mu, \sigma|\hat{\Phi}\right) &= \chi^2_{\text{filtered}}\left(\alpha, A, \mu, \sigma|\hat{\Phi}\right) \\ &= \left\|\hat{\Phi} - A_c \cdot \Phi_{\alpha,A,\mu,\sigma}\right\|^2_{\left(V_{\hat{\Phi}}+\alpha^2 A_c \cdot V_{\Phi_{\text{HM}}} \cdot A_c^T\right)^{-1}}\end{aligned} \tag{6.31}$$

Let's note that the filter matrix is applied on both the predicted spectrum and its covariance matrix. We discuss in Appendix C why this test statistic enables to correct for the unfolding bias in antineutrino energy space.

We also perform the test statistic in reconstructed energy space, where the unfolded spectrum passes through the response matrix instead of the filter matrix. It is defined as follows and without unfolding:

$$\begin{aligned}\Delta\chi^2_D &= \chi^2\left(\hat{\alpha}, A = 0, \mu = 0, \sigma = 0|D\right) - \chi^2\left(\hat{\alpha}, \hat{A}, \hat{\mu}, \hat{\sigma}|D\right) \\ \chi^2\left(\alpha, A, \mu, \sigma|D\right) &= \left\|D - R \cdot \Phi_{\alpha,A,\mu,\sigma}\right\|^2_{\left(V+\alpha^2 R \cdot V_{\Phi_{\text{HM}}} \cdot R^T\right)^{-1}}\end{aligned}$$

The result of each test statistic in antineutrino and reconstructed energy spaces is shown in Table 6.2, the reference being the one carried out in antineutrino energy space with the filter matrix. This latter test yields to identical results with respect to the test statistic performed in reconstructed energy space. In other words, in terms of statistical inference, the reconstructed energy data set $\{D, V, R\}$ yields to equivalent results to the antineutrino energy data set $\left\{\hat{\Phi}, V_{\hat{\Phi}}, A_c\right\}$. This shows that providing the triplet: unfolded spectrum, covariance matrix and filter matrix as the unfolding result fully encodes the experimental constraints without biases, thus allowing to render the analysis results framework-independent.

The rescaled nominal Huber prediction is found to be in poor agreement with the data, with a $\chi^2/\text{dof} = 47.3/21$. The addition of the gaussian bump on top of this prediction is found to improve the χ^2 by 29 units, corresponding to a (one-sided) significance of 4.6σ for the bump. The amplitude of the 5.5 MeV bump is reconstructed at $(15.6 \pm 5.2)\%$ and its width at (0.308 ± 0.143) MeV. The data-to-prediction comparison as well as the best-fit bump are all summarized in Figure 6.23, in antineutrino energy space. Up to the 5.5 MeV bump, the summation model is found to be in rather good agreement with the STEREO data, yielding to a $\chi^2/\text{dof} = 30.1/22$.

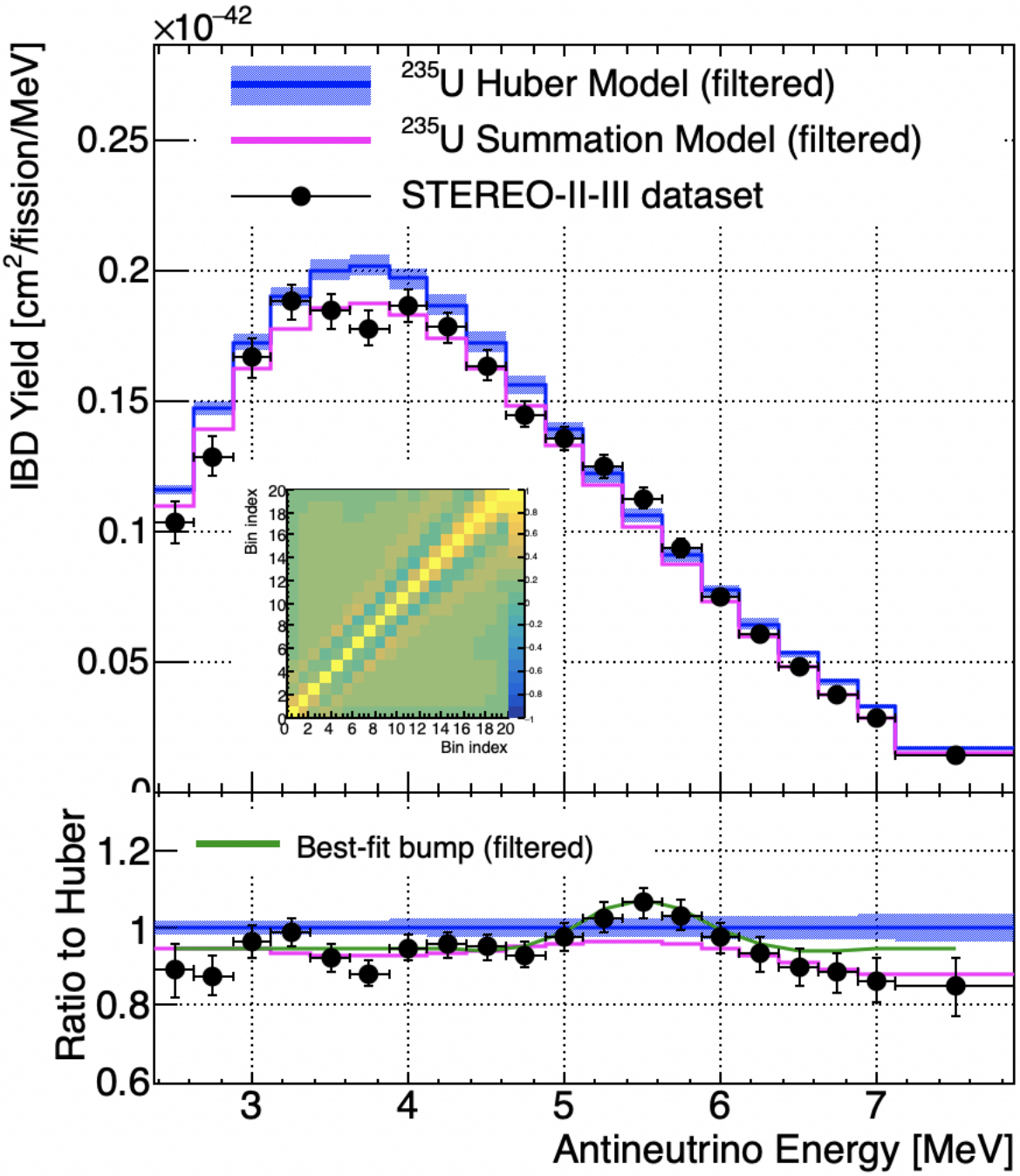

Figure 6.24: **Comparison of ^{235}U Phase-II+III unfolded spectrum with Huber and Summation filtered model spectra**. The unfolded spectrum is compared to filtered predictions, accounting for the unfolding bias. Let's remind that the filtered Huber model equals the nominal Huber model, whereas small high energy biases are corrected for the summation model. Up to the 5.5 MeV event excess, the summation model is found to fairly describe the STEREO data. Furthermore, the correlation matrix of the unfolded spectrum is displayed in the inset of the top pad. It is dominated by short-range correlations induced by the regularization. The moderate long-range correlations originate mostly from the normalization uncertainty of the Phase-II+III data spectrum.

ST-II-III	Antineutrino Energy space				Reconstructed Energy space	
	w/o. Filter		w. Filter		w. Response	
HM Comparison	**Shape–only**	**Best-fit bump**	**Shape–only**	**Best–fit bump**	**Shape–only**	**Best–fit bump**
α	0.945 ± 0.026	0.943 ± 0.027	$\mathbf{0.944 \pm 0.026}$	$\mathbf{0.943 \pm 0.027}$	0.944 ± 0.026	0.943 ± 0.027
A [%]	0 ± 0	14.4 ± 3.6	$\mathbf{0 \pm 0}$	$\mathbf{15.6 \pm 5.2}$	0 ± 0	15.5 ± 5.1
μ **[MeV]**	0 ± 0	5.505 ± 0.089	$\mathbf{0 \pm 0}$	$\mathbf{5.500 \pm 0.092}$	0 ± 0	5.500 ± 0.092
σ **[MeV]**	0 ± 0	0.339 ± 0.112	$\mathbf{0 \pm 0}$	$\mathbf{0.308 \pm 0.143}$	0 ± 0	0.311 ± 0.143
χ^2**/dof**	41.3/21	12.3/18	**47.3/21**	**18.3/18**	66.0/43	36.7/40
$\Delta\chi^2/\Delta$**dof**	29.0/3		**29.0/3**		29.3/3	
Significance (one-sided)	4.6σ		$\mathbf{4.6\sigma}$		4.6σ	

Table 6.2: **Best-fit bump for ^{235}U Phase-II+III unfolded spectrum**. In antineutrino energy space, the fit is done alternatively without and with the application of the filter matrix. As expected, the reconstructed bump is flattened (i.e. lower amplitude A and higher width σ) when not correcting the fit from the regularization filter. Furthermore, as predicted, the fit through the filter matrix in antineutrino energy space and through the response matrix in reconstructed energy space yield to nigh-identical fitted parameters for the best-fit bump. Overall, the local event excess at 5.5 MeV is found to be at the $(15.6 \pm 5.2)\%$ level, with a 4.6σ (one-sided) significance.

Chapter 7

Global analyses of reactor antineutrino spectra

In this Chapter, we present the extension of the framework to the joint unfolding of STEREO and PROSPECT highly-enriched in ^{235}U (HEU) data sets, to provide the most accurate measurement of the ^{235}U spectrum to date. At last, the extension of this approach to the unfolding of Daya Bay lowly-enriched in ^{235}U (LEU) data allowed to shed a new light on the antineutrino spectrum induced by the fission of plutonium, complementary to the published study of the Daya Bay collaboration.

7.1 HEU global analysis

In Section 6.2, we provided a reference ^{235}U fission-induced antineutrino spectrum extracted from the full data set of the STEREO experiment. Another leading HEU-based effort is the one of the PROSPECT collaboration [145]. Operating also in close vicinity to a research nuclear reactor highly-enriched in ^{235}U, the PROSPECT experiment exhibits a similar physics reach to that of STEREO, and the collaboration already published their own searches for short-baseline neutrino oscillations and measurement of the ^{235}U antineutrino spectrum [114, 146].

Thanks to the large statistics available and accurate control of all detection effects, PROSPECT and STEREO provide an opportunity to study the ^{235}U antineutrino spectrum with unprecedented precision. This ambition triggered a cross-collaboration between both experiments, that led to the publication of a jointly ^{235}U unfolded spectrum, using the unnormalized PROSPECT and STEREO Phase-II data sets to feed the Tikhonov unfolding framework described in the previous section [147]. In particular, this approach was compared to the Wiener-SVD unfolding approach, and it was checked that both frameworks indeed yield to the same results in terms of shape analysis, provided the appropriate filter matrix is handed over [148].

We present in this section an update of the HEU spectrum analysis of [147], now including the full information provided by the final Phase-II+III STEREO data set. The ^{235}U unfolded spectrum that will be derived will then be constrained with the largest HEU statistical data set to date. Such a combined analysis is expected to reduce the effect of experiment-related systematics and produce a robust ^{235}U unfolded spectrum.

7.1.1 The PROSPECT experiment

The PROSPECT experiment is located within the High Flux Isotope Reactor (HFIR) facility at Oak Ridge National Laboratory. HFIR uses a 85 MW_{th} compact core, of 50 cm height and 45 cm diameter. It is enriched with 93% ^{235}U fuel and operates with a 24-day reactor-on cycle. More than 99% of the antineutrino flux at the detector site comes from ^{235}U fissions, with small non-fuel contributions coming from activated ^{28}Al and ^{6}He in structural materials [149].

The PROSPECT detector (see Figure 7.1) is placed at a very short baseline (6.7 – 9.3 m) from the reactor core. It consists of a ∼4 t ^{6}Li-loaded liquid scintillator (LiLS) target, in which antineutrinos are detected through the IBD process. The IBD neutron preferentially captures on ^{6}Li within ∼50 μs, producing ^{3}H and ^{4}He ions with 4.78 MeV energy. This energy is locally deposited in the liquid scintillator and produces visible light. The detector, sketched in Figure 7.1, is separated into 154 segments by reflector panels with enclosed PMTs on each end, dedicated to the light collection. The PSD capability of the LiLS allows a good separation of both electron-like recoil events from the prompt IBD signal *and* nuclear-like recoil events from the delayed IBD signal. This key feature of the PROSPECT detection technology, combined with background suppression from fiducialization, cosmic vetoing, and position reconstruction, makes up for the mild cosmic shielding of the experiment (at the level of only 0.5 m.w.e.), and allows to reach a signal-to-correlated background ratio of 1.4 in the signal energy range.

Comprehensive detector simulations, coupled to extensive calibrations carried out with point-like γ sources and neutron sources, as well as the study of the cosmogenic ^{12}B spectrum, enable to achieve a percent level accuracy in the description of the detector energy response.

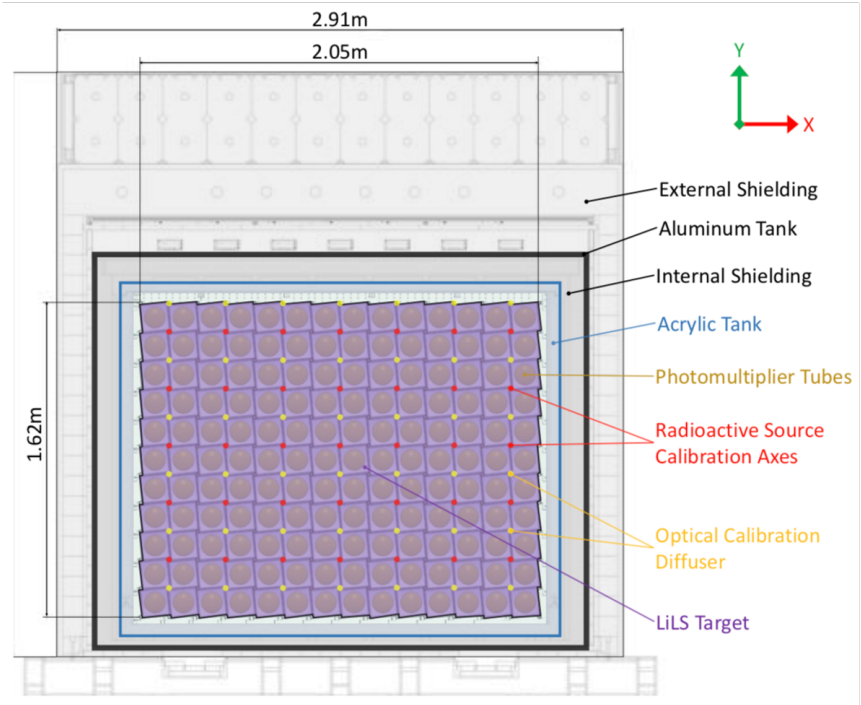

Figure 7.1: **Top-view diagram of the PROSPECT detector design**. Source [114].

7.1.2 PROSPECT Inputs

Detected spectrum and uncertainties

The PROSPECT detected antineutrino spectrum, displayed in Figure 7.2, consists of 32 200keV-wide reconstructed energy bins, ranging from 0.800 MeV (lower edge of first bin) to 7.200 MeV (upper edge of last bin). It corresponds to 82 live-days of exposure, yielding ∼50k IBD candidates after background subtraction. Therefore, the dominant source of uncertainty is statistics, to which add up sub-dominant contributions coming from detector- and model-related uncertainties. They are summarized in Figure 7.3 and included in the PROSPECT experimental covariance matrix. While the PROSPECT spectrum shows hints for a local event excess around 5 MeV with respect to the Huber prediction, it is not normalized to the IBD fission yield.

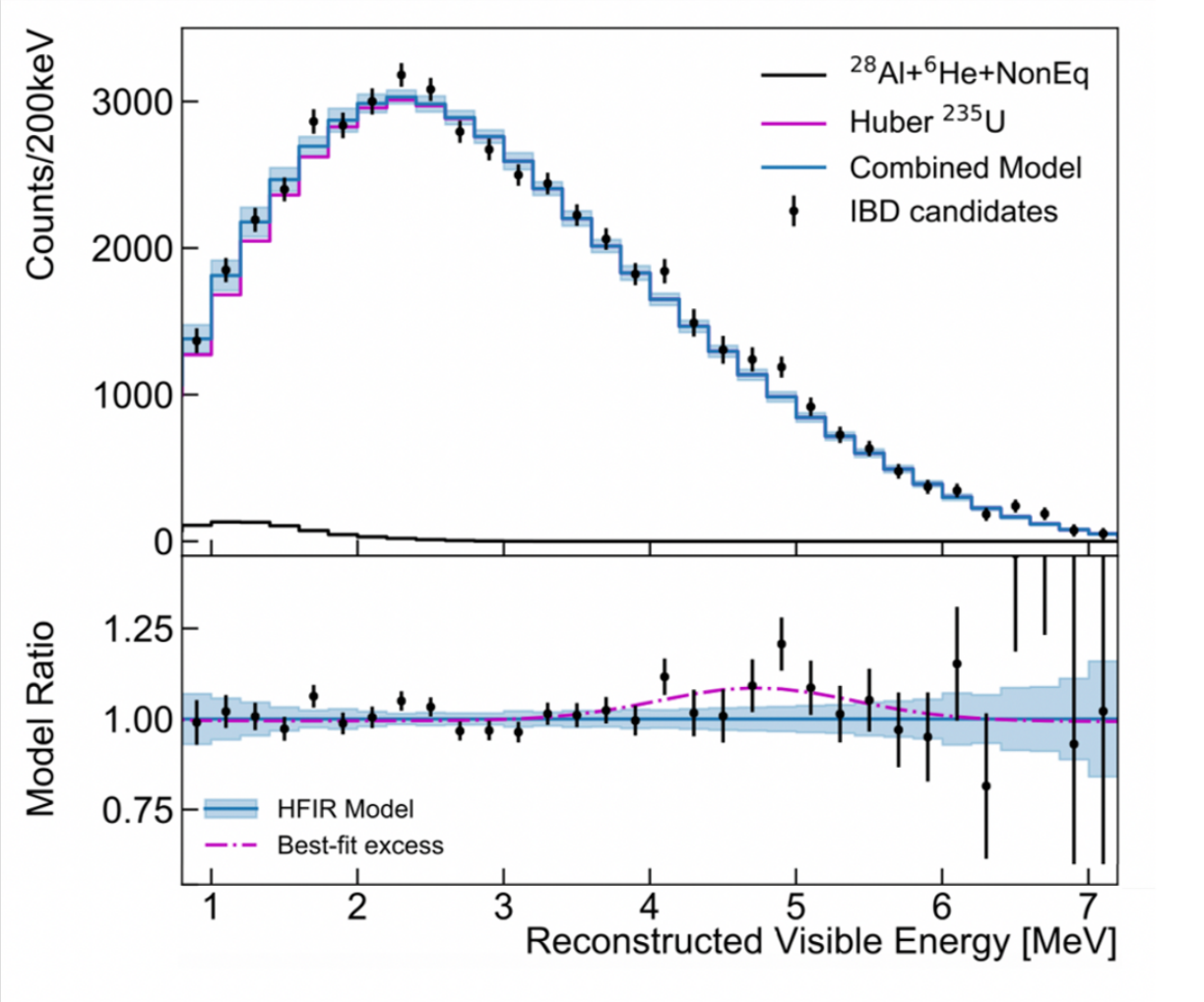

Figure 7.2: **PROSPECT measured ^{235}U spectrum**. *Top*: Detected spectrum (black dots), ranging from 0.8 to 7.2 MeV in reconstructed energy space. It is compared to the Huber ^{235}U model completed with the HFIR flux corrections (plain blue line). The normalization factor of the overall prediction with respect to the detected spectrum is determined by means of a least-square method. *Bottom*: Ratio of the detected spectrum to the combined prediction. The 5 MeV event excess is fitted with a gaussian model, with fixed mean and sigma, extracted from the Daya Bay spectrum [111], and free-floating amplitude. The best-fit bump size relative to Daya Bay was found to be 84% ± 39%. Source [114].

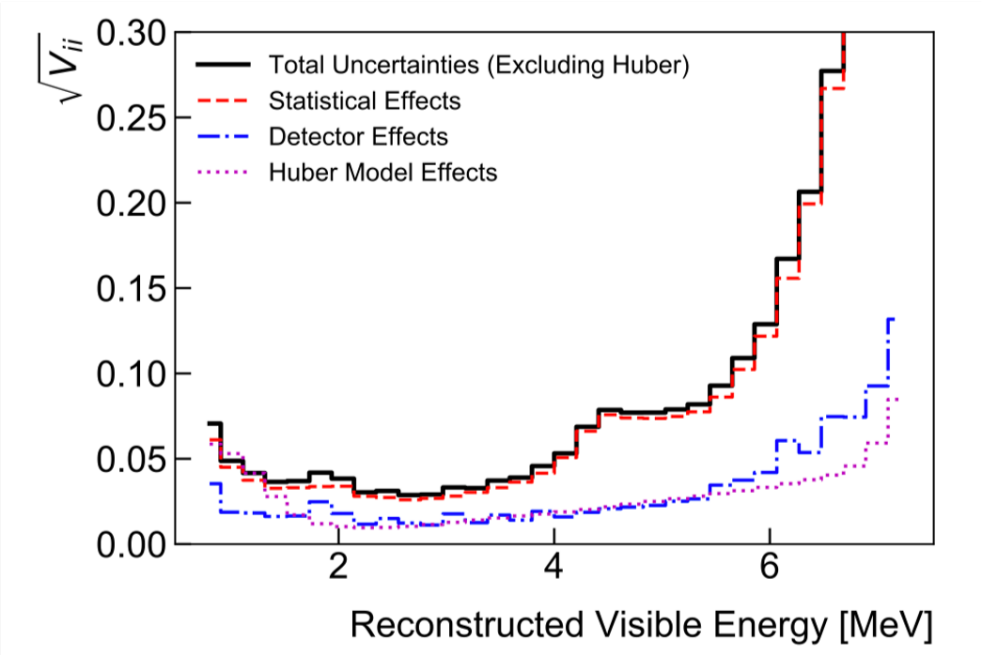

(a) Uncertainties on PROSPECT measured spectrum

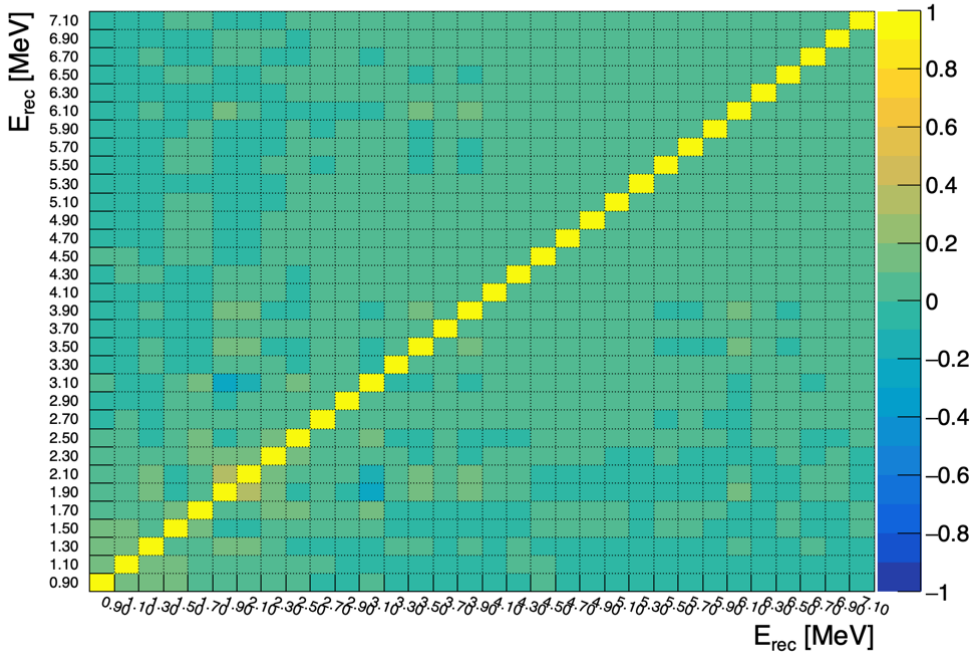

(b) PROSPECT experimental correlation matrix

Figure 7.3: **Uncertainty budget of PROSPECT reconstructed energy spectrum**. (a) The reported uncertainties correspond to the breakdown of the contributions to the overall diagonal elements of PROSPECT experimental covariance matrix. The PROSPECT data set is found to be statistics limited, with sub-leading contributions coming from detector effects and model uncertainties [114]. The bin-to-bin correlations, encompassed in the experimental correlation matrix (b), mostly consist of short-range correlations, with mild long-range correlations. Given the absence of absolute normalization of the PROSPECT spectrum, no normalization uncertainty is included.

Response matrix

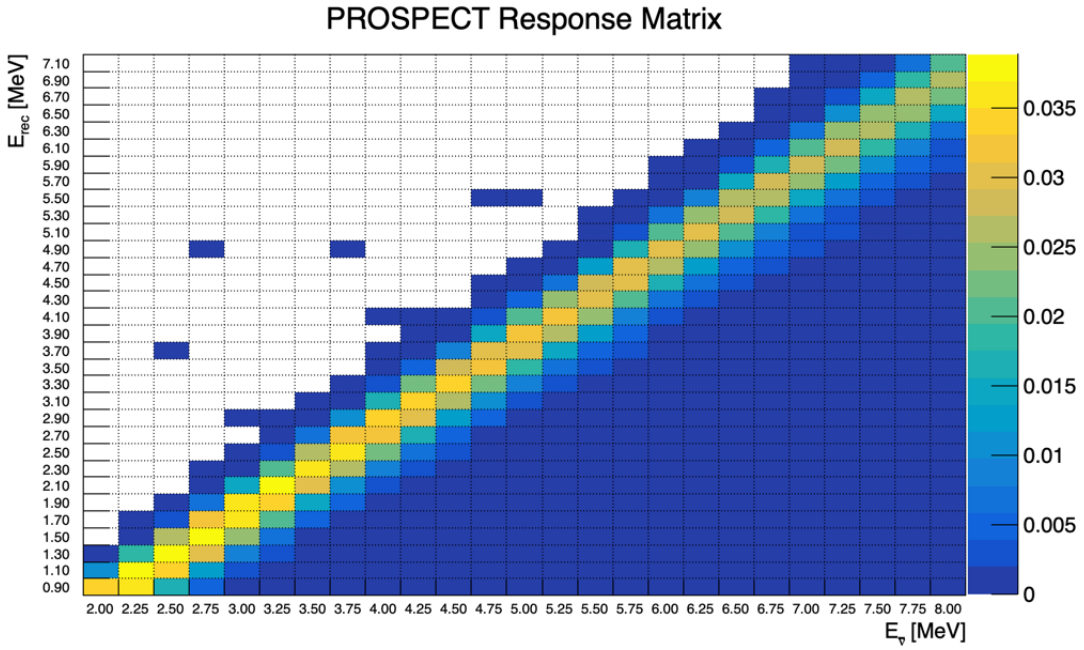

Figure 7.4: **PROSPECT Response Matrix**.

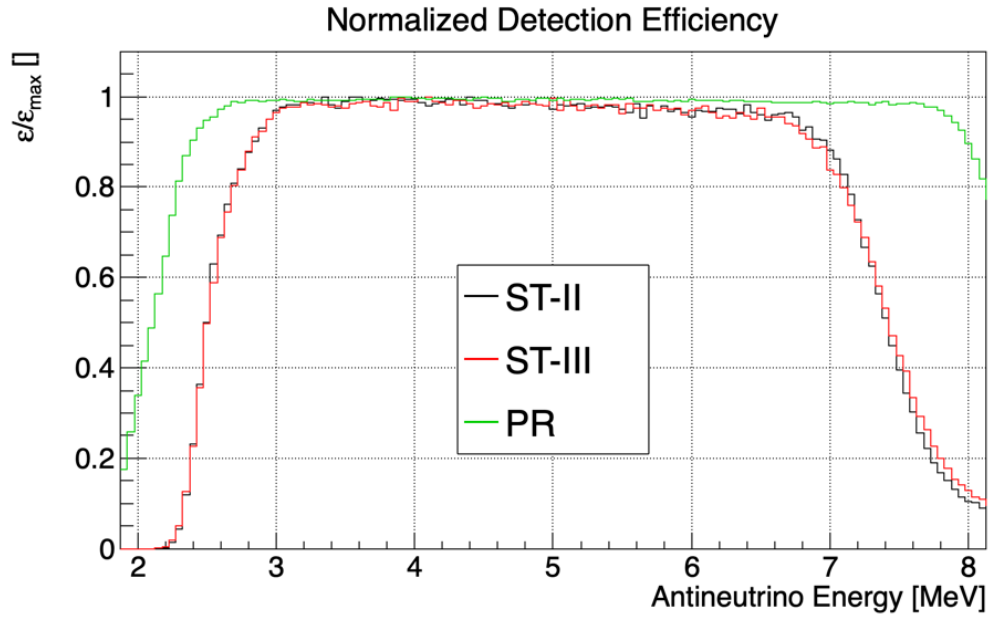

Figure 7.5: **Normalized selection efficiency for STEREO and PROSPECT data sets**, reported in 50-keV wide antineutrino energy bins. Noticeably, the PROSPECT data set brings constraints on the low and high energy ends of the antineutrino spectrum, that are poorly constrained by the sole STEREO data set.

The PROSPECT response matrix is shown in Figure 7.4. Its matrix element is given by Equation 6.12, as for the STEREO experiment.

Additionally, we compare in Figure 7.5 the selection efficiency of the STEREO and PROSPECT data sets. Given that the PROSPECT spectrum is not normalized as compared

to the STEREO spectrum, the comparison is carried out on the normalized efficiencies. The PROSPECT efficiency exhibits a flatter trend across the antineutrino energy range, thus bringing stringent experimental constraints on the low and high energy parts of spectrum, to which STEREO is less sensitive. This allows to define a finer antineutrino energy binning in the low and high energy ends of the spectrum for the overall STEREO-PROSPECT unfolding, still ranging from 1.875 to 8.125 MeV, yet with 250keV-wide bins across the whole range.

7.1.3 Normalization of PROSPECT data

In the absence of absolute normalization for the PROSPECT data set, we decide to normalize it to the STEREO data set, prior to the joint STEREO-PROSPECT unfolding. Given that the PROSPECT and STEREO reconstructed energy spaces cannot be put on an equal footing, the normalization must be done through the respective response matrices in antineutrino energy space. Thus, the relative normalization factor α is obtained from the numerical minimization of the subsequent χ^2:

$$\chi^2(\alpha) = \left\| D_{\mathrm{ST}} - R_{\mathrm{ST}} \cdot \hat{\Phi}(\alpha) \right\|^2_{V_{\mathrm{ST}}^{-1}} + \left\| D_{\mathrm{PR}} - \alpha * R_{\mathrm{PR}} \cdot \hat{\Phi}(\alpha) \right\|^2_{V_{\mathrm{PR}}^{-1}} \tag{7.1}$$

where the subscript ST refers to ST-II+III and PR to PROSPECT:

$$\hat{\Phi}(\alpha) = \left(R_{\mathrm{ST}}^T V_{\mathrm{ST}}^{-1} R_{\mathrm{ST}} + \alpha^2 * R_{\mathrm{PR}}^T V_{\mathrm{PR}}^{-1} R_{\mathrm{PR}} \right)^{-1} \cdot \left(R_{\mathrm{ST}}^T V_{\mathrm{ST}}^{-1} D_{\mathrm{ST}} + \alpha * R_{\mathrm{PR}}^T V_{\mathrm{PR}}^{-1} D_{\mathrm{PR}} \right)$$

proceeding from the minimization of Equation 7.1 with respect to Φ, at fixed α.

Doing so, the STEREO and PROSPECT data sets cannot be treated anymore as independent sets, given the correlations introduced by the *ad hoc* normalization. To propagate these correlations to the joint STEREO-PROSPECT experimental covariance matrix, one proceeds as follows:

1. Generate 10^6 STEREO and PROSPECT uncorrelated pseudo-data,
2. For each pseudo-data, compute the associated PROSPECT normalization parameter α. The normalized PROSPECT reconstructed energy spectrum is then merely $\alpha^{-1} * D_{\mathrm{PR}}$,
3. Compute numerically the STEREO-PROSPECT covariance matrix element for the normalized spectra. It is defined as: $V^{i,i'}_{\mathrm{ST-PR}} = \mathrm{Cov}\left(D^i_{\mathrm{ST-PR}}, D^{i'}_{\mathrm{ST-PR}}\right)$, where:

$$D_{\mathrm{ST-PR}} = \begin{bmatrix} D_{\mathrm{ST-II}} \\ D_{\mathrm{ST-III}} \\ \alpha^{-1} * D_{\mathrm{PR}} \end{bmatrix}$$

With this procedure, one obtains the PROSPECT spectrum normalized to STEREO data displayed in Figure 7.6. The joint STEREO-PROSPECT correlation matrix is given in Figure 7.7. The non-vanishing long-range correlations that appears now in the PROSPECT block-diagonal covariance matrix and the cross-correlations between STEREO and PROSPECT originate from the propagation of the uncertainties of the *ad hoc* normalization.

At last, let's note that the minimization of the χ^2 in Equation 7.1 yields to a value of $\chi^2/\mathrm{dof} = 52.4/76$, which demonstrates the statistical compatibility of STEREO and PROSPECT data sets in terms of spectral shape, and justifies *a priori* the joint unfolding of both sets.

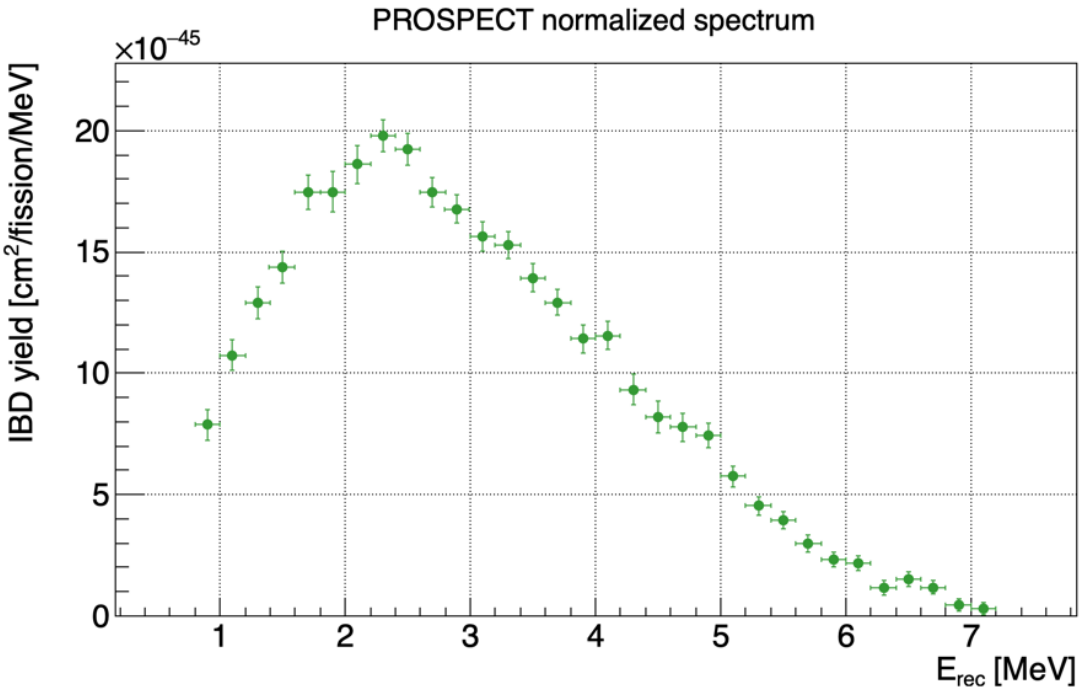

Figure 7.6: **Prospect measured ^{235}U spectrum, normalized to Stereo data set.**

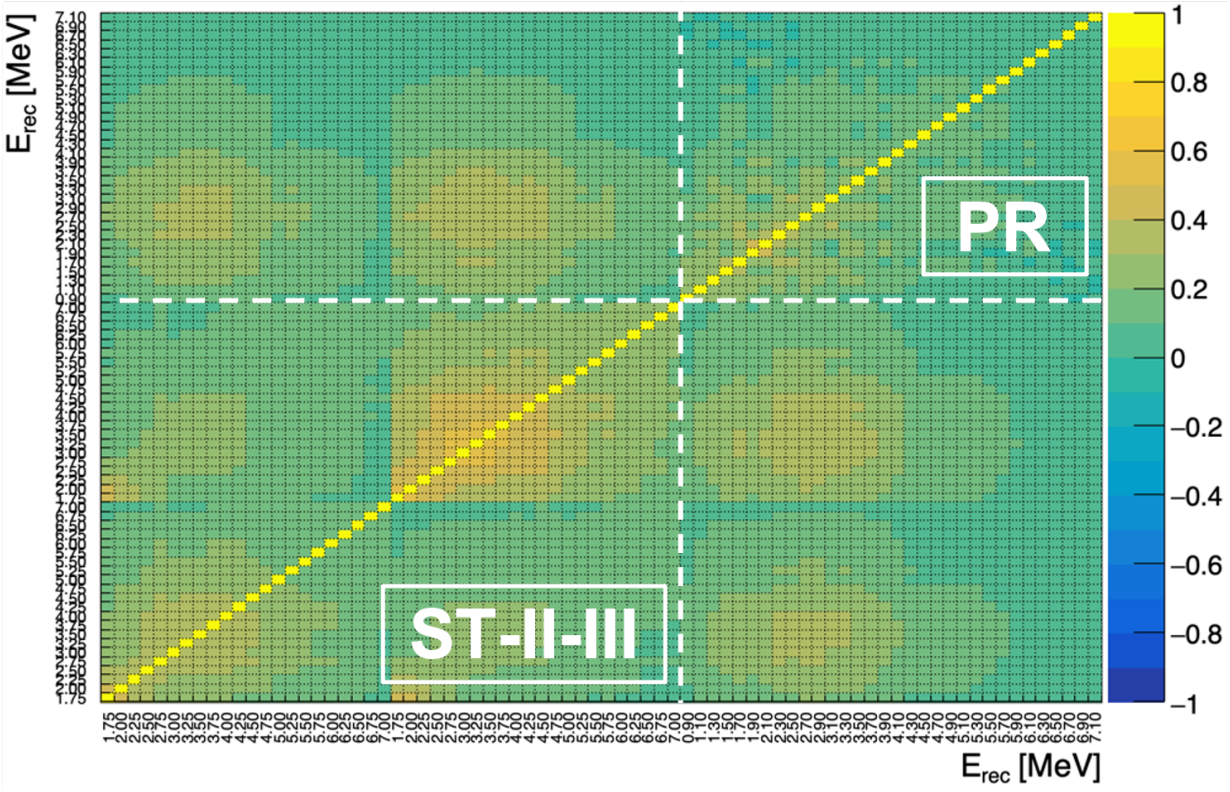

Figure 7.7: **Stereo-Prospect joint correlation matrix**. The ST-II-III diagonal block is equal to the Stereo prompt correlation matrix of Figure 6.13. The long-range correlations in Prospect diagonal block as well as the Stereo-Prospect cross-correlations originate from the propagation of Stereo normalization uncertainties in Prospect data.

7.1.4 HEU unfolding results

We apply the routine described in the STEREO-only unfolding, on the HEU variables defined as follows:

$$\begin{cases} D_{HEU} &= \begin{bmatrix} D_{\text{ST-II}} \\ D_{\text{ST-III}} \\ D_{\text{PR}} \end{bmatrix} \\ R_{HEU} &= \begin{bmatrix} R_{\text{ST-II}} \\ R_{\text{ST-III}} \\ R_{\text{PR}} \end{bmatrix} \\ V_{HEU} &= \begin{bmatrix} V_{\text{ST-II}} & V_{\text{ST-II/III}} & V_{\text{ST-II/PR}} \\ V^T_{\text{ST-II/III}} & V_{\text{ST-III}} & V_{\text{ST-III/PR}} \\ V^T_{\text{ST-II/PR}} & V^T_{\text{ST-III/PR}} & V_{\text{PR}} \end{bmatrix} \end{cases} \tag{7.2}$$

where the PROSPECT spectrum and covariance are normalized to the STEREO data, with the aforementioned procedure. The regularization strength associated to this HEU joint unfolding is found to be of the order of unity, yielding regularization-induced smoothing comparable to that of the STEREO-only unfolding.

In Figure 7.8, we compare the result of the STEREO-PROSPECT ^{235}U unfolding with the prediction. The 5.5 MeV bump is now found with an amplitude of $(13.5 \pm 3.3)\%$, with a 4.7σ significance, as summarized in Table 7.1. Noticeably, a "well" appears in the high energy part of the unfolded spectrum. Its origin is two-fold: first, the experimental constraints coming from the STEREO Phase-II data set whose downward high energy bins fluctuation drives the deficit at 7 MeV, and from the PROSPECT data set that exhibits an event excess at high energy, thus pushing the high energy end of the spectrum towards higher values. Second, the positive short-range correlations induced by the regularization, that tends to smooth the rise of the spectrum. As shown in the correlation matrix of the unfolded spectrum (see inset of Figure 7.8), these correlations become prominent at high energy[1]. This augmented smoothing translates into a more diffuse behaviour of the filter matrix in the high energy end of the spectrum, as visible in Figure 7.9[2].

To quantify the significance of the distortion of the high energy end of the spectrum, we apply the same test statistics as for the 5.5 MeV bump. A local minimum for the χ^2 is found, for a bump at 7.0 MeV, with a fitted amplitude of $(-25.5 \pm 21.3)\%$ (resp. $(-15.9 \pm 5.3)\%$) when applying (resp. without applying) the filter matrix, yielding to a low significance of 1.9σ (resp. 2.1σ). The discrepancies of test statistics with and without the filter matrix become sizeable, as the high energy end of the spectrum is more subject to unfolding biases. Not applying the filter would yield to slightly overestimate the significance of the 7 MeV distortion.

Besides, let's add that there is *a priori* no physical motivation to choose the gaussian function as a parameterization for the local spectral distortions in the studies that we carried out so far. It is only meant to quantify the amplitude of the distortions as well as their associated statistical significance.

[1] As already discussed, this comes from the fact that the regularization is inversely proportional to the prior spectrum amplitude, that vanishes at high energy.

[2] It could not be seen in the STEREO-only unfolding, due to the coarser energy binning used beyond 7 MeV.

At last, let's note as well that the significance of the local event excess derived in our global HEU unfolding procedure did not significantly increase with respect to the STEREO-only unfolding. This does not rule out the interest of such global approach, that rather lies in producing more robust results by combining the data of independent experiments, with different treatments of systematics.

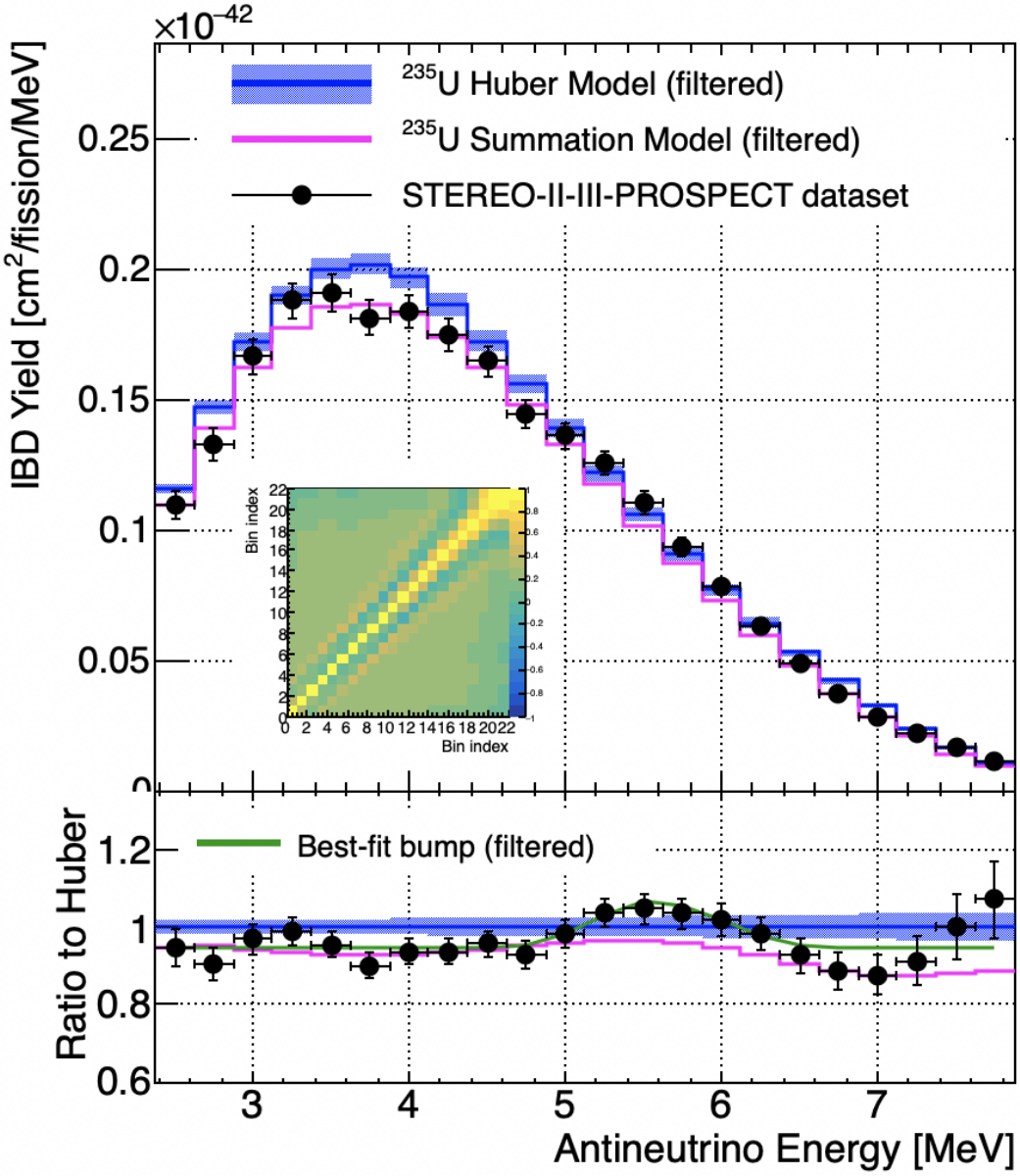

Figure 7.8: **Comparison of ^{235}U STEREO-PROSPECT unfolded spectrum with Huber and Summation filtered model spectra**. See text for details.

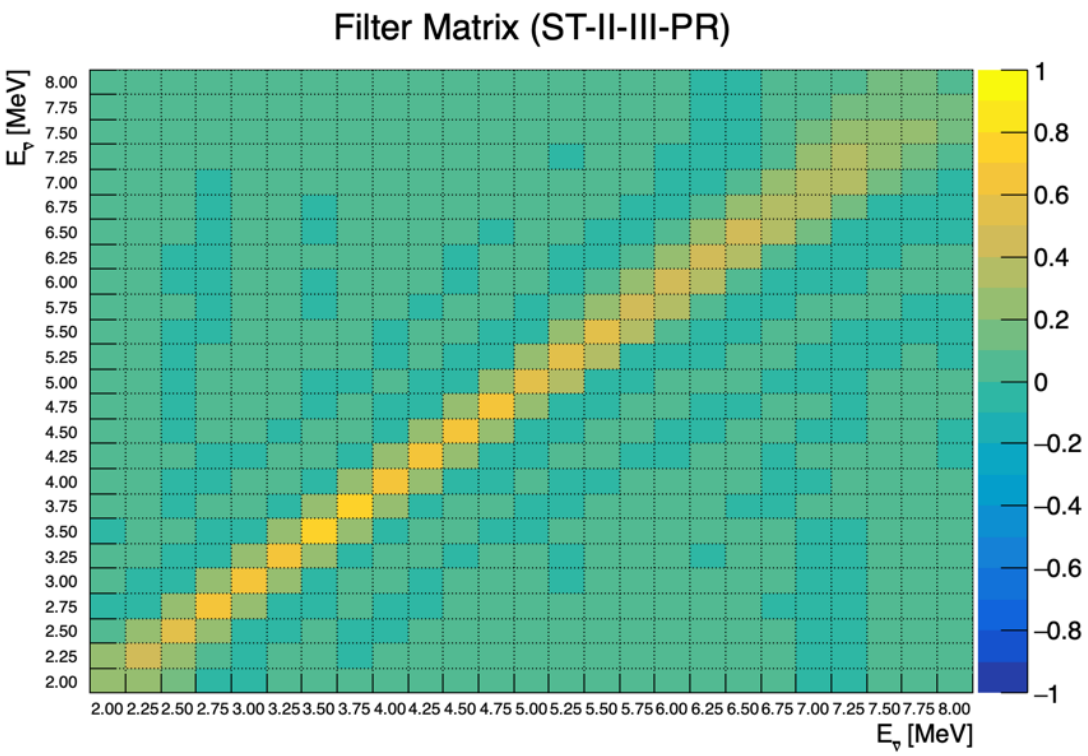

Figure 7.9: **Filter matrix of Stereo-Prospect unfolding**.

ST-II-III-PR	Antineutrino Energy space				Reconstructed Energy space	
	w/o. Filter		w. Filter		w. Response	
HM Comparison	**Shape–only**	**Best-fit bump**	**Shape–only**	**Best–fit bump**	**Shape–only**	**Best–fit bump**
α	0.941 ± 0.026	0.944 ± 0.027	$\mathbf{0.941 \pm 0.026}$	$\mathbf{0.944 \pm 0.027}$	0.941 ± 0.026	0.944 ± 0.027
A [%]	0 ± 0	12.9 ± 2.8	$\mathbf{0 \pm 0}$	$\mathbf{13.5 \pm 3.3}$	0 ± 0	13.5 ± 3.3
μ **[MeV]**	0 ± 0	5.588 ± 0.103	$\mathbf{0 \pm 0}$	$\mathbf{5.583 \pm 0.101}$	0 ± 0	5.583 ± 0.101
σ **[MeV]**	0 ± 0	0.392 ± 0.104	$\mathbf{0 \pm 0}$	$\mathbf{0.369 \pm 0.116}$	0 ± 0	0.369 ± 0.116
χ^2**/dof**	42.5/21	13.0/18	**48.0/21**	**18.0/18**	104.5/75	74.5/72
$\Delta\chi^2/\Delta$**dof**	29.5/3		**30.0/3**		30.0/3	
Significance (one-sided)	4.7σ		$\mathbf{4.7\sigma}$		4.7σ	

Table 7.1: **Best-fit bump for ^{235}U Stereo-Prospect unfolded spectrum**. The local event excess at 5.5 MeV is found to be, with a 4.7σ (one-sided) significance, at the $(13.5 \pm 3.3)\%$ level, and is slightly flatter than the bump obtained from the Stereo unfolding (see Table 7.1).

7.2 HEU+LEU global analysis

The results obtained on the STEREO-PROSPECT HEU data set, that corresponds to an overall statistics of $\sim$ 150k antineutrinos events, unambiguously indicated a ^{235}U bump independent of any other isotopes present in commercial reactors, lowly-enriched in ^{235}U (LEU). Furthermore, the accurate absolute normalization of the STEREO data confirmed the 5.5% deficit for the case of the pure ^{235}U spectrum. In order to gain further insights on the reactor anomalies, we propose in this section to extend the analysis to a joint analysis with the published data set of the Daya Bay LEU experiment.

7.2.1 The Daya Bay experiment

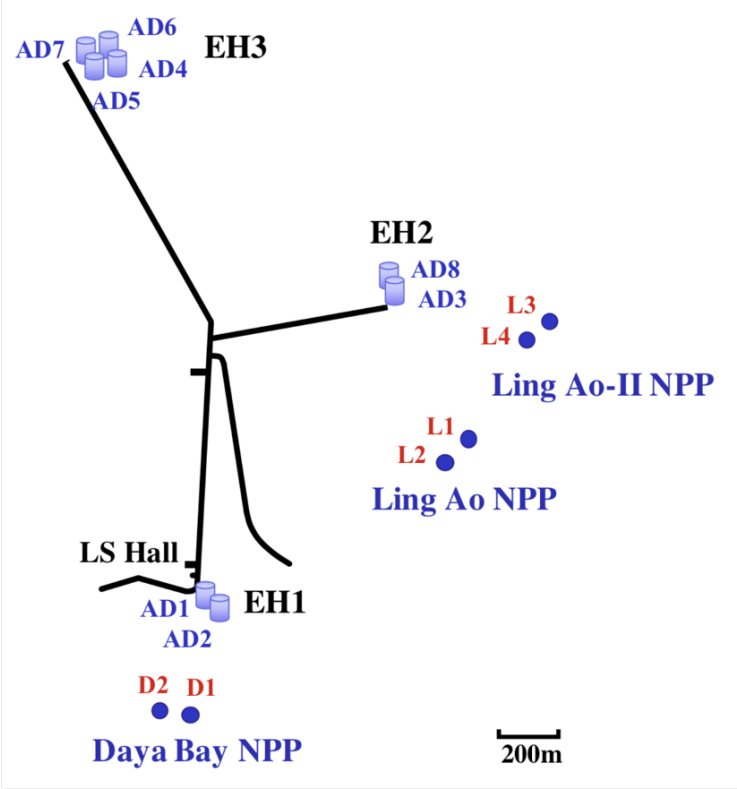

Figure 7.10: **Layout of the Daya Bay experiment**. The dots represent the reactor cores, labelled as D1, D2, L1-4. Eight antineutrino detectors, labelled as AD1 to AD8, are installed in three underground experimental halls (EH1–3). Source [111].

The Daya Bay experiment studies the antineutrino spectrum at the Daya Bay nuclear power complex, consisting of 2.9 GW_{th} six commercial reactor cores, 4.5% enriched in ^{235}U [150]. They are grouped into three pairs, with each pair referred to as a nuclear power plant (NPP) [151]. Eight identically designed antineutrino detectors (ADs) are distributed at two near-site underground experimental halls (EH1 and EH2) and one far-site underground experimental hall (EH3) (see Figure 7.10). Based on the IBD reaction channel, the technology of detection is very similar to that of STEREO. Each detector consists of an inner target volume containing 20 t of Gd-loaded liquid scintillator, surrounded by a gamma-catcher crown filled with 22 t of unloaded liquid scintillator to reduce energy leakage [143]. At last, these volumes are enclosed in an outer volume filled with 36 t of mineral

oil, to shield the detector against background radiations. The combination of the high antineutrino flux from power reactors, that cumulate a total thermal power of 17.4 GW_{th}, and a total target mass of 160 t allowed to reach an overall statistics of a few millions of IBD candidates, despite the $\sim 0.1 - 1$ km baseline. It is one order of magnitude higher than the STEREO-PROSPECT overall statistics, obtained by operating close to more compact research reactors with smaller detectors. In what follows, the data that will be analyzed are those from the four near-site ADs, amounting to 3.5 millions of IBD candidates within 1958 days of data-taking [143, 152].

7.2.2 Daya Bay Analysis

Fission fractions and detected spectrum

In commercial reactors, over 99.7% of the antineutrino flux is produced from the beta-decay branches of the fission products from four major parent isotopes: ^{235}U, ^{238}U, ^{239}Pu and ^{241}Pu. The fraction of nuclear fissions attributed to a parent isotope is called the fission fraction. This quantity evolves with the burn-up of the considered nuclear reactor core, as shown in Figure 7.11. The fissile ^{235}U gets consumed over time, while the ^{239}Pu and ^{241}Pu isotopes are produced by neutron captures on ^{238}U and subsequent neutron captures and beta-decay of its daughter isotopes. The contribution of the non-fissile ^{238}U isotope is stable over time.

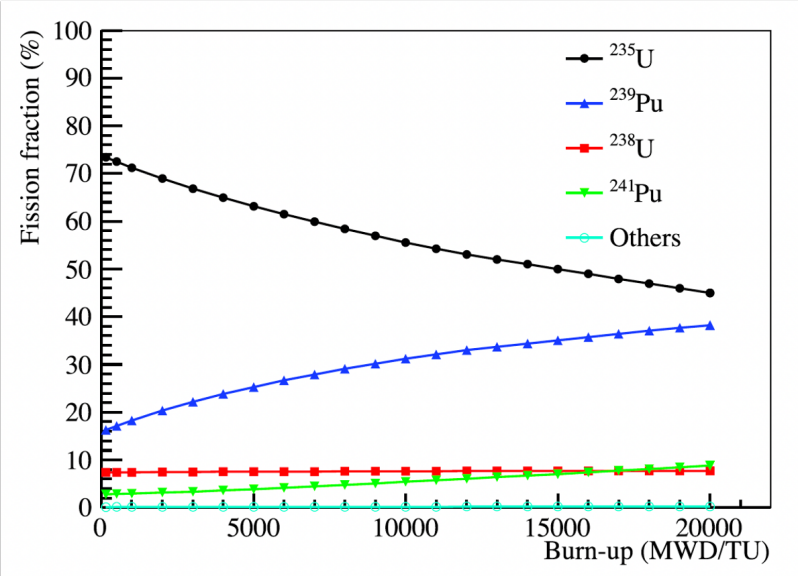

Figure 7.11: **Fission fractions of isotopes in reactor core D1 as a function of cycle burn-up**, expressed in megawatts-day per ton of uranium, from a simulation of a complete refueling cycle. Other isotopes contribute less than 0.3% in total. Source [111].

For each AD d, the detected antineutrinos originate from 6 reactor cores r, with different baselines L_{dr}. The fractional isotopic contributions to the total number of IBD events in the 4 ADs, also known as effective fission fractions, write:

$$f_{eff}^{iso} = \frac{\sum_{d=1}^{4}\sum_{r=1}^{6} N_r^f / L_{dr}^2 \cdot f_r^{iso}}{\sum_{d=1}^{4}\sum_{r=1}^{6} N_r^f / L_{dr}^2} \tag{7.3}$$

where f_r^{iso} is the isotopic fission fraction of the r-th reactor core and N_r^f the isotopic predicted number of fissions from the r-th core. For the considered Daya Bay data set,

the average effective fissions are $f_{eff}^{235} : f_{eff}^{238} : f_{eff}^{239} : f_{eff}^{241} = 0.564 : 0.076 : 0.304 : 0.056$, respectively for ^{235}U, ^{238}U, ^{239}Pu, ^{241}Pu [152]. By definition, they sum up to 1.

As the fission fraction of ^{241}Pu is approximately proportional to the fission fraction of ^{239}Pu over the entire reactor cycle, with a proportionality coefficient of 0.183, the overall ^{239}Pu + ^{241}Pu spectrum can be treated as one spectrum, called Pu combo, whose effective fission fraction is $f_{eff}^{239+241} = f_{eff}^{239} + f_{eff}^{241} = 0.360$. The overall antineutrino spectrum as measured by the Daya Bay experiment $D_{\mathrm{DB}}^{\mathrm{tot}}$ then reads:

$$D_{\mathrm{DB}}^{\mathrm{tot}} = f_{eff}^{235} * D_{\mathrm{DB}}^{235} + f_{eff}^{239+241} * D_{\mathrm{DB}}^{239+241} + f_{eff}^{238} * D_{\mathrm{DB}}^{238} \tag{7.4}$$

where D_{DB}^{235}, D_{DB}^{238} and $D_{\mathrm{DB}}^{239+241}$ are respectively the ^{235}U, ^{238}U and Pu combo reconstructed energy spectra to be separated.

^{235}U/Pu separation

Due to the evolving composition of the reactor cores and the different antineutrino spectra induced by the fissioning isotopes, the emitted antineutrino spectrum changes over time. Exploiting to the fullest the reactor simulations to obtain the values of the effective fission fractions over time, Daya Bay rebinned its data into 20 groups ordered by values of ^{239}Pu effective fission fraction. From one group to another, the relative contribution of ^{235}U with respect to Pu combo changes, whilst the contribution of ^{238}U remains stable. This translates into discrepancies of the overall detected spectrum from one group to another, that, when traced back, can allow to separate the ^{235}U and Pu combo individual contributions. Doing so, and assuming as the ^{238}U spectrum the prediction given by the Mueller model [50], Daya Bay was able to extract the ^{235}U and Pu combo reconstructed energy spectra from their data set [152], as shown in Figure 7.12. They reported a $(8.0 \pm 2.3\ [\mathrm{exp.}] \pm 2.1\ [\mathrm{model}])\%$ (resp. $(1.0 \pm 5.7\ [\mathrm{exp.}] \pm 2.5\ [\mathrm{model}])\%$) deficit of detected antineutrinos for ^{235}U (resp. Pu combo) with respect to the Huber-Mueller prediction, which hints towards the ^{235}U as the primary contributor to the RAA.

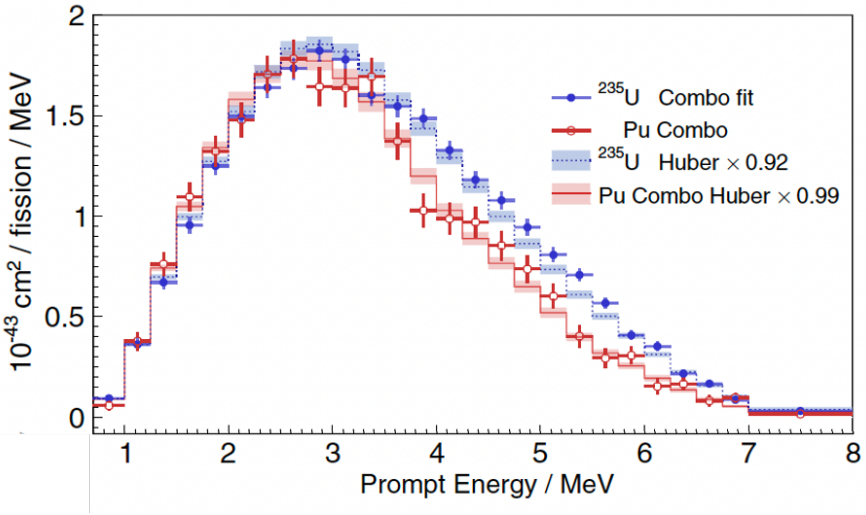

Figure 7.12: **Comparison of the extracted ^{235}U and Pu combo spectra with the corresponding Huber-Mueller predicted spectra**, with the normalization factors 0.92 and 0.99. One must add that the Pu combo spectrum, is normalized to the number of ^{239}Pu fissions. The event excess in the 4-6 MeV region are clearly visible for both spectra. Source [152].

^{235}U/Pu unfolding

In [143], Daya Bay reported the unfolded spectra of their separated ^{235}U and Pu combo reconstructed energy spectra. They are expressed in a 250keV-wide antineutrino energy binning between 1.800 and 7.800 MeV, with a supplemental 1.700MeV-wide bin between 7.800 and 9.500 MeV (see Figure 7.13). To obtain these spectra, they applied a dedicated Wiener filter to each spectrum, such that in principle, the unfolding results read:

$$\hat{\Phi}_{iso} = A_{c,iso}^{\text{Wiener}} \cdot H_{iso} \cdot D_{iso} \tag{7.5}$$

where iso = ^{235}U / Pu combo and $H_{iso} = \left(R_{DB}^T V_{iso}^{-1} R_{DB}\right)^{-1} R_{DB}^T V_{iso}^{-1}$, with R_{DB} the Daya Bay response matrix, that is independent of the isotopic origin of the interacting antineutrinos, and V_{iso} the covariance matrix of the ^{235}U or Pu combo reconstructed energy spectrum.

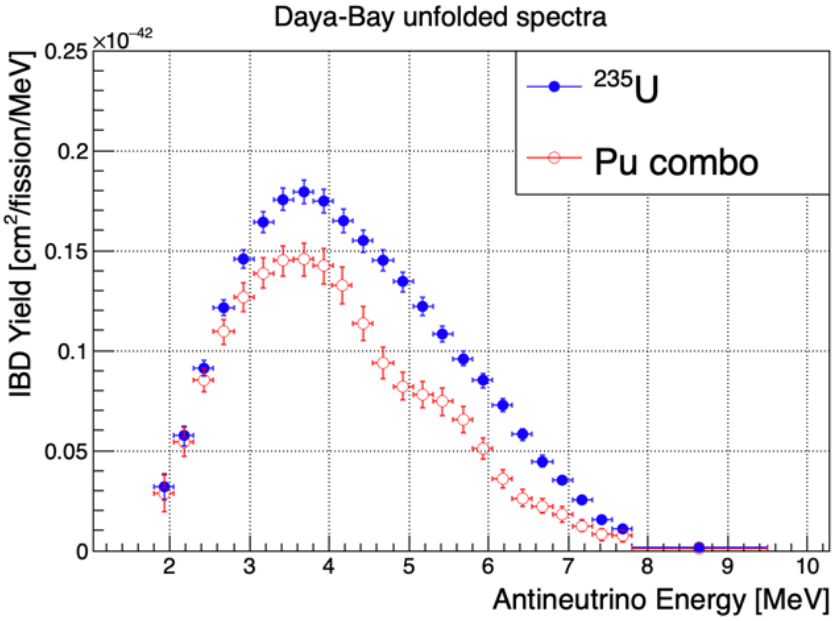

Figure 7.13: **Daya Bay unfolded ^{235}U and Pu combo spectra**. Source [143].

Let's emphasize the main features of the Daya Bay overall spectrum analysis. First, this is a two-step analysis, that consists in separating the ^{235}U and Pu combo spectra in reconstructed energy space, before separately unfolding them in antineutrino energy space. In particular, the separation analysis is highly dependent on reactor simulations that provide the only leverage to discriminate the uranium from the plutonium contribution. Furthermore, the choice to unfold separately the uranium and the plutonium could be criticized as both spectra are strongly (anti-)correlated from the separation procedure.

In the following, we propose a complementary approach to that of the Daya Bay collaboration in order to extract from their data set the ^{235}U and Pu combo antineutrino spectra. We present a one-step analysis where the separation and the unfolding are done simultaneously, such that all the correlations between the extracted spectra are naturally taken into account and propagated. Furthermore, instead of using as the main leverage to separate the spectra the (unpublished) time-evolution of the effective fission fractions given by reactor simulations, we will only use the average effective fission fractions in our procedure. The leverage for the separation will arise from the supplemental constraint of

the HEU experimental data set. This global HEU+LEU unfolding will yield to a more data-driven analysis of the isotopic spectra of the Daya Bay experiment. We present in the next subsection, the LEU inputs used for the analysis.

7.2.3 Daya Bay Inputs

7.2.3.1 Predicted spectra

Similarly to Daya Bay, we use the Huber conversion prediction [55] for the ^{235}U and Pu combo spectra and the Mueller summation prediction [50] for the ^{238}U spectrum[3]. They are reported in Figure 7.14. Given the wider antineutrino energy range used by Daya Bay for its unfolding, the spectra have been extrapolated at high energy.

It is worth mentioning that the converted spectrum for ^{238}U was obtained from a measurement in 2014 by Haag et al. [153]. Yet, it is not discussed here.

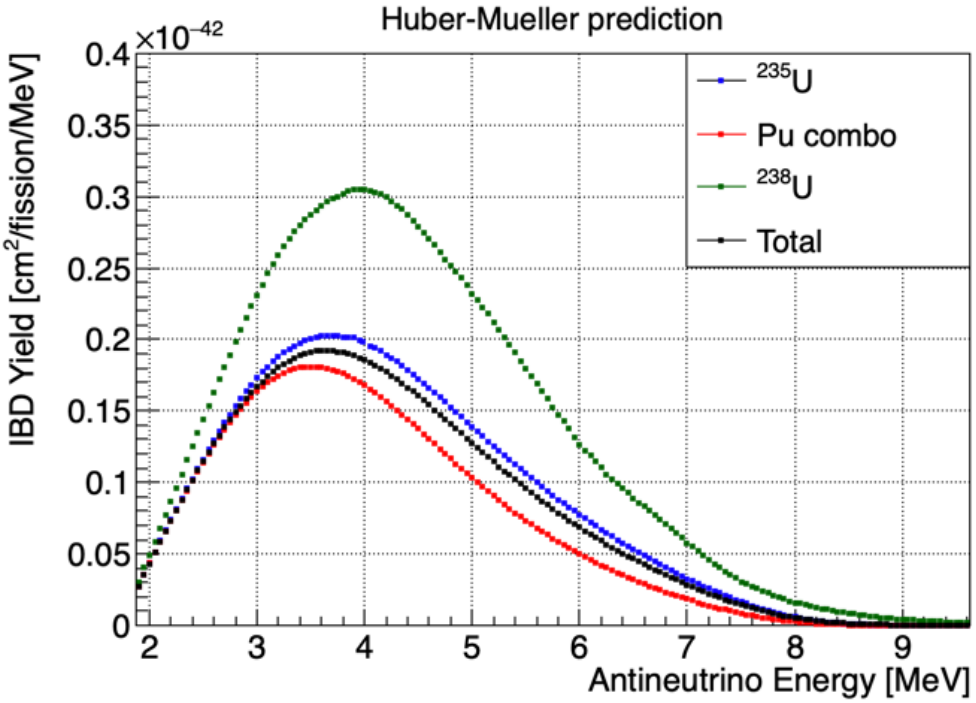

Figure 7.14: **Huber-Mueller predicted antineutrino spectra**, reported in 50-keV wide antineutrino energy bins spanning [1.875, 9.575]MeV. The Huber and Mueller published antineutrino flux have been extrapolated at higher energy, with an exponential of fifth order polynomial, following the suggested best-fit parameterization of [55] and [50]. The total Huber-Mueller predicted spectrum for the Daya Bay experiment (in black) corresponds to the summation of the isotopic predictions (in blue, green, red) weighted by their respective average effective fission fraction.

7.2.3.2 Measured spectrum, Fission fractions and overall Covariance matrix

We use the same total measured spectrum as in the Daya Bay unfolding analysis [143]. This spectrum is corrected from the overall detection efficiency and flux corrections have already been removed, such that only the isotopic contributions from ^{235}U, ^{238}U, ^{239}Pu and ^{241}Pu remain. It is reported in 26 reconstructed energy bins, ranging from 0.700 MeV

[3]We use the prediction corresponding to 450-day irradiation time.

(lower edge of first bin) to 8.000 MeV (upper edge of last bin) and consisting of 1 300keV-wide energy bin for [0.700, 1.000]MeV, 24 250keV-wide energy bins for [1.000, 7.000]MeV and 1 1MeV-wide energy bin for [7.000, 8.000]MeV.

Following a study carried out with the DRAGON reactor simulation code [154], the Daya Bay collaboration set a 5% uncertainty on each isotopic effective fission fractions. In our analysis, the ^{235}U and Pu combo fission fraction uncertainties are considered as fully anti-correlated between each other and uncorrelated with the ^{238}U fission fraction uncertainty.

In order to include the uncertainties on these fission fractions in the unfolding framework, we build the overall covariance matrix of the Daya Bay data set, that encapsulates the experimental and model uncertainties: $V_{\mathrm{DB}} = V_{\mathrm{DB}}^{\mathrm{exp}} + V_{\mathrm{DB}}^{\mathrm{model}}$. The experimental covariance matrix is given in [143]. We build the model covariance matrix through a first order error propagation formalism. It includes the fission fraction uncertainties, as well as the uncertainties on the reconstructed energy ^{238}U predicted spectrum that is to be subtracted from the total measured spectrum to isolate the ^{235}U and Pu combo contributions. The measured reconstructed energy spectrum resulting from the subtraction of the ^{238}U contribution is shown in Figure 7.15.

Similarly to Daya Bay, we set the shape uncertainty on the ^{238}U reconstructed energy predicted spectrum to be 15% in 0.7–4.5 MeV, 20% in 4.5–6 MeV, 30% in 6–7 MeV, and 60% in 7–8 MeV, uncorrelated between energy bins. An additional 10% normalization uncertainty, fully correlated between energy bins, is added.

The resulting overall correlation matrix is shown in Figure 7.16. It exhibits strong correlations due to the model uncertainties on one hand, and to the experimental systematic uncertainties that are dominant over statistical uncertainties on the other hand. In particular, the dominant uncertainty on the detection efficiency amounts to 1.2% [152], yielding to an equivalent irreducible uncertainty on the IBD yield of the total measured spectrum.

7.2.3.3 Response matrix

Shifted Response

The response matrix published by Daya Bay [152] is expressed in a 50keV-wide antineutrino binning, spanning [0, 12]MeV. Therefore, this binning is shifted by 25keV with respect to the 50keV-wide binning we used so far in our HEU unfolding analyses. In order to combine the HEU and LEU data sets in a global unfolding procedure, the Daya Bay response matrix has to be projected in our antineutrino energy binning. To do so, we work on the raw Daya Bay response matrix, whose matrix element is defined in Equation 6.8. We assume as a prior spectrum the total Huber-Mueller prediction, such that the value of the new matrix elements, expressed in the shifted antineutrino energy binning, $\mathfrak{R}^{i(j+\frac{1}{2})}$ may be derived by a linear interpolation of the matrix elements of the original Daya Bay response:

$$\mathfrak{R}^{ij}_{\mathrm{shifted}} = \text{“ } \mathfrak{R}^{i(j+\frac{1}{2})} \text{ ”} = \frac{\mathfrak{R}^{i(j+1)} + \mathfrak{R}^{ij}}{2} \tag{7.6}$$

To evaluate the bias of the procedure, one may compare the reconstructed energy Huber-Mueller predictions that proceed on one hand from the forward-folding of the Huber-Mueller antineutrino energy prediction expressed in the original response binning, and on

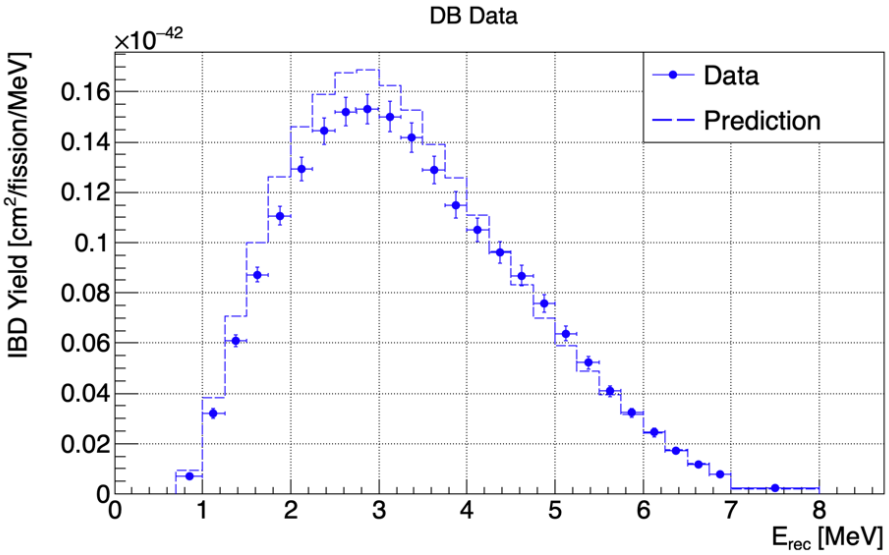

Figure 7.15: **Daya Bay ^{235}U + Pu combo reconstructed energy spectrum**, resulting from the subtraction of the Mueller ^{238}U isotopic contribution [50] to the total measured spectrum published in [143]. It is compared to the ^{235}U + Pu combo Huber prediction [55]. The global antineutrino deficit and the $4-6$ MeV event excess are clearly visible. The reported uncertainties on the spectrum include both the experimental and model uncertainties.

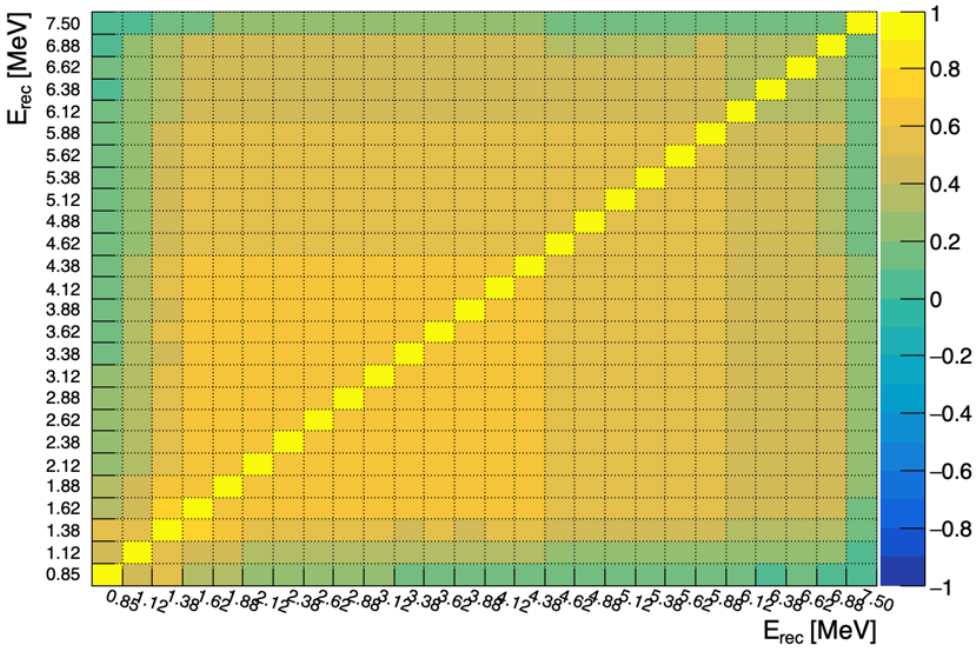

Figure 7.16: **Daya Bay correlation matrix**.

the other hand from the forward-folding of the Huber-Mueller antineutrino energy prediction expressed in the shifted binning. The residuals between the two reconstructed energy predictions are found to be negligible, mostly at the permil level and only reaching the percent level in the first energy bin, as displayed in Figure 7.17.

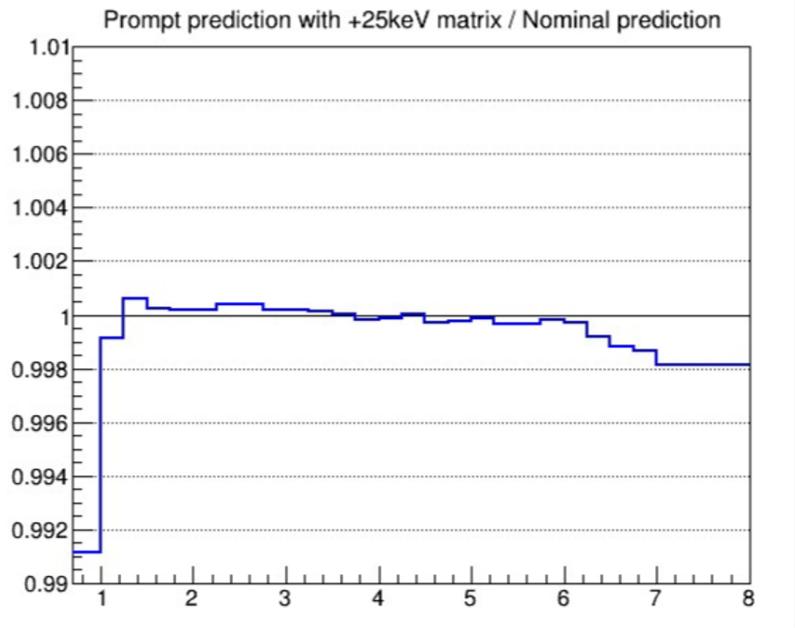

Figure 7.17: **Comparison between the reconstructed energy predictions**, obtained from the forward-folding through Daya Bay original and shifted responses matrices. The residuals are found to be at the permil level across the whole reconstructed energy range, except in the first bin where they reach the percent level. Source [155].

Normalization of the Response

The detection efficiency as encapsulated by the published Daya Bay response matrix is displayed in Figure 7.18a. It corresponds *a priori* to a number of selected events per antineutrino energy bin, given a flat prior spectrum, and therefore is not normalized to a value ≤ 1. A fit with a constant in the antineutrino energy range [2, 12]MeV shows that the efficiency can be safely assumed as constant in this range. Furthermore, the fact that the measured spectrum to be unfolded is *a priori* already corrected from the detection efficiency suggests to normalize the efficiency of the response to 1. Thus, the efficiency of the response is forced to 1 beyond 2 MeV, and is rescaled accordingly to values lower than 1 below 2 MeV. The final efficiency, that includes the cuts on the reconstructed energy[4] is shown in Figure 7.18b. It is encapsulated in the response matrix used for the unfolding, that is finally rebinned in a 250keV-wide antineutrino energy binning between 1.875 and 8.125 MeV, with an additional 1.450MeV-wide bin between 8.125 and 9.575 MeV, to match as close as possible the Daya Bay antineutrino energy binning used for their unfolding. It is shown in Figure 7.19.

At last, let's add that the normalization of the response is of crucial importance for the analysis that will be carried out in the next subsection. In Appendix D, we discuss the impact of a misnormalization of the Daya Bay response on the plutonium unfolded spectrum, and a dedicated cross-check of the accuracy of the hand-made normalization of the response is performed.

[4]The reconstructed energy is set to lie between 0.700 MeV and 8.000 MeV, to match the binning of the measured spectrum.

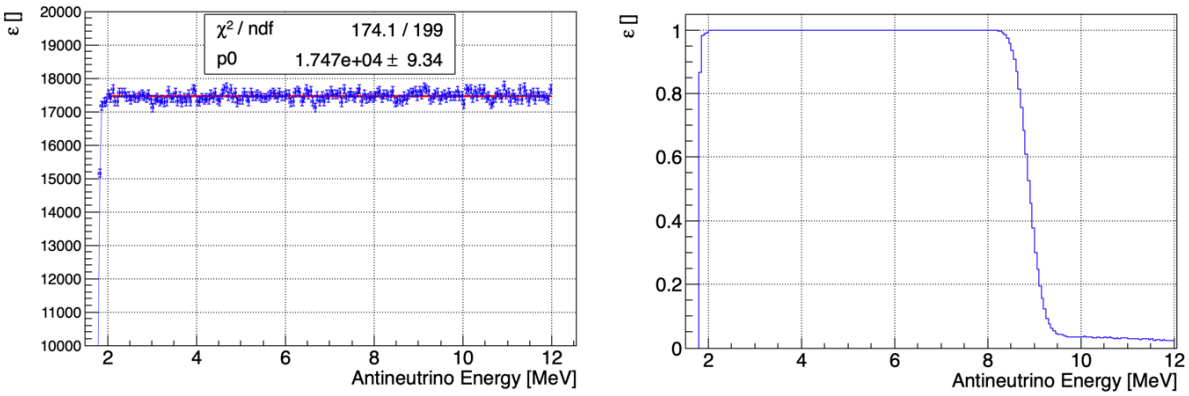

(a) Published (without E_{rec} cuts) (b) Renormalized (with E_{rec} cuts)

Figure 7.18: **Efficiency of Daya Bay Response matrix**. (a) Efficiency as published by the Daya Bay collaboration. There is no reconstructed energy cut, such that for the antineutrino energy range that is displayed, the reconstructed energy lies between 0 and 12 MeV. The efficiency is expressed as a number of selected events, obtained from a Monte-Carlo simulation of the detector response, such that the error bars on the efficiency values are assumed to be the standard poissonian error of counting rate experiments. From a constant fit of the efficiency between 2 and 12 MeV, we obtain a $\chi^2/\text{dof} = 174.1/199$, that shows that the efficiency can be assumed as constant beyond 2 MeV. (b) Final efficiency, encoded in the Daya Bay response matrix used for the unfolding. It includes the reconstructed energy cuts, such that E_{rec} is required to lie between 0.7 and 8 MeV. Between 2 and ∼8.5 MeV, where no efficiency loss occurs, the efficiency value is forced to 1 from the normalization procedure.

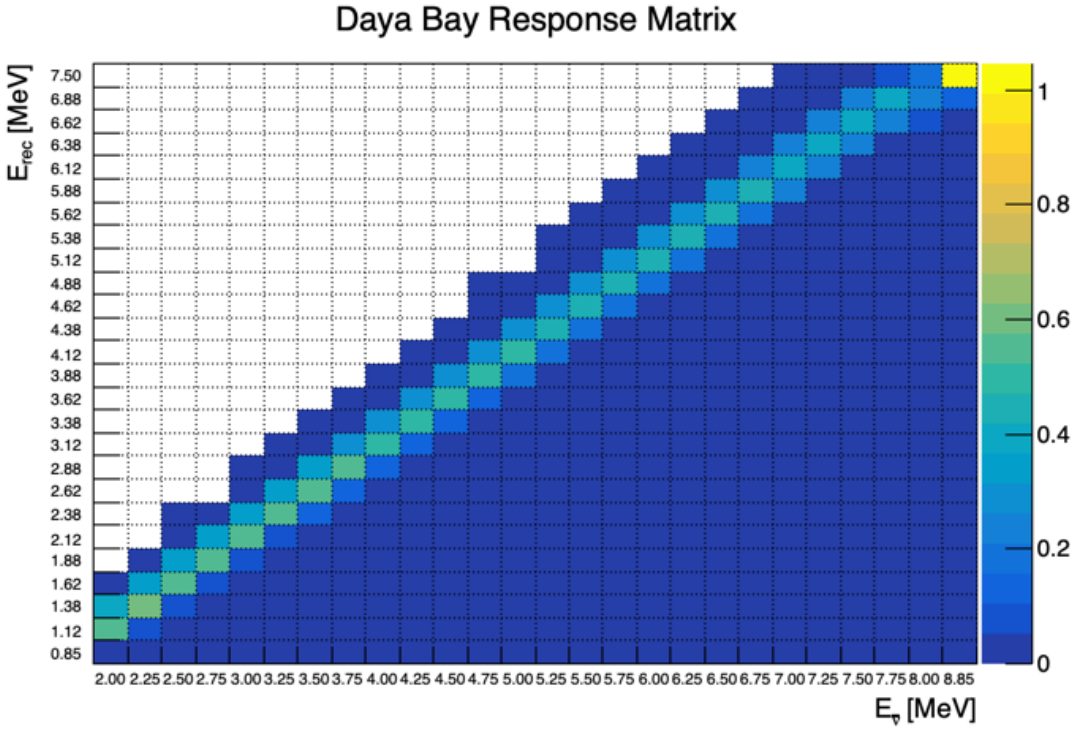

Figure 7.19: **Daya Bay Response matrix**, shifted, renormalized and rebinned from the original Daya Bay response.

7.2.4 HEU+LEU unfolding framework

7.2.4.1 χ^2 writing and minimization

In the global HEU+LEU unfolding approach, the χ^2 to be minimized reads:

$$\begin{aligned}\chi^2\left(\Phi_{\mathrm{U5}},\Phi_{\mathrm{Pu}}\right) &= \left\|D_{\mathrm{HEU}}-R_{\mathrm{HEU}}\cdot\Phi_{\mathrm{U5}}\right\|^2_{V^{-1}_{\mathrm{HEU}}}\\ &+ \left\|D_{\mathrm{LEU}}-R_{\mathrm{LEU}}\cdot\left(f^{235}_{eff}*\Phi_{\mathrm{U5}}+f^{239+241}_{eff}*\Phi_{\mathrm{Pu}}\right)\right\|^2_{V^{-1}_{\mathrm{LEU}}}\\ &+ \lambda_{\mathrm{U5}}\left\|\Phi_{\mathrm{U5}}\right\|^2_{M_{\mathrm{U5}}}\\ &+ \lambda_{\mathrm{Pu}}\left\|\Phi_{\mathrm{Pu}}\right\|^2_{M_{\mathrm{Pu}}}\end{aligned} \tag{7.7}$$

where:

- HEU can refer to the STEREO or STEREO-PROSPECT data set,
- $D_{\mathrm{LEU}} = D^{\mathrm{tot}}_{\mathrm{DB}} - f^{238}_{eff} * D^{238}_{\mathrm{HM}}$, with D^{238}_{HM} the Mueller prediction for the ^{238}U reconstructed energy spectrum,
- $R_{\mathrm{LEU}} = R_{\mathrm{DB}}$, the Daya bay response matrix shifted and renormalized according the afore-described procedure,
- $V_{\mathrm{LEU}} = V^{\mathrm{exp}}_{\mathrm{DB}} + V^{\mathrm{model}}_{\mathrm{DB}}$,
- Φ_{U5} (resp. Φ_{Pu}) is the ^{235}U (resp. Pu combo) unfolded spectrum,
- M_{U5} (resp. M_{Pu}) is the regularization matrix using as a prior spectrum the Huber prediction for ^{235}U (resp. Pu combo), and with an associated regularization strength λ_{U5} (resp. λ_{Pu}). It is defined in the exact same fashion as for the HEU unfolding.

We define the stacked HEU+LEU variables as:

$$\begin{cases} D_{\mathrm{HL}} &= \begin{bmatrix} D_{\mathrm{HEU}} \\ D_{\mathrm{LEU}} \end{bmatrix} \\ R_{\mathrm{HL}} &= \begin{bmatrix} R_{\mathrm{HEU}} & 0 \\ f^{235}_{eff} * R_{\mathrm{LEU}} & f^{239+241}_{eff} * R_{\mathrm{LEU}} \end{bmatrix} \\ V_{\mathrm{HL}} &= \begin{bmatrix} V_{\mathrm{HEU}} & 0 \\ 0 & V_{\mathrm{LEU}} \end{bmatrix} \\ \Phi_{\mathrm{HL}} &= \begin{bmatrix} \Phi_{\mathrm{U5}} \\ \Phi_{\mathrm{Pu}} \end{bmatrix} \\ M_{\mathrm{HL}} &= \begin{bmatrix} M_{\mathrm{U5}} & 0 \\ 0 & M_{\mathrm{Pu}} \end{bmatrix} \end{cases} \tag{7.8}$$

Denoting $r_{\mathrm{Pu/U5}} := \lambda_{\mathrm{Pu}}/\lambda_{\mathrm{U5}}$, we can also define the $(N_{\Phi_{\mathrm{U5}}} + N_{\Phi_{\mathrm{Pu}}}) \times (N_{\Phi_{\mathrm{U5}}} + N_{\Phi_{\mathrm{Pu}}})$ relative regularization strength matrix Λ_{HL} as:

$$\Lambda_{\mathrm{HL}}\left(r_{\mathrm{Pu/U5}}\right) = \begin{bmatrix} 1 & 0 & \dots & \dots & \dots & \dots & \dots & 0 \\ 0 & \ddots & \ddots & & & & & \vdots \\ \vdots & \ddots & \ddots & \ddots & & & & \vdots \\ \vdots & & \ddots & 1 & \ddots & & & \vdots \\ \vdots & & & \ddots & r_{\mathrm{Pu/U5}} & \ddots & & \vdots \\ \vdots & & & & \ddots & \ddots & \ddots & \vdots \\ \vdots & & & & & \ddots & \ddots & 0 \\ 0 & \dots & \dots & \dots & \dots & \dots & 0 & r_{\mathrm{Pu/U5}} \end{bmatrix} \tag{7.9}$$

Equation 7.7 can then be rewritten as:

$$\begin{aligned} \chi^2_{\lambda_{\mathrm{U5}}, r_{\mathrm{Pu/U5}}}\left(\Phi_{\mathrm{HL}}\right) &= \left\| D_{\mathrm{HL}} - R_{\mathrm{HL}} \cdot \Phi_{\mathrm{HL}} \right\|^2_{V^{-1}_{\mathrm{HL}}} \\ &+ \lambda_{\mathrm{U5}} \left\| \Phi_{\mathrm{HL}} \right\|^2_{\Lambda_{\mathrm{HL}}\left(r_{\mathrm{Pu/U5}}\right) \cdot M_{\mathrm{HL}}} \end{aligned} \tag{7.10}$$

which is a formulation equivalent to that of Equation 6.13. Therefore, we can apply the same formulae as for the HEU unfolding, such that the solution of this inverse problem reads:

$$\begin{cases} \hat{\Phi}_{\mathrm{HL}} &= H_{\mathrm{HL}}\left(\lambda_{\mathrm{U5}}, r_{\mathrm{Pu/U5}}\right) \cdot D_{\mathrm{HL}} \\ V_{\hat{\Phi}_{\mathrm{HL}}} &= H_{\mathrm{HL}}\left(\lambda_{\mathrm{U5}}, r_{\mathrm{Pu/U5}}\right) \cdot V_{\mathrm{HL}} \cdot H_{\mathrm{HL}}\left(\lambda_{\mathrm{U5}}, r_{\mathrm{Pu/U5}}\right)^T \end{cases} \tag{7.11}$$

where:

$$H_{\mathrm{HL}}\left(\lambda_{\mathrm{U5}}, r_{\mathrm{Pu/U5}}\right) = A_{c,\mathrm{HL}}\left(\lambda_{\mathrm{U5}}, r_{\mathrm{Pu/U5}}\right) \cdot H_{\mathrm{HL}}(0,0) \tag{7.12}$$

with:

$$H_{\mathrm{HL}}(0,0) = \left(R^T_{\mathrm{HL}} V^{-1}_{\mathrm{HL}} R_{\mathrm{HL}}\right)^{-1} R^T_{\mathrm{HL}} V^{-1}_{\mathrm{HL}}$$

and the filter matrix:

$$A_{c,\mathrm{HL}}\left(\lambda_{\mathrm{U5}}, r_{\mathrm{Pu/U5}}\right) = \left(I + \left(R^T_{\mathrm{HL}} V^{-1}_{\mathrm{HL}} R_{\mathrm{HL}}\right)^{-1} \cdot \left(\lambda_{\mathrm{U5}} \cdot \Lambda_{\mathrm{HL}}\left(r_{\mathrm{Pu/U5}}\right) \cdot M_{\mathrm{HL}}\right)\right)^{-1} \tag{7.13}$$

Yet, we note a substantial difference between the HEU-only and the HEU+LEU unfoldings. Indeed, contrary to the HEU unfolding, the HEU+LEU unfolding procedure requires to set the values of two regularization strengths, associated respectively to ^{235}U and Pu combo. In the formulae above, this translates into the multiplication of the overall regularization matrix M_{HL} by the relative regularization strength matrix $\Lambda_{\mathrm{HL}}\left(r_{\mathrm{Pu/U5}}\right)$, which depends on $r_{\mathrm{Pu/U5}}$, the ratio of regularization strengths between ^{235}U and Pu combo. The (modified) GCV prescription used so far is not meant to cover the case of multiple tunable regularization strengths. Therefore, the value of $r_{\mathrm{Pu/U5}}$ must be set prior to our standard unfolding routine, in order to reduce to the case of a unique regularization to be tuned, namely λ_{U5}.

7.2.4.2 Tuning of U/Pu regularization strengths

There is *a priori* no reason why we should regularize more one unfolded spectrum with respect to the other. A first approach would then consist in imposing the same regularization strength for ^{235}U and Pu combo, that is: $r_{\mathrm{Pu/U5}} = 1$ such that Λ_{HL} is merely the identity matrix. Thereupon applying the GCV criterion and the subsequent unfolding, one ends up with the following correlation matrix of the ^{235}U + Pu combo unfolded spectra (see Figure 7.20). We remark that the bin-to-bin correlations, and especially the short-range correlations which are mostly induced by the regularization, are much more pronounced in the Pu combo spectrum than in the ^{235}U spectrum. This is a direct signature of an over-regularization of the Pu combo unfolding with respect to the ^{235}U unfolding. In other words, the ratio $r_{\mathrm{Pu/U5}}$ should *a minima* be smaller than 1.

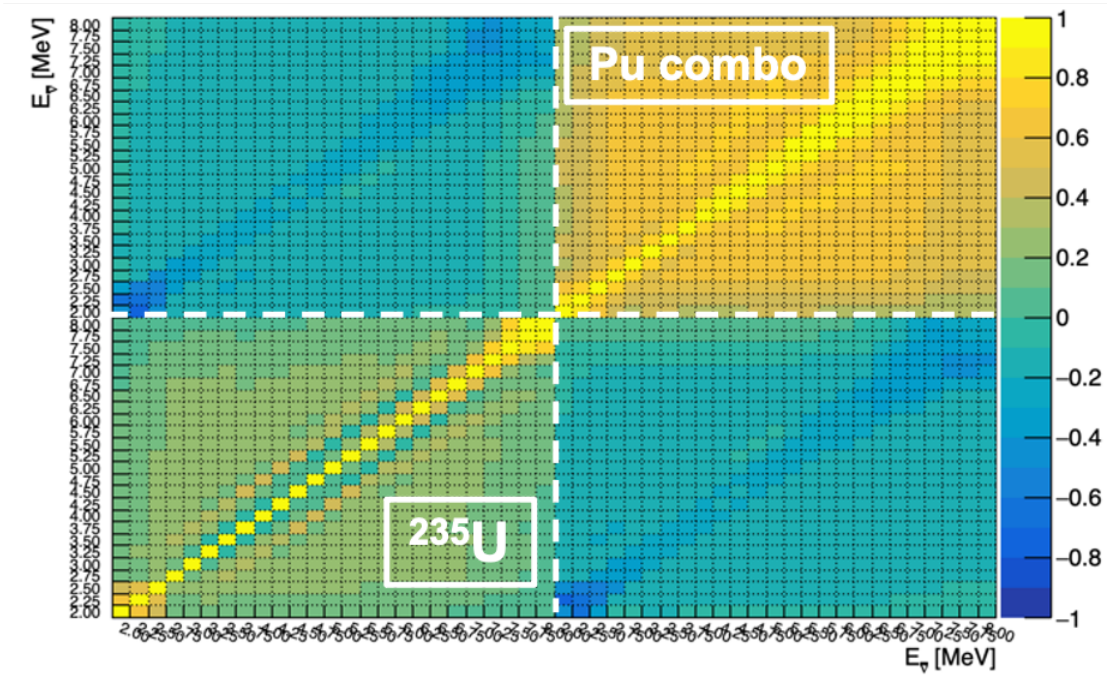

Figure 7.20: **Correlation matrix of ^{235}U + Pu combo unfolded spectra, assuming $\mathbf{r_{Pu/U5} = 1}$.** The HEU data set is the STEREO-PROSPECT data set, whereas the LEU data set is the Daya Bay data set. The off-diagonal blocks of the matrix show that the ^{235}U and Pu combo spectra are anti-correlated with each other, as expected from the separation procedure. Yet, the correlations (and especially the short-range correlations) in the Pu combo spectrum turn out to be significantly stronger than in the ^{235}U spectrum, hinting towards an over-regularization of Pu with respect to ^{235}U.

Such features is actually a patent illustration of the discussion we laid out in Section 6.2.2.4 about the difference between regularization *strength* and regularization *power*. Indeed, the ^{235}U and Pu combo spectra are constrained by data sets that are not statistically equivalent: whereas ^{235}U is constrained by the HEU and LEU data, Pu combo is only constrained by LEU data, such that one should at least assign a smaller regularization *strength* to the Pu combo spectrum in order to get a regularization *power* similar to ^{235}U. To formalize this intuition, we derived an *ad hoc* criterion to set the value of $r_{\mathrm{Pu/U5}}$. It

reads as:

$$r_{\mathrm{Pu/U5}} = \frac{\mathrm{Tr}\left(M_{\mathrm{U5}}\right) \cdot \mathrm{Tr}\left(\left(f_{eff}^{239+241}\right)^2 * R_{\mathrm{LEU}}^T V_{\mathrm{LEU}}^{-1} R_{\mathrm{LEU}}\right)}{\mathrm{Tr}\left(M_{\mathrm{Pu}}\right) \cdot \mathrm{Tr}\left(R_{\mathrm{HEU}}^T V_{\mathrm{HEU}}^{-1} R_{\mathrm{HEU}} + \left(f_{eff}^{235}\right)^2 * R_{\mathrm{LEU}}^T V_{\mathrm{LEU}}^{-1} R_{\mathrm{LEU}}\right)} \tag{7.14}$$

where Tr is the trace operator. The full derivation of this criterion is explained in Appendix E. It yields to a value: $r_{\mathrm{Pu/U5}} \sim 0.1$, that gives a similar short-range correlation pattern between ^{235}U and Pu combo, as shown in Figure 7.21. This completes the HEU+LEU unfolding procedure. In the next section, we will analyze the result of the framework.

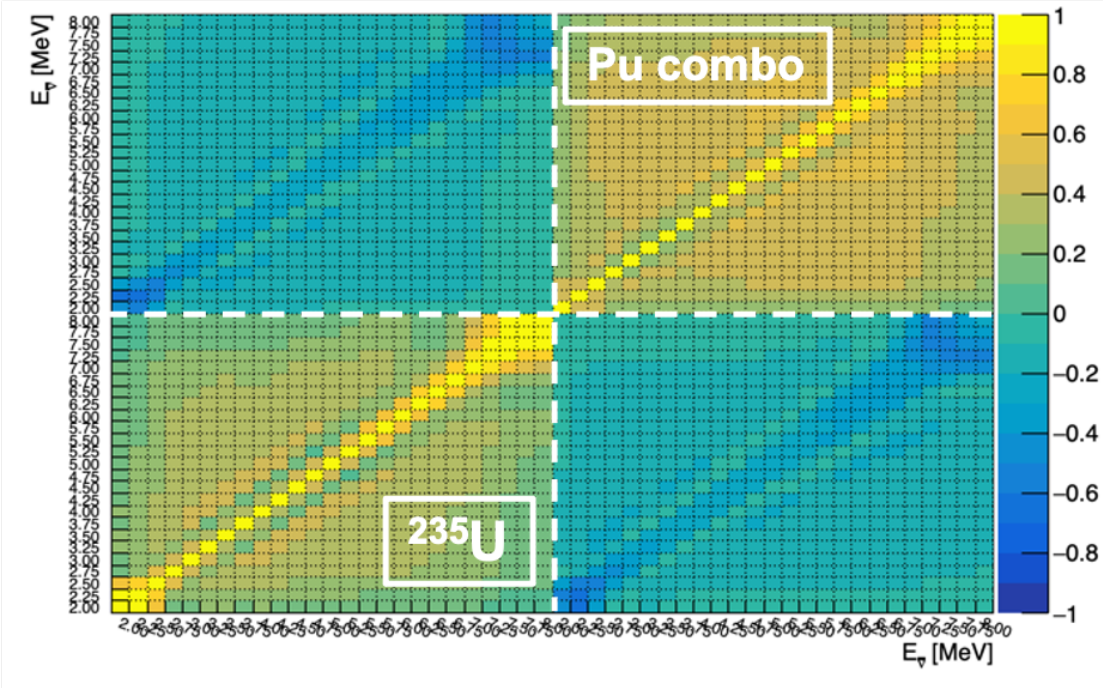

Figure 7.21: **Correlation matrix of ^{235}U + Pu combo unfolded spectra, assuming $\mathbf{r_{Pu/U5} \sim 0.1}$.** The HEU data set is the STEREO-PROSPECT data set, whereas the LEU data set is the Daya Bay data set. The short-range correlations in the Pu combo spectrum exhibit a similar intensity than in the ^{235}U spectrum, hinting towards a comparable regularization of Pu with respect to ^{235}U. The long-range correlations being more pronounced in Pu combo than in ^{235}U is expected, as the Pu combo is only constrained by the Daya Bay data set, whose dominant uncertainty is the normalization uncertainty, fully correlated between energy bins.

7.2.5 HEU+LEU unfolding results

In the HEU+LEU case, the filter matrix (shown in Figure 7.22) also allows to correct for the unfolding bias. Figure 7.23 shows the (small) biases corrected by this filter matrix when applied to the predicted spectra of the summation model. It also confirms that in the case of the prior Huber model no bias is introduced by the unfolding process. In the following, one carries out a full rate and shape analysis of the ^{235}U + Pu combo unfolded spectra.

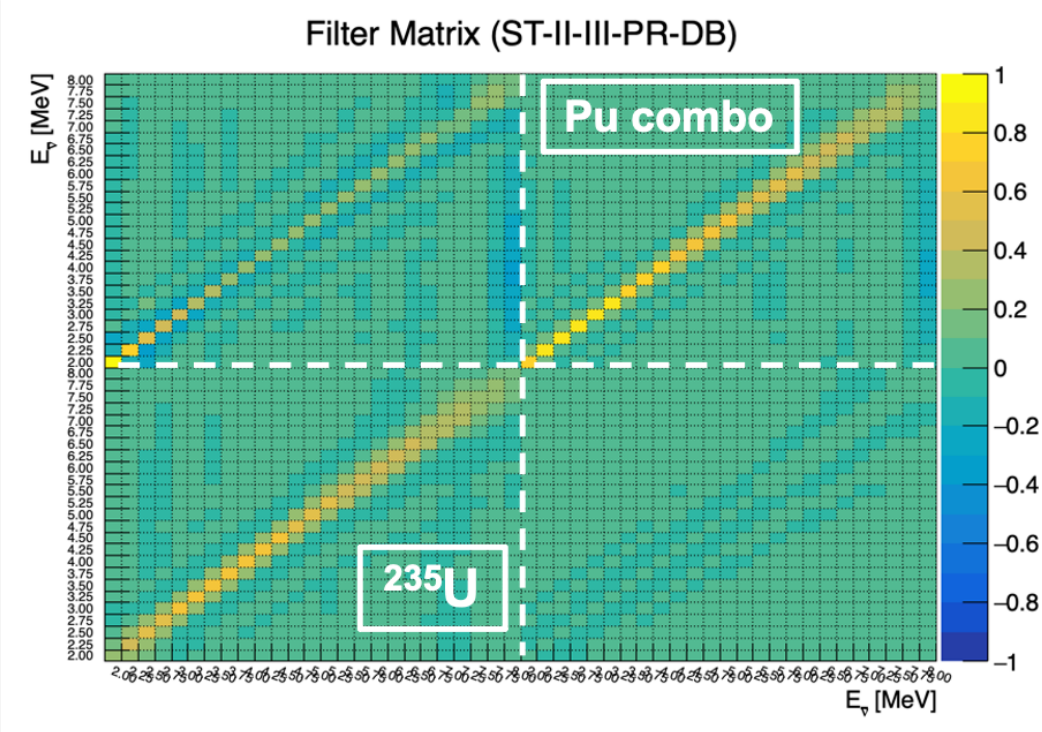

Figure 7.22: **Filter matrix of HEU+LEU unfolding**, taking as a HEU data set the STEREO-PROSPECT data set.

7.2.5.1 Rate analysis

In order to avoid potential biases in the rate analysis, we consider as the HEU data set the STEREO data set, as PROSPECT data do not have an absolute normalization. The addition of the PROSPECT data set will only be done for the shape analysis, detailed below. Integrating the result of the HEU+LEU STEREO-Daya Bay unfolding in the antineutrino range [1.875, 8.125]MeV, one ends up with an unchanged $(5.5 \pm 2.2\ [\text{unf.}] \pm 2.1\ [\text{model}])\%$ ^{235}U deficit and a $(8.2 \pm 11.1\ [\text{unf.}] \pm 2.5\ [\text{model}])\%$ deficit for Pu combo, as summarized in Figure 7.24. Here, the "unf." label still refers to the uncertainty in the unfolded spectrum. However, contrary to the HEU-only unfolding, the stacked HEU+LEU covariance matrix (see Equation 7.8) contains model uncertainties from its LEU part, stemming from fission fraction uncertainties and ^{238}U prediction overall uncertainties. Therefore, the uncertainties encoded in the covariance matrix of the unfolded spectra cannot purely be labelled "exp.", as we did for the HEU unfoldings. Let's note however that, given the ^{235}U unfolded spectrum is mostly constrained by the HEU data set, its rate uncertainty is nearly not modified in the HEU+LEU unfolding. This suggests that almost all the model uncertainty encoded in the LEU overall covariance matrix is absorbed in the uncertainty on the Pu

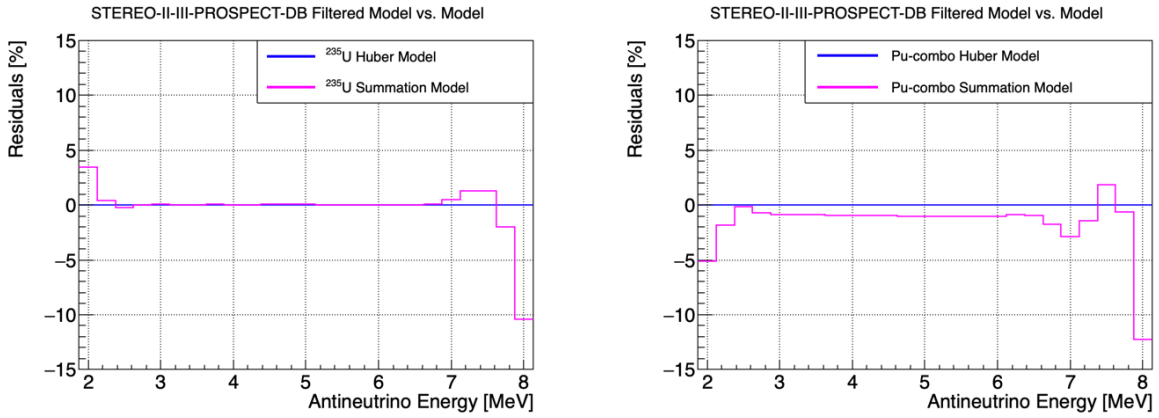

(a) ^{235}U (b) Pu combo

Figure 7.23: **Comparison of the filtered and unfiltered predictions**, for ^{235}U (a) and Pu combo (b). Similarly to the HEU case, the residuals are 0 for the Huber model spectra used as priors for the regularization, whereas small biases are highlighted for the summation model spectra.

combo spectrum. When indeed turning off the Daya Bay model uncertainties, such that $V_{\text{LEU}} = V_{\text{DB}}^{\text{exp}}$, the rate uncertainty on the Pu combo spectrum significantly decreases from 11.1% down to 6.9% while it remains stable for the ^{235}U spectrum.

Comparing our results to those of Daya Bay, three main features must be emphasized. First, we find a higher central value for the plutonium deficit with respect to their published result $(1.0 \pm 5.7\ [\text{exp.}] \pm 2.5\ [\text{model}])\%$, although with a very low significance (0.7σ level). This was expected from the fact that the deficit of ^{235}U is found to be less pronounced in this analysis, constrained by experimental HEU data, than in the Daya Bay analysis $(8.0 \pm 2.3\ [\text{exp.}] \pm 2.1\ [\text{model}])\%$. Yet, all measurements remain compatible within error bars.

Second, let's note that the uncertainty on the rate of the Pu combo in this analysis is twice as high as the Daya Bay uncertainty. This comes from our working with only averaged fission fraction data, that provide less leverage to separate ^{235}U from Pu combo. Yet, as already stated, it presents the advantage to be more data-driven and less dependent on reactor simulations.

Third, with this separation procedure, the correlation coefficient between the absolute IBD fission yields of ^{235}U and Pu combo is -0.43. The yields are found to be anti-correlated, which is a sound result since the total rate has to fit the rate measured by Daya Bay. Surprisingly, the ^{235}U and Pu combo yields obtained from the Daya Bay analysis are found positively correlated, with a correlation coefficient of 0.62.

ST-II-III-DB	$\hat{\Phi}$ IBD Yield Unf. [cm^2/fission/MeV]	$\Phi_{HM} = A_c \cdot \Phi_{HM}$ IBD Yield Pred. [cm^2/fission/MeV]	$\hat{\Phi}/\Phi_{HM}$ IBD Yield Ratio [Unf./Pred.]	$V_{\hat{\Phi}}$ Ratio Error [Unf.]	$V_{\Phi_{HM}}$ Ratio Error [Model]	$A_c^T \cdot V_{\Phi_{HM}} \cdot A_c$ Ratio Error [Filtered Model]
^{235}U	$6.26 \cdot 10^{-43}$	$6.63 \cdot 10^{-43}$	**0.945**	0.022	0.021	0.021
Pu combo	$4.22 \cdot 10^{-43}$	$4.60 \cdot 10^{-43}$	**0.918**	0.111	0.025	0.025

Figure 7.24: **Rate analysis of STEREO and Daya Bay HEU+LEU unfolding**. The fission yields are calculated in the range [1.875, 8.125]MeV in antineutrino energy space.
1st column: IBD fission yield of the isotopic unfolded spectra.
2nd column: IBD fission yield of Huber-Mueller predictions. We remind that the filtered predictions equal the predictions.
3rd column: ratio between the unfolded and predicted yields.
4th column: error on the ratio purely coming from the uncertainties on the unfolded spectra.
5th column: error on the ratio purely coming from the uncertainties on the predicted spectra.
6th column: filtered error on the ratio purely coming from the uncertainties on the predicted spectra.

7.2.5.2 Shape analysis

For the shape analysis, we use the STEREO-PROSPECT data set as a HEU data set to carry out the HEU+LEU unfolding. Let's note that the covariance matrix of the unfolded spectrum (Equation 7.11, Figure 7.21), as well as the unfolding filter matrix $A_{c,\mathrm{HL}}$ (Equation 7.13, Figure 7.22) fully encode the cross-correlations between the ^{235}U and Pu Combo unfolded spectra.

For the Huber ^{235}U + Pu combo stacked prediction, $\Phi^{\mathrm{HM}}_{\mathrm{HL}} = \begin{bmatrix} \Phi^{\mathrm{HM}}_{\mathrm{U5}} \\ \Phi^{\mathrm{HM}}_{\mathrm{Pu}} \end{bmatrix}$, we then include in the Huber covariance matrix all the isotopic cross-correlations, on top of the energy bin-to-bin correlations. In details, the normalization errors, the errors due to the weak magnetism, and the errors due to the effective nuclear charge are fully correlated between isotopes and energy bins [55].

The comparison between the unfolded spectra and their respective predictions is shown in the subsequent Figure 7.25.

The large overall rate deficit is well visible in the Pu combo spectrum, with a substantial local event excess in the 6-7 MeV region, at slightly higher energy than the ^{235}U, and with a significantly higher amplitude than the ^{235}U excess. Therefore, we apply the same test statistics than for the HEU-only unfolding, now fitting simultaneously the ^{235}U and Pu combo bumps, and still assuming for each a (filtered) gaussian shape. Again, we remind that there is no physical reason to choose the gaussian parameterization for the event excess, yet it provides a convenient way to quantify the excess and its significance.

The bumped prediction of Equation 6.28 becomes in the case of the joint unfolding of ^{235}U and Pu combo spectra:

$$\Phi^{\alpha_{\mathrm{U5}},A_{\mathrm{U5}},\mu_{\mathrm{U5}},\sigma_{\mathrm{U5}}}_{\alpha_{\mathrm{Pu}},A_{\mathrm{Pu}},\mu_{\mathrm{Pu}},\sigma_{\mathrm{Pu}}} = \begin{bmatrix} \Phi^{\alpha_{\mathrm{U5}},A_{\mathrm{U5}},\mu_{\mathrm{U5}},\sigma_{\mathrm{U5}}}_{\mathrm{U5}} \\ \Phi^{\alpha_{\mathrm{Pu}},A_{\mathrm{Pu}},\mu_{\mathrm{Pu}},\sigma_{\mathrm{Pu}}}_{\mathrm{Pu}} \end{bmatrix} \tag{7.15}$$

where:

$$\begin{cases} \Phi^{\alpha_{\mathrm{U5}},A_{\mathrm{U5}},\mu_{\mathrm{U5}},\sigma_{\mathrm{U5}}}_{\mathrm{U5}}(E_{\bar{\nu}}) &= \Phi^{\mathrm{HM}}_{\mathrm{U5}}(E_{\bar{\nu}}) \cdot \alpha_{\mathrm{U5}} \left(1 + A_{\mathrm{U5}} \cdot \exp - \frac{(E_{\bar{\nu}} - \mu_{\mathrm{U5}})^2}{2\sigma^2_{\mathrm{U5}}}\right) \\ \Phi^{\alpha_{\mathrm{Pu}},A_{\mathrm{Pu}},\mu_{\mathrm{Pu}},\sigma_{\mathrm{Pu}}}_{\mathrm{Pu}}(E_{\bar{\nu}}) &= \Phi^{\mathrm{HM}}_{\mathrm{Pu}}(E_{\bar{\nu}}) \cdot \alpha_{\mathrm{Pu}} \left(1 + A_{\mathrm{Pu}} \cdot \exp - \frac{(E_{\bar{\nu}} - \mu_{\mathrm{Pu}})^2}{2\sigma^2_{\mathrm{Pu}}}\right) \end{cases}$$

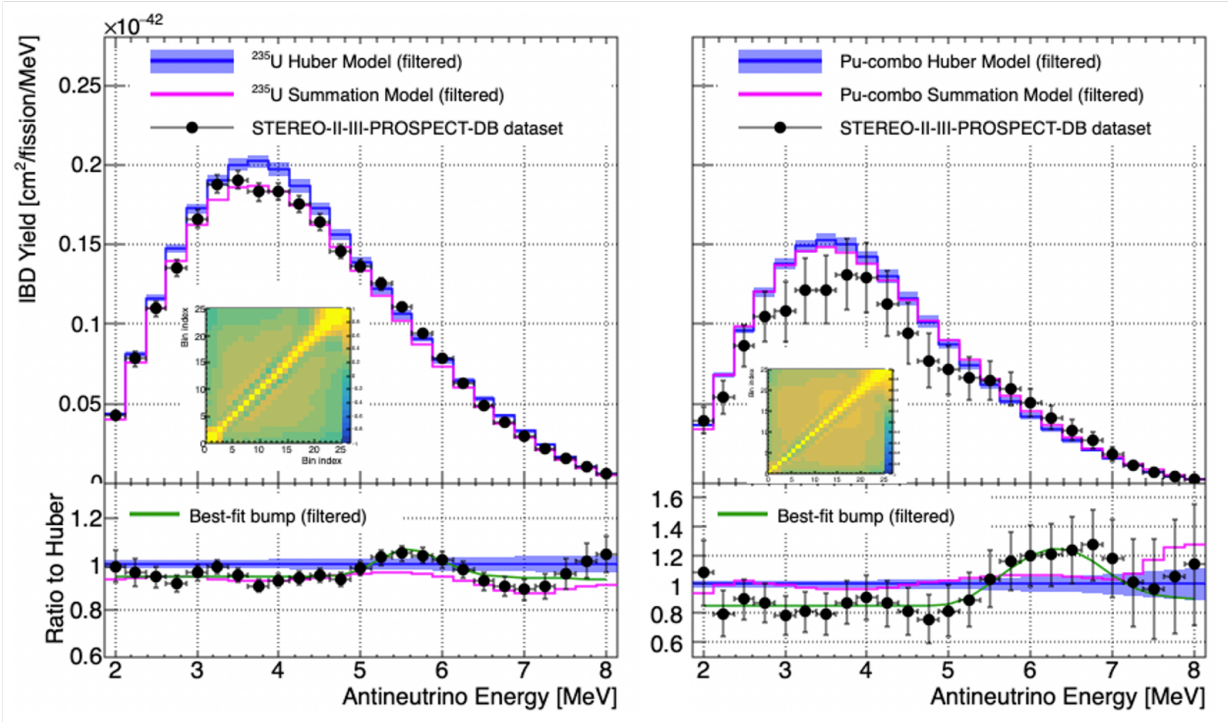

Figure 7.25: **Comparison of HEU+LEU Stereo-Prospect-Daya Bay unfolded spectra with Huber and Summation filtered model predictions**, for the ^{235}U (left) and Pu combo (right). The insets feature the correlation matrices associated to each spectrum. The joint correlation matrix is shown in Figure 7.21. See text for further details.

and the free parameters respectively associated to ^{235}U and Pu combo are to be fitted. The results of the best-fit bumps are summarized in the subsequent Table 7.2.

First, we notice that the best-fit parameters for the ^{235}U unfolding are very similar to those of the HEU unfolding, as expected. This confirms that the HEU data serves as an anchor point in this procedure to separate the uranium from the plutonium contributions in the Daya Bay spectrum.

We may notice as well the low value for the fitted normalization factor in the shape-only comparisons (where no bump is added to the prediction) between Pu combo unfolded and predicted spectra. We performed a quick sensitivity study that showed that gradually reducing the correlations in the Pu combo covariance matrix tended to increase the value of the best-fit normalization parameter up to the ~ 0.9 level, which is the order of magnitude that would be expected from the rate analysis. This bias in the fitted normalization value that appears only for the shape-only comparison is then interpreted as a patent manifestation of the infamous Peelle Pertinent Puzzle (PPP), that arises when fitting the average of strongly correlated data [156, 157]. The fitted value tends to be biased to lower values. To be exhaustive, one should add that this issue also affects the ^{235}U spectrum, yet to a smaller extent than for the Pu combo, because of the reduced (long-range) correlations in the uranium unfolding. This feature is inherent to the covariance matrix formalism, that proceed from a first order linearization of the problem. Alleviating the PPP would require to have the break down of each systematic uncertainties, *in antineutrino energy space*, to write the χ^2 defining the test statistics in a non-linear nuisance parameters formalism [156]. However, let's note that the addition of the gaussian bump to the overall fitted model already allows to circumvent the issue, as the value of the normalization parameter

ST-II-III-PR-DB	Antineutrino Energy space				Reconstructed Energy space	
	w/o. Filter		w. Filter		w. Response	
HM Comparison	Shape–only	Best-fit bump	Shape–only	Best–fit bump	Shape–only	Best–fit bump
α_{U5}	0.940 ± 0.025	0.945 ± 0.026	$\mathbf{0.940 \pm 0.025}$	$\mathbf{0.944 \pm 0.026}$	0.940 ± 0.025	0.944 ± 0.026
A_{U5} [%]	0 ± 0	13.2 ± 2.7	$\mathbf{0 \pm 0}$	$\mathbf{14.4 \pm 3.4}$	0 ± 0	14.5 ± 3.4
μ_{U5} [MeV]	0 ± 0	5.612 ± 0.091	$\mathbf{0 \pm 0}$	$\mathbf{5.593 \pm 0.092}$	0 ± 0	5.593 ± 0.092
σ_{U5} [MeV]	0 ± 0	0.379 ± 0.081	$\mathbf{0 \pm 0}$	$\mathbf{0.330 \pm 0.097}$	0 ± 0	0.330 ± 0.097
α_{Pu}	0.656 ± 0.068	0.861 ± 0.085	$\mathbf{0.651 \pm 0.068}$	$\mathbf{0.850 \pm 0.086}$	0.656 ± 0.068	0.850 ± 0.086
A_{Pu} [%]	0 ± 0	47.6 ± 13.2	$\mathbf{0 \pm 0}$	$\mathbf{50.4 \pm 15.2}$	0 ± 0	50.4 ± 15.3
μ_{Pu} [MeV]	0 ± 0	6.399 ± 0.284	$\mathbf{0 \pm 0}$	$\mathbf{6.325 \pm 0.268}$	0 ± 0	6.324 ± 0.268
σ_{Pu} [MeV]	0 ± 0	0.618 ± 0.215	$\mathbf{0 \pm 0}$	$\mathbf{0.531 \pm 0.244}$	0 ± 0	0.531 ± 0.244
χ^2/dof	76.1/46	18.2/40	**84.7/46**	**25.9/40**	141.2/100	82.5/94
$\Delta\chi^2/\Delta$dof	57.9/6		**58.8/6**		58.8/6	
Significance (one-sided)	6.3σ		$\mathbf{6.4\sigma}$		6.4σ	

Table 7.2: **Best-fit bumps for the HEU+LEU Stereo-Prospect-Daya Bay unfolded spectra**. See text for details.

is compatible with the offset in the data, as clearly visible in Figure 7.25.

Interestingly, the $\sim$ 8% deficit in the Pu combo spectrum highlighted by the rate analysis appears to break down in a -15% offset in the spectrum normalization with respect to both Huber and Summation model predictions and a $\sim 50\%$ local event excess around 6.3 MeV, wider than the ^{235}U bump. They are highlighted in red in Table 7.2.

Besides, the 6.4σ significance that we report is the significance associated to combined bumps in both ^{235}U and Pu combo, as the derivation of this quantity stems from the $\Delta\chi^2$ comparison of the jointly bumped and rescaled stacked prediction with the rescaled stacked prediction. In order to derive a significance that would be associated to a pure Pu combo bump, whilst taking into account the cross-(anti)correlations of the Pu combo and ^{235}U unfolded spectra, one must make a $\Delta\chi^2$ comparison of the jointly bumped and rescaled stacked prediction (column "best-fit bump" in Table 7.2) with a prediction that would be bumped and rescaled in ^{235}U and only rescaled in Pu combo. For this latter prediction, we obtain a $\chi^2/\text{dof} = 37.3/43$ for the agreement with the ^{235}U + Pu combo unfolding, which yields to a $\Delta\chi^2/\Delta\text{dof} = 11.4/3$ for the model comparison, corresponding to a 2.3σ significance for the Pu combo bump. At last, let's note that, doing the same to quantify the significance of the ^{235}U only bump in this HEU+LEU separation procedure, one ends up with an unchanged 4.7σ significance, as we would have naively expected.

7.3 On the possible origin of reactor anomalies...

The HEU and HEU+LEU unfoldings and analyses provided strong hints for a combined rate and shape anomaly in the ^{235}U spectrum, and indications for such anomaly in the plutonium spectrum. Still, the oscillation analysis detailed in Section 6.1 ruled out the sterile neutrino hypothesis as an explanation for the rate anomaly, for a large fraction of the preferred phase space region. These results then suggest long-standing biases in the derivation of the predictions, such that the explanation of the anomalies would rather lie in a better treatment of the model computation.

In particular, for the ^{235}U spectrum, the summation EF model [51] proved to be in better agreement with the HEU data, up to the 5 MeV local event excess (see Figures 6.24 and 7.8). In this approach, complementary to the conversion (Huber) method, one builds a prediction with the sum of the antineutrino spectra of all fission products taken from the nuclear data bases. A key ingredient of these models is the correction of the beta strengths involved in the decay of fission products. Experimentally, it is difficult to measure beta transitions to the highly excited levels of the daughter nucleus, because of the high density of states and the complex gamma cascades that are associated [158]. This results in a well-known bias in nuclear data bases, the so-called pandemonium effect, that tend to underestimate the contribution of low energy beta transitions. In [49], an effective correction of this effect is investigated and yields to unprecedented agreement with the STEREO unfolded spectrum (see Figure 7.26). Therefore, it seems that correcting this bias is a key element in bringing the summation model in agreement with the data. Furthermore, using the correspondence between electron and antineutrino spectra in the summation approach, the shape and rate anomalies would translate into similar deviations on the electron side [159], suggesting that the reactor antineutrino anomalies would find their origin in a norm and shape bias for all measured electron spectra, that are used as inputs in the Huber conversion method.

In a recent effort, Kopeikin *et al.* reevaluated the reactor antineutrino spectra [160] with new measurements of the ratio between the cumulative fission β spectra of ^{235}U and ^{239}Pu, performed at a research reactor in National Research Center Kurchatov Institute (KI) [161]. The original β spectra of the ILL measurements [52, 53, 54] were obtained by *alternatively* irradiating with a high neutron flux thin target foils of uranium and plutonium, such that the normalization of each spectrum directly depends on the precise knowledge of the neutron flux used for each measurement. Notably, two measurements were performed for ^{235}U and, even if the final measurement is taken as the reference, they exhibited discrepancies in their absolute normalization at the level of several percents [160]. In the KI measurement, the cumulative fission β spectra of ^{235}U and ^{239}Pu are measured *simultaneously*, such that reconstructing their ratio alleviates any bias due to the absolute normalization of each measurement. Their ratio showed an excess of $(5.4 \pm 0.2)\%$ with respect to the ILL ratio, pointing towards a relative normalization bias between U and Pu. Based on Daya Bay results [152] and the $\sim 5\%$ ^{235}U deficit reported by STEREO in [125], they suggested the 5% excess to be fully born by the ^{235}U isotope and proposed to renormalize the Huber-Mueller prediction accordingly. This new model proved to be the best conversion model to date for fitting the antineutrino reactor rates [43]. Yet, it still fails to reproduce the 5 MeV bump.

Overall, these studies point towards the need to have better descriptions of the fission β spectra, both on the theoretical and experimental points of view. To this end, the isotopic antineutrino spectra, measured at research and commercial reactors with compelling accuracy, bring supplemental constraints, such that they can now be seen as nuclear data in their own right.

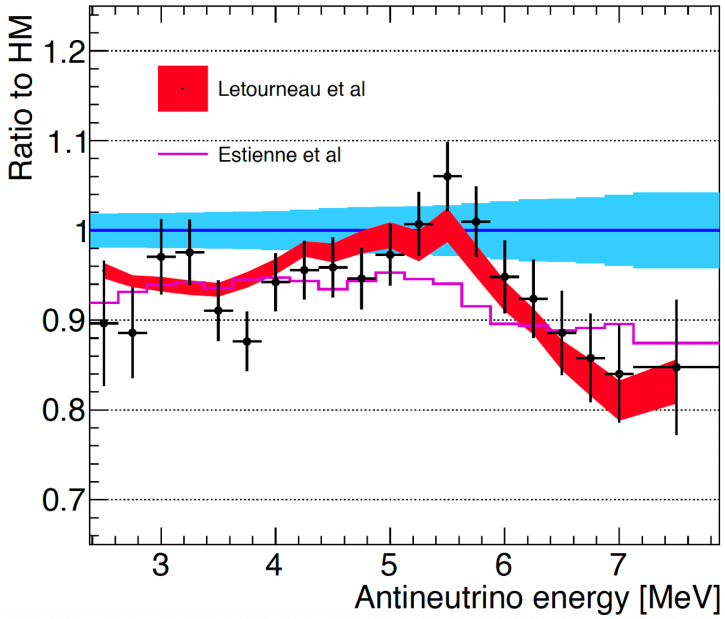

Figure 7.26: **Comparison of STEREO unfolded spectrum with recent summation models**, as a ratio to the Huber ^{235}U prediction (blue). The unfolded spectrum is depicted as black dots. The prediction of Estienne *et al.* [51] (magenta) corrects the evaluated nuclear data by including the most recent measurements of the β-strengths of the main fission products. It is in good agreement with the mean deficit measured by STEREO and could indicate the beginning of a shape distortion at high energy. A complementary approach by Letourneau *et al.* [49] (red band, featuring a 1σ uncertainty) generalizes the correction of the β-spectra to all nuclei by completing the β-decay schemes of the ENSDF nuclear data base [162] with a simple phenomenological Gamow-Teller β-decay strength model. Remarkable agreement with the STEREO spectrum is obtained both in normalization and in shape.

Chapter 8

The NUCLEUS experiment

NUCLEUS is an experiment aiming at measuring the cross-section of the coherent elastic neutrino-nucleus scattering (CEνNS). To this end, the experiment will be operated in the Chooz nuclear power plant (les Ardennes, France) and will detect reactor antineutrinos via this neutrino-matter interaction. As we saw with the STEREO experiment, the energy of reactor antineutrinos is typically below 10 MeV, thus falling in the full coherent regime where the scattering neutrino sees the nucleus as a whole, and is insensitive to its nucleonic structure. As detailed in the introductory chapter, in the coherent neutrino-nucleus scattering interaction regime, the interaction cross-section is boosted by a factor $\propto N^2$, where N is number of neutrons of the target nucleus, such that the CEνNS interaction cross-section could exceed by up to three orders of magnitude the IBD interaction cross-section used in standard neutrino detection experiments, e.g. STEREO. This feature allowed to miniaturize the detector concept of the NUCLEUS experiment to gram-scale calorimeters. On top of being a new low-energy probe to test the Standard Model, the CEνNS thresholdless process will also be sensitive to the unexplored part of the reactor antineutrino flux, that lies below the IBD threshold of 1.8 MeV. This region is out of reach for experiments such as STEREO.

The NUCLEUS collaboration was founded in 2018. It is a joint effort from various European research institutes and laboratories: CEA-Saclay/Irfu (France), Istituto Nazionale di Fisica Nucleare (INFN, Italy), Institute of High Energy Physics (HEPHY, Austria), Technische Universität Wien (TUWien, Austria), Technische Universität München (TUM, Germany) and Max-Planck-Institut für Physik (MPIP, Germany). The technical design of the experiment is finished and the blank assembly of the full NUCLEUS setup is currently ongoing in TUM underground laboratory. This will allow a full commissioning of the detector before its relocation in the Chooz nuclear power plant, most likely by the end of 2023. The first physics run is expected in the beginning of 2024.

In the subsequent sections, we present the experimental site as well as the overall detector concept and shielding strategy for the NUCLEUS setup, designed to reach the specifications for the background index of the experiment.

8.1 Experimental site

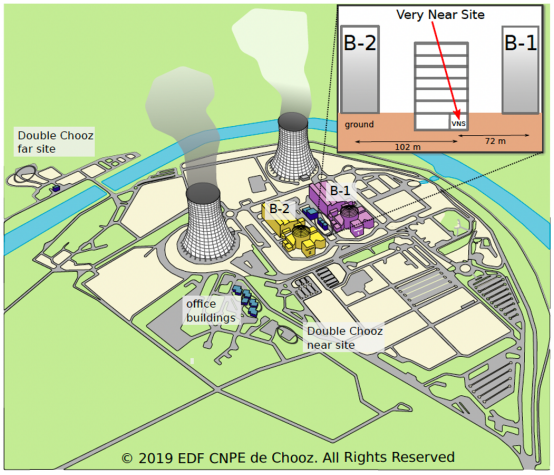

Figure 8.1: **Sketch of the Chooz nuclear power plant and the Very Near Site (VNS)**. The inset shows the office building between the reactor cores hosting the VNS. Taken from [163].

The Chooz nuclear power plant, sketched in Figure 8.1, operates two N4-type commercial nuclear reactors, labelled B-1 and B-2, and about 160 m apart. Each reactor runs at a nominal thermal power of 4.25 GWth and is switched off for refueling operations approximately one month per year.

The NUCLEUS experiment will be installed in the so-called Very Near Site (VNS). It consists in a 24 m^2 basement room of an administrative building located at respectively 72 m and 102 m from B-1 and B-2 reactor cores. At this distance, the reactor antineutrino flux is expected to be $\mathcal{O}(10^{12})$ $\bar{\nu}_e/(s \cdot cm^2)$. Yet, the exiguity of the room requires a compact design of the full NUCLEUS assembly, at the level of a few cubic meters, and a weight of the order of $\mathcal{O}(10$ t) [163].

The background sources of interest for the experiment may be categorized as: reactor induced background, cosmic-ray induced, external and internal radiogenic background.

Thanks to the shielding of the reactor core and a $\mathcal{O}(10$ m) layer of rock and concrete between the VNS and the reactor building, the reactor induced background is expected to be negligible.

The VNS building provides a shallow overburden for the attenuation of cosmic ray induced particles, such as muons and neutrons, that has been measured to be (2.9 ± 0.1) m.w.e. [163]. In particular, a neutron can mimic the CEνNS signal by elastic scattering on a target nucleus. Given the neutron mass and the sub-keV recoil energy of the NUCLEUS energy range of interest, only fast neutrons reaching the detector with few keV energy are critical. On-site measurements are ongoing in order to further validate the design of the passive shielding established with the simulation for the mitigation of this background.

At last, natural radioactivity, coming either from the building or surrounding materials (external background), or the detector components themselves (internal background), has to be considered, due to their γ, β and α induced radiations. While the external background can be reduced with dedicated external passive shielding, analogous to those of STEREO experiment, the internal background can be mitigated by appropriate radio-purity study and cleaning procedure in the detector production and assembly, and actively vetoed by the instrumentation of the detector inner surrounding materials.

8.2 Detector concept

General principle

As detailed in the introductory chapter, the signature of a CEνNS interaction is a nuclear recoil of the target nucleus induced by the scattering antineutrino. Detecting such event requires ultra-low threshold technology of detection. The NUCLEUS collaboration opted for cryogenic calorimeters, reinvesting the R&D effort carried out by the CRESST collaboration in the conception of their own cryogenic detectors, designed for direct low mass dark matter search [164]. They consist in $CaWO_4$ and Al_2O_3 crystals, brought to gram-scale ultra-low threshold cryogenic calorimeters [165], down to 20 eV (recoil energy equivalent). NUCLEUS has been conceived as a two-phase experiment: first, NUCLEUS-10g and, in a second step NUCLEUS-1kg, that will operate a detector with respective target masses of 10g and 1kg.

The target detector for the first phase of the experiment will consist of two arrays of 3×3 cubic crystals. Each crystal is 5 mm in size and made of $CaWO_4$ (6 g) or Al_2O_3 (4 g). This multi-target approach fully exploits the N^2-dependence of the CEνNS cross-section to characterize the background in the direct vicinity of the target tungsten nuclei of the $CaWO_4$ crystal. Indeed, given the light nuclear composition of the Al_2O_3 crystal, the CEνNS event rate is found to be ~ 2 orders of magnitude lower than in the $CaWO_4$ crystal, as illustrated in Figure 8.2. Consequently, the signal induced by neutrino scattering will be heavily suppressed in Al_2O_3 , whereas the background induced by fast neutron scattering is expected to be similar in both crystals. Thus, the Al_2O_3 crystal provides us with a benchmark measurement allowing to constrain the background model of the experiment [163]. The targeted background index for NUCLEUS is at the level of 100 counts/(keV·kg·day), such that a 5σ observation of CEνNS in the 20-100 eV (recoil energy equivalent) region of interest can be achieved in $\sim$ 40 days of data taking [166].

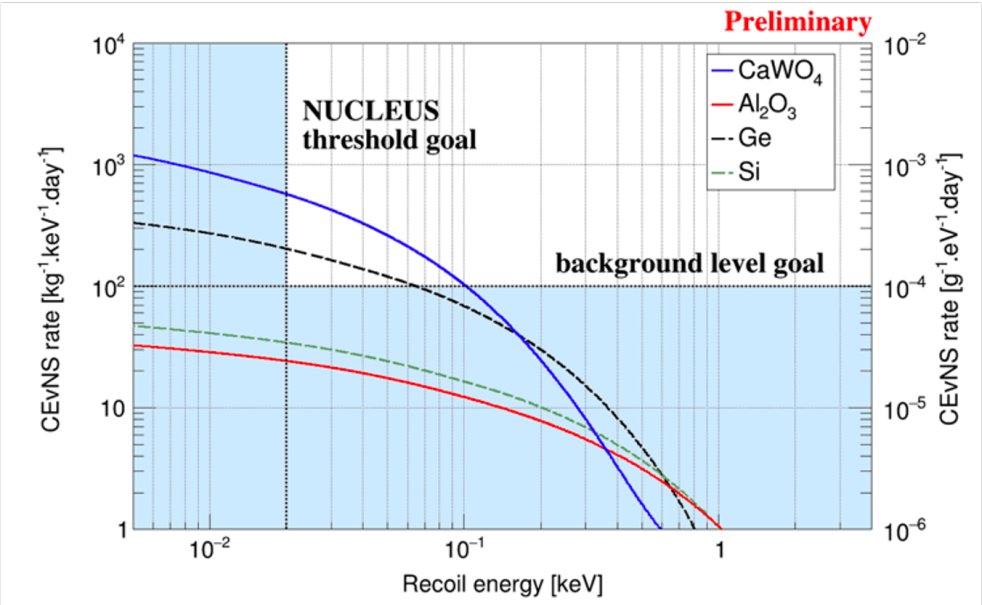

Figure 8.2: **Differential CEνNS rate expected at the VNS** for different target materials assuming an average loading factor of 80% of the reactors. Taken from [166].

Signal measurement

The crystals will be operated at a temperature $\mathcal{O}$(mK). As cryogenic calorimeters, they allow to measure a small temperature rise $\Delta T = \Delta E/C$ given an energy deposition ΔE in the target detector characterized by a heat capacity C. At mK temperatures, C is small enough to achieve measurable ΔT, at the level of $\mathcal{O}(\mu\text{K})$, for typical CEνNS nuclear recoil energy [163].

The crystals will be equipped with thin-film tungsten Transition Edge Sensors (W-TES), shown in Figure 8.3. These sensors exploit the steep resistance change occurring in a thin metal film in a normal-to-superconducting transition at sub-Kelvin temperature, and have proven to be highly sensitive thermometers [167]. The TES readout currents, kept below few tens of μA, are coupled to Superconducting Quantum Interference Devices (SQUIDs) based electronics, allowing to have a sizeable pulse signal as an output [168, 169]. The amplitude of the pulse gives a precise measurement of the deposited energy. With such device and the small Al_2O_3 prototype shown in Figure 8.3, an unprecedented ultra-low threshold of $E_{th} = (19.7 \pm 0.9)$ eV in nuclear recoil energy has been reached [165].

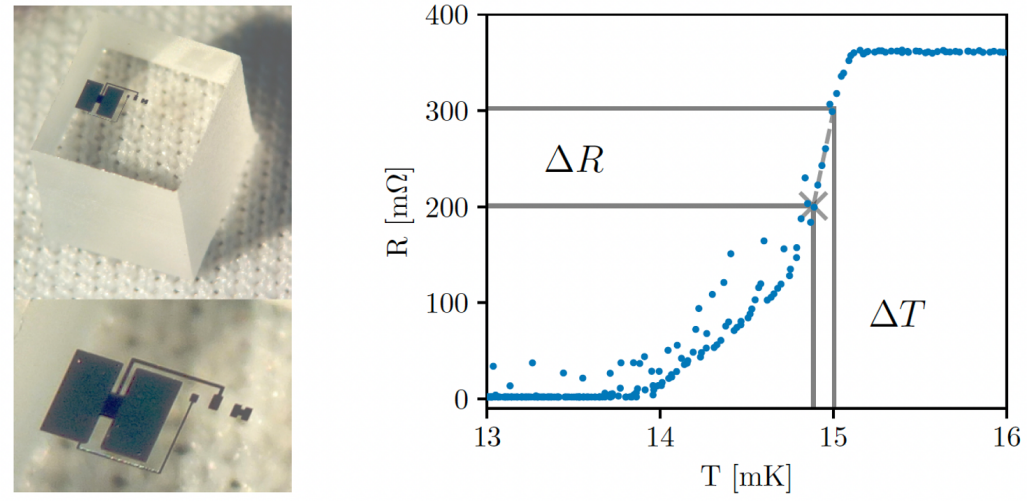

Figure 8.3: *(Left)* $(5\times5\times5)\text{mm}^3$ Al_2O_3 crystal equipped with W-TES (zoomed in on the bottom plot). *(Right)* W-TES resistance as a function of temperature. Illustrated is the transition where a small increase in temperature of 120 μK translates into a sizeable increase in the resistance of 102 mΩ. Taken from [170].

Overall design of the experiment

The technical design of the experiment has been extensively detailed in [166, 171, 172], which I simply summarize here. The overall setup is illustrated in Figure 8.4.

The target detectors are embedded into an instrumented inner veto detector, made of 200 μm thick silicon wafers mounted in a 4π box assembly. They are read out by W-TES, with a sub-keV trigger threshold. They allow to veto surface backgrounds coming from alpha and beta radiation, as well as low energy holder-related events potentially induced by mechanical stress relaxation [173].

The inner veto detector is in itself enclosed in a cryogenic outer veto, which is a 4π assembly consisting of 2.5 cm thick high-purity Germanium (HPGe) crystals to actively

reject external neutron and gamma backgrounds. The outer veto is installed inside a Bluefors cryostat, allowing to reach a temperature of ∼10 mK for the cryogenic detectors.

The cryostat is surrounded by a compact, $\mathcal{O}(\mathrm{m}^3)$, external passive shielding consisting of a 5 cm thick layer of lead and a 20 cm thick layer of 5%-borated polyethylene (PE), to dampen the gamma and neutron backgrounds. An additional 4 cm thick boron carbide layer (B_4C) will surround the Ge outer veto, inside the cryostat, in order to further mitigate the neutron background in the vicinity of the target detectors [172].

The passive shielding is encapsulated in a muon veto assembly, designed to ensure a 4π coverage for the rejection of muon induced background. It has been shown that, without the muon veto, 26 ± 1 muon-induced neutron events are expected below 100 eV per (kg · day) exposure in $CaWO_4$ (resp. Al_2O_3), compared to 32 (resp. 1.9) CEνNS events [170]. Thus, the NUCLEUS signal-to-background ratio highly depends on the rejection power of the designed muon veto. Targeting an overall muon tagging efficiency of >99%, the R&D effort carried out to develop the NUCLEUS muon veto will be extensively detailed in Chapter 9.

At last, to close the hole in the muon veto where the cryostat enters the shielding, a disk-shaped cryogenic muon veto, operated at a temperature of 800 mK, is installed at the same height as the room-temperature muon veto [174].

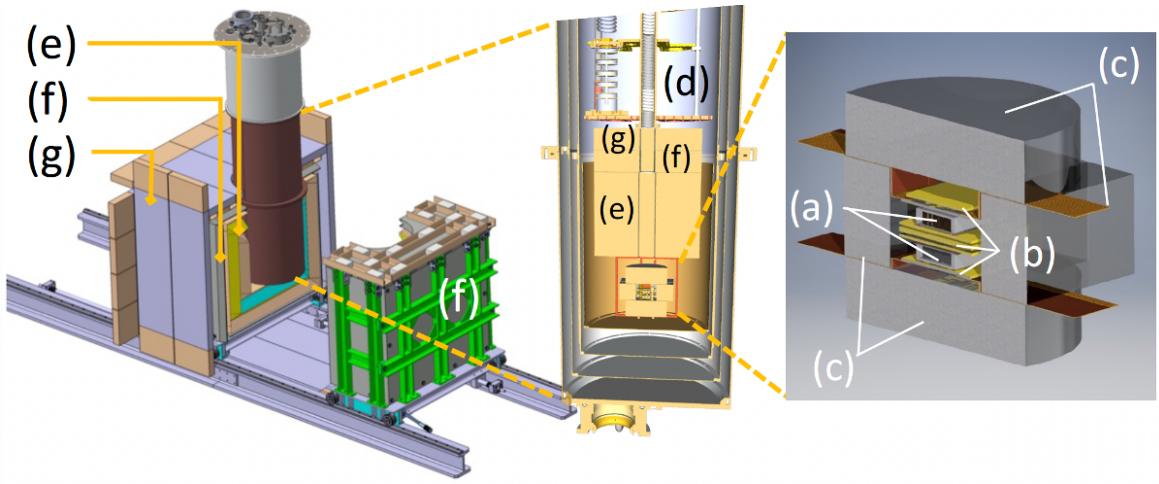

Figure 8.4: **Sketch of the NUCLEUS experimental setup**. *Right*: the target detectors (a) are arranged in two 3×3 arrays with a total mass of 6 g ($CaWO_4$) and 4 g (Al_2O_3) which are mounted inside an instrumented Si holder, the inner veto (b). The inner cryogenic detectors are surrounded by cryogenic HPGe detectors (c), forming the outer veto. *Middle*: The cryogenic detectors are operated inside a cryostat (d). *Left*: The cryostat enters the passive shielding consisting of PE (e) and Pb (f). The passive shielding is surrounded by an active muon veto (g). The full shielding is mounted on a movable mechanical structure. Taken from [171].

8.3 Expected signal and background

Extensive Monte-Carlo simulations, including the implementation of the full assembly of the NUCLEUS experimental setup, have been run in order to evaluate the expected background event rate in the target crystals, when applying all relevant selection cuts, and check whether it meets the background index specifications. These cuts consist of anti-coincidence trigger schemes between the target crystals and the inner veto, the Ge cryogenic outer veto, and the muon veto, with respective energy thresholds of 30 eV, 1 keV and 5 MeV [172]. Additionally, an anti-coincidence between each target crystal is required to further reject background events, as it is very unlikely for an antineutrino to interact in two crystals of the 3×3 array. Preliminary results showed the feasibility to achieve a background index $\lesssim 100$ counts/(keV·kg·day), thus meeting the specifications. As shown in Figure 8.5, atmospheric neutrons remain the dominant background, followed by atmospheric muons and ambient gammas.

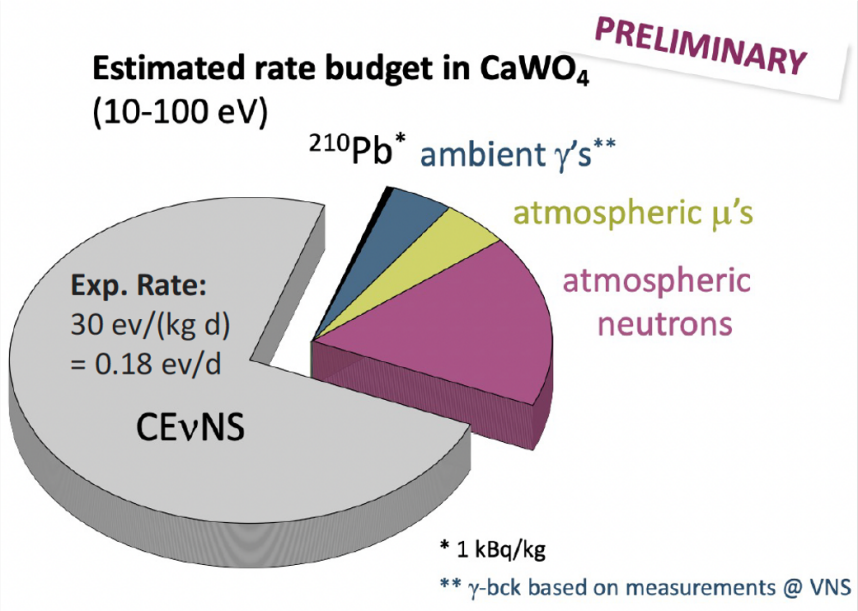

Figure 8.5: **Estimated rate budget in NUCLEUS $CaWO_4$ crystal**, in the recoil energy region of interest [10, 100]eV. The background distribution originating from the decay of radio-elements present in lead has been constrained from radio-purity measurements, whereas the γ background distribution is based on in-situ measurements, at the VNS. Taken from [172].

The physics runs of the first phase of the NUCLEUS experiment are planned to start no later than 2024. Whereas this first phase should provide us with strong evidence of CEνNS signal, it will be statistically limited. The second phase of the experiment, NUCLEUS-1kg, will alleviate this limitation by deploying a target mass of 1 kg, such that a percent-level precision measurement of the CEνNS cross-section will be within reach [163].

Chapter 9

Preparation of the NUCLEUS Muon Veto

In this chapter, we detail the work and studies that were undertaken to prepare the final assembly of the NUCLEUS muon veto. The apparatus was designed as a cubic assembly of plastic scintillator panels, fully encapsulating the cryogenic target detectors, in order to tag the passage of muons in their vicinity. If a muon is tagged, a typical veto time window enclosing the muon event is removed from the total exposure time. For dead time considerations, only the muon-induced prompt events are therefore discarded. The veto time is determined from the rise time of the signal in the target detectors, which constitutes the main limitation in the definition of time coincidence. This rise time is of the order of a few tens of μs, such that the veto time window has been set to be $\sim 50\mu$s wide [163]. To limit the veto induced dead time to a few percent level, the rate of tagged muon events must be at the level of a few hundreds of Hz. This imposes a very compact design of the veto around the experimental setup. Furthermore, as discussed in the previous chapter, the main requirement of the veto is the capability to identify muons with an efficiency $> 99\%$. Considering all these prerequisites, we fully characterized in this doctoral work the performance of one compact muon veto panel, in terms of light yield, muon identification power, and response homogeneity. We also extensively worked on the online calibration of the read-outs, for the operation of the final experiment. This work resulted in a published technical report [175], that we largely reinvest in this chapter.

9.1 Prototype panel and test stand

9.1.1 Prototype panel

The muon veto prototype panel consists of a $L \times l \times h = 120.0 \times 28.0 \times 5.0$ cm^3 polyvinyltoluene-based BC-408 plastic scintillator from Saint-Gobain [176], and recycled from the CAMERA experiment [177]. This module features a large light output ($\sim$ 11k photons/MeV) and large attenuation length ($\sim$ 2 m). At minimum ionization energy loss, a muon deposits 2.02 MeV/cm along its passage through such scintillating material [178]. As a consequence, a typical vertical muon is expected to deposit 10.1 MeV in the 5 cm thick prototype, enabling a clean separation from the ambient γ-rays signal which extend up to 2.6 MeV (^{208}Tl γ-line).

The plastic scintillator is equipped with optical fibers to absorb and guide the scintillation light towards a dedicated light sensor (Figure 9.1a), placed either at one end or at both ends of the scintillator. The fibers run in 2 mm deep grooves along the full length of the plastic scintillator, each separated by a distance of 30 mm. Three fiber configurations were tested. First, the straight fiber configuration (Figure 9.1b) consisting of 9 fibers running along the bottom side of the prototype panel and connected to the read-outs at both ends of the prototype. Second, the U-turn fiber configuration (Figure 9.1c) running on the top side of the prototype. This latter configuration is formed by 4 fibers that perform a U-turn in a dedicated "pool" area at one end of the prototype, and are read at the other end with 1 additional straight fiber running in the middle groove of the prototype. The $275 \times 60 \times 5$ mm^3 pool is a 5 mm thick rectangular-shaped gap carved into the plastic scintillator, and where the fibers merely stand in the air. In a third side attempt, the second SiPM in Figure 9.1b is replaced by a mirror at the open fiber end. This one-sided read-out configuration is called the mirror configuration.

The configuration with the straight fibers is the simplest design, expected to perform best in terms of light collection. However, this comes at the expense of a second SiPM read-out channel and thus, additional uninstrumented volume inside the module box. This dead volume can be saved in the U-turn or mirror configuration.

As light sensors and read-outs, we chose the Silicon Photo-Multiplier (SiPM) module PE3325-WB-TIA-SP from KETEK [179], that features an integrated trans-impedance amplifier. As optical fibers, we chose multi-clad wavelength-shifting (WLS) fibers of type BC-91A from Saint-Gobain [180] with a cross-section of 1×1 mm^2. Their absorption and emission spectra match well the transmission spectrum of the BC-408 plastic scintillator and the range of high photo-detection efficiency of the chosen SiPMs. For good optical coupling between the fibers and the scintillator on one hand, and between the fibers and the SiPMs on the other hand, optical grease is inserted into the grooves and at the fibers-SiPM junction. Additionally, tiny drops of glue at each end of the grooves keep the fibers in place. The fibers and SiPMs are attached all-together by means of a 3D printed connector, that ensures a precise alignment of the fiber cross-section with the active area of the SiPM, as well as a safety gap of a few hundred microns between the surfaces. Prior to their connection, the fibers are accordingly cut and polished. Moreover, the SiPM modules are placed with a distance of 17 cm with respect to the plastic scintillator in order to respect the WLS fibers recommended minimum bending radius of 5 cm.

To enhance the scintillation light collection, the plastic scintillator is wrapped in a diffusive Lumirror E6SR foil from TORAY [181]. At last, the full module including the

SiPMs is enclosed in an aluminum light-tight box to mitigate the light leaks in the setup.

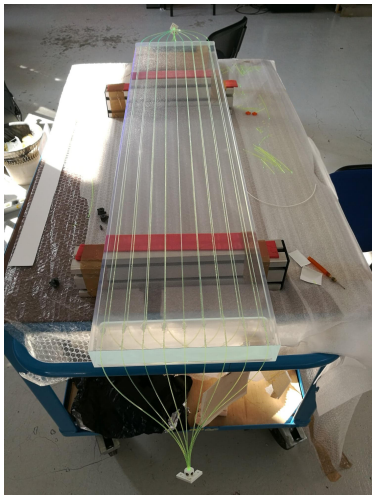

(a) Prototype muon veto module

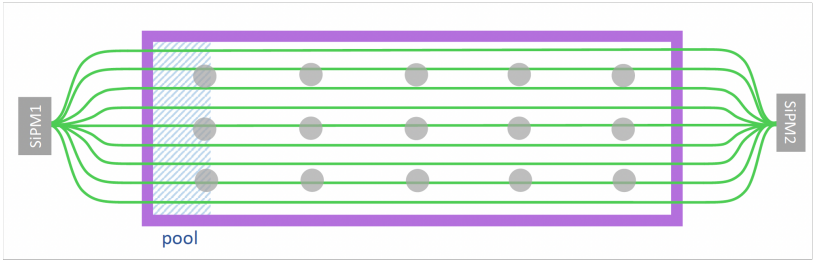

(b) Straight fiber configuration (bottom side)

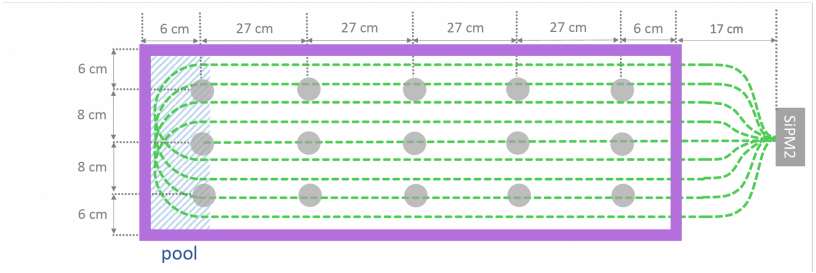

(c) U-turn fiber configuration (top side)

Figure 9.1: **NUCLEUS muon veto prototype panel.** (a) Photograph of the panel with the straight fiber configuration on the bottom side, and the U-turn fiber configuration on the top side. (b) Straight fiber configuration, read at both ends with SiPMs. (c) U-turn fiber configuration, read at one end with one SiPM. The grey circles mark the position mapping allowing to perform local measurements to evaluate the homogeneity of the response of the panel. They are discussed in Section 9.4.

9.1.2 Test stand

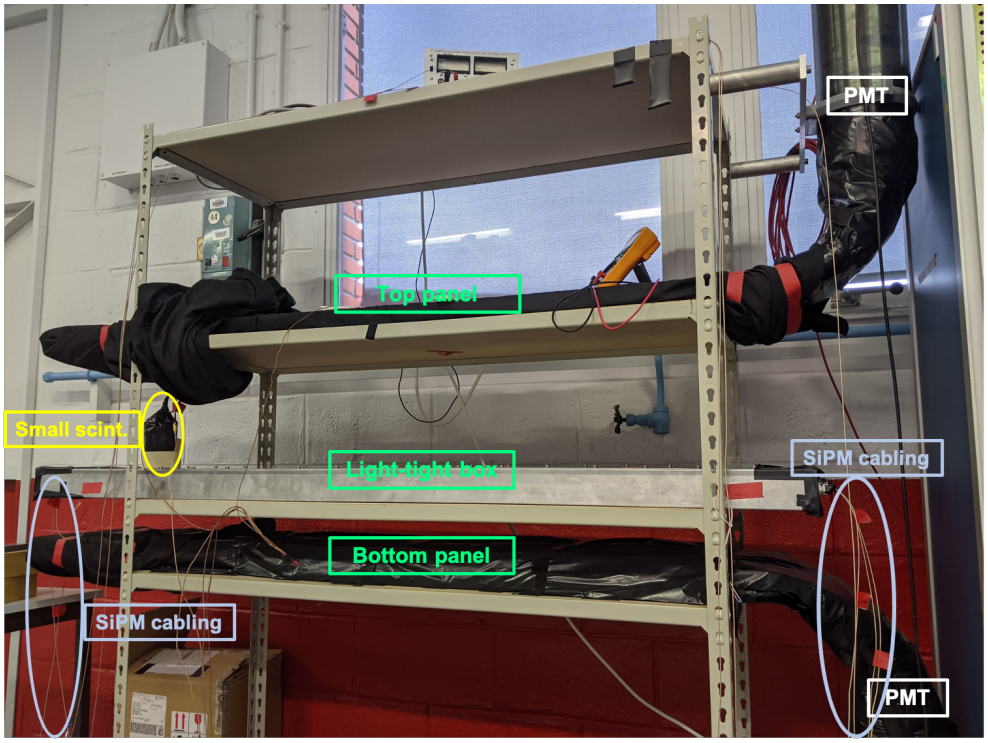

(a) Photograph

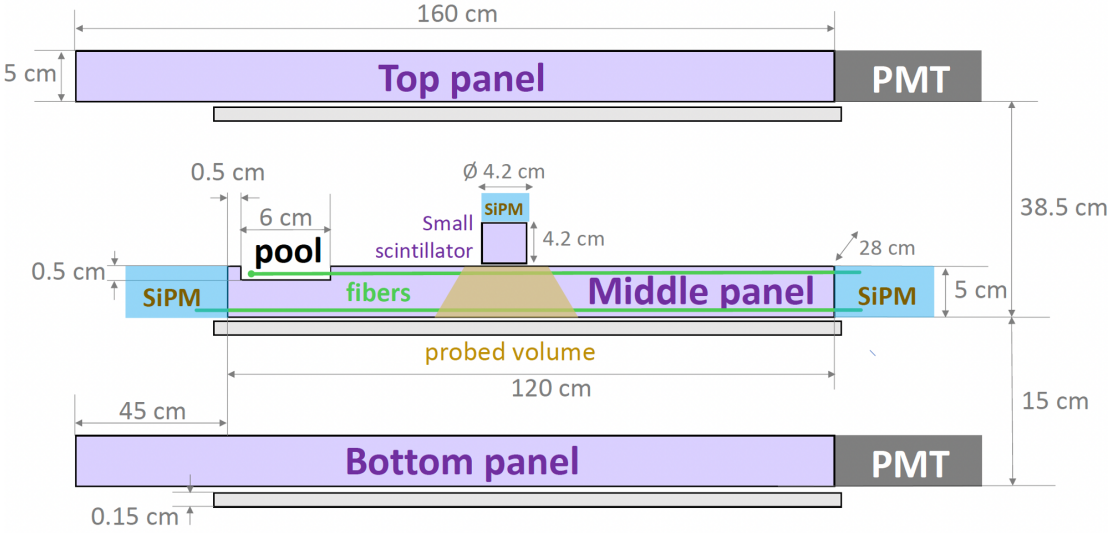

(b) Scheme

Figure 9.2: **Muon veto test bench**, illustrated with a photograph (a) and a scheme (b). Wood shelves are drawn in grey and plastic scintillators in purple. The top and bottom plastic scintillator panels are packed in a black and opaque coverage to prevent light leaks, and optically connected to PMT read-outs. The middle panel is the NUCLEUS muon veto prototype, that is enclosed in the aluminum light-tight box with the SiPM read-outs. Two series of grooves are machined in the plastic scintillator, and host the U-turn and straight fiber configurations on each side. In the case of the mirror fiber configuration, one SiPM read-out of the straight fiber configuration is replaced by a mirror. The blue area marks the non-instrumented part of the aluminium box where the SiPM module is placed.

To characterize and compare the performance of the different fiber configurations, we built a dedicated test stand, shown in Figure 9.2. The prototype (middle panel) is placed in-between two 1.6 m-long plastic scintillator panels, each one optically coupled to a PMT read-out. These two panels (denoted top and bottom panels) are used to select muon events by means of a three-fold coincidence between the two PMT signals and the SiPM signal(s). To select muons passing through a small volume of the prototype, an additional plastic scintillator with a diameter and a height of 4.2 cm, read out with a SiPM, is used.

Figure 9.3 shows a scheme of the data acquisition (DAQ) system that was used for the prototype testing. The SiPM signal is split by a linear fan-in fan-out (FIFO), out of which one output signal is used for trigger generation and the second one is fed into a 2-channel fast analog-to-digital converter (FADC) with a sampling frequency of 250 MHz. Optionally, the signal can be amplified with a fast amplifier providing an amplification factor of 10.2, and an internal gain of 10 provided by the FADC card. This acquisition mode, that we call calibration mode, will be used for the study of the photo-electron spectrum of the SiPMs in Section 9.2.

Only the integrated charge of the SiPM pulse within a 200ns-wide window following the generated external trigger is recorded. The trigger for the signal acquisition is generated by analog NIM electronics, composed of a constant fraction discriminator (CFD), a coincidence module and a level translator. The recorded charge is corrected online for the integrated baseline, which is calculated in a 40 ns window prior to the trigger.

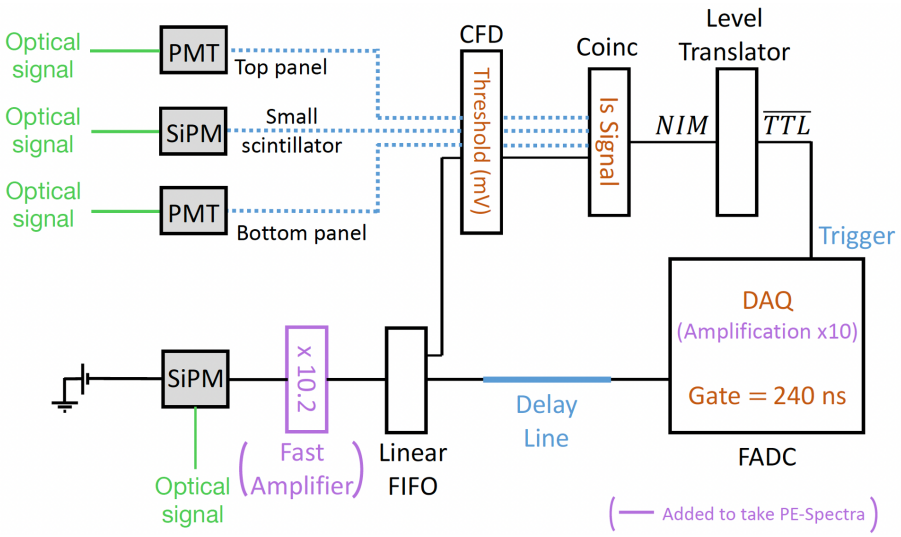

Figure 9.3: **DAQ scheme**. The prototype SiPM signals are processed by an FADC. The external trigger is generated by a constant fraction discriminator (CFD), a coincidence module (Coinc) and a level translator. By demanding a coincidence of the prototype SiPM signal(s) with the top and bottom PMT signals, or the SiPM signal of the small plastic scintillator, different muon samples can be selected. Optionally, for calibration measurements, the SiPM signals can be amplified by a fast amplifier and a FADC-internal amplification.

9.2 Silicon Photomultipliers

9.2.1 Working principle

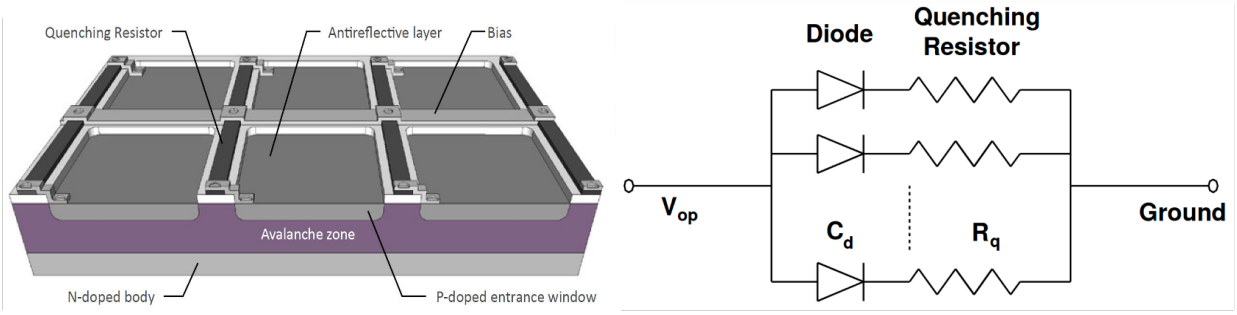

(a) (b)

Figure 9.4: (a) Schematic drawing of a SiPM. The p-n junctions and quenching resistors are interconnected via a silicon substrate that forms the avalanche zone. Anti-reflective coating layer increases the transmission for impinging photons. Source [182]. (b) Equivalent circuit of a SiPM, corresponding to an arrangement of SPADs and their associated series quenching resistors connected in parallel. Source [183].

SiPMs are sensors consisting of an arrangement of independent Single Photon Avalanche Diodes (SPADs).

A SPAD is formed by a semi-conductive silicon p-n junction that creates a depletion region, free of mobile charge carriers. A photon travelling through silicon may be absorbed by an electron and create an electron-hole pair by photo-electric effect. When applying a strong enough reverse bias to the SPAD, one can induce a sufficiently high electric field inside the silicon such that this electron-hole pair carries enough energy to trigger a ionization cascade. This cascade will spread throughout the silicon volume towards the electrodes (p- and n- regions), resulting in a macroscopic current flow. In this process called Geiger discharge, the silicon region then breaks down and become conductive, and can be referred to as the avalanche zone. The current is quenched by associating the photodiode with a resistor placed in series. The relevant quantity to consider when operating the SPAD with a bias voltage V_{bias} is then the over-voltage ΔV applied with respect to the minimal voltage value required to operate the SPAD in Geiger mode and called the breakdown voltage $V_{\text{breakdown}}$: $\Delta V = V_{\text{bias}} - V_{\text{breakdown}}$. Notably, the amplification of the original electron-hole pair signal is proved to increase linearly with respect to the applied over-voltage [184].

Yet, Geiger-mode SPADs are binary devices, that produce the same output signal regardless of the number of impinging photons absorbed at the same time, so that any information on the intensity of the impinging photon flux is lost. To alleviate this loss of proportionality to the magnitude of the input optical signal, the SiPM integrates a dense array of small, independent SPAD sensors with their own quenching resistor. Each independently operating unit of SPAD and resistor is referred to as a "microcell". The microcells are mounted in parallel, and the combined current from each individual and independent microcell constitutes the output signal of the SiPM. The KETEK PE3325-WB-TIA-SP SiPM model that will be used in the NUCLEUS experiment consists of an arrangement of 13920 (25×25) μm^2 microcells, forming a 3×3 mm^2 active area.

9.2.2 Calibration

Dark Count Rate

To calibrate each SiPM, we make use of the so-called SiPM Dark Count Rate (DCR), which is the rate of SiPM output signal when placed in complete dark conditions. This signal, not induced by any optical signal, is the main source of noise in a SiPM. It originates from thermally generated charge carriers in the active volume, that initiate an ionization cascade in the avalanche region when a positive over-voltage is applied. The signal resulting from the breakdown of the microcell in which the ionization cascade was triggered is identical to the signal that would originate from photon absorption. Therefore, the DCR is a good proxy to measure the SiPM signal at the photo-electron (PE) level.

To carry out the calibration of each SiPM, one varies the applied over-voltage between 2.5 and 7 V. In order to record spectra with single or few Geiger discharges, the SiPM signals are amplified by combining the fast amplifier and the internal amplification of the FADC shown in Figure 9.3. A low CFD threshold value of 1 mV is chosen in order to trigger the DAQ on low-charge events from the dark count rate. Ten-ish second-long runs are taken, corresponding to a statistics of $\sim$ 100k events.

Photo-electron signal

The DCR noise in the microcells of the SiPM can be divided in 2 categories [185, 186]:

1. Primary noise, that refers to the avalanche pulse triggered by thermally generated charge carriers.

2. Secondary or correlated noise, that identifies all the avalanche pulses generated subsequently to a primary event. They are due to: (i) after-pulsing (in the same microcell) or (ii) optical cross-talk (in neighboring microcells).

After-pulse During an avalanche, some of the charge carriers can be trapped and released subsequently, with a typical exponential distribution over time, generating a secondary spurious avalanche, called after-pulse. Due to occurring during the recovery state of the cell following a primary avalanche, the after-pulse signal exhibits an amplitude lower than that of the primary signal [187]. After-pulsing can also be optically-induced, as secondary photons produced during each avalanche can be absorbed in the same microcell, thus triggering a photo-induced secondary avalanche.

Prompt and delayed cross-talks As stated before, secondary photons are produced during an avalanche. If they are not absorbed in the same microcell in which they were generated, they can still be absorbed in a neighboring microcell and trigger a primary avalanche in this cell. This process is called prompt optical cross-talk. It can formally be distinguished from the delayed optical cross-talk, that describes secondary photons generating electron-hole pairs in the un-depleted region of a neighboring microcell, and that will reach the depletion region by diffusion after a typical delay of a few nano- to micro-seconds. Yet, in practice, this signal may be indistinguishable from the prompt cross-talk, depending on the diffusion time. Due to triggering a primary avalanche on the fired neighboring microcells, the cross-talk events exhibit the same amplitude than the primary event signal.

All DCR components are summarized in the subsequent Figure 9.5.

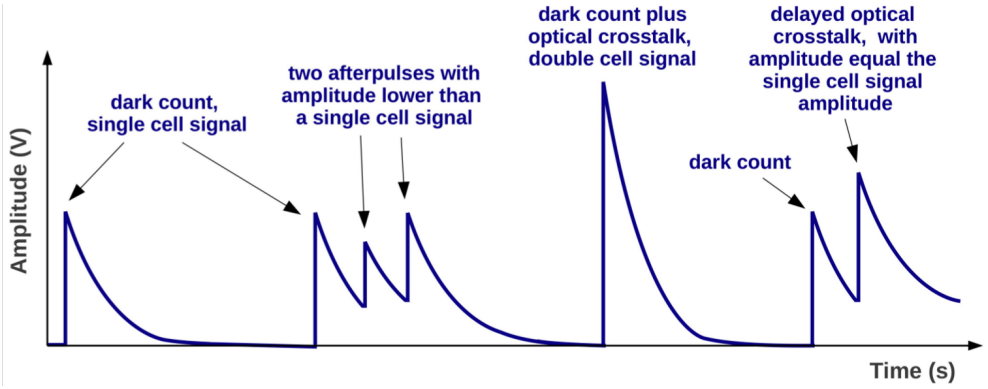

Figure 9.5: **Representation on the SiPM output signal of the different kinds of noise observable**: primary events, prompt cross-talk, after-pulsing and delayed cross-talk events. Source [185].

Photo-electron charge spectrum

In order to be able to fit the charge spectrum of the photo-electron signals, measured with the SiPM dark count rate, one has to include all the aforementioned components in the modelling of the noise. To do so, the charge spectrum is fitted with a slightly modified model than in [188], to which we add a general exponentially decreasing background. As detailed in Appendix F, the model takes into account the electronic noise of the system, the number of initiated Geiger charges, after-pulses, as well as prompt and delayed cross-talks.

Figure 9.6a shows a photo-electron charge spectrum recorded from dark count events at an over-voltage of 4.8 V. It is expressed in QDC units. Peaks corresponding to 1, 2, 3 and 4 Geiger discharges are clearly visible. The quantity of interest to calibrate the SiPM is the so-called SiPM gain. Herein, the gain does not directly refer to the number of electric charges initiated per Geiger discharge, but, equivalently, to the number of QDC channels initiated per Geiger discharge. It is then expressed in QDC per number of photo-electron [QDC/PE] and is merely the constant inter-peak distance in Figure 9.6a.

Figure 9.6b shows the extracted gain for different bias voltages for the two SiPMs used in the prototype. As expected, we observe a linear increase of the gain with the over-voltage. The linear fit corresponds to the gain calibration curve, which is used to convert the measured QDC charge of the integrated SiPM signal into the number of detected photons. In the following, all spectrum measurements will then be expressed in number of PE instead of QDC units.

The calibration of the measured spectra has two advantages: it allows for a direct comparison of the different fiber configurations using independent SiPMs, and a monitoring of the stability of the SiPMs performance. The latter is a key requirement for the long-term operation of the NUCLEUS muon veto with a constant high efficiency. We observe no significant difference in the gain between measurements in which the WLS fibers are connected to the SiPMs compared to the fibers disconnected. Therefore, we conclude that the stability of the final NUCLEUS muon veto modules can be monitored by regular and short gain calibration measurements with WLS fibers attached. Neither hardware changes of the modules themselves nor the installation of a LED-based calibration system inside the light-tight boxes are needed.

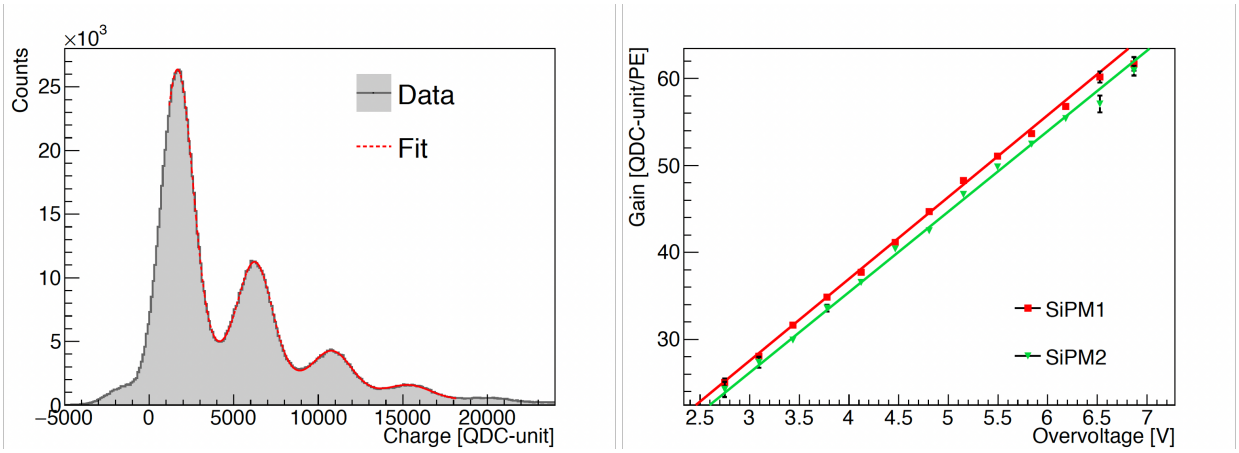

(a) PE charge spectrum

(b) Calibration curve

Figure 9.6: **SiPM calibration**. (a) Charge distribution of the photo-electron (PE) spectrum measured at an over-voltage of 4.8 V. The data are taken with an additional gain of 102, provided by the FADC card and the fast amplifier (see figure 9.3). The charge spectrum is fitted with a general fitting model to extract the gain, i.e. charge (in QDC units) per PE. (b) Gain calibration curves of the two SiPMs as a function of the over-voltage. For the characterization measurements, a working point of 4.8 V was chosen. Since the characterization data presented in Section 9.3 are taken without the additional amplification, the gain curve is corrected for it.

9.3 Panel performance

In the following, we quantify the light yield, the separation of muon events from ambient γ-background and the muon identification power of the prototype panel in the three different fiber configurations. The purpose of this study is to understand the differences between the fiber configurations in view of their use in a compact and efficient assembly of panels covering the full solid angle around the central target detectors of the NUCLEUS experiment. The full characterization of the panel performance relies on Figure 9.7 and the results are summarized in Table 9.1. Their full derivation is explained subsequently.

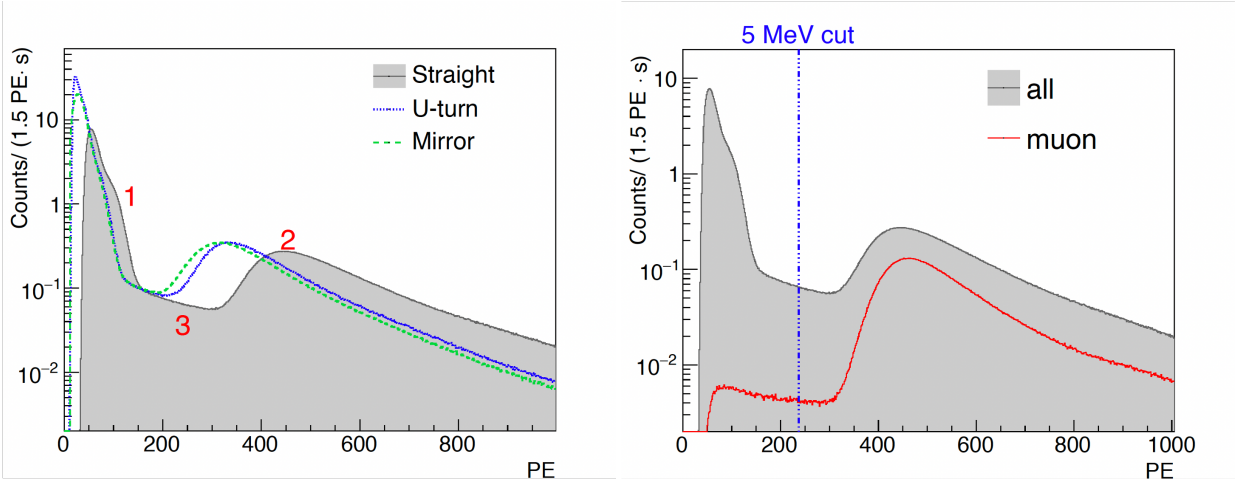

(a) Full spectrum (three config.)

(b) Muon spectrum (straight config.)

Figure 9.7: **Measured spectra for the the prototype panel characterization**. (a) Full spectra measured with the three fiber configurations. The CFD threshold is set to 10 mV. For the straight fiber configuration, a coincidence in the two SiPMs is required. All spectra show the same features: (1) an external γ-background, (2) Landau-like distributed muon events and (3) a well-defined "plateau" separating these two contributions. (b) Comparison of the full spectrum (grey area) with the muon spectrum (red line) both measured in the straight fiber configuration. Muon events are identified by means of a three-fold coincidence in the NUCLEUS prototype, the top and the bottom panels of the test stand (see Figure 9.2). The muon identification power is defined as the fraction of detected muon events above a certain threshold. The threshold value is here set to 5 MeV, defined as half the value of the muon peak ($\sim$ 10 MeV), and lying in the middle of the "plateau" region.

Configuration	LY [PE/MeV]	P/V []	$\Delta\epsilon$ []
Straight fibers	47.47 $\pm$ 0.02	4.86 $\pm$ 0.06	1.00
U-turn fibers	32.13 $\pm$ 0.02	4.25 $\pm$ 0.04	0.99
Straight fibers + mirror	30.24 $\pm$ 0.02	3.89 $\pm$ 0.03	0.99

Table 9.1: **Summary of the performance of the three fiber configurations**. The total light yield (LY) and the peak-to-valley ratio (P/V) are shown. Only statistical uncertainties are given. $\Delta\epsilon$ gives the relative muon identification power compared to the straight fiber configuration. See text for details.

The separation of the ambient γ-background from muon events is of key importance, for limiting the dead time induced from the vetoing of events tagged by the NUCLEUS muon veto. Therefore, as a first step, we characterized the full spectra of events in the prototype panel triggering at a low CFD threshold of 10 mV. Such threshold is sufficiently low to select muon events, for which a typical pulse is shown in Figure 9.8, and low energy γ events. Figure 9.7a shows the measured spectra, in calibrated PE charge. For the straight fiber configuration, the sum of the calibrated SiPMs charge is used. All three spectra show the same features: (1) an external γ-background sharply increasing towards the threshold, (2) muon events following a Landau-like distribution[1], (3) a well-defined "plateau" region separating these two contributions.

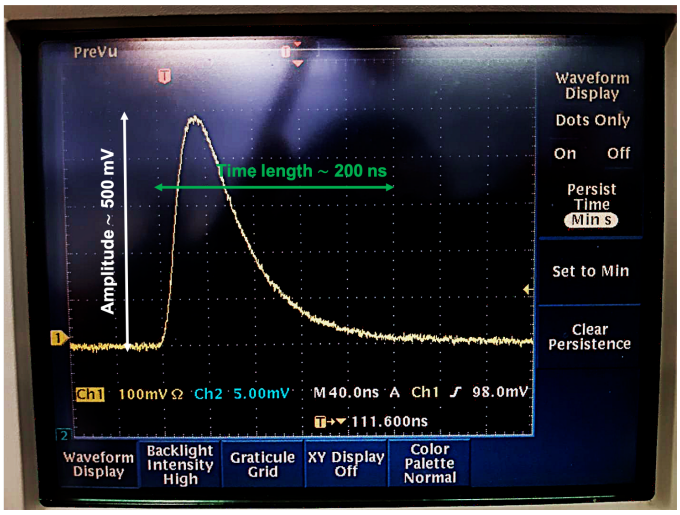

Figure 9.8: **Typical SiPM pulse signal for a muon event**, as observed on the oscilloscope. Its amplitude is at the few hundreds of mV level, and the signal is contained in a typical 200 ns wide time window, constituting the integration window to calculate the QDC charge of the signal.

We defined the light yield (LY) of a given fiber configuration as the ratio between the most probable value of the muon peak, extracted from a local Landau fit, with the most probable 10.1 MeV energy deposited by the statistically dominant vertical muons going through the 5 cm thickness of the panel. As expected, the straight fiber configuration yields the highest light output (see Table 9.1), as the spectra of the U-turn and the mirror configuration are shifted to lower PE values. However, the photo-statistics for muon events remains large, at the level of several hundreds of PE for the muon signal, and so is their separation from the γ-background.

To further quantify this separation, we computed the so-called peak-to-valley ratio (P/V), which is defined as the ratio of the rate at the maximum of the muon distribution over the rate at the minimum of the plateau, extracted from a 8th order polynomial fit of the plateau region [189]. The three fiber configurations exhibit satisfactory separation power, with P/V of the order of $4 \sim 5$, and again the best value for the straight fiber configuration (see Table 9.1).

At last, we quantify the muon identification power by applying a three-fold coincidence of the prototype panel with the top and bottom panels of the test stand (see Figure 9.3).

[1]Strictly speaking, they follow a Landau distribution [17] convolved with the response of the prototype.

Taking advantage of the directionality of the atmospheric muon flux, this allows to select a distinct sample of muon events, whose spectrum is displayed in red in Figure 9.7b, and compared to the $\gamma + \mu$ full spectrum, in grey, in the straight fiber configuration. The coincidence scheme with the top and bottom panels restricts the angular acceptance of the muons and hence their total rate, but suppresses the omni-directional γ-background, thus revealing the full structure of the plateau. This plateau is then interpreted as clipping muon events, traversing the prototype close to an edge. Such events feature a reduced track length through the plastic scintillator and hence deposit less energy.

For each configuration, we then define the muon identification power ϵ as the fraction of detected muon events above a certain threshold, set at an equivalent of 5 MeV (see Figure 9.7b), well above the highest natural γ-line of ^{208}Tl at 2.6 MeV. The straight fiber configuration exhibits an identification power of $\epsilon = (97.26 \pm 0.01)\%$. While the LY and P/V are significantly increased for the straight fiber configuration, the muon identification power differs only by $\sim$1% among the different configurations (see Table 9.1). The study validates that the mirror and U-turn configuration *in fine* reach a similar performance as the straight fiber configuration.

Yet, the muon identification power of a single panel evaluated this way depends on the selected muon sample and, thus, on the geometry and imposed trigger conditions of the coincidence scheme. Therefore, it cannot thoroughly be scaled to the overall performance of the final NUCLEUS muon veto assembly, where the panels will be packed closely to a 4π-coverage of the NUCLEUS target detector. In particular, the non-negligible number of clipping muon events, that are missed in a single panel when applying a 5 MeV threshold, may leave a longer track length in the neighboring panels and then be detected. For the final muon veto assembly, we then expect a higher muon identification power than the $\sim 97\%$ we computed in this study. It will be discussed in Section 9.5.

9.4 Response homogeneity

Sizeable differences in the LY throughout the muon veto module may result in local differences in the muon identification power. Therefore, in addition to the total LY computed in the previous section, we measured the local LY for the three fiber configurations.

The LY can be influenced by local differences in the emission, collection and propagation of the scintillation light, that may originate from local variations of the optical coupling between fibers and plastic scintillator, or loss of light due to e.g. the propagation in the fibers or the bending of the fibers for the U-turn.

To measure the local LY, we select a sample of muons by means of a three-fold coincidence in the prototype (middle panel), the bottom panel and the small plastic scintillator shown in Figure 9.2. Setting the position of the small scintillator following the grid displayed in Figures 9.1b and 9.1c, we can directly measure the PE spectrum of atmospheric muons depositing their energy within a local volume of the prototype. From muon track simulations that we detail below, we assessed that 90% of the atmospheric muons interacting through this three-fold coincidence scheme deposit their energy in the prototype within a truncated conic volume of ⌀ 12 cm × ⌀ 22 cm × 5 cm (see Figure 9.2).

9.4.1 GEANT4 simulation

As we expect a position dependence of the energy deposited by the selected muons, we performed a Monte-Carlo simulation of atmospheric muons interacting in the setup within the three-fold coincidence scheme. The simulation relies on the GEANT4 based framework "Choozerent", already implemented by the NUCLEUS collaboration [163].

We implemented a simplified test stand, only accounting for the wood shelves and the PVT-based plastic scintillators, as sketched in Figure 9.9a. Its geometry follows the one described in Figure 9.2b, and the small plastic scintillator can be placed on the middle prototype panel, according to the position mapping of Figures 9.1b and 9.1c.

An atmospheric muon generator is used to generate realistic muon events in the test stand (see Figure 9.9b). In spherical coordinates (z, θ, ϕ) given a center point, the atmospheric muon flux at surface only depends on the zenith angle θ and follows a $\cos(\theta)^2$ distribution for $\theta \in [0, \pi/2]$ [17]. Thus, to generate realistic atmospheric muons, one should "shoot" muons from the surface of hemispheres centered at each interacting point of the simulated volumes. A geometrically equivalent and more convenient way to proceed is to replace those multiple hemispheres with point-like muon generations along planes tangent to a unique hemisphere centered on a reference point, and that encompasses all the simulated volume. The reference point is set to be the center of the small plastic scintillator. The size of the plane is tuned to the size of the area of the volume to be "illuminated", which is nothing but the maximal transverse dimension of the small scintillator. For each generated event, the energy of the muon is set to lie between 0.1 and 10^4 GeV, and is distributed according to a Gaisser parameterization, well reproducing the measured energy spectrum of atmospheric muons at surface [190].

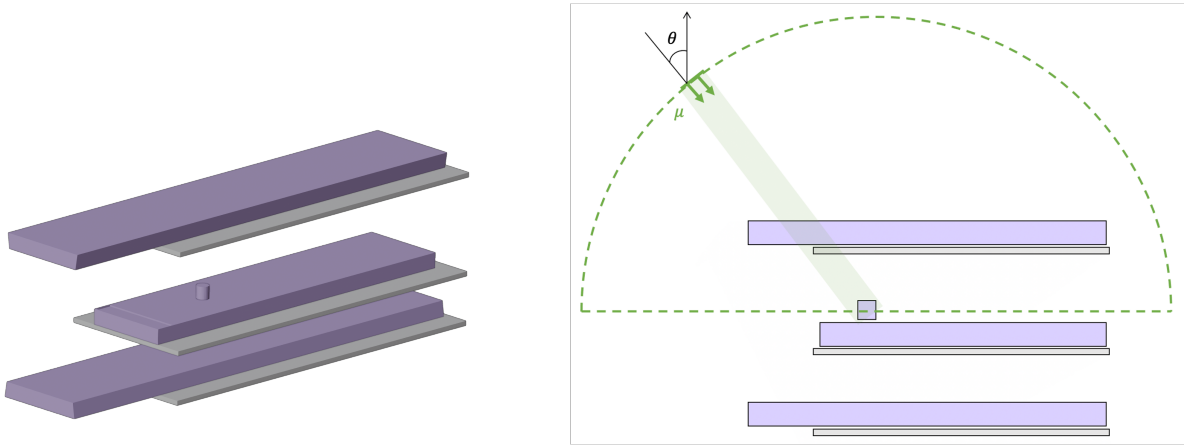

(a) Test bench (b) Generation of atmospheric muons

Figure 9.9: **GEANT4 implementation of the test stand**. (b) illustrates the generator of atmospheric muons, for the considered test bench geometry shown in (a). Muons are generated along a tangent plane to a hemisphere, centered on the small plastic scintillator. The muon flux is set to be $\propto \cos^2(\theta)$, where θ is the zenith angle in spherical coordinates.

The simulation returns, on an event-by-event basis, the energy deposited [MeV] by the interacting muon into each volume defining the test stand. The three-fold coincidence applied in the simulation requires for an event to deposit a non-zero energy in the small scintillator, middle panel and bottom panel volumes. The physics of the scintillation light emission, collection and propagation is not accounted for. Therefore, in order to extract the physical quantity of interest, namely the local light yield, these predicted energy depositions must be coupled to an energy response model in order to be compared with the data.

9.4.2 Local light yield

The detection process converts a local deposit of energy E_j into a number of photo-electrons NPE_j, so that $NPE_j = \eta \cdot E_j$ where η is to be interpreted as the local light yield [PE/MeV]. As a simple response model, we assume the local detector smearing to be described by standard poissonian statistics (encoding the photon emission and detection), that can be modelled by a gaussian distribution centered at NPE_j with a standard deviation of $\sqrt{NPE_j}$:

$$R_{ij}^{\eta} = \frac{1}{\sqrt{2\pi \cdot NPE_j}} \cdot e^{-\frac{(NPE_i - NPE_j)^2}{2NPE_j}} \tag{9.1}$$

with

$$NPE_j = \eta \cdot E_j$$

In this formulation, we assume the detector response to be linear in the energy range of interest as the conversion factor η is taken to be energy-independent.

For each local muon spectrum, the predicted PE charge spectrum D_{pred}^{η} proceeds from the folding of the GEANT4 simulated energy spectrum S_{pred} through the local detector response:

$$D_{pred}^{\eta} = R^{\eta} \cdot S_{pred} \tag{9.2}$$

For each position of the small plastic scintillator and each fiber configuration, one can then fit the local light yield η by comparing the predicted charge spectrum D_{pred}^{η} with

the measured charge spectrum D_{exp}, through the least-square method. We only take into account the statistical uncertainties of the measurement, and we allow a free-floating normalization parameter between measured and predicted spectra. This method yields satisfactory data-to-simulation agreement, as shown in Figure 9.10.

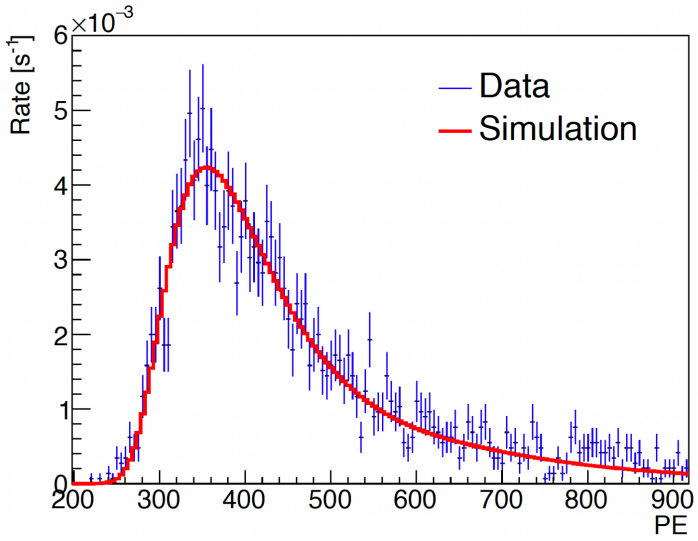

Figure 9.10: **Comparison of local muon charge spectra**, from the folded simulation and the measurement at the central position in the U-turn configuration. The fitted local light yield is $\eta = (33.3 \pm 0.2)$ PE/MeV, for a $\chi^2/\text{dof} = 97.5/87$.

We report in the subsequent Figure 9.11 the results for the extracted local light yields for each position of the small plastic scintillator and for the three fiber configurations. For simplicity, we average the local light yield values over the three transverse positions at the same longitudinal position. The reported uncertainties on the average value encode the few percent level dispersion of the light yield in the transverse plane of a given longitudinal position.

Let's note that comparing the local light yield extracted for each position instead of the raw PE charge allows to correct the study for discrepancies in energy deposition, that occur at the borders of the panel, with clipping muon events, and in the pool region, that features a 10% lower thickness than in the bulk of the scintillator. With the local light yield, only the effects due to discrepancies in the light emission and collection remain.

The straight fiber configuration shows the least inhomogeneities in the LY: the longitudinal positions from 6 cm to 87 cm show a 2% variation. The drop in LY at 114 cm, close to SiPM2, may hint towards additional light losses at the side of SiPM2, e.g. by poor coupling of the WLS fibers to the SiPM. The mirror configuration shows a 30%-level inhomogeneity in the LY. As expected, the LY increases towards the SiPM used as a read-out, and decreases towards the mirror. This effect can be largely attributed to light attenuation in the fibers. Similarly, the U-turn configuration shows an 11%-level inhomogeneity along the prototype, with the LY being reduced towards the U-turn, i.e. the pool region. This result hints towards a significant reduction of losses during light propagation in the U-turn fiber configuration with respect to the use of a mirror, regardless of the additional bending of the fibers.

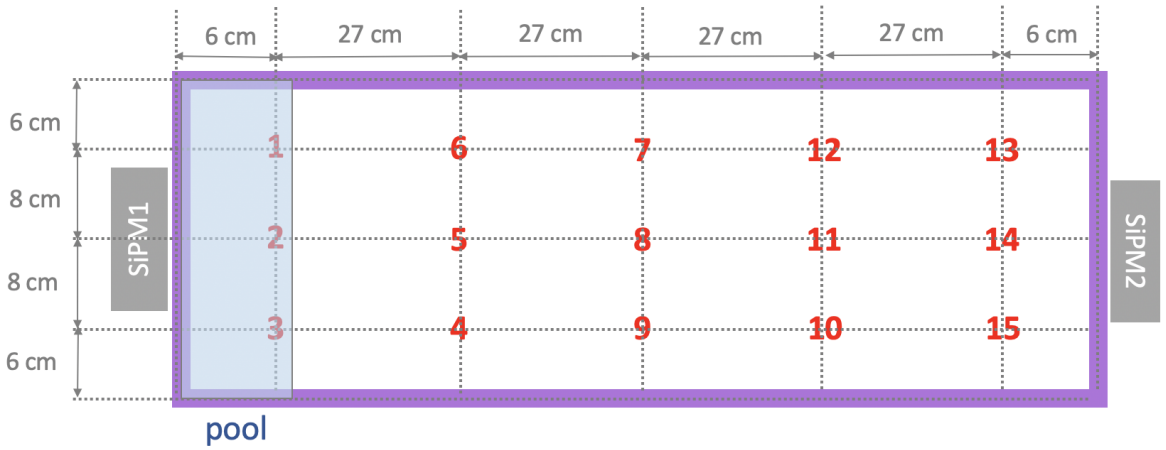

(a)

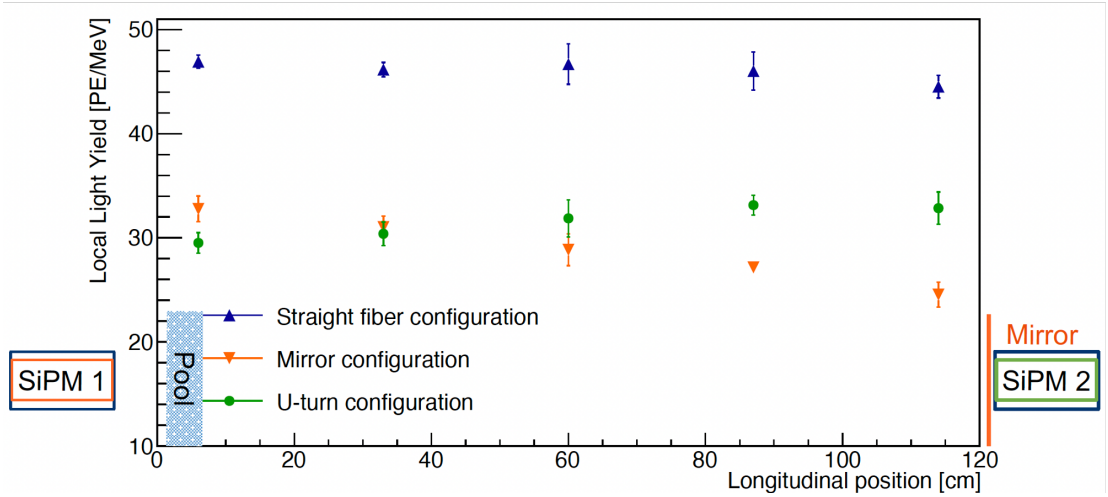

(b)

Figure 9.11: **Light yield homogeneity study.** (a) Position mapping for the local muon signal measurements. (b) Local Light Yield in the prototype for the three fiber configurations. We average over the three transverse positions at same longitudinal position. The uncertainties include the dispersion of the measurements at a given longitudinal position. For the measurement in the straight fiber configuration, SiPM1 and SiPM2 are used ; for the U-turn configuration, the read-out was performed with SiPM2 ; and for the mirror configuration, SiPM1 was used as a read-out whereas SiPM2 was replaced by a mirror.

9.5 Final design of the NUCLEUS Muon Veto

For a successful operation of the NUCLEUS experiment, a 4π coverage of the passive shielding by the muon veto is essential. Yet, due to the distance between the scintillator and the SiPM, each muon veto module features a significant proportion of non-instrumented volume, twice as large in the straight fiber configuration as in the U-turn or mirror configuration. This calls for a compromise between the light output and the geometrical efficiency of the overall muon veto.

The studies presented in the aforementioned sections showed that all three fiber configurations exhibited similar performance in terms of muon power identification, and satisfactory overall light yields. Bearing this in mind, we found an optimal coverage of the passive shielding with active plastic scintillators by combining straight fiber modules with the ones carrying a single SiPM read-out. Given that the U-turn configuration proved to outperformed the mirror configuration in terms of response homogeneity, this configuration is chosen as the reference one-sided read-out configuration. The final arrangement for the NUCLEUS muon veto is shown on the left part of Figure 9.12:

- the top part consists of two large stainless steel boxes, in order to be able to open the shielding. Each box contains four 62.8 cm long panels, half as long as the prototype panel. The 45.6 cm diameter central hole occupied by the cryostat is mostly filled by operating a disk-shaped scintillator inside the cryostat, the so-called cryogenic muon veto. Only a 6.5 cm wide annular gap remains open between the muon veto boxes and the most inner vessel of the cryostat. Each panel is read out at one end with a simple straight fiber configuration. As the panels are only 62.8 cm long at most, we expect the light yield inhomogeneity due to the attenuation in the fibers to be reduced to a $\sim 15\%$ level.

- the front/rear (left/right) side walls consist of 8 (8) modules, each featuring a $24.3 \times 5.0 \times 125.4$ cm^3 ($28.2 \times 5.0 \times 118$ cm^3) plastic scintillator hosted inside a separate stainless steel box. The combined arrangement of horizontal and vertical side modules allow to avoid large gaps. Horizontal modules feature a two-sided straight fiber configuration, while the vertical modules are in U-turn configuration with the SiPM placed at their top part. Importantly, the choice of a one-sided configuration allows to extend the active volume down to the bottom of the muon veto, thus increasing the efficiency to detect muons which enter the experimental setup through the annular gap and exit at the bottom of the muon veto.

- the bottom part consists of four identical $25.9 \times 5.0 \times 124.3$ cm^3 plastic scintillator panels hosted inside a separate stainless steel box, and read out at both ends with the straight fiber configuration.

A preliminary study carried out in [98], with the ROOT TGeometry package, allowed to assess the geometrical efficiency of the final NUCLEUS muon veto assembly, by means of a dedicated atmospheric muon track simulation in the overall assembly (see right part of Figure 9.12). Only the tracks of the muons travelling through the muon veto were considered and no physical process of energy deposition was implemented, yielding to a pure geometrical simulation.

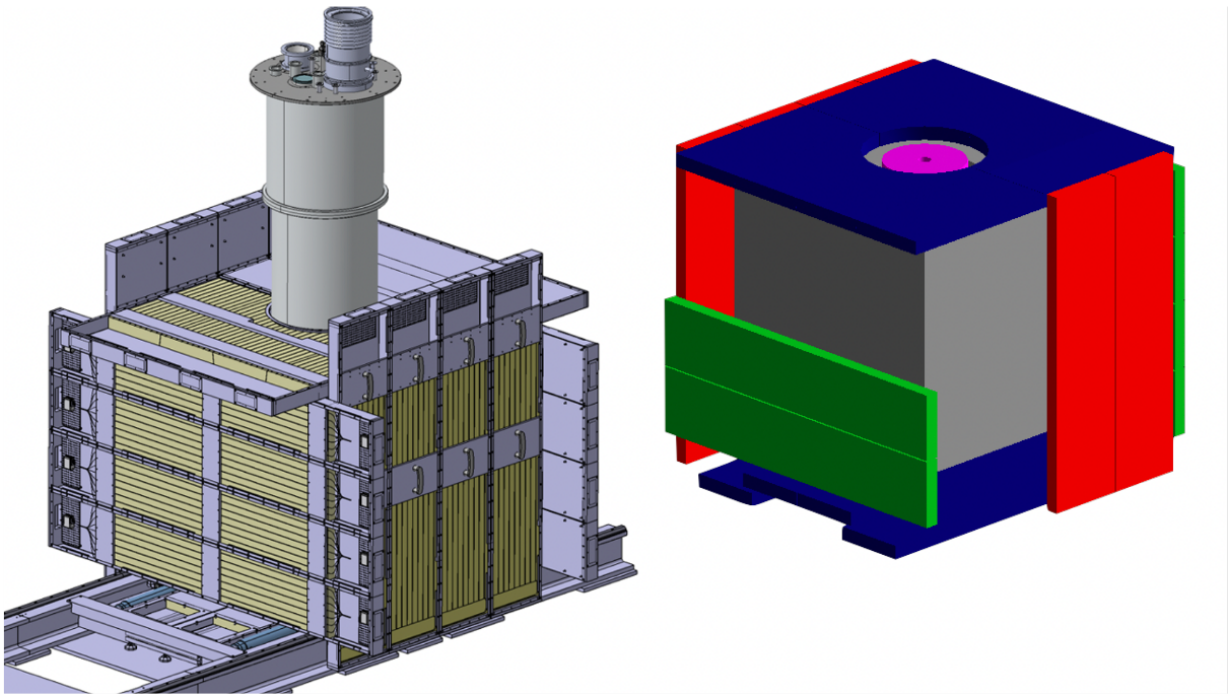

Figure 9.12: *(Left)* 3D view of the arrangement of the 28 scintillator panels (displayed in yellow color) forming around the cryostat the hermetic muon veto of the NUCLEUS experiment. For an optimal coverage for muon detection, the bottom part and two of the four side walls are read out by the two-sided straight configuration, the shorter top panels with a one-sided straight configuration, and the remaining two side walls are equipped with a U-turn fiber configuration. The whole assembly, arranged as two half-cubes, is placed on rails and allows the opening of the shielding in order to access the cryostat and the target detector inside. *(Right)* Geometrical arrangement as implemented in the muon track simulation [98]. The cryogenic muon veto, shown in magenta, is positioned on the same level as the top panel. The passive lead shielding is shown in grey.

From the track length distributions, the muon geometrical efficiency has been defined as the ratio of detected muons to the total number of muons entering the lead shielding, which contains the cryogenic detectors at its center and all the dense materials of the apparatus in which muons can generate secondary neutrons by spallation reactions. A muon is considered as "detected" by the muon veto if its track length in at least one panel is greater than 2.5 cm, equivalent to an energy threshold of 5 MeV as set on the prototype panel study. This study estimated a geometrical efficiency of 99.7% for the NUCLEUS muon veto, showing that the targeted efficiency $> 99\%$ is within reach for the NUCLEUS experiment. Furthemore, the muon rate was estimated at the level of 325 Hz, inducing a dead time of only 1.6% in the cryogenic target detectors [175]. The efficiency loss can be mostly attributed to muons entering the setup from the annular gap on top, and either clipping one panel or directly exiting the setup through the remaining small gaps of the muon veto without crossing any panel. Yet, the total muon identification efficiency will be determined during the commissioning of the NUCLEUS muon veto, which is ongoing at the time of the writing of this doctoral thesis.

Conclusion

In this doctoral work, we reported the most accurate measurement to date of the ^{235}U induced antineutrino spectrum, from the STEREO HEU experiment. On the road to produce the reference result, great care was taken on the accurate determination and control of the detector energy response. In particular, part of this work consisted in constraining the energy scale of the experiment, a prerequisite for an accurate spectrum analysis as this systematic uncertainty was expected to be the dominant uncertainty on the shape of the antineutrino spectrum. To this end, we implemented a general fitting framework, allowing to constrain the energy scale with the calibration residuals, obtained with γ radioactive sources, and the extracted ^{12}B spectrum as data sets, and with minimal prior assumption on the shape of the fitted energy scale non-linearity.

On top of the detailed work carried out by the collaboration in the evaluation of all systematics, it allowed to carry out the oscillation analysis of STEREO high quality data of Phase-II and -III. This analysis took advantage of the segmented design of the STEREO detector in order to track cell-to-cell relative spectral distortions that would be the sign of an eV-scale oscillation towards a sterile state. With this model independent analysis, we rejected a significant part of the oscillation parameter space favored by the Reactor Antineutrino Anomaly (RAA) and found our data to be statistically compatible with the no-oscillation hypothesis. In particular, the initial RAA oscillation best fit point was rejected at more than 99.99% confidence level.

This opened the avenue for an accurate measurement of the ^{235}U fission induced antineutrino spectrum, reconstructed at the full detector level. In order to provide the community with a reference spectrum, free of detector effects, we developed in this work a comprehensive unfolding framework, that allows to express the measured spectrum in true antineutrino energy space, with small unfolding biases. Yet, extending the idea of a filter encoding the unfolding bias, that was developed in the Wiener-SVD unfolding approach, we took care to provide the associated filter matrix of our unfolding procedure, thus allowing to perform unbiased comparison between our unfolded spectrum and a given prediction. With the STEREO unfolded spectrum that we derived, we provided the most accurate measurement of the IBD yield from the fission of ^{235}U, and confirmed the RAA for this one isotope with an observed $(5.5 \pm 2.1$ [exp.])% rate deficit with respect to the Huber prediction.

Then, we extended our framework to a joint analysis with the PROSPECT experiment, another leading HEU experiment, and reported a complete measurement of the ^{235}U spectrum with the largest HEU data set to date. We observed a local event excess with respect to the Huber prediction similar to the spectral distortion reported by LEU experiments, and with a significance of 4.7σ. Then, we generalized our framework to a global analysis including the Daya Bay LEU data, in order to investigate the reactor anomalies with the

combined uranium and plutonium spectra. Although statistically limited in the extraction of the plutonium spectrum, our analysis is found in agreement with previous analyses, that point towards the ^{235}U as the principal contributor to the RAA. Furthermore, the high accuracy of neutrino data favors biases in the predictions as the most plausible explanation to the reactor anomalies: in particular, a normalization bias for ^{235}U for the conversion method and biases in nuclear data bases (e.g. the pandemonium effect) for the summation models. The PROSPECT-II detector, that is expected to collect an even larger statistics than the full data set of STEREO , should complement in a near future this investigation of the reactor anomalies for the ^{235}U case.

The direct measurements of the reactor induced antineutrino spectrum will directly benefit the NUCLEUS experiment. In order to interpret the results of their CEνNS experiment, an accurate knowledge of the reactor antineutrino spectrum is needed. The studies undertaken in this doctoral work encompassed the full commissioning of a prototype module of the NUCLEUS muon veto, that will allow to reject part of the cosmogenic background, a critical requirement for ground level particle physics experiments. We implemented a routine to calibrate the SiPM read-outs that will be used in the experiment, and fully characterized the performance of the muon veto panels. The assembly of the muon veto is now ongoing, for a full validation of the complete NUCLEUS experimental setup in the upcoming year. The first phase of the experiment should confirm the observation of CEνNS events with a high significance, whereas the second phase of the experiment will alleviate statistical limitations with augmented target detector mass to allow a measurement of the CEνNS cross section with a percent level accuracy.

Résumé en français

Dans cette thèse de doctorat, j'ai reporté les résultats obtenus dans le cadre de mon travail sur deux expériences de détection d'antineutrinos de réacteur nucléaire, à savoir les expériences STEREO et NUCLEUS.

Les antineutrinos de réacteur sont générés dans la saveur électronique, à des énergies typiques de quelques MeV, par le processus de désintrégation β^- des produits de fission des isotopes fissiles du combustible nucléaire utilisé. Selon le réacteur, ce combustible peut être faiblement ou fortement enrichi en uranium 235. Dans le premier cas, on parle de reacteurs LEU (pour "Lowly Enriched in ^{235}U"). Cela concerne notamment les réacteurs commerciaux, appelés aussi réacteurs de puissance, de telle sorte que les isotopes fissiles contribuant à la quasi-totalité du flux d'antineutrinos sont au nombre de quatre: ^{235}U, ^{238}U, ^{239}Pu, ^{241}Pu. Dans le deuxième cas, on parle de reacteurs HEU (pour "Highly Enriched in ^{235}U"), et cela concerne notamment des réacteurs de recherche, comme celui de l'Institut Laue-Langevin (ILL) à Grenoble. Tout le flux d'antineutrinos provient alors (quasi-)intégralement des désintégrations β^- des produits de fission d'un seul isotope fissile, l'^{235}U.

Les antineutrinos de réacteur sont émis avec une certaine distribution en énergie, qui dépend de la nature du réacteur nucléaire, LEU ou HEU. Prédire ces spectres n'est pas chose aisée, car cela requiérait de sommer toutes les branches de désintégration β^- de tous les produits de fission, en s'appuyant sur les bases de données nucléaires. Par construction, cette méthode, appelée *méthode par sommation* [47, 48], souffre de l'incomplétude et de biais de longue date de ces bases de données [191]. Une méthode effective, développée en parallèle, a permis de fournir une estimation plus robuste du spectre d'antineutrinos émis par les réacteurs nucléaires, en convertissant le spectre d'électrons émis par les mêmes processus de désintégration β^-, et qui a été mesuré, en un spectre d'antineutrinos. Cette méthode, dite *méthode par conversion* et dont la référence est le modèle Huber-Mueller [50, 55], est prise comme prédiction de base pour la comparaison avec la mesure. Néanmoins dans cette approche, il est à noter que tout biais dans la mesure initiale du spectre d'électrons est propagé dans l'estimation du spectre d'antineutrinos.

Par ailleurs, le spectre d'antineutrinos de réacteur a été mesuré par plusieurs expériences au cours des dernières décennies. *Stricto sensu*, toutes ces expériences ayant utilisé comme processus de détection la réaction beta inverse (IBD, pour "Inverse Beta Decay"), le spectre mesuré résulte de la multiplication du spectre antineutrino émis (prédit par la méthode de conversion) par la section efficace d'interaction du processus IBD [46], le tout convolué par la réponse en énergie du détecteur. En comparant ces spectres IBD mesurés avec les spectres IBD prédits, tenant compte de la réponse du détecteur, des écarts significatifs ont été constatés. Le premier est une anomalie en flux à hauteur de 2.8σ, se traduisant par un déficit d'antineutrinos de l'ordre de $\sim 6\%$ constaté à courte de distance de vol ($\sim 10 - 100$ m) du réacteur nucléaire [56]. Le deuxième est une anomalie

en forme, figurant une distortion spectrale locale de l'ordre de 10% entre les spectres IBD mesurés et prédits, pour une énergie de l'ordre de 5 MeV, et récemment évaluée à 6.3σ [152]. La première anomalie est communément appelée RAA, pour "Reactor Antineutrino Anomaly", alors que la seconde est souvent citée comme le bump à 5 MeV, ou "5 MeV bump". Tandis que la RAA a été mise en lumière à la fois sur des réacteurs HEU et LEU, le bump à 5 MeV n'a été étudié que pour des expériences auprès de réacteurs de puissance, LEU. Pour expliquer ces anomalies, on peut invoquer un biais de la prédiction issue de la méthode de conversion, ou encore convoquer une nouvelle physique. Avec la découverte du phénomène d'oscillation des neutrinos au cours des dernières décennies, il est par exemple tentant d'interpréter la RAA comme la disparition d'antineutrinos électroniques causée par une oscillation vers un autre état des antineutrinos, indétectable par le processus IBD. Cette disparition se produisant à très courte distance de la source d'antineutrinos électroniques, i.e. le réacteur nucléaire, les oscillations vers les autres états d'antineutrinos connus, muonique et tauique, sont négligeables, de telle sorte que seulement une oscillation vers un nouvel état, nécessairement stérile, peut être envisagée pour expliquer la RAA. Sa masse serait alors de l'ordre de 1 eV. Tous les aspects susmentionnés sont développés dans le Chapitre 1 de ce manuscript.

L'expérience STEREO a été concue afin d'isoler la seule contribution de l'^{235}U aux deux anomalies et d'investiguer l'hypothèse d'une oscillation mettant en jeu un neutrino stérile comme explication à la RAA. Il s'agit ainsi d'une expérience de détection à courte distance de vol ($\sim$ 10 m) d'antineutrinos émis par le réacteur de recherche de l'ILL, fortement enrichi en ^{235}U. La conception segmentée du volume cible, en 6 cellules identiques, permet de détecter des antineutrinos à différentes distances de vol du réacteur. En procédant à une comparaison des spectres mesurés cellule à cellule, on peut ainsi tester la compatibilité des données avec divers scénarios, incluant ou non une oscillation vers un neutrino stérile. De plus, la haute précision dont on dispose sur la puissance thermique du réacteur de l'ILL ($\sim$ 1.4 %), combinée à un travail fin de détermination de la réponse du détecteur et de toutes les systématiques associées, ont permis de réaliser une mesure de précision du spectre d'antineutrinos induit par la fission de l'^{235}U, à la fois en flux et en forme.

Après avoir décrit précisemment le détecteur dans le Chapitre 2 de ce manuscrit ainsi que la simulation qui a été implementée pour décrire sa réponse dans le Chapitre 3, j'ai présenté dans le Chapitre 4 la première partie de mon travail de thèse qui a porté sur la contrainte de l'échelle en énergie de l'expérience. Cette échelle en énergie est définie ici comme la relation entre l'énergie reconstruite dans les données et dans la simulation. Elle est donc cruciale lorsqu'on procède à une comparaison entre les données et un modèle. Pour être comparés, ces derniers sont par définition supposés être projetés dans le même espace d'énergie reconstruite, si bien qu'une échelle en énergie imparfaite peut induire des distortions systématiques entre données et modèle. Dans un premier temps, j'ai donc procédé à une étude de cas permettant de quantifier l'impact d'une imperfection de l'échelle en énergie dans la comparaison entre des spectres antineutrinos mesuré et prédit. Cette échelle en énergie est directement contrainte par les résidus de calibration de l'expérience, qui encodent l'écart entre l'énergie reconstruite dans les données et dans la simulation, pour un ensemble discret de valeurs nominales d'énergie déposée dans le détecteur. Ils sont obtenus dans la région d'énergie d'intérêt à l'aide de diverses sources radioactives émettrices de γ, déployées dans le volume du détecteur STEREO. La question à laquelle je me suis attaqué dans un premier temps était donc de savoir si une non-linéarité résiduelle de l'échelle en énergie, contrainte par les résidus de calibration, pouvait induire des distortions

significatives dans le ratio des spectres antineutrinos mesuré et prédit.

Pour ce faire, je me suis appuyé sur le formalisme exposé dans [104]. J'ai ainsi developpé une procédure analytique d'ajustement global d'une non-linéarité de l'échelle en énergie, au sens des moindres carrés, contrainte à la fois par les résidus de calibration et de spectre. Pour une telle procédure, j'ai mis en lumière le caractère crucial de la paramétrisation de la distortion de l'échelle en énergie à ajuster et ai exploré deux approches de paramétrisation. Une approche "classique" consistant en une paramétrisation polynomiale de la distortion, mais qui souffre de l'absence de prescription quant au choix du degré du polynôme. J'ai donc couplé cette approche à un critère de sélection de modèle issu de la théorie de l'information, le critère d'information d'Akaike corrigé (AICc) [109], qui a mené au choix d'un polynôme de haut degré. Dans un second temps, j'ai opté pour une approche plus souple, qui plaçait moins d'*a priori* sur la forme ajustée de la non-linéarité, de telle sorte à maximiser la sensibilité à des distortions locales. Ces dernières seraient faiblement contraintes par les seuls résidus de calibration, du fait de leur nature discrète. Il s'agit de l'approche par Estimation par Densité de Noyau (KDE, pour "Kernel Density Estimation") où les noyaux monomiaux, non-compacts, de l'approche polynomiale sont remplacés par des noyaux gaussiens, compacts. La grande flexibilité sur la forme ajustée de la distortion que permet cette approche est à contrebalancer avec le risque de sur-ajustement de la distortion aux données. Pour contourner cet effet, la méthode d'ajustement suivant la méthode des moindres carrés classique doit être complétée par un terme de régularisation, avec l'introduction d'un hyperparamètre, appelé *force de régularisation*, qui encode le compromis entre l'accord aux données et la contrainte de regularité de la distortion. Ce paramètre est fixé en amont de la procédure d'ajustement en elle-même, en minimisant l'erreur de validation croisée généralisée ("Generalized Cross-Validation error", ou GCV error), qui encode l'erreur de prédiction du modèle ajusté en fonction de la force de régularisation choisie [106]. Ce faisant, j'ai pu ajuster des formes très générales de non-linéarité de l'échelle en énergie, qui étaient globalement compatibles avec les résidus de calibration, et dont les distortions locales dans les régions peu contraintes par la calibration, induisaient des déviations significatives dans le ratio entre les spectres antineutrinos mesuré et prédit.

Ainsi, dans un second temps, afin de mieux contraindre l'échelle en énergie de l'expérience, je me suis concentré sur la simulation du spectre cosmogénique du ^{12}B dans STEREO. En combinant ce travail avec l'extraction du spectre expérimental du ^{12}B qui a été entreprise dans la collaboration, une contrainte complémentaire des résidus de calibration a pu être obtenue, consistant en l'information apportée par les résidus des spectres mesuré et prédit du ^{12}B, *continue* sur toute la région en énergie d'intérêt. La non-linéarité de l'échelle en énergie a ainsi pu être dérivée, par un ajustement global sur les contraintes fournies par les résidus de calibration et de spectre ^{12}B. Il est apparu que l'échelle en énergie de STEREO était contrainte au pourcent près au niveau de chacune des cellules du volume cible, et à quelques pourmilles au niveau de l'entièreté du volume cible. En propageant l'impact de cette distortion sur la forme du spectre antineutrino mesuré, j'ai pu assigner l'erreur systématique induite par une imperfection de l'échelle en énergie. Cette erreur constitue la systématique dominante sur la forme du spectre, intervenant à la fois dans l'analyse d'oscillation pour la recherche du neutrino stérile et la mesure de précision du spectre.

Après avoir présenté dans le Chapitre 5 la procédure d'extraction du spectre antineutrino de STEREO ainsi que les autres erreurs systématiques de l'expérience, je me suis concentré dans le Chapitre 6 sur les résultats de l'expérience, à commencer par l'analyse d'oscillation. Le point fort de l'analyse de STEREO pour la recherche d'un neutrino stérile

est qu'elle ne repose sur aucune prédiction de spectre antineutrino, tirant pleinement avantage de la conception segmentée du détecteur permettant de scanner le spectre antineutrino à différentes distances de vol (une par cellule) pour révéler un potentiel schéma d'oscillation. Cette approche a révélé que les données de STEREO sont compatibles avec le scénario sans oscillation vers un neutrino stérile (p-value de 0.52), et a permis d'exclure une partie significative de l'espace de phase des paramètres d'oscillation vers un état stérile permis par la RAA avec un niveau de confiance de 95%.

Le fait que les données soient compatibles avec l'hypothèse sans oscillation a justifié dans un second temps la fusion des spectres antineutrinos de chaque cellule du détecteur afin de reconstruire le spectre antineutrino au niveau de l'entièreté du volume cible, permettant alors une mesure de précision dudit spectre. Néanmoins, ce spectre est exprimé en énergie reconstruite, propre à l'expérience STEREO et inclut donc les effets de détection (quenching, résolution, non-linéarités diverses de la réponse...). Afin de fournir une mesure de référence du spectre antineutrino induit par la fission de l'^{235}U, une procédure de déconvolution du spectre mesuré par l'expérience doit être implémentée afin de l'exprimer en énergie vraie antineutrino. Ce travail constitue une autre contribution principale de ma thèse de doctorat. Pour ce faire, je me suis inspiré du travail entrepris sur la contrainte de l'échelle en énergie de l'expérience, pour implémenter un formalisme de déconvolution basée sur la minimisation analytique d'un χ^2 régularisé, dans une approche dite de Tikhonov [105], où la force de régularisation est choisie une fois de plus en suivant la prescription GCV. Cette approche permet de s'affranchir de fluctuations bin à bin significatives et non physiques dans le spectre déconvolué, typiques de tels problèmes inverses. Ces dernières résultent de la déconvolution du bruit inhérent à la mesure et sont atténuées par la contrainte de régularité du spectre déconvolué. Par construction, cette solution introduit donc un bias par rapport à l'estimateur non biaisé de la méthode des moindres carrés classique, biais d'autant plus grand que la force de régularisation est grande. Une étude de biais a néanmoins confirmé que le critère GCV permettait d'atteindre des biais inférieurs au pourcent sur la forme du spectre déconvolué. Le résultat de la procédure de déconvolution analytique est alors le spectre antineutrino exprimé en énergie antineutrino, ainsi que sa matrice de covariance. Par ailleurs, m'inspirant d'un autre formalisme de déconvolution basé sur l'application d'un filtre dit de Wiener [142], j'ai complété le résultat de la procédure de déconvolution de Tikhonov classique par l'ajout d'une matrice dite de filtrage, qui permet d'encoder le biais induit par le terme de régularisation. J'ai montré de cette façon que la comparaison du spectre déconvolué avec la prédiction filtrée par ladite matrice permettait de s'affranchir du biais de déconvolution présent dans la comparaison classique entre le spectre déconvolué et la prédiction nominale, non filtrée. Ainsi, le triplet composé du spectre déconvolué, sa matrice de covariance et la matrice de filtrage de Tikhonov, constituant le résultat final de ma procédure de déconvolution, permet d'encoder pleinement l'information de la mesure experimentale dans l'espace de l'énergie vraie antineutrino et d'effectuer des comparaisons dont le résultat ne dépend pas du formalisme de déconvolution choisi.

Avec cette procédure robuste, j'ai ainsi pu déconvoluer le spectre antineutrino de fission de l'^{235}U mesuré par STEREO. La comparaison avec la prédiction de référence Huber-Mueller a confirmé un déficit d'antineutrinos dans le secteur du pur ^{235}U, à hauteur de $(5.5 \pm 2.1$ [exp.])%. Cette valeur est en excellent accord avec la moyenne mondiale des expériences opérant auprès de réacteurs HEU et est à ce jour la mesure la plus précise du rendement de fission de l'^{235}U. La comparaison en forme du spectre avec la prédiction a mis en lumière un "bump" d'amplitude (15.6 ± 5.2)% autour de 5.5 MeV en énergie vraie antineutrino. Ainsi, STEREO a confirmé les deux anomalies des antineutrinos de réacteur,

en flux et en forme de spectre, pour le seul isotope fissile ^{235}U.

Par la suite, dans le Chapitre 7, j'ai poussé encore plus loin cette analyse en incluant des données provenant d'expériences autres que STEREO dans mon formalisme de déconvolution. Tout d'abord, j'ai étendu mon étude à une déconvolution jointe des données STEREO et PROSPECT, une autre expérience de précision pour la mesure du spectre antineutrino induit par la fission de l'^{235}U. Etant donné que les données de PROSPECT publiées ne sont pas normalisées au rendement de fission, seule une étude en forme du spectre issu de la déconvolution jointe des données STEREO-PROSPECT est pertinente. Cette analyse en forme a confirmé la présence du "bump" autour de 5.5 MeV dans les données pur ^{235}U, à hauteur de 4.7σ.

Dans un dernier souci d'élargissement de l'analyse aux anomalies de réacteurs comprenant aussi du plutonium comme combustible nucléaire, j'ai par la suite étendu mon formalisme à une déconvolution jointe des données HEU et LEU, en ajoutant les données publiées par l'expérience Daya Bay, opérant auprès de réacteurs commerciaux. Mon analyse a permis une déconvolution et une séparation simultanées des spectres antineutrinos de fission de l'^{235}U et du plutonium. Bien que limitée statistiquement dans la précision du spectre antineutrino du plutonium, cette analyse a pour avantage de propager naturellement les (anti-)corrélations entre les spectres séparés ^{235}U et plutonium et d'utiliser de manière minimale l'information provenant de simulations réacteur, par rapport à l'analyse publiée par Daya Bay. En particulier, l'analyse en forme du spectre du plutonium obtenu de mon analyse a donné des indications pour un "bump" dans le Pu à hauteur de 2.3σ.

Globalement, les analyses sur les spectres antineutrinos de fission des réacteurs nucléaires entreprises dans le cadre de ma thèse ont donc confirmé les anomalies d'antineutrinos de réacteur, et ont établi une nouvelle référence de spectre antineutrino issu de la fission de l'^{235}U, utilisable par l'ensemble de la communauté car corrigé des effets expérimentaux. Avec la réjection par STEREO de l'hypothèse d'un neutrino stérile à l'eV comme explication de la RAA, ces analyses sont venues enrichir un tableau qui pointerait plutôt vers des biais de la prédiction de spectre comme principale explication de ces anomalies. Dans un travail récent [49], une tentative de correction effective de biais connus des bases de données nucléaires pour la prédiction des spectres antineutrinos par la méthode dite *de sommation*, a permis d'atteindre un accord sans précédent avec le spectre déconvolué de STEREO, si bien que l'on peut dire que l'on assiste à un changement de paradigme où la précision désormais atteinte sur les données neutrinos de réacteur permet à présent de contraindre les bases de données nucléaires.

Enfin, la dernière partie de ma thèse de doctorat a porté sur une autre expérience de détection des antineutrinos de réacteur dans laquelle je fus impliqué, l'expérience NUCLEUS, présentée dans le Chapitre 8. L'originalité de cette expérience est qu'elle détecte les antineutrinos par un processus par courant faible neutre désormais accessible expérimentalement, la diffusion cohérente élastique neutrino-noyau, ou CEνNS (pour "Coherent Elastic Neutrino-Nucleus Scattering"). Ce processus de détection fournit entre autres un nouveau canal pour tester le Modèle Standard de la physique des particules à basse énergie. La détection d'un événement antineutrino dans NUCLEUS est basée sur la mesure d'un recul nucléaire de quelques dizaines d'eV, nécessitant une technologie à très bas seuil de détection. Pour ce faire, des bolomètres cryogéniques sont utilisés. Dans une telle expérience, où le taux de comptage attendu pour la première phase est de l'ordre de 1 antineutrino tous les deux jours, la réjection du bruit de fond est critique, de telle sorte

que les bolomètres sont encapsulés dans une structure mécanique comprenant plusieurs couches de blindage passif et actif pour atténuer ou rejeter les événements bruit de fond.

Dans mon travail de thèse, je me suis axé sur la réjection d'un des bruits de fond dominants de l'expérience: le bruit de fond induit par les muons atmosphériques, qui peuvent notamment générer des neutrons de spallation dans les matériaux de structure entourant les bolomètres. Ces neutrons peuvent par la suite induire dans les détecteurs cibles des reculs nucléaires dans la région en énergie d'intérêt, par diffusion élastique. Dans NUCLEUS, un tel bruit de fond est rejeté en identifiant les muons traversant le veto muon et en arrêtant l'acquisition dans une fenêtre en temps de quelques dizaines de microsecondes entourant chaque événement muon. Ce veto constitue la couche la plus externe du blindage de NUCLEUS et se décline en une structure cubique de 28 panneaux, qui ne sont autres que des plastiques scintillants couplés à des fibres optiques, connectées elles-mêmes à des photomultiplicateurs en silicium, ou SiPMs pour "Silicon photomultipliers". Dans le Chapitre 9 de ma thèse, je détaille le travail que j'ai entrepris pour valider les performances d'un prototype de panneau, de la calibration des SiPMs au montage, à l'opération et la simulation du banc de test. J'ai ainsi pu valider la mesure en ligne (i.e. avec les fibres optiques connectées) du gain des SiPMs pour le monitoring de l'expérience NUCLEUS. J'ai également quantifié le rendement photo-electron d'un panneau (de l'ordre de quelques dizaines de photo-electrons par MeV d'énergie déposée) et les inhomogénéités de collection de lumière pour les différentes configurations de fibres optiques testées, et notamment pu valider les performances de la configuration en U-turn pour 8 des panneaux, permettant un assemblage compact du véto muon autour de l'expérience avec la meilleure couverture angulaire. J'ai également validé la capacité des panneaux à séparer le signal muon du bruit de fond gamma de la radioactivité ambiante, point crucial pour n'identifier que les muons et atteindre un temps mort modéré dans le rejet de ces événements. Enfin, j'ai pu quantifier l'effacité de détection d'un panneau, qui, couplée à des simulations géométriques de muons traversant l'assemblage complet du véto, ont permis de valider une efficacité totale de détection $> 99\%$. Ces travaux ont donc montré que les panneaux de véto muon conçus pour NUCLEUS permettaient en effet d'atteindre les spécifications de l'expérience sur les performances du véto muon global. Cela a permis de lancer la procédure de fabrication de tous les modules, et d'utiliser les procédures de test que j'ai implémentées durant ma thèse pour les valider. Ils devront ensuite être envoyés à Munich pour un premier montage à blanc de l'expérience, avec en ligne de mire un premier run de physique prévu à l'aube 2024.

Remerciements

Au sortir de ces trois années de thèse, je ne saurai être complet sans adresser quelques chaleureux remerciements.

Je tiens tout d'abord à remercier Christine Marquet et Susanne Mertens pour avoir relu si méticuleusement mon manuscrit. Nos échanges qui ont précédé et suivi la soutenance ont été autant de retours précieux pour approfondir la réflexion sur mon travail. Je remercie également Nathaniel Bowden, Joachim Kopp ainsi que Guillaume Mention pour m'avoir fait l'honneur d'accepter de faire partie de mon jury de thèse et de juger la qualité de mon travail.

Bien sûr, ce travail n'aurait pas été possible sans mon directeur de thèse, David Lhuillier. David, merci de m'avoir accepté dans l'aventure et surtout, merci pour ces trois magnifiques années, aussi bien sur le plan scientifique qu'humain. Je n'aurais sans doute pas pu imaginer meilleur déroulement pour ce chapitre de ma jeune vie, et je t'en suis très reconnaissant. Je tiens également à remercier les permanents, post-docs et doctorants du CEA, que j'ai eu la chance de côtoyer durant ces trois années. C'était un réel plaisir de vous voir et d'échanger avec vous au quotidien (hors période de confinement...), et vous avez, chacun à votre façon, contribué à embellir le tableau de ces trois années. J'associe également à ces pensées les collègues de TUM, du MPIK, du LAPP, de l'ILL et aussi du LPSC avec qui j'ai eu le privilège de travailler et d'apprendre au sein des collaborations Stereo et Nucleus.

Enfin, je remercie ma famille, mes proches et amis, aussi bien d'hier que d'aujourd'hui, pour m'avoir épaulé et aidé à devenir celui que je suis.

Appendix A

Ridge regression

Let's consider $D = (D_i)_i$ a vector of data, whose uncertainties are encapsulated in the experimental covariance matrix V. Let's then denote $\Phi = (\Phi_j)_j$ a set of explanatory variables that ought to describe the data through the linear model $R = (R_{ij})_{i,j}$. We consider the problem ill-posed, which suggests the implementation of a regularization constraint.

The Tikhonov regularization or Ridge regression consists in estimating Φ by minimizing the subsequent χ^2:

$$\chi^2_\lambda(\Phi) \;=\; \|D - R\Phi\|^2_{V^{-1}} \;+\; \lambda \|\Phi\|^2_M \tag{A.1}$$

where $\|X\|^2_A \;:=\; X^T A X$.

In Equation A.1, M is the regularization matrix, which is in general a symmetric positive matrix, that induces a semi-norm in the euclidian space of the estimated parameters. λ is called the regularization strength, or Ridge parameter. It is an hyperparameter of the regression, that can be set with an heuristic criterion (see Appendix B).

The χ^2 defined in equation A.1 can be minimized analytically. Indeed:

$$\frac{\partial \chi^2_\lambda}{\partial \Phi} \;=\; 2R^T V^{-1} R\Phi \;-\; 2R^T V^{-1} D \;+\; 2\lambda M \Phi$$

Solving:

$$\frac{\partial \chi^2_\lambda}{\partial \Phi} \;=\; 0$$

one then finds:

$$\begin{aligned} \hat{\Phi} \;&=\; \left(R^T V^{-1} R \;+\; \lambda M\right)^{-1} R^T V^{-1} D \\ &:=\; H(\lambda) D \end{aligned} \tag{A.2}$$

$H(\lambda) \;=\; \left(R^T V^{-1} R \;+\; \lambda M\right)^{-1} R^T V^{-1}$ is often referred to as the hat matrix of the inverse problem, that linearly maps the fitted parameters to the data. Naturally, it depends on the strength of the regularization. The covariance matrix of $\hat{\Phi}$ immediately follows as:

$$V_{\hat{\Phi}} \;=\; H(\lambda) \cdot V \cdot H(\lambda)^T \tag{A.3}$$

Appendix B

GCV error and effective number of degrees of freedom

Let's consider the Ridge regression problem of Appendix A. We propose to estimate the regularization strength, or ridge parameter, of the problem by minimizing the Generalized Cross-Validation error, following the prescription of Wahba *et al.* [106].

Expression of the GCV error

The GCV error function to be minimized reads:

$$\begin{aligned} GCV(\lambda) &= \frac{\left\| D - \hat{D} \right\|_{V^{-1}}^2}{\left(Tr\left[I - H_D(\lambda) \right] \right)^2} \\ &= \frac{\left\| \left(I - H_D(\lambda) \right) D \right\|_{V^{-1}}^2}{\left(Tr\left[I - H_D(\lambda) \right] \right)^2} \end{aligned} \tag{B.1}$$

where $\hat{D} = R \cdot \hat{\Phi}$ and $H_D(\lambda) = R \cdot H(\lambda)$.

Actually, this expression is not directly the one from Wahba's article. The expression that we derive now will help us in the interpretation of the denominator in terms of degrees of freedom. Nonetheless, we will see in the end that both expressions amount to exactly the same.

In Wahba's article, the numerator of the GCV error function is built out of the classical euclidian scalar product $\|.\|_I^2$ instead of $\|.\|_{V^{-1}}^2$. We then perform a change of variable to reduce to this case. To do so, we introduce $V^{\frac{1}{2}}$ the square-root matrix of the symmetric positive-definite covariance matrix V. For a given vector X, we have:

$$\begin{aligned} \|X\|_{V^{-1}}^2 &= X^T V^{-1} X \\ &= X^T V^{-\frac{1}{2}} V^{-\frac{1}{2}} X \\ &= \left(V^{-\frac{1}{2}} X \right)^T \left(V^{-\frac{1}{2}} X \right) \\ &= \left\| V^{-\frac{1}{2}} X \right\|_I^2 \end{aligned}$$

From which we infer:

$$\begin{aligned}
\left\|D-\hat{D}\right\|_{V^{-1}}^2 &= \left\|V^{-\frac{1}{2}}\left(D-\hat{D}\right)\right\|_I^2 \\
&= \left\|V^{-\frac{1}{2}}D - V^{-\frac{1}{2}}H_D(\lambda)D\right\|_I^2 \\
&= \left\|V^{-\frac{1}{2}}D - V^{-\frac{1}{2}}H_D(\lambda)V^{\frac{1}{2}}V^{-\frac{1}{2}}D\right\|_I^2 \\
&= \left\|\left(I - V^{-\frac{1}{2}}H_D(\lambda)V^{\frac{1}{2}}\right)V^{-\frac{1}{2}}D\right\|_I^2
\end{aligned}$$

If we thoroughly apply Wahba's formula, the GCV error then reads:

$$GCV(\lambda) = \frac{\left\|\left(I - V^{-\frac{1}{2}}H_D(\lambda)V^{\frac{1}{2}}\right)V^{-\frac{1}{2}}D\right\|_I^2}{\left(Tr\left[I - V^{-\frac{1}{2}}H_D(\lambda)V^{\frac{1}{2}}\right]\right)^2}$$

Actually, the numerator has not changed and has just been rewritten to bring out the $I - V^{-\frac{1}{2}}H_D(\lambda)V^{\frac{1}{2}}$ matrix. Also, the value of the denominator is unchanged with respect to the previous expression because of the invariance of the trace under cyclic permutations:

$$\begin{aligned}
Tr\left[I - V^{-\frac{1}{2}}H_D(\lambda)V^{\frac{1}{2}}\right] &= Tr[I] - Tr\left[V^{-\frac{1}{2}}H_D(\lambda)V^{\frac{1}{2}}\right] \\
&= Tr[I] - Tr\left[H_D(\lambda)V^{\frac{1}{2}}V^{-\frac{1}{2}}\right] \\
&= Tr[I] - Tr\left[H_D(\lambda)\right] \\
&= Tr\left[I - H_D(\lambda)\right]
\end{aligned}$$

Analytical expression of the trace

In the following, we consider the generally symmetric positive matrix M to be invertible.

Let's now rewrite the explicit expression of the matrix $H_D(\lambda)$:

$$H_D(\lambda) = R\left(R^TV^{-1}R + \lambda M\right)^{-1}R^TV^{-1}$$

We want to compute $Tr\left[(H_D(\lambda)\right]$:

$$\begin{aligned}
Tr\left[H_D(\lambda)\right] &= Tr\left[V^{-\frac{1}{2}}H_D(\lambda)V^{\frac{1}{2}}\right] \\
&= Tr\left[V^{-\frac{1}{2}}R\left(R^TV^{-1}R + \lambda M\right)^{-1}R^TV^{-1}V^{\frac{1}{2}}\right] \\
&= Tr\left[V^{-\frac{1}{2}}R\left(R^TV^{-\frac{1}{2}}V^{-\frac{1}{2}}R + \lambda M\right)^{-1}R^TV^{-\frac{1}{2}}\right] \\
&= Tr\left[\left(V^{-\frac{1}{2}}R\right)\left(\left(V^{-\frac{1}{2}}R\right)^T\left(V^{-\frac{1}{2}}R\right) + \lambda M\right)^{-1}\left(V^{-\frac{1}{2}}R\right)^T\right]
\end{aligned}$$

We then have the expression:

$$Tr\left[H_D(\lambda)\right] = Tr\left[R'\left(R'^{\,T}R' + \lambda M\right)^{-1} R'^{\,T}\right]$$

where $R' = V^{-\frac{1}{2}}R$.

Likewise:

$$\begin{aligned} R'\left(R'^{\,T}R' + \lambda M\right)^{-1} R'^{\,T} &= R'\left(M^{\frac{1}{2}}\left(M^{-\frac{1}{2}}R'^{\,T}R'M^{-\frac{1}{2}} + \lambda I\right)M^{\frac{1}{2}}\right)^{-1} R'^{\,T} \\ &= R'M^{-\frac{1}{2}}\left(M^{-\frac{1}{2}}R'^{\,T}R'M^{-\frac{1}{2}} + \lambda I\right)^{-1} M^{-\frac{1}{2}}R'^{\,T} \\ &= \left(R'M^{-\frac{1}{2}}\right)\left(\left(R'M^{-\frac{1}{2}}\right)^T\left(R'M^{-\frac{1}{2}}\right) + \lambda I\right)^{-1}\left(R'M^{-\frac{1}{2}}\right)^T \end{aligned}$$

Denoting $\tilde{R} = R'M^{-\frac{1}{2}} = V^{-\frac{1}{2}}RM^{-\frac{1}{2}}$, we get:

$$Tr\left[H_D(\lambda)\right] = Tr\left[\tilde{R}\left(\tilde{R}^T\tilde{R} + \lambda I\right)^{-1}\tilde{R}^T\right]$$

Using the invariance of the trace under cyclic permutations:

$$\begin{aligned} Tr\left[H_D(\lambda)\right] &= Tr\left[\left(\tilde{R}^T\tilde{R} + \lambda I\right)^{-1}\tilde{R}^T\tilde{R}\right] \\ &= Tr\left[\left(\left(\tilde{R}^T\tilde{R}\right)^{-1}\left(\tilde{R}^T\tilde{R} + \lambda I\right)\right)^{-1}\right] \\ &= Tr\left[\left(I + \lambda\left(\tilde{R}^T\tilde{R}\right)^{-1}\right)^{-1}\right] \\ &= Tr\left[\left(I + \lambda K^{-1}\right)^{-1}\right] \end{aligned} \tag{B.2}$$

where $K = \tilde{R}^T\tilde{R} = M^{-\frac{1}{2}}R^TV^{-1}RM^{-\frac{1}{2}}$.

The K matrix being a real (positive) symmetric $N_\Phi \times N_\Phi$ matrix, it is diagonalizable. Let's denote $\left(\mu_i^K\right)_i$ its (positive) eigenvalues. One can now express analytically the function $f(\lambda) = Tr\left[I - H_D(\lambda)\right]$:

$$\begin{aligned} Tr\left[I - H_D(\lambda)\right] &= Tr\left[I\right] - Tr\left[H_D(\lambda)\right] \\ &= Tr\left[I\right] - Tr\left[\left(I + \lambda K^{-1}\right)^{-1}\right] \\ &= N_R - \sum_{i=1}^{N_\Phi}\left(\frac{1}{1 + \frac{\lambda}{\mu_i^K}}\right) \end{aligned} \tag{B.3}$$

From this writing, it appears that $Tr\left[I - H_D(\lambda)\right]$ is an increasing function of λ that spans the domain $[N_D - N_\Phi,\ N_D]$ when λ spans $[0,\ +\infty]$.

Interpretation in terms of effective number of degrees of freedom

Let's first consider the classical case where we turn off the regularization ($\lambda = 0$). Using the change of variable $D \to V^{-\frac{1}{2}}D$, we have:

$$\begin{aligned} V^{-\frac{1}{2}}\hat{D} &= V^{-\frac{1}{2}}H_D(0)V^{\frac{1}{2}}\left(V^{-\frac{1}{2}}D\right) \\ &= \left(V^{-\frac{1}{2}}R\right)\left(\left(V^{-\frac{1}{2}}R\right)^T\left(V^{-\frac{1}{2}}R\right)\right)^{-1}\left(V^{-\frac{1}{2}}R\right)^T\left(V^{-\frac{1}{2}}D\right) \end{aligned}$$

$V^{-\frac{1}{2}}H_D(0)V^{\frac{1}{2}}$ is a symmetric and idempotent matrix. So it is the matrix of an orthogonal projector, whose rank $r = N_\Phi$ is the dimension of the projected subspace on which the fit is performed. It can also be interpreted as the number of parameters used for the fitted estimation.

Similarly, $I - V^{-\frac{1}{2}}H_D(0)V^{\frac{1}{2}}$ is also an orthogonal projector whose rank $r = N_D - N_\Phi$ refers to the remaining number degrees of freedom.

As orthogonal projectors, their rank is merely their trace so that, in the case where $\lambda = 0$, $Tr\left[I - H_D(\lambda)\right]$ is the number of degrees of freedom.

By extension, this quantity defines the effective number of degrees of freedom when $\lambda > 0$. This interpretation is consistent with its spanning the domain $[N_D - N_\Phi,\ N_D]$ when λ spans $[0,\ +\infty]$.

Appendix C

Filter matrix and unbiased test statistic

Notations

We consider an experimental spectrum D with its associated covariance matrix V, that is to be unfolded in true energy space through the injective response matrix of the experiment R, from a Tikhonov regularized unfolding routine, characterized by a regularization strength λ and a symmetric positive regularization matrix M. We denote $\hat{\Phi}(\lambda)$ the unfolded spectrum, $V_{\hat{\Phi}}(\lambda)$ its covariance matrix and $A_c(\lambda)$ the filter matrix of the unfolding, that encapsulates the regularization bias.

Let's consider that we have a true energy prediction Φ_0 and its covariance matrix V_{Φ_0} to be compared to the data. In order to correct for the unfolding bias, we propose to compare the filtered prediction to the unfolded spectrum via the subsequent χ^2:

$$\chi^2(\lambda) = \left\| \hat{\Phi}(\lambda) - A_c(\lambda) \cdot \Phi_0 \right\|^2_{\left(V_{\hat{\Phi}}(\lambda) + A_c(\lambda) \cdot V_{\Phi_0} \cdot A_c^T(\lambda)\right)^{-1}} \tag{C.1}$$

where $\|Y\|_A^2 := Y^T A Y$.

We propose to show that this test statistic, performed in true energy space, is actually independent of λ and is indeed mathematically corrected for the unfolding bias.

Demonstration

Let's remind that the unfolded spectrum of the Tikhonov regularized unfolding and its associated covariance matrix may be expressed as:

$$\begin{cases} \hat{\Phi}(\lambda) & = A_c(\lambda) \cdot \hat{\Phi}_{\text{LLS}} \\ V_{\hat{\Phi}}(\lambda) & = A_c(\lambda) \cdot V_{\hat{\Phi}_{\text{LLS}}} \cdot A_c^T(\lambda) \end{cases} \tag{C.2}$$

where $\hat{\Phi}_{\text{LLS}}$ is the unbiased linear least-square estimator.

We then have:

$$\begin{cases} \hat{\Phi}(\lambda) - A_c(\lambda) \cdot \Phi_0 & = A_c(\lambda) \cdot \left(\hat{\Phi}_{\text{LLS}} - \Phi_0 \right) \\ V_{\hat{\Phi}}(\lambda) + A_c(\lambda) \cdot V_{\Phi_0} \cdot A_c^T(\lambda) & = A_c(\lambda) \cdot \left(V_{\hat{\Phi}_{\text{LLS}}} + V_{\Phi_0} \right) \cdot A_c^T(\lambda) \end{cases} \tag{C.3}$$

Assuming that the filter matrix $A_c(\lambda)$ is invertible whatever value of λ, Equation C.1 reduces to:

$$\begin{aligned}
\chi^2(\lambda) &= \left\|\hat{\Phi}(\lambda) - A_c(\lambda)\cdot\Phi_0\right\|^2_{\left(V_{\hat{\Phi}}(\lambda)+A_c(\lambda)\cdot V_{\Phi_0}\cdot A_c^T(\lambda)\right)^{-1}} \\
&= \left\|A_c(\lambda)\cdot\left(\hat{\Phi}_{\text{LLS}} - \Phi_0\right)\right\|^2_{A_c(\lambda)\cdot\left(V_{\hat{\Phi}_{\text{LLS}}}+V_{\Phi_0}\right)\cdot A_c^T(\lambda)} \\
&= \left\|A_c(\lambda)\cdot\left(\hat{\Phi}_{\text{LLS}} - \Phi_0\right)\right\|^2_{A_c^{-T}(\lambda)\cdot\left(V_{\hat{\Phi}_{\text{LLS}}}+V_{\Phi_0}\right)^{-1}\cdot A_c^{-1}(\lambda)} \\
&= \left(\hat{\Phi}_{\text{LLS}} - \Phi_0\right)^T\cdot A_c^T(\lambda)A_c^{-T}(\lambda)\cdot\left(V_{\hat{\Phi}_{\text{LLS}}} + V_{\Phi_0}\right)^{-1}\cdot A_c^{-1}(\lambda)A_c(\lambda)\cdot\left(\hat{\Phi}_{\text{LLS}} - \Phi_0\right) \\
&= \left(\hat{\Phi}_{\text{LLS}} - \Phi_0\right)^T\left(V_{\hat{\Phi}_{\text{LLS}}} + V_{\Phi_0}\right)^{-1}\left(\hat{\Phi}_{\text{LLS}} - \Phi_0\right)
\end{aligned}$$

such that:

$$\chi^2(\lambda) = \chi^2 = \left\|\hat{\Phi}_{\text{LLS}} - \Phi_0\right\|^2_{\left(V_{\hat{\Phi}_{\text{LLS}}}+V_{\Phi_0}\right)^{-1}} \tag{C.4}$$

which is nothing but the χ^2 comparison between the unbiased unfolded spectrum and the nominal prediction. Finally, we justify in the subsequent section, that the filter matrix is indeed invertible for each $\lambda \geq 0$.

Non-singularity of the filter matrix

Let's remind that the filter matrix is, by construction, assumed non-singular as it is expressed as:

$$A_c = \left(I + \lambda\left(R^T V^{-1} R\right)^{-1} M\right)^{-1} \tag{C.5}$$

where I is the identity matrix. We then show that the matrix $I + \lambda\left(R^T V^{-1} R\right)^{-1} M$ is indeed invertible whatever value of λ.

This result follows from the two subsequent lemmas:

***Lemma 1*:** Let A be a symmetric positive-definite matrix and B a symmetric matrix. Then AB is diagonalizable.

***Proof*:**

$A \in S_n^{++}(\mathbb{R})$ and $B \in S_n(\mathbb{R})$ then $(ABA)^T = A^T B^T A^T = ABA$. Therefore, $ABA \in S_n(\mathbb{R})$ and is diagonalizable.

As a matrix similar to ABA, $A(ABA)A^{-1} = A^2 B$ is then diagonalizable. This is possible because A is invertible as a matrix from $S_n^{++}(\mathbb{R})$. We then have: $A \in S_n^{++}(\mathbb{R})$ and $B \in S_n(\mathbb{R}) \implies A^2 B$ is diagonalizable.

The square root function $\sqrt{\cdot} : S_n^{++}(\mathbb{R}) \mapsto S_n^{++}(\mathbb{R})$ is a bijection, hence the lemma by replacing A with $\sqrt{A}$ in the Proof above.

***Lemma 2*:** Let A and B be two symmetric positive matrices. Then the eigenvalues of AB are positive.

***Proof*:** Let be $A, B \in S_n^+(\mathbb{R})$. Let's show that $Sp(AB) \subset \mathbb{R}_+$.

Let $x \in \mathbb{R}^n \setminus \{0\}$ be an eigenvector of AB, with μ the associated eigenvalue. We can suppose that $\mu \neq 0$, i.e. $x \notin Ker(AB)$. As $Ker(\sqrt{B}) = Ker(B) \subset Ker(AB)$, then $x \notin Ker(\sqrt{B})$.

$$\begin{aligned}
< BABx, x > &= < ABx, Bx > \\
&= < A(Bx), Bx > \\
&= < \sqrt{A}(Bx), \sqrt{A}Bx > \\
&= ||\sqrt{A}Bx||^2 \\
&\geq 0 \\
< BABx, x > &= < B(ABx), x > \\
&= \mu < Bx, x > \\
&= \mu < \sqrt{B}x, \sqrt{B}x > \\
&= \mu ||\sqrt{B}x||^2
\end{aligned}$$

We then have $\mu||\sqrt{B}x||^2 \geq 0$ with $||\sqrt{B}x||^2 > 0$, hence $\mu \geq 0$. Therefore, $\mu \in \mathbb{R}_+$.

Noting that $\left(R^T V^{-1} R\right)^{-1}$ is a symmetric positive-definite matrix and M is a symmetric positive matrix, it follows that $\left(R^T V^{-1} R\right)^{-1} M$ is diagonalizable with positive eigenvalues $\{\mu_i\}_i$. Therefore, the eigenvalues of $I + \lambda \left(R^T V^{-1} R\right)^{-1} M$ are $\{1 + \lambda \cdot \mu_i\}_i$ which are strictly positive. This shows that this matrix is always invertible and that the filter matrix is always well-defined and non-singular, whatever positive value of λ.

This is an interesting result, that is quite non-intuitive when applied to the high λ limit. Indeed, when $\lambda \longrightarrow \infty$, one tends to completely smooth out the unfolded spectrum and the filtered prediction, such that one may expect a degeneracy of the test-statistic defined in Equation C.1. Yet, the non-singularity of the filter matrix tells us that this effect is in principle still corrected by the filter matrix. But this is "in principle", because as $\lambda \longrightarrow \infty$, some eigenvalues of the filter matrix may tend to 0[1] and the matrix becomes "less and less invertible". In other words, even if, mathematically, the unfolded bias is corrected for any value of the regularization strength by the test statistic defined in Equation C.1, in practice, in the high λ limit, this test statistic is subjected to numerical biases. It should be applied only for "reasonable" values of regularization strength.

[1] Those corresponding to non-zero eigenvalues of $\left(R^T V^{-1} R\right)^{-1} M$.

Appendix D

Normalization of Daya Bay response matrix

Impact of a misnormalization of Daya Bay response

We denote D^{tot} the experimental Daya Bay LEU measured spectrum.

The ^{235}U, ^{238}U and Pu combo antineutrino energy spectra are respectively labelled as Φ^{U5}, Φ^{U8} and Φ^{Pu}, and the Daya Bay response matrix R.

We propose to study the impact of a misnormalization of the Daya Bay response matrix on the HEU+LEU unfolded spectra. Given that the ^{235}U spectrum will be fully constrained by the HEU data and the ^{238}U spectrum is assumed to be given by the Mueller prediction, the normalization bias, denoted $\delta\alpha$ is expected to be fully absorbed by the Pu combo unfolded spectrum. This provides us with the following system:

$$\left\{ \begin{array}{ll} D^{\text{tot}} & = R \cdot \left(f_{eff}^{235} * \Phi^{\text{U5}} + f_{eff}^{238} * \Phi^{\text{U8}} + f_{eff}^{239+241} * \Phi_1^{\text{Pu}} \right) \\ D^{\text{tot}} & = (1+\delta\alpha) \cdot R \cdot \left(f_{eff}^{235} * \Phi^{\text{U5}} + f_{eff}^{238} * \Phi^{\text{U8}} + f_{eff}^{239+241} * \Phi_2^{\text{Pu}} \right) \end{array} \right. \tag{D.1}$$

In terms of IBD fission yields, this system translates into:

$$\left\{ \begin{array}{ll} \sigma^{\text{tot}} & = f_{eff}^{235} * \sigma^{\text{U5}} + f_{eff}^{238} * \sigma^{\text{U8}} + f_{eff}^{239+241} * \sigma_1^{\text{Pu}} \\ \sigma^{\text{tot}} & = (1+\delta\alpha) \cdot \left(f_{eff}^{235} * \sigma^{\text{U5}} + f_{eff}^{238} * \sigma^{\text{U8}} + f_{eff}^{239+241} * \sigma_2^{\text{Pu}} \right) \end{array} \right.$$

which directly provides us with the following identity:

$$\frac{\sigma_1^{\text{Pu}}}{\sigma_2^{\text{Pu}}} - 1 = \delta\alpha \cdot \left(\frac{f_{eff}^{235} * \sigma^{\text{U5}} + f_{eff}^{238} * \sigma^{\text{U8}}}{f_{eff}^{239+241} * \sigma_2^{\text{Pu}}} \right)$$

In the case of Daya Bay, we have: $f_{eff}^{235} = 0.564$, $f_{eff}^{239+241} = 0.360$, $f_{eff}^{238} = 0.076$. Using the Huber-Mueller predictions for the ^{235}U, ^{238}U and Pu combo IBD fission yields lead to:

$$\frac{\sigma_1^{\text{Pu}}}{\sigma_2^{\text{Pu}}} - 1 \approx 2.7 \cdot \delta\alpha \tag{D.2}$$

Thus, a 1% bias on the normalization of the response would translate into a sizeable $\sim$ 3% bias on the normalization of the Pu combo unfolded spectrum. This requires to check the normalization of the Daya Bay response to a sub-percent level accuracy.

Cross-check of the accuracy of Daya Bay response normalization

To check the accuracy of the normalization of the Daya Bay response matrix with their data set, we will operate in antineutrino energy space. We propose to use their published unfolded spectra (total, ^{235}U and Pu combo) and associated filter matrices and check the consistency with our hand-made renormalized response matrix. The reasoning relies on the formula:

— : Published
— : Hand-Made

$Isotope = {}^{235}$U / Pu combo / Total

$$\hat{\Phi}^{Isotope} = A_c^{Isotope} \cdot \left(R_{DB}^T (V_{DB}^{Isotope})^{-1} R_{DB}\right)^{-1} R_{DB}^T (V_{DB}^{Isotope})^{-1} \cdot D_{DB}^{Isotope}$$

which is nothing but the Wiener-SVD unfolding formula used by the Daya Bay collaboration to unfold their separated isotopic spectra $D_{DB}^{isotope}$ to produce the associated unfolded spectra $\hat{\Phi}^{isotope}$. The key point of this formula is that the scale of the unfolded spectrum is found to be inversely proportional to the scale of the response matrix: $\hat{\Phi}^{isotope} \propto 1/R_{\mathrm{DB}}$. Thus, comparing the integrated yield of the published spectrum on the left of the identity above to the integrated yield of the hand-made spectrum built out of the right part of this identity provides us with a direct measurement of the consistency of the normalization of the Daya Bay response matrix.

This is what is done in Figure D.1 for the total, ^{235}U and Pu combo spectra. Overall, the spectral agreement is very satisfactory between the published and hand-made spectra, except for the last energy bin where sizeable discrepancies, that we are not able to explain, appear. Thus, we decide to perform the yield comparison not taking into account this last bin. For the three spectra, we achieve a permil level consistency on the integrated fission yields, yielding to equivalent accuracy on the normalization of the Daya Bay response matrix. In comparison with the 1.2% uncertainty on the normalization of the Daya Bay spectrum [152], we conclude that there is no need to add a supplemental normalization uncertainty coming from the normalization of the response matrix.

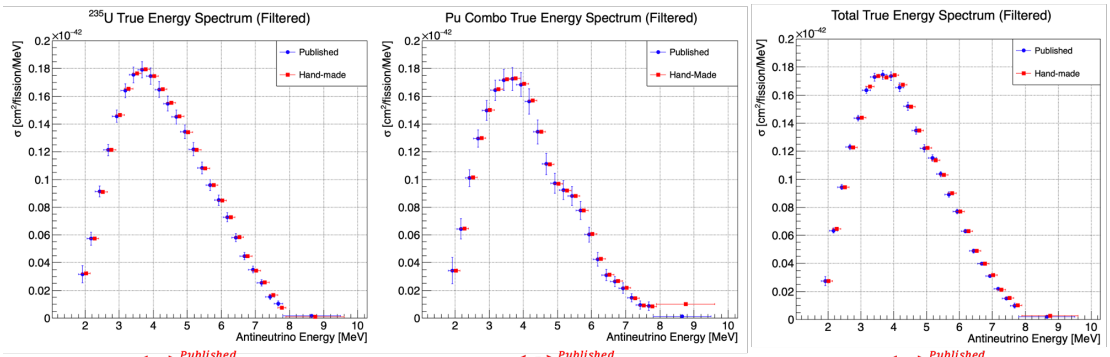

Figure D.1: **Comparison of the fission yields between the published (blue) and hand-made (red) unfolded Daya Bay spectra**, for ^{235}U, Pu combo and total spectra. For display purposes, the hand-made spectra have been slightly shifted. Below each spectrum, we show the ratio of the integrated fission yields between the published and hand-made spectra. The yields are calculated without taking into account the last energy bin, and show a permil level agreement.

Appendix E

Regularization power in HEU+LEU unfolding

We remind in Figure E.1 the solution of the HEU+LEU unfolding, and detail the exact writing of the matrix: $R_{\mathrm{HL}}^T V_{\mathrm{HL}}^{-1} R_{\mathrm{HL}} + \lambda_{\mathrm{U5}} \cdot \Lambda_{\mathrm{HL}} \left(r_{\mathrm{Pu/U5}}\right) \cdot M_{\mathrm{HL}}$. What matters in this matrix is the block-diagonal terms that propagate the self-correlations of ^{235}U and Pu coming from the experimental and regularization constraints.

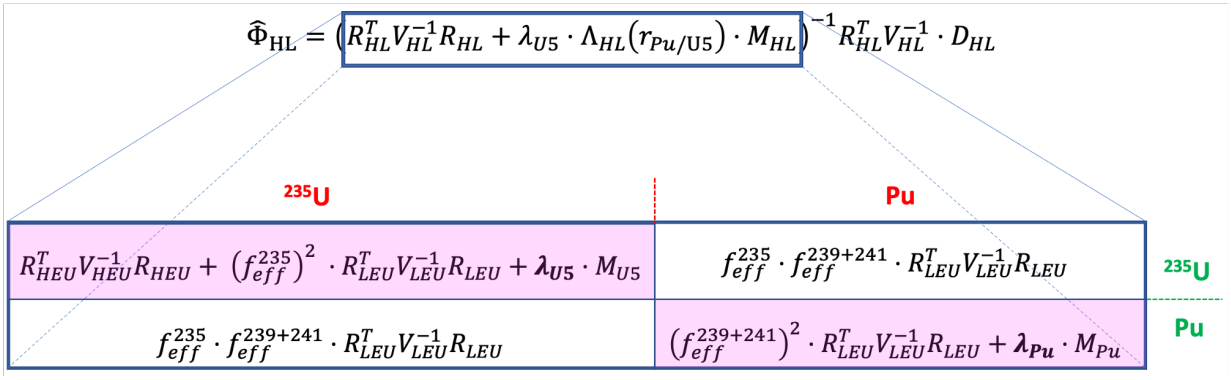

Figure E.1: **Solution of the HEU+LEU unfolding**.

We would like to derive a criterion that would set comparable regularization powers for ^{235}U and Pu combo unfoldings. Similarly to the definition of regularization power that we gave in Section 6.2.2.4, we would be tempted to write something like:

$$\ll \frac{\lambda_{\mathrm{U5}} \cdot M_{\mathrm{U5}}}{R_{\mathrm{HEU}}^T V_{\mathrm{HEU}}^{-1} R_{\mathrm{HEU}} + \left(f_{eff}^{235}\right)^2 \cdot R_{\mathrm{LEU}}^T V_{\mathrm{LEU}}^{-1} R_{\mathrm{LEU}}} = \frac{\lambda_{\mathrm{Pu}} \cdot M_{\mathrm{Pu}}}{\left(f_{eff}^{239+241}\right)^2 \cdot R_{\mathrm{LEU}}^T V_{\mathrm{LEU}}^{-1} R_{\mathrm{LEU}}} \gg \quad \text{(E.1)}$$

Naturally, this is not possible. However, we can exploit the fact that, as short-range regularization matrices, M_{U5} and M_{Pu} are close-to-diagonal matrices (see Figure E.2 for the case of ^{235}U). Similarly, the dominant coefficients of the $R^T V^{-1} R$ matrices appear to be on the diagonal (see Figure E.3 for the case of the LEU Daya Bay data set).

Thus, an average estimate of the criterion of Equation E.1 can be more rigorously formulated thanks to the Trace operator, which is nothing but the sum of the diagonal matricial elements:

$$\frac{\lambda_{\mathrm{U5}} \cdot \mathrm{Tr}\left(M_{\mathrm{U5}}\right)}{\mathrm{Tr}\left(R_{\mathrm{HEU}}^T V_{\mathrm{HEU}}^{-1} R_{\mathrm{HEU}} + \left(f_{eff}^{235}\right)^2 \cdot R_{\mathrm{LEU}}^T V_{\mathrm{LEU}}^{-1} R_{\mathrm{LEU}}\right)} = \frac{\lambda_{\mathrm{Pu}} \cdot \mathrm{Tr}\left(M_{\mathrm{Pu}}\right)}{\mathrm{Tr}\left(\left(f_{eff}^{239+241}\right)^2 \cdot R_{\mathrm{LEU}}^T V_{\mathrm{LEU}}^{-1} R_{\mathrm{LEU}}\right)}$$

such that, finally:

$$
\begin{aligned}
r_{\mathrm{Pu/U5}} &= \frac{\lambda_{\mathrm{Pu}}}{\lambda_{\mathrm{U5}}} \\
&= \frac{\mathrm{Tr}\left(M_{\mathrm{U5}}\right) \cdot \mathrm{Tr}\left(\left(f_{eff}^{239+241}\right)^2 \cdot R_{\mathrm{LEU}}^T V_{\mathrm{LEU}}^{-1} R_{\mathrm{LEU}}\right)}{\mathrm{Tr}\left(M_{\mathrm{Pu}}\right) \cdot \mathrm{Tr}\left(R_{\mathrm{HEU}}^T V_{\mathrm{HEU}}^{-1} R_{\mathrm{HEU}} + \left(f_{eff}^{235}\right)^2 \cdot R_{\mathrm{LEU}}^T V_{\mathrm{LEU}}^{-1} R_{\mathrm{LEU}}\right)}
\end{aligned}
\tag{E.2}
$$

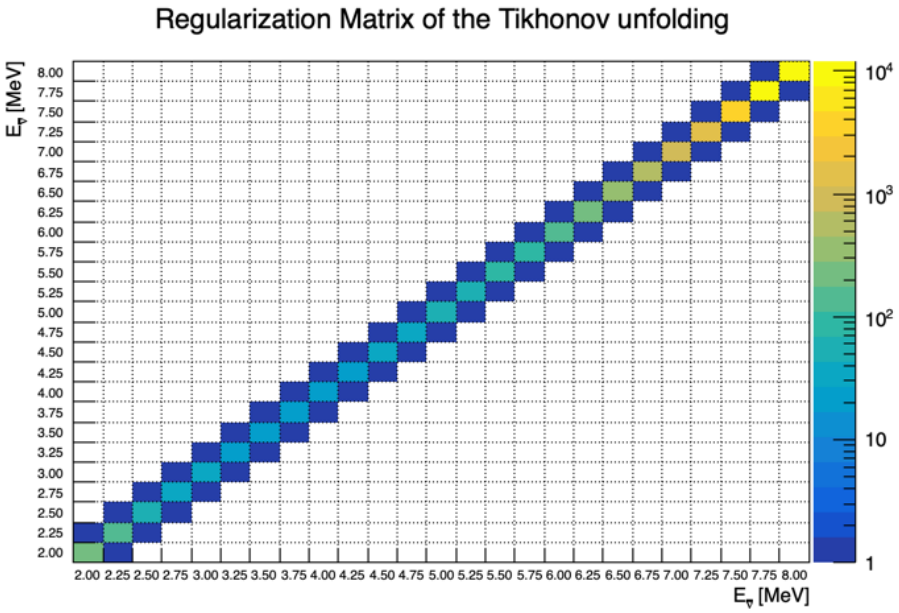

Figure E.2: ^{235}U **Regularization matrix**.

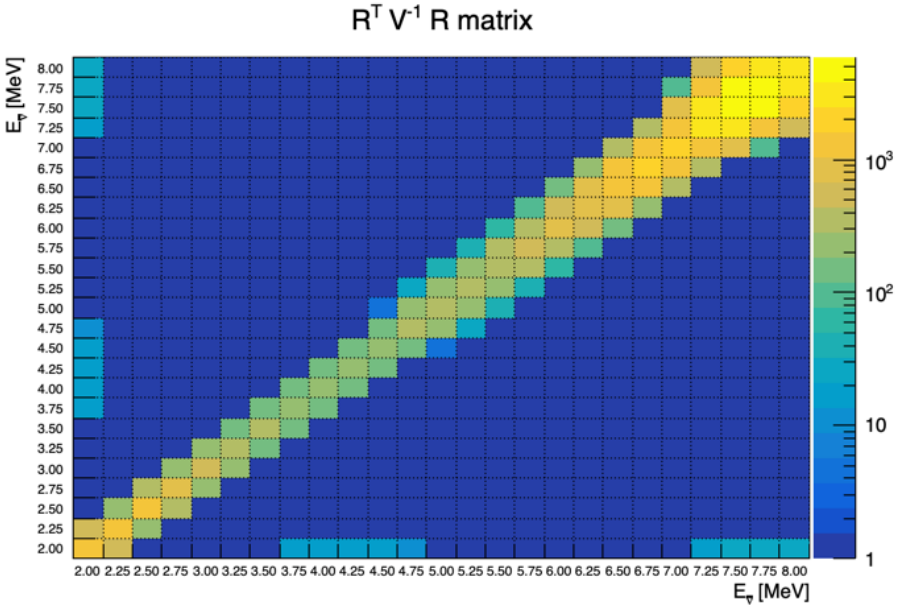

Figure E.3: $R_{\mathrm{DB}}^T V_{\mathrm{DB}}^{-1} R_{\mathrm{DB}}$ **matrix**, for the Daya Bay data set.

Appendix F

Model for the SiPM photo-electron charge spectrum

For the tests carried out in Section 9.2.2, the photo-electron (PE) charge spectrum of each SiPM is measured with the Dark Count Rate (DCR). It is composed of equally spaced peaks. The distance inter-peak is called the SiPM gain. It corresponds to the measured charge per initiated Geiger discharge, or equivalently to the measured charge per detected photon or photo-electron. It is expressed in QDC/PE.

The pure photo-electron peak spectrum, resulting from the primary avalanche triggered by thermally generated charge carriers, can be described by a Gaussian function. In our case, the width of the gaussian is dominated by the electronic noise of the DAQ. In the absence of secondary correlated avalanche events, the overall PE charge spectrum of the SiPM DCR is then expressed as:

$$\frac{dS}{dQ} = \sum_{k=1}^{N_{peaks}} A_k \cdot Gauss(Q, q_k, \sigma_k) \tag{F.1}$$

where:

$$Gauss(Q, q_k, \sigma_k) = \frac{1}{\sqrt{2\pi}\sigma_k} e^{-\frac{(Q-q_k)^2}{2\sigma_k^2}}$$

with:

$$\begin{cases} q_k = q_0 + k \cdot Gain & \textbf{position of k-th peak} \\ \sigma_k^2 = \sigma_0^2 + k \cdot (\sigma_1^2 - \sigma_0^2) & \textbf{width of k-th peak} \end{cases}$$

σ_0 is the width of the pedestal, whereas σ_1 is the width of the first PE peak, corresponding to the detection of one photo-electron. The amplitude A_k in Equation F.1 is the number of events associated to the detection of k photo-electrons, induced by primary Geiger discharges.

Cross-talk The number of primary Geiger discharges can be safely assumed to follow a Poisson distribution of mean μ. Each Geiger discharge can then initiate other primary Geiger discharges on neighbouring microcells, via cross-talk. In [188], this kind of cross-talk is assumed to follow a Borel distribution with parameter λ, so that the probability of having k Geiger discharges, and thus k detected photo-electrons, follows a Generalized Poisson distribution [192]:

$$GP_{\mu,\lambda}(k) = \frac{\mu \cdot (\mu + k \cdot \lambda)^{k-1} \cdot e^{-(\mu + k \cdot \lambda)}}{k!} \tag{F.2}$$

where μ is the mean number of photo-electrons initiating a primary Geiger discharge in a given microcell, and $1 - e^{-\lambda}$ is the probability that this Geiger discharge triggers other primary discharges in neighboring microcells, via cross-talk. We use $GP_{\mu,\lambda}(k)$ as a model for the amplitude A_k. For the range of over-voltage values that we tested, we find typical values: $\mu \sim 1$ and $1 - e^{-\lambda} \sim 0.1 - 0.2$.

After-pulse As discussed in Section 9.2.2, a primary Geiger discharge in a given microcell can trigger secondary Geiger discharges, due to the trapping and subsequent release of charge carriers in the *same* microcell. This is the so-called after-pulsing.

For a given microcell, the primary and secondary Geiger discharges must be distinguished, as secondary discharges, occurring during the recovery state of the microcell, yield to a number of collected charge lower than the nominal value of the primary discharge signal. As a consequence, after-pulse events tend to populate the regions in-between the PE peaks, such that the overall PE charge spectrum cannot be fully described by a mere summation of gaussian functions as in Equation F.1.

Denoting α the probability for one primary Geiger discharge to produce one after-pulse, the probability that k primary discharges produce i after-pulses can be expressed as a binomial distribution:

$$B_{k,\alpha}(i) = \binom{k}{i} \alpha^i (1-\alpha)^{k-i} \tag{F.3}$$

On the other hand, the charge spectrum AP of the after-pulse signal of KETEK SiPMs proved to be well-described by a convolution of i exponentials of slope β [188], multiplied by a smooth step function built out of the cumulative distribution of the considered peak (denoted here as k-th peak, at position q_k):

$$AP_{k,i,\beta}(Q) = \frac{(Q-q_k)^{i-1}}{(i-1)! \cdot \beta^i} e^{-(Q-q_k)/\beta} \cdot \frac{1}{\sqrt{2\pi} \cdot \sigma_k} \int_{-\infty}^{Q} e^{-\frac{(q-q_k)^2}{2\sigma_k^2}} \, dq \tag{F.4}$$

General exponential background At last, we assume a general background exponentially rising at low charge, that superimposes on top of the PE charge spectrum [83]:

$$Bckg_{A,\gamma}(Q) = A \cdot e^{-Q/\gamma} \tag{F.5}$$

General fitting model Overall, the general function used to fit the PE spectra is the following one:

$$\frac{dS}{dQ} = \begin{cases} Norm \cdot \Big[GP_{\mu,\lambda}(0) \cdot Gauss(Q, q_0, \sigma_0) \\ + \sum_{k=1}^{Npeaks} \Big(GP_{\mu,\lambda}(k) \cdot \big(B_{0,\alpha}(0) \cdot Gauss(Q, q_k, \sigma_k) \\ + \sum_{i=1}^{k} B_{i,\alpha}(k) \cdot AP_{k,i,\beta}(Q) \big) \Big) \; + \; Bckg_{A,\gamma}(Q) \Big] \end{cases} \tag{F.6}$$

Its free parameters are the absolute normalization of the PE charge spectrum $Norm$, the relative normalization of the background A, the exponential slope of the background γ, the SiPM gain $Gain$, the position of the pedestal q_0, the width of the pedestal σ_0 and of the first PE peak σ_1, the mean number of thermally generated charge carriers μ, the cross-talk probability λ, the after-pulse probability α, and the exponential slope of the after-pulse charge distribution β.

Bibliography

[1] W. Pauli. Liebe Radioaktive Damen und Herren. *Open letter to the group of radioactive people at the Gauverein meeting in Tübingen*, Dec. 1930.

[2] C. L. Cowan, F. Reines, F. B. Harrison, H. W. Kruse, and A. D. McGuire. Detection of the Free Neutrino: a Confirmation. *Science*, 124(3212):103–104, Jul. 1956.

[3] D. Z. Freedman. Coherent effects of a weak neutral current. *Phys. Rev. D*, 9(5):1389–1392, Mar. 1974.

[4] D. Akimov *et al.* Observation of Coherent Elastic Neutrino-Nucleus Scattering. *Science*, 357(6356):1123–1126, Aug. 2017.

[5] M. Aker *et al.* New Constraint on the Local Relic Neutrino Background Overdensity with the First KATRIN Data Runs. *Phys. Rev. Lett.*, 129(1):011806, Jun. 2022.

[6] E. Baracchini *et al.* PTOLEMY: A Proposal for Thermal Relic Detection of Massive Neutrinos and Directional Detection of MeV Dark Matter. *arXiv:2203.07349*, Aug. 2018.

[7] A. Ashtari Esfahani *et al.* The Project 8 Neutrino Mass Experiment. *arXiv:1808.01892*, Mar. 2022.

[8] J. F. Beacom. The Diffuse Supernova Neutrino Background. *Annual Review of Nuclear and Particle Science*, 60:439–462, Nov. 2010.

[9] K. Abe *et al.* Diffuse supernova neutrino background search at Super-Kamiokande. *Phys. Rev. D*, 104(12):122002, Dec. 2021.

[10] K. Abe *et al.* First gadolinium loading to Super-Kamiokande. *Nucl. Instr. and Meth. A*, 1027:166248, Mar. 2022.

[11] J. Drees. Deep Inelastic Scattering. *Nucl. Instr. and Meth. A*, 1027:122002, Dec. 1980.

[12] C. S. Wu *et al.* Experimental Test of Parity Conservation in Beta Decay. *Phys. Rev.*, 105(4):1413, Feb. 1957.

[13] G. Boireau *et al.* Online monitoring of the Osiris reactor with the Nucifer neutrino detector. *Phys. Rev. D*, 93(11):112006, Jun. 2016.

[14] S. Schael *et al.* Precision electroweak measurements on the Z resonance. *Physics Reports*, 427(5-6):257–454, May 2006.

[15] B. Pontecorvo. Neutrino experiments and the problem of conservation of leptonic charge. *JETP*, 6(5), May 1968.

[16] Z. Maki, M. Nakagawa, and S. Sakata. Remarks on the Unified Model of Elementary Particles. *Progress of Theoretical Physics*, 28(5):870–880, Nov. 1962.

[17] R. L. Workman *et al.* Particle Data Group, 2022.

[18] B. T. Cleveland *et al.* Measurement of the Solar Electron Neutrino Flux with the Homestake Chlorine Detector. *The Astrophysical Journal*, 496(1):505–526, Mar. 1998.

[19] K. S. Hirata *et al.* Observation of ^{8}B solar neutrinos in the Kamiokande-II detector. *Phys. Rev. Lett.*, 63(1), Jul. 1989.

[20] K. Abe *et al.* Solar neutrino measurements in Super-Kamiokande-IV. *Phys. Rev. D*, 94(5), Sep. 2016.

[21] V. N. Gavrin *et al.* The russian-american gallium experiment SAGE. *Physics-Uspekhi*, 54(9), Sep. 2011.

[22] D. Vignaud. The GALLEX solar neutrino experiment. *Nucl. Phys. B (Proc. Suppl.)*, 60(3):20–29, Jan. 1998.

[23] W. C. Haxton *et al.* Solar Neutrinos: Status and Prospects. *Annual Review of Astronomy and Astrophysics*, 51:21–61, Aug. 2013.

[24] Q. R. Ahmad *et al.* Direct Evidence for Neutrino Flavor Transformation from Neutral-Current Interactions in the Sudbury Neutrino Observatory. *Phys. Rev. Lett.*, 89(1):011301, Jun. 2002.

[25] K. S. Hirata *et al.* Experimental study of the atmospheric neutrino flux. *Phys. Lett. B*, 205(2-3):416–420, Apr. 1988.

[26] D. Casper *et al.* Measurement of atmospheric neutrino composition with the IMB-3 detector. *Phys. Rev. Lett.*, 66(20):2561, May 1991.

[27] Y. Fukuda *et al.* Measurement of a small atmospheric ν_μ/ν_e ratio. *Phys. Lett. B*, 433(1-2):9–18, Aug. 1998.

[28] K. Abe *et al.* Atmospheric neutrino oscillation analysis with external constraints in Super-Kamiokande I-IV. *Phys. Rev. D*, 97(7):072001, Apr. 2018.

[29] Y. Ashie *et al.* Evidence for an Oscillatory Signature in Atmospheric Neutrino Oscillations. *Phys. Rev. Lett.*, 93(10):101801, Sep. 2004.

[30] T. Kajita, E. Kearns, and M. Shiozawa. Establishing atmospheric neutrino oscillations with Super-Kamiokande. *Nucl. Phys. B*, 908:14–29, Jul. 2016.

[31] T. Nakaya and R. K. Plunkett. Neutrino oscillations with the MINOS, MINOS+, T2K, and NOvA experiments. *New J. Phys.*, 18:015009, Jan. 2016.

[32] P. Adamson *et al.* Precision Constraints for Three-Flavor Neutrino Oscillations from the Full MINOS+ and MINOS Dataset. *Phys. Rev. Lett*, 125(13):131802, Sep. 2020.

[33] M. A. Acero *et al.* Improved measurement of neutrino oscillation parameters by the NOvA experiment. *Phys. Rev. D*, 106(3):032004, Aug. 2022.

[34] K. Abe *et al.* T2K measurements of muon neutrino and antineutrino disappearance using 3.13 × 1021 protons on target. *Phys. Rev. D*, 103(1):L011101, Jan. 2021.

[35] M. P. Decowski. KamLAND's precision neutrino oscillation measurements. *Nucl. Phys. B*, 908:52–61, Jul. 2016.

[36] K. Eguchi *et al.* First Results from KamLAND: Evidence for Reactor Antineutrino Disappearance. *Phys. Rev. Lett.*, 90(2):021802, Jan. 2003.

[37] H. de Kerret *et al.* Improved measurements of the neutrino mixing angle θ_{13} with the Double Chooz detector. *Nature Physics*, 16:558–564, Apr. 2020.

[38] F. P. An *et al.* Observation of Electron-Antineutrino Disappearance at Daya Bay. *Phys. Rev. Lett.*, 108(17):171803, Apr. 2012.

[39] S. H. Seo *et al.* Spectral Measurement of the Electron Antineutrino Oscillation Amplitude and Frequency using 500 Live Days of RENO Data. *Phys. Rev. D*, 98(1):012002, Jul. 2018.

[40] U. Rahaman and S. K. Raut. On the tension between the latest NOvA and T2K data. *arXiv:2112.13186*, Sep. 2022.

[41] F. Capozzi *et al.* Global constraints on absolute neutrino masses and their ordering. *Phys. Rev. D*, 95(9):096014, May 2017.

[42] M. Tanabashi *et al.* Particle Data Group, 2018.

[43] C. Giunti, Y. F. Li, C. A. Ternes, and Z. Xin. Reactor antineutrino anomaly in light of recent flux model refinements. *Phys. Lett. B*, 829:137054, Jun. 2022.

[44] C. H. Llewellyn Smith. Neutrino reactions at accelerator energies. *Physics Reports*, 3(5):261–379, Jun. 1972.

[45] P. Vogel and J. F. Beacom. Angular distribution of neutron inverse beta decay, $\bar{\nu}_e + p \to e^+ + n$. *Phys. Rev. D*, 60(5):053003, Jul. 1999.

[46] A. Strumia and F. Vissani. Precise quasielastic neutrino/nucleon cross-section. *Phys. Lett. B*, 564(1-2):42–54, Jul. 2003.

[47] B. R. Davis *et al.* Reactor antineutrino spectra and their application to antineutrino-induced reactions. *Phys. Rev. C*, 19(6):2259, Jun. 1979.

[48] P. Vogel *et al.* Reactor antineutrino spectra and their application to antineutrino-induced reactions II. *Phys. Rev. C*, 24(4):1543, Oct. 1981.

[49] A. Letourneau *et al.* On the origin of the reactor antineutrino anomalies in light of a new summation model with parameterized beta transitions. *arXiv:2205.14954*, May 2022.

[50] T. A. Mueller *et al.* Improved predictions of reactor antineutrino spectra. *Phys. Rev. C*, 83(5):054615, May 2011.

[51] M. Estienne *et al.* Updated Summation Model: An Improved Agreement with the Daya Bay Antineutrino Fluxes. *Phys. Rev. Lett.*, 123(2):022502, Jul. 2019.

[52] F. von Feilitzsch, A. A. Hahn, and K. Schreckenbach. Experimental beta-spectra from ^{239}Pu and ^{235}U thermal neutron fission products and their correlated antineutrino spectra. *Phys. Lett. B*, 118(1-3):162–166, Dec. 1982.

[53] K. Schreckenbach, G. Colvin, W. Gelletly, and F. von Feilitzsch. Determination of the antineutrino spectrum from ^{235}U thermal neutron fission products up to 9.5 MeV. *Phys. Lett. B*, 160(4-5):325–330, Oct. 1985.

[54] A. A. Hahn, K. Schreckenbach, W. Gelletly, F. von Feilitzsch, G. Colvin, and B. Krusche. Antineutrino spectra from ^{241}Pu and ^{239}Pu thermal neutron fission products. *Phys. Lett. B*, 218(3):365–368, Feb. 1989.

[55] P. Huber. On the determination of anti-neutrino spectra from nuclear reactors. *Phys. Rev. C*, 84(2):024617, Aug. 2011. [Erratum: Phys. Rev. C **85**, 029901 (2012)].

[56] G. Mention *et al.* Reactor antineutrino anomaly. *Phys. Rev. D*, 83(7):073006, Apr. 2011.

[57] J. Kostensalo, J. Suhonen, C. Giunti, and P. C. Srivastava. The gallium anomaly revisited. *Phys. Lett. B*, 795:542–547, Aug. 2019.

[58] V. V. Barinov *et al.* Results from the Baksan Experiment on Sterile Transitions (BEST). *Phys. Rev. Lett.*, 128(23):232501, Jun. 2022.

[59] A. Aguilar *et al.* Evidence for neutrino oscillations from the observation of $\bar{\nu}_e$ appearance in a $\bar{\nu}_\mu$ beam. *Phys. Rev. D*, 64(11):112007, Nov. 2001.

[60] A. A. Aguilar-Arevalo *et al.* Improved Search for $\bar{\nu}_\mu \to \bar{\nu}_e$ Oscillations in the MiniBooNE Experiment. *Phys. Rev. Lett.*, 110(16):161801, Apr. 2013.

[61] B. Dasgupta and J. Kopp. Sterile neutrinos. *Physics Report*, 928:1–63, Sep. 2021.

[62] Y. Abe *et al.* Improved measurements of the neutrino mixing angle θ_{13} with the Double Chooz detector. *J. High Energ. Phys.*, 10:86, Oct. 2014.

[63] F. P. An *et al.* Measurement of the Reactor Antineutrino Flux and Spectrum at Daya Bay. *Phys. Rev. Lett.*, 116(6):061801, Feb. 2016.

[64] J. Choi *et al.* Observation of Energy and Baseline Dependent Reactor Antineutrino Disappearance in the RENO Experiment. *Phys. Rev. Lett.*, 116(21):211801, May 2016.

[65] Y. J. Ko *et al.* Observation of Energy and Baseline Dependent Reactor Antineutrino Disappearance in the RENO Experiment. *Phys. Rev. Lett.*, 118(12):121802, Mar. 2017.

[66] E. Ciuffoli, J. Evslin, Q. Fu, and J. Tang. Extracting nuclear form factors with coherent neutrino scattering. *Phys. Rev. D*, 97(11):113003, Jun. 2018.

[67] D. Akimov *et al.* First Measurement of Coherent Elastic Neutrino-Nucleus Scattering on Argon. *Science*, 126(1):012002, Jan. 2021.

[68] Ciaran A. J. O'Hare. Fog on the horizon: a new definition of the neutrino floor for direct dark matter searches. *Phys. Rev. Lett.*, 127(25):251802, Dec. 2021.

[69] C. von Raesfeld and P. Huber. Use of CEvNS to monitor spent nuclear fuel. *Phys. Rev. D*, 105(5):056002, Mar. 2022.

[70] M. Vivier. Magnificent CEvNS: an (incomplete) summary talk. In *Magnificent CEvNS workshop*, 2020.

[71] S. R. Klein and J. Nystrand. Exclusive vector meson production in relativistic heavy ion collisions. *Phys. Rev. C*, 60(1):014903, Jun. 1999.

[72] The Yellow Book: Guide to the Neutron Research Facilities, 2005. http://rencurel.essworkshop.org/documents/YellowBookCDrom/.

[73] N. Allemandou *et al.* The STEREO experiment. *Journal of Instrumentation*, 13(07):P07009, Jul. 2018.

[74] Y. Calzavara A. Bergeron, B. Dionne. Neutronics Conversion Analyses of the Laue-Langevin Institute (ILL) High Flux Reactor (RHF), Sep. 2014. https://publications.anl.gov/anlpubs/2015/11/122482.pdf.

[75] H. Almazán *et al.* Improved Sterile Neutrino Constraints from the STEREO Experiment with 179 Days of Reactor-On Data. *Phys. Rev. D*, 102(16):052002, Sep. 2020.

[76] D. Motta *et al.* Prototype scintillator cell for an In-based solar neutrino detector. *Nucl. Instr. and Meth. A*, 547(2-3):368–388, Aug. 2005.

[77] T. Salagnac. *Recherche d'un neutrino stérile avec l'expérience STEREO : développement de l'électronique et identification des neutrinos.* PhD thesis, Université Grenoble Alpes, 2017. https://tel.archives-ouvertes.fr/tel-01757168.

[78] W. Wang *et al.* Performance of the 8-in. R5912 photomultiplier tube with super bialkali photocathode. *Journal of Instrumentation*, 10:T08001, Aug. 2015.

[79] J. B. Birks. *The Theory and Practice of Scintillation Counting.* Pergamon Press Ltd., 1964.

[80] C. Buck *et al.* Production and properties of the liquid scintillators used in the STEREO reactor neutrino experiment. *Journal of Instrumentation*, 14:P01027, Jan. 2019.

[81] C. Aberle *et al.* Large scale Gd-beta-diketonate based organic liquid scintillator production for antineutrino detection. *Journal of Instrumentation*, 7:P06008, Jun. 2012.

[82] A. Bonhomme. *Anomalie des antineutrinos de réacteurs : recherche d'un état stérile avec l'expérience STEREO.* PhD thesis, Université Paris-Saclay, 2018. https://tel.archives-ouvertes.fr/tel-01931309.

[83] E. H. Bellamy *et al.* Absolute calibration and monitoring of a spectrometric channel using a photomultiplier. *Nucl. Instr. and Meth. A*, 339(3):468–476, Feb. 1994.

[84] M. Vialat. *Détection des neutrinos stériles auprès de l'ILL, l'expérience Stéréo*. PhD thesis, Université Grenoble Alpes, 2021. https://tel.archives-ouvertes.fr/tel-03562694.

[85] O. Bourrion *et al.* Trigger and readout electronics for the STEREO experiment. *Journal of Instrumentation*, 11:C02078, Feb. 2016.

[86] J.-S. Réal. STEREO Internal communication, 2016. https://lpsc.in2p3.fr/stereo-private/ShowDocument?docid=179.

[87] S. Agostinelli *et al.* GEANT4: A Simulation toolkit. *Nucl. Instr. and Meth. A*, 506(3):250–303, Jul. 2003.

[88] J. Allison *et al.* Recent developments in GEANT4. *Nucl. Instr. and Meth. A*, 835:186–225, Nov. 2016.

[89] G. Horton-Smith. Generic liquid-scintillator antineutrino detector Geant4 simulation, Feb. 2005. https://www.phys.ksu.edu/personal/gahs/GLG4sim/.

[90] C. Hagmann *et al.* Cosmic-ray shower generator (CRY) for Monte Carlo transport codes. *2007 IEEE Nuclear Science Symposium Conference Record*, pages 1143–1146, 2007.

[91] J.-S. Réal. STEREO Internal communication, 2017. https://lpsc.in2p3.fr/stereo-private/ShowDocument?docid=354.

[92] J.-Ch. Sublet *et al.* FISPACT-II: An Advanced Simulation System for Activation, Transmutation and Material Modelling. *Nucl. Data Sheets*, 139:77–137, Jan. 2017.

[93] I. El Atmani. Search for eV neutrino sterile: Status of STEREO experiment. *J. Phys.: Conf. Ser. Submitted*, 2019.

[94] G. Horton-Smith. Additional gadolinium support for GLG4sim, Mar. 2006. http://neutrino.phys.ksu.edu/ GLG4sim/Gd.html.

[95] O. Litaize, O. Serot, and L. Berge. Fission modelling with FIFRELIN. *Eur. Phys. J. A*, 51(177), Dec. 2015.

[96] H. Almazán *et al.* Improved STEREO simulation with a new gamma ray spectrum of excited gadolinium isotopes using FIFRELIN. *Eur. Phys. J. A*, 55:183, Oct. 2019.

[97] H. Almazán *et al.* Improved FIFRELIN de-excitation model for neutrino applications. *arXiv:2207.10918*, Jul. 2022.

[98] V. Savu. *Reactor neutrino studies: STEREO and NUCLEUS experiments*. PhD thesis, Université Paris-Saclay, 2021. https://tel.archives-ouvertes.fr/tel-03563659.

[99] A. Blanchet. *Recherche du neutrino stérile auprès du réacteur de l'ILL : expérience Stereo*. PhD thesis, Université Paris-Saclay, 2019. https://tel.archives-ouvertes.fr/tel-02428996.

[100] A. Stutz. STEREO Internal communication, 2021. https://lpsc.in2p3.fr/stereo-private/ShowDocument?docid=1373.

[101] J. B. Birks. Scintillations from Organic Crystals: Specific Fluorescence and Relative Response to Different Radiations. *Proc. Phys. Soc. A*, 64(10):874–877, Oct. 1951.

[102] T. Pöschl *et al.* Measurement of ionization quenching in plastic scintillators. *Nucl. Instr. and Meth. A*, 988:164865, Feb. 2021.

[103] L.-R. Labit. *Étude des oscillations de neutrinos à très courtes distances dans le détecteur STEREO à l'ILL, et calibration de celui-ci.* PhD thesis, Université Savoie Mont-Blanc, 2021.

[104] G. Mention *et al.* Reactor antineutrino shoulder explained by energy scale nonlinearities ? *Phys. Lett. B*, 773, Oct. 2017.

[105] A. N. Tikhonov and V. Y. Arsenin. *Solutions of ill-posed problems.* V. H. Winston & Sons, Washington, D.C.: John Wiley & Sons, New York, 1977.

[106] G. Wahba, G. H. Golub, and M. Heath. Generalized Cross-Validation as a Method for Choosing a Good Ridge Parameter. *Technometrics*, 21(2):215–223, May 1979.

[107] K. P. Burnham and D. R. Anderson. *Model Selection and Multimodel Inference: A Practical Information-Theoretic Approach.* Springer, 2002.

[108] H. Akaike. A new look at the statistical model identification. *IEEE Trans. Autom. Control*, 19(6):716–723, Dec. 1974.

[109] C. M. Hurvich and C.-L. Tsai. Regression and time series model selection in small samples. *Biometrika*, 76(2):297–307, Jun. 1989.

[110] J. H. Choi *et al.* Observation of Energy and Baseline Dependent Reactor Antineutrino Disappearance in the RENO Experiment. *Phys. Rev. Lett.*, 116(21):211801, May 2016.

[111] F. P. An *et al.* Improved measurement of the reactor antineutrino flux and spectrum at Daya Bay. *Chin. Phys. C*, 41(1):013002, Jan. 2017.

[112] Y. J. Ko *et al.* Sterile Neutrino Search at the NEOS Experiment. *Phys. Rev. Lett.*, 118(12):121802, Mar. 2017.

[113] M. Danilov and N. Skrobova. New results from the DANSS experiment. *PoS*, European Physical Society Conference on High Energy Physics (EPS-HEP2021), Jul. 2021.

[114] M. Andriamirado *et al.* Improved short-baseline neutrino oscillation search and energy spectrum measurement with the PROSPECT experiment at HFIR. *Phys. Rev. D*, 103(3):032001, Feb. 2021.

[115] G. T. Reynolds *et al.* Muon Capture on Carbon. *Phys. Rev.*, 129(4):1790, Feb. 1963.

[116] L. Michel. Interaction between Four Half-Spin Particles and the Decay of the μ-Meson. *Proc. Phys. Soc. A*, 63(514), May 1950. [Erratum: Proc. Phys. Soc. A **63** 1371 (1950)].

[117] X. Mougeot. Reliability of usual assumptions in the calculation of β and ν spectra. *Phys. Rev. C*, 91(5):055504, May 2015.

[118] L. Périssé. *Modeling of reactor antineutrino spectra.* PhD thesis, Université Paris-Saclay, 2021. https://tel.archives-ouvertes.fr/tel-03538198.

[119] IAEA. ^{12}B Beta minus spectra, 2015. https://www-nds.iaea.org/relnsd/vcharthtml/betashape.html#NUCID=12B&LEVEL=0&DECTYPE=2&DS_SEQNO=103376.

[120] D. Adey *et al.* A high precision calibration of the nonlinear energy response at Daya Bay. *Nucl. Instr. and Meth. A*, 940:230–242, Oct. 2019.

[121] A. Stutz. STEREO Internal communication, 2022. https://lpsc.in2p3.fr/stereo-private/ShowDocument?docid=1405.

[122] J.-S. Réal. STEREO Internal communication, 2017. https://lpsc.in2p3.fr/stereo-private/ShowDocument?docid=254.

[123] L. Bernard. *Recherche d'un neutrino stérile avec l'expérience STEREO : détermination des spectres neutrinos et caractérisation du bruit de fond.* PhD thesis, Université Grenoble Alpes, 2019. https://tel.archives-ouvertes.fr/tel-02471164.

[124] J.-S. Réal. STEREO Internal communication, 2022. https://lpsc.in2p3.fr/stereo-private/ShowDocument?docid=1365.

[125] H. Almazán *et al.* Accurate Measurement of the Electron Antineutrino Yield of ^{235}U Fissions from the STEREO Experiment with 119 Days of Reactor-On Data. *Phys. Rev. Lett.*, 125(20):201801, Nov. 2020.

[126] M. Licciardi. STEREO Internal communication, 2022. https://lpsc.in2p3.fr/stereo-private/ShowDocument?docid=1334.

[127] C.-E. Fillon. *Détermination de la puissance du réacteur de l'ILL pour la prédiction du flux de neutrinos, Internship report.* PhD thesis, CEA Paris-Saclay, 2017. https://hal-cea.archives-ouvertes.fr/cea-01668555.

[128] J. Neyman and E. S. Pearson. On the Problem of the Most Efficient Tests of Statistical Hypotheses. *Phil. Trans. R. Soc. Lond. A*, 231(694-706):289–337, Feb. 1993.

[129] G. J. Feldman and R. D. Cousins. Unified approach to the classical statistical analysis of small signals. *Phys. Rev. D*, 57(7):3873, Apr. 1998.

[130] S. S. Wilks. The Large-Sample Distribution of the Likelihood Ratio for Testing Composite Hypotheses. *Annals Math. Statist.*, 9(1):60–62, Mar. 1938.

[131] X. Qian *et al.* The Gaussian CL$_s$ method for searches of new physics. *Nucl. Instr. and Meth. A*, 827:63–78, Aug. 2016.

[132] M. Agostini and B. Neumair. Statistical Methods Applied to the Search of Sterile Neutrinos. *Eur. Phys. J. C*, 80(750), Aug. 2020.

[133] P. Coloma, P. Huber, and T. Schwetz. Statistical interpretation of sterile neutrino oscillation searches at reactors. *Eur. Phys. J. C*, 81(2), Jan. 2021.

[134] H. Almazán *et al.* Note on arXiv:2005.05301, 'Preparation of the Neutrino-4 experiment on search for sterile neutrino and the obtained results of measurements'. *arXiv.2006.13147*, Jun. 2020.

[135] A. L. Read. Presentation of search results: the CLs technique. *J. Phys. G: Nucl. Part. Phys*, 28(10):2693, Sep. 2002.

[136] T. Junk. Confidence level computation for combining searches with small statistics. *Nucl. Instr. and Meth. A*, 434(2-3):435–443, Sep. 1999.

[137] P. Adamson *et al.* Limits on Active to Sterile Neutrino Oscillations from Disappearance Searches in the MINOS, Daya Bay, and Bugey-3 Experiments. *Phys. Rev. Lett.*, 117(15):151801, Oct. 2016.

[138] A. P. Serebrov *et al.* Search for sterile neutrinos with the Neutrino-4 experiment and measurement results. *Phys. Rev. D*, 104(3):032003, Aug. 2021.

[139] I. G. Alekseev and N. Skrobova. Recent results of the DANSS experiment. *PoS*, The 22nd International Workshop on Neutrinos from Accelerators (NuFact2021), Sep. 2021.

[140] A. M. Ankowski. Improved estimate of the cross section for inverse beta decay. *J. Phys. Conf. Ser.*, 1216(1):012015, Apr. 2019.

[141] G. D'Agostini. A multidimensional unfolding method based on Bayes' theorem. *Nucl. Instr. and Meth. A*, 362(2–3):487–498, Aug. 1995.

[142] W. Tang *et al.* Data Unfolding with Wiener-SVD Method. *Journal of Instrumentation*, 12(10):P10002, Oct. 2017.

[143] F. P. An *et al.* Antineutrino Energy Spectrum Unfolding Based on the Daya Bay Measurement and Its Applications. *Chin. Phys. C*, 45(7):073001, Jul. 2021.

[144] J. Friedman T. Hastie, R. Tibshirani. *The Elements of Statistical Learning. Data Mining, Inference, and Prediction, Second Edition.* Springer, 2001.

[145] J. Ashenfelter *et al.* The PROSPECT Reactor Antineutrino Experiment. *Nucl. Instr. and Meth. A*, 922:287–309, Apr. 2019.

[146] J. Ashenfelter *et al.* Measurement of the Antineutrino Spectrum from ^{235}U Fission at HFIR with PROSPECT. *Phys. Rev. Lett.*, 122(25):251801, Jun. 2019.

[147] H. Almazán *et al.* Joint Measurement of the ^{235}U Antineutrino Spectrum by PROSPECT and STEREO. *Phys. Rev. Lett.*, 128(8):081802, Feb. 2022.

[148] R. Rogly. STEREO-PROSPECT Internal communication, 2021. https://lpsc.in2p3.fr/stereo-prospect/ShowDocument?docid=110.

[149] A. B. Balantekin *et al.* Nonfuel antineutrino contributions in the ORNL High Flux Isotope Reactor (HFIR). *Phys. Rev. C*, 101(5), May 2020.

[150] Nuclear Engineering International. Chinese reactor design evolution, May 2014. https://www.neimagazine.com/features/featurechinese-reactor-design-evolution-4272370/.

[151] J. Cao and K.-B. Luk. An overview of the Daya Bay reactor neutrino experiment. *Nucl. Phys. B*, 908:62–73, Jul. 2016.

[152] D. Adey *et al.* Extraction of the ^{235}U and ^{239}Pu Antineutrino Spectra at Daya Bay. *Phys. Rev. Lett.*, 123(11):111801, Sep. 2019.

[153] N. Haag *et al.* Experimental Determination of the Antineutrino Spectrum of the Fission Products of ^{238}U. *Phys. Rev. Lett.*, 112(12):122501, Mar. 2014.

[154] X. B. Ma *et al.* Uncertainty analysis of fission fraction for reactor antineutrino experiments. *Mod. Phys. Lett. A*, 31(20):1650120, Jun. 2016.

[155] M. Licciardi. STEREO Internal communication, 2021. https://lpsc.in2p3.fr/stereo-private/ShowDocument?docid=1361.

[156] S. Chiba and D. L. Smith. Impacts of Data Transformations on Least-Squares Solutions and Their Significance in Data Analysis and Evaluation. *Journal of Nuclear Science and Technology*, 31(8):770–781, Aug. 1994.

[157] R. Frühwirth, D. Neudecker, and H. Leeb. Peelle's Pertinent Puzzle and its Solution. *EPJ Web of Conferences*, 27(00008), May 2012.

[158] J. C. Hardy, L. C. Carraz, B. Jonson, and P. G. Hansen. The essential decay of pandemonium: A demonstration of errors in complex beta-decay schemes. *Phys. Lett. B*, 71(2):307–310, Nov. 1977.

[159] D. A. Dwyer and T. J. Langford. Spectral Structure of Electron Antineutrinos from Nuclear Reactors. *Phys. Rev. Lett.*, 114(1):012502, Jan. 2015.

[160] V. Kopeikin, M. Skorokhvatov, and O. Titov. Reevaluating reactor antineutrino spectra with new measurements of the ratio between ^{235}U and ^{239}Pu β spectra. *Phys. Rev. D*, 104(7):L071301, Oct. 2021.

[161] V. Kopeikin, Yu. N. Panin, and A. A. Sabelnikov. Measurement of the Ratio of Cumulative Spectra of Beta Particles from ^{235}U and ^{239}Pu Fission Products for Solving Problems of Reactor-Antineutrino Physics. *Physics of Atomic Nuclei*, 84(1):1–10, Apr. 2021.

[162] E. A. McCutchan. Evaluated Nuclear Structure Data File. `https://www.nndc.bnl.gov/ensdf/`, Jun. 2022.

[163] G. Angloher *et al.* Exploring CEvNS with NUCLEUS at the Chooz nuclear power plant. *Eur. Phys. J. C*, 79(1018), Dec. 2019.

[164] G. Angloher *et al.* Results on light dark matter particles with a low-threshold CRESST-II detector. *Eur. Phys. J. C*, 76(25), Jan. 2016.

[165] R. Strauss *et al.* Gram-scale cryogenic calorimeters for rare-event searches. *Phys. Rev. D*, 96(2), Jul. 2017.

[166] A. Onillon *et al.* The NUCLEUS experiment: a search for coherent elastic neutrino-nucleus scattering with reactor antineutrinos. *PoS*, Particles and Nuclei International Conference 2021 (PANIC2021), Sep. 2021.

[167] K. D. Irwin and G. C. Hilton. *Transition-edge sensors*. Springer, 2005.

[168] M. Tinkham. *Introduction to Superconductivity, 2nd Edition*. Dover Publications, 1996.

[169] S. Henry *et al.* The 66-channel SQUID readout for CRESST-II. *Journal of Instrumentation*, 2(11), Nov. 2007.

[170] J. Rothe. *Low-Threshold Cryogenic Detectors for Low-Mass Dark Matter Search and Coherent Neutrino Scattering*. PhD thesis, Technische Universität München, 2021. https://mediatum.ub.tum.de/doc/1576351/.

[171] V. Wagner *et al.* Exploring CEvNS of reactor neutrinos with the NUCLEUS experiment. *J. Phys.: Conf. Ser.*, 2156(012118), Aug. 2021.

[172] C. Goupy. Exploring coherent elastic neutrino-nucleus scattering of reactor neutrinos with the NUCLEUS experiment. In *14th International Conference on Identification of Dark Matter*, Vienna, Austria, Jul. 2022.

[173] R. K. Romani. Stress Induced Background in Cryogenic Crystal Calorimeters. In *EXCESS Workshop*, Vienna, Austria, Jul. 2022.

[174] A. Erhart *et al.* Development of an Organic Plastic Scintillator-based Muon Veto Operating at Sub-Kelvin Temperatures for the NUCLEUS Experiment. *J. Low Temp. Phys.*, Sep. 2022.

[175] V. Wagner *et al.* Development of a compact muon veto for the NUCLEUS experiment. *Journal of Instrumentation*, 17(05), May 2022.

[176] Saint Gobain Crystals. BC-408. https://www.crystals.saint-gobain.com/products/bc-408-bc-412-bc-416, 2021.

[177] COMPASS collaboration. COMPASS-II proposal. *CERN-SPSC-2010-014*, SPSC-P-340, May 2010.

[178] D. E. Groom, N. V. Mokhov, and S. I. Striganov. Muon stopping power and range tables 10 MeV to 100 TeV. *Atom. Data Nucl. Data Tabl.*, 78(2):183–356, Jul. 2001.

[179] KETEK. SiPM TIA Module. https://www.ketek.net/wp-content/uploads/KETEK-SiPM-Module-PE33xx-WB-TIA-xP.pdf, 2022.

[180] Saint Gobain Crystals. BC-91A. https://www.crystals.saint-gobain.com/products/scintillating-fiber, 2021.

[181] TORAY. Lumirror Foil. https://www.toray.eu/products/films/fil_0010.html, 2021.

[182] T. Eggert, W. Gebauer, and F. Wiest. Latest Developments in KETEK's Silicon Photomultiplier Solutions. https://indico.cern.ch/event/774201/contributions/3429249/attachments/1878071/3093392/C04_190618_-_KETEK_SiPM_-_TEG_-_iWorid_Tobias.pdf, 2019.

[183] R. Bayerlein and I. Fleck. Characterization of a Silicon-Photomultiplier Using Ultra-Fast Pulsed LED. https://www.hep.physik.uni-siegen.de/teaching/masterlab/manuals/SiPM_Manual.pdf, 2021.

[184] SensL. An Introduction to the Silicon Photomultiplier. https://www.seti.net/cosmic-rays/SETIPixel/CosmicWatch-Desktop-Muon-Detector-v2-master/Datasheets/Intro_to_SiPMs.pdf, 2011.

[185] F. Acerbi and S. Gundacker. Understanding and simulating SiPMs. *Nucl. Instr. and Meth. A*, 926:16–35, May 2019.

[186] F. Nagy *et al.* Afterpulse and delayed crosstalk analysis on a STMicroelectronics silicon photomultiplier. *Nucl. Instr. and Meth. A*, 759:44–49, Sep. 2014.

[187] First Sensor. Introduction to silicon photomultipliers (SiPMs). https://www.first-sensor.com/cms/upload/appnotes/AN_SiPM_Introduction_E.pdf, 2019.

[188] V. Chmill, E. Garutti, R. Klanner, M. Nitschke, and J. Schwandt. On the characterisation of SiPMs from pulse-height spectra. *Nucl. Instr. and Meth. A*, 854:70–81, May 2017.

[189] L. Klinkenberg. NUCLEUS Internal communication, 2021. https://twiki.cern.ch/twiki/bin/view/NUCLEUS/2021_03_31.

[190] A. Tang, G. Horton-Smith, V. A. Kudryavtsev, and A. Tonazzo. Muon simulations for Super-Kamiokande, KamLAND, and CHOOZ. *Phys. Rev. D*, 74(5):053007, Sep. 2006.

[191] A. A. Sonzogni, E. A. McCutchan, T. D. Johnson, and P. Dimitriou. Effects of Fission Yield Data in the Calculation of Antineutrino Spectra for 235U (n,fission) at Thermal and Fast Neutron Energies. *Phys. Rev. Lett*, 116(13):132502, Apr. 2016.

[192] S. Vinogradov. Analytical models of probability distribution and excess noise factor of Solid State Photomultiplier signals with crosstalk. *Nucl. Instr. and Meth. A*, 695:247–251, Dec. 2012.

université PARIS-SACLAY

ÉCOLE DOCTORALE
Particules, hadrons, énergie et noyau : instrumentation, imagerie, cosmos et simulation (PHENIICS)

Titre: Mesure du spectre antineutrino de fission de l'^{235}U par l'expérience STEREO et préparation de l'expérience NUCLEUS de diffusion cohérente de neutrinos.
Mots clés: neutrino stérile, spectre antineutrino, anomalie de réacteur, diffusion cohérente

Résumé:

La présente thèse de doctorat porte sur l'étude des antineutrinos de réacteurs nucléaires, via les expériences STEREO et NUCLEUS.

STEREO est une expérience se focalisant sur les anomalies des antineutrinos de réacteurs, portant sur des déviations de la forme et de la norme du spectre en énergie mesuré des antineutrinos par rapport à leur prédiction. L'expérience investigue la possibilité d'une oscillation du neutrino vers un éventuel état stérile comme explication de l'anomalie en flux, tout en mesurant avec précision le spectre d'antineutrino induit par la fission de l'^{235}U du réacteur de recherche de l'Institut Laue-Langevin. Dans ce contexte, mon travail a consisté à contraindre l'échelle en énergie de l'expérience, point crucial pour une comparaison de la mesure avec une prédiction, et à développer un formalisme de déconvolution pour fournir le spectre de référence corrigé de tous les effets de détection. J'ai étendu ce formalisme à l'analyse jointe des données des expériences STEREO, PROSPECT et Daya Bay, pour fournir des spectres antineutrinos de référence issus de la fission de l'uranium et du plutonium.

La motivation de l'expérience NUCLEUS est l'étude d'un nouveau canal d'interaction du neutrino avec la matière, la diffusion cohérente neutrino-noyau. Cette expérience prendra des données à la centrale nucléaire de Chooz à partir de 2024. Le faible taux de comptage attendu pour le signal requiert une rejection du bruit de fond extrêmement efficace, combinant blindage actif et passif. J'ai ainsi pris la responsabilité de l'implémentation complète d'un prototype du véto muon qui sera utilisé pour rejeter le bruit de fond induit par les muons atmosphériques, typique de ces expériences en surface. J'ai validé les performances de ce prototype permettant le lancement en production du détecteur final.

Title: Measurement of the ^{235}U fission antineutrino spectrum by the STEREO experiment and preparation of the NUCLEUS coherent neutrino scattering experiment.
Keywords: sterile neutrino, antineutrino spectrum, reactor anomaly, coherent scattering

Abstract:

The present doctoral thesis focuses on the study of antineutrinos emitted by nuclear reactors, with the STEREO and NUCLEUS experiments.

STEREO is an experiment exploring the anomalies of reactor antineutrino physics, consisting in deviations in the shape and rate of the measured antineutrino energy spectrum with respect to the prediction. The experiment investigates the scenario of an oscillation towards a sterile neutrino state as an explanation of the flux anomaly, while performing a precision measurement of the antineutrino spectrum induced by the fission of ^{235}U of the Institut Laue-Langevin research reactor core. In this context, my work consisted in constraining the energy scale of the experiment, a prerequisite for an accurate comparison of the measurement with a prediction, and in developing an unfolding framework to provide the reference spectrum free of detector effects. I extended this framework to a joint analysis of STEREO, PROSPECT and Daya Bay data, to provide reference antineutrino spectra from the fission of uranium and plutonium.

The motivation of the NUCLEUS experiment is to study a new neutrino-matter interaction channel, the neutrino-nucleus coherent scattering. This experiment will be operated at Chooz nuclear power plant, from 2024 onwards. The moderate expected counting rate for the neutrino signal commands to be able to properly reject background events, with a highly efficient active and passive shielding strategy. I was in charge of the full commissioning of a prototype panel of the muon veto that will be used in the experiment to reject the atmospheric muons induced background, typical of ground-level particle physics experiments. I validated the performance of this prototype, allowing to launch the production of the final detector.